UNIVERSIDAD DE CHILE
FACULTAD DE CIENCIAS FÍSICAS Y MATEMÁTICAS
DEPARTAMENTO DE INGENIERÍA QUÍMICA, BIOTECNOLOGÍA Y MATERIALES

HYDROGEN FROM WASTEWATER: A PHENOMENOLOGICAL MODEL FOR COMPOSITE BIOACTIVE MEMBRANE REACTORS

TESIS PARA OPTAR AL GRADO DE MAGÍSTER EN CIENCIAS DE LA INGENIERÍA, MENCIÓN QUÍMICA

MEMORIA PARA OPTAR AL TÍTULO DE INGENIERA CIVIL QUÍMICA

ISABELLA BOESE CORTÉS

PROFESOR GUÍA:
FELIPE DÍAZ ALVARADO

PROFESORA CO-GUÍA:
ANA LUCÍA PRIETO SANTA

MIEMBROS DE LA COMISIÓN:
JUAN SALGADO HERRERA
JUAN ASENJO DE LEUZE DE LANCIZOLLE

Este trabajo ha sido parcialmente financiado por ANID FONDECYT 11191123

SANTIAGO DE CHILE
2024

RESUMEN DE LA TESIS PARA OPTAR AL GRADO DE:
MAGÍSTER EN CIENCIAS DE LA INGENIERÍA, MENCIÓN QUÍMICA
Y MEMORIA PARA OPTAR AL TÍTULO DE INGENIERA CIVIL QUÍMICA
POR: ISABELLA BOESE CORTÉS
FECHA: 2024
PROF. GUÍA: FELIPE DÍAZ ALVARADO

HIDRÓGENO DESDE AGUAS RESIDUALES: UN MODELO FENOMENOLÓGICO PARA REACTORES DE MEMBRANA COMPUESTA BIOACTIVA

Los bioreactores anaerobios de membrana para la simultánea inmovilización celular y separación de gases son novedosos y pueden aumentar la conversión fermentativa de aguas residuales en hidrógeno (H_2). A pesar de su potencial rentable para intensificar procesos, los modelos de H_2 están subdesarrollados y se basan en ecuaciones empíricas simples que carecen de una base física.

Este trabajo tiene como objetivo crear un modelo fenomenológico de un reactor de membrana compuesta bioactiva (CBMem), para la intensificación del proceso de H_2 a partir de aguas residuales. Para esto, (i) se formuló e implementó un conjunto de ecuaciones que integra mecanismos biológicos, cinéticos y de transferencia de masa; (ii) se caracterizó la evolución de la capa bioactiva para la evaluación del desempeño y vida útil de la CBMem, y (iii) se propusieron nuevas condiciones operativas y parámetros de membrana basado en un análisis de sensibilidad.

El sistema de ecuaciones consiste en ecuaciones diferenciales basadas en balances de masa para seguir los perfiles de concentración de células, sustrato e H_2 en cada dominio. Además de la cinética y la transferencia de masa, se consideraron los efectos del crecimiento celular en la difusión y la migración celular estimulada por el gradiente de sustrato y limitación de espacio. Mediante adecuadas condiciones de borde, se garantizó el acoplamiento de dominios y el seguimiento de la dinámica del proceso.

El modelo se discretizó para su implementación en GNU Octave. Tras calibraciones secuenciales, el modelo fue ajustado y validado utilizando datos experimentales de una CBMem a escala de laboratorio, demostrando poder seguir el flujo másico de H_2 de salida. Además, simulaciones para operaciones extendidas confirmaron su capacidad para representar la dinámica de los fenómenos biológicos, identificar riesgos operativos, tales como el agotamiento del sustrato, la inhibición de H_2 y el crecimiento excesivo de células, y predecir el desempeño del proceso y la vida útil de la membrana basándose en criterios de eficiencia de captura, crecimiento celular y agotamiento del sustrato. Finalmente, se realizó un análisis de sensibilidad para comprender los efectos de los cambios en los parámetros de operación y diseño en el rendimiento del proceso, variando la demanda química de oxígeno, la masa celular inicialmente inmovilizada o el ancho de la capa bioactiva.

Este trabajo ofrece el primer modelo fenomenológico para bioreactores de membrana de múltiples dominiospara la producción de H_2 a partir de aguas residuales, contribuyendo a una mejor comprensión del comportamiento del sistema y permitiendo futuras mejoras en la toma de decisiones relacionadas con el diseño de membranas biológicas.

RESUMEN DE LA TESIS PARA OPTAR AL GRADO DE:
MAGÍSTER EN CIENCIAS DE LA INGENIERÍA, MENCIÓN QUÍMICA
Y MEMORIA PARA OPTAR AL TÍTULO DE INGENIERA CIVIL QUÍMICA
POR: ISABELLA BOESE CORTÉS
FECHA: 2024
PROF. GUÍA: FELIPE DÍAZ ALVARADO

HYDROGEN FROM WASTEWATER: A PHENOMENOLOGICAL MODEL FOR COMPOSITE BIOACTIVE MEMBRANE REACTORS

Anaerobic membrane bioreactors for simultaneous cell immobilization and gas separation are novel and can increase fermentative conversion of wastewater into hydrogen (H_2). Despite being a cost-effective approach for process intensification, H_2 models are undeveloped and rely on simple empirical equations without a physical basis.

This work aims to create a phenomenological model of a composite bioactive membrane reactor (CBMem) for process intensification of H_2 from wastewater. To achieve this goal, (i) a set of equations that integrates biological, kinetic, and mass transfer mechanisms was formulated and implemented; (ii), the evolution of the bioactive layer was characterized for the evaluation of the H_2 yield, capture efficiency, and CBMem lifespan, and (iii) new operational conditions and membrane parameters were proposed to intensify the process based on a sensitivity analysis.

The systems of equations were coupled second-order partial or ordinary differential equations based on mass balances to follow the concentration profiles of cells, substrate, and H_2 in each domain. Besides biochemical kinetics and mass transfer, the effects of cell growth on diffusion and cell migration stimulated by the substrate gradient and space limitation were included. Through suitable boundary conditions, domain coupling and process dynamics were ensured.

The model was transformed using the finite-difference method for implementation in GNU Octave. After a sequential calibration strategy, model calibration and validation were performed based on experimental data from a lab-scale CBMem. The developed model was able to follow the H_2 mass flow outlet with a good confidence. Simulations for extended operations confirmed the model's capacity to represent biological phenomena dynamics, and identify operational risks, such as substrate depletion, H_2 inhibition, and excessive cell growth. The model could also predict process performance and the membrane's lifespan based on capture efficiency, cell growth, and substrate depletion criteria. Finally, the sensitivity analysis allowed the comprehension of the effects of changing operation and design parameters, such as the chemical oxygen demand and the initially immobilized cell mass or bioactive layer width.

This work offers the first phenomenological model for multi-domain membrane bioreactors for H_2 production and separation from wastewater, contributing to a better comprehension of the system's behavior and enabling future improvements in model-based decision making on next-generation biological membrane designs.

"Live the questions now.
Perhaps then, someday far in the future,
you will gradually, without even noticing it,
live your way into the answer."

— ***Rainer María Rilke***

Agradecimientos

La escritura de esta sección va más allá del trabajo de título; permite detenerse a mirar, reconocer el camino recorrido y a los que lo acompañaron, y agradecer todo momento vivido. Cerrar esta etapa de aprendizaje profesional es un gran hito para mí.

Quisiera partir agradeciendo a mi mamá, una mujer resiliente y dulce, a quien he tenido el honor de tener a mi lado. Mamá, trazas nuestro camino para ser feliz hoy y siempre. Gracias por pensar siempre en nosotras.

También quiero agradecer a Crisitan, mi chiqui. He aprendido mucho de tu calma y fuerza al enfrentar los desafíos de la vida. Espero que mi futuro cuente con tu compañía.

A Felipe, mi profesor guía: gran parte de mi desarrollo como profesional ha sido influenciado por tu apoyo y creatividad. Permitiste a que me detuviera en las preguntas, más que en las respuestas, manteniéndome positiva durante el proceso. Además de ser un excelente profesor, eres una gran persona.

A profesora Ana, mi co-guía. Su trabajo inspiró la concepción del mío y su espíritu de investigadora me impulsó ha alcanzar varios logros profesionales. Gracias por su empuje.

A las amigas y amigos que me dio este ciclo llamado universidad; por enseñarnos, acompañarnos, provocarnos risas. Gracias a ustedes estos años fueron un disfrute. A mis amig*s desde los inicios de la Universidad: Flo, Martín, Iván, Mati, Alex, Peluka, Joako, Pancho, Pichún. A mis amig*s del DIQBM: Cami, Debo, Mati, Seba, Mika, Nico S., Benja, Paula y Belén. A las personas que conocí por los juegos de la vida: Gabri y Gabi. A los compañer*s motivados de la UVM y el CEIQBM 2020. A todos ustedes, gracias.

A los compañer*s de mi experiencia laboral. Si no hubiera empezado a trabajar tempranamente, no hubiera tenido la oportunidad de conocer a personas tan geniales. A mis amig*s de la era H2 Chile: Jesu, Enrique, Ignacia y Caro. También gracias totales a las personas del Clúster de Energía de GIZ que me animaron en los últimos días previo a la entrega.

A los amig*s del colegio, una etapa que es por mi muy querida; especialmente Cata, Nacho y Jorge.

A mis amigas de Alemania; pueden pasar muchos años pero seguimos entendiéndonos como en aquella época: Nele, Sarah, Denise, Mariam, gracias.

Table of Content

Tables Index

Figures Index

Chapter 1

Introduction

This chapter presents the introduction of the thesis. The first section delivers the motivation and general background considering the global energy and water perspectives to develop wastewater-to-hydrogen processes by dark fermentation and techniques for improved fermentative hydrogen production. The chapter also presents the research questions, goals, and scientific contribution. Finally, the thesis structure is outlined.

1.1. Motivation and general background

1.1.1. Water and energy nexus

The increasing global energy demand and the reduction of carbon footprint are challenging the world to find new energy sources. Energy sources can be categorized as nonrenewable or renewable. Nonrenewable energy sources are stock limited, which include coal, natural gas, petroleum, hydrocarbon gas liquids, and nuclear energy. In contrast, renewable energy sources are naturally replenishing, but flow-limited. The major types are solar, geothermal, biomass, hydropower, and wind energy [1]. Fig. 1.1A illustrates the world historical total energy supply by source, where the intransigent practice of nonrenewable over renewable energy supply is identified.

Energy is used in the residential, industrial, and transport sector [2]. Globally in 2018, the highest total final consumption was used by the transport sector with 2,891 Mtoe[1], equal to 29.1 %, followed by the industry sector with 28.6 % (Fig. 1.1B). At present, petroleum based fuels are the sole source of energy for these sectors [3, 4]. As the global energy demand is mainly met by fossil fuels, combustion gases are emitted, such as CO_2, CO, SO_2, NOx, PM, and heavy metals (see Annex A for abbreviations) [5].

Almost all combustion byproducts have negative effects on the environment and human health; specifically CO_2 contributes to the greenhouse effect, and thereby to global warming and climate change [6]. Fig. 1.1C shows the global historic energy-related CO_2 emissions by sector and by fuel source. To abate greenhouse gas emissions and uncontrolled climate change, net-zero transition is necessary. Effective decarbonization actions include shifting the energy mix away from fossil fuels and towards "clean" energy sources [7].

[1] 1 tonne of oil equivalent (toe) is equivalent to 11.63 MWh. Thus, 2,891 Mtoe is equal to 33,622.33 TWh.

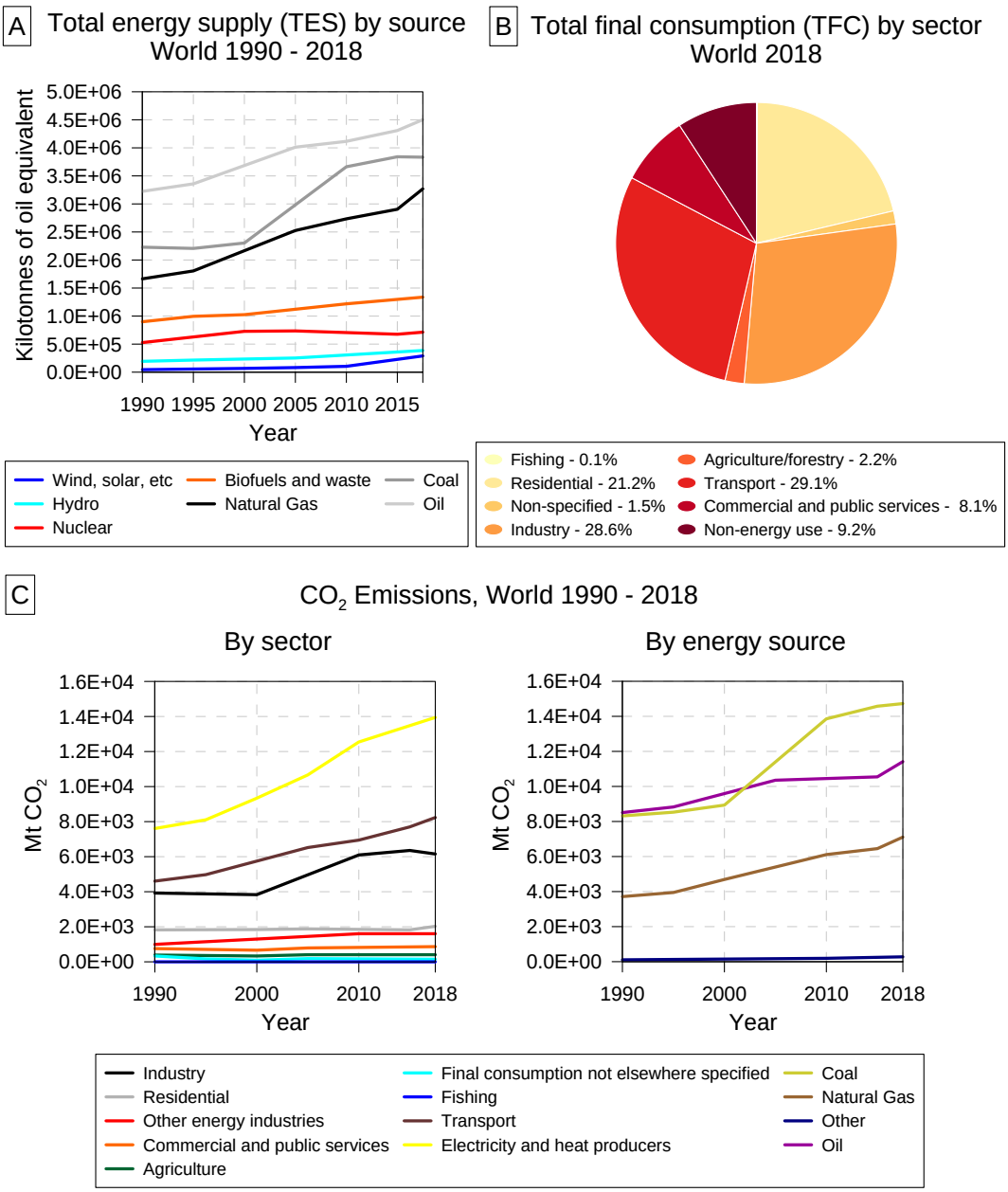

Fig. 1.1: (A) Total energy supply by source, World 1990-2018. Reconstructed from data published by IEA [8]; (B) total final consumption by sector, World 2018. Reconstructed from data published by IEA [9]; and (C) energy-related CO_2 emissions by sector (left) and by fuel (right), World 1990 - 2018. Reconstructed from data published by IEA [10, 11].

Both renewable and nonrenewable energy sources can be transformed into secondary energy sources, such as electricity and hydrogen (H_2) [12]. H_2 is considered an attractive energy vector because of the variety of production methods (some of them with a low carbon footprint) [3, 13], and its high energy content per unit mass (120 $\frac{MJ}{kg}$), which is nearly three times the energy content of gasoline [14].

The global demand for H_2, which has increased more than threefold since 1975, continues to rise (Fig. 1.2). As of 2018, it reached approximately 74 Mt, with 42.6 % in ammonia production

and 51.8 % in the refinery sector [15]. However, H_2 is almost entirely supplied by fossil fuels. Consequently, the production accounts for 830 Mt CO_2 per year globally [16]. Promoting H_2 production processes with a low carbon footprint will have a significant impact in decarbonizing the industry sector [4]. Thus, alternative technologies, such as water electrolysis or biological pathways, are currently being discussed.

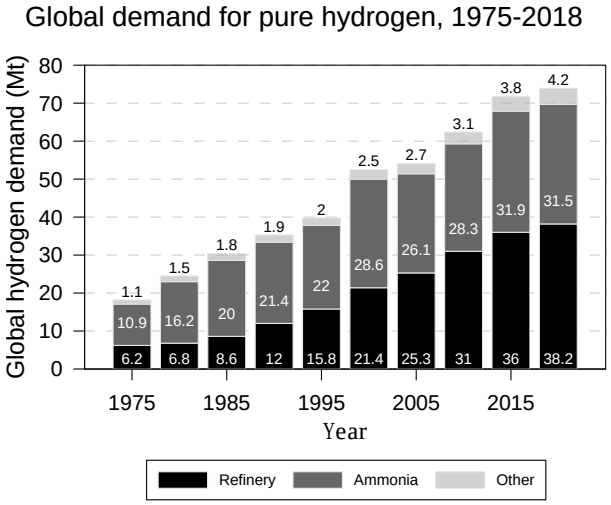

Fig. 1.2: Global demand of pure H_2 in refinery, ammonia and other sectors for the period 1975-2018. Reconstructed from data published by IEA in 2019 [16].

Due to the flows of the H_2 production technologies, process design will have to take into account the water balance besides carbon footprint. At a global level, water use has grown continuously at an annual rate of about 1 % [17]. Moreover, the world could face a 40 % global water deficit by 2030 under a business-as-usual scenario [18]. Whereas agriculture currently uses the major share (69 %) of global water withdrawals, the industry (including energy and power generation) accounts for 19 %, and cities are responsible for the remaining 12 % [19]. Furthermore, in many regions, the water use strategies are inefficient and intensify environmental degradation, including depletion of aquifers, reduction of river flows, degradation of wildlife habitats, and pollution [19].

The problems presented above are not foreign to most of the world's nations. Moreover, as the effects of climate change continue to exacerbate water stress, location-specific evaluation of water footprint is required [20]. Water security considerations will arise in countries that are potential major clean H_2 producers and exporters, such as Chile.

Wastewater is a useful source for H_2 production. Its abundance and accessibility, which is unlikely to diminish in volume in the near future, can improve residual management by closing waste loops and generating additional value streams [21], e.g. through wastewater-to-energy processes [22]. These have several advantages. On the one hand, biogas can be produced for electricity or heat generation [23]; on the other hand, adopting water reuse technology can lead to a more resilient water supply, a decrease in transportation costs of disposal of wastewater sludge [21], avoidance of effluent discharge to the local waterway, and nutrient recovery (with the production of low-carbon fertilizers) [24]. Thereby, simultaneous wastewater treatment and H_2 production could assist in meeting some of the local and global energy and water challenges.

1.1.2. Technologies for H_2 production

H_2 does not exist freely in nature and is only produced from other sources of energy, such as water, fossil fuels, or biomass; therefore it is considered an energy carrier [4, 25]. H_2 production can be achieved by electrochemical, thermochemical, and biological processes where each method has its advantages and disadvantages [3, 26]. The maturity status and efficiency of existing technologies are shown in Table 1.1.

H_2 production mainly occurs via steam reforming of natural gas (a thermal process), which requires a direct fuel input. Alternatively, water electrolysis has gained attention as it splits water into hydrogen and oxygen without producing CO_2 emissions. But, it needs electricity, which today is mainly produced from fossil fuels (65 % of total electricity production [27]), and requires purified water as a feedstock (9 $\frac{L_{H_2O}}{kg_{H_2}}$ [28]) [20]. Although both methods are popular, their sustainability is under debate [29–32]. Instead, H_2 can also be produced from biomass through biological processes, including dark fermentation (see Annex B). Fermentation has attractive operating conditions related to ambient temperature and atmospheric pressure, and a less intensive dependence on natural resources [3, 33]. However, this technology will be mature in the long-term [34].

Table 1.1: Current status of existing H_2 production technologies [34].

Technology	**Feedstock**	**Efficiency**	**Maturity**
Steam reforming	Hydrocarbons	70 % - 85 %	Commercial
Partial oxidation	Hydrocarbons	60 % - 75 %	Commercial
Autothermal reforming	Hydrocarbons	60 % - 75 %	Near-term
Plasma reforming	Hydrocarbons	9 % - 85 %	Long-term
Aqueous phase reforming	Carbohydrates	35 % - 55 %	Middle-term
Ammonia reforming	Ammonia	NA[a]	Near-term
Biomass gasification	Biomass	35 % - 50 %	Commercial
Photolysis	Sunlight+water	0.5 %	Long-term
Dark fermentation	Biomass	60 % - 80 %	Long-term
Photofermentation	Biomass+sunlight	0.1 %	Long-term
Microbial electrolysis cells	Biomass+electricity	78 %	Long-term
Alkaline electrolyzer	H_2O+electricity	50 % - 60 %	Commercial
PEM electrolyzer	H_2O+electricity	55 % - 70 %	Near-term
Solid oxide electrolysis cells	H_2O+electricity+heat	40 % - 60 %	Middle-term
Thermochemical water splitting	H_2O+heat	NA[a]	Long-term
Photoelectrochemical water splitting	H_2O+sunlight	12.4 %	Long-term

[a] NA = Not available.

1.1.3. Dark fermentation

Dark fermentation (DF), also called acidogenic fermentation, occurs in nature within anaerobic digestion (Fig. 1.3). During this process, organic matter is degraded in anaerobic conditions by microbial consortia (hydrolyzers, acetogens, facultative anaerobic H_2 producers, methanogens, and *archaea*) to produce CH_4 and CO_2 as end products. H_2 is an intermediate product and is imme-

diately utilized by other microbes [35]. Nevertheless, DF can also be reproduced under controlled conditions using a single species or a consortium of microorganism [36].

Based on their sensitivity towards the presence of oxygen, H_2-producing microorganisms are classified as facultative anaerobes (are viable in both anaerobic and aerobic conditions) and obligate anaerobes (require strictly anaerobic conditions) [35]. The yield of the H_2 production depends on the metabolic pathway [35], which in turn depends on the involved microorganism. In case of facultative anaerobes, for instance *E. coli*, the production of H_2 is via the pyruvate formate lyase (PFL) pathway with a limit on the H_2 yield of a maximum of 2 $\frac{mol_{H_2}}{mol_{glucose}}$ [3, 35]. In case of strict anaerobes, such as *Clostridium sp.*, the production of H_2 is via the pyruvate ferredoxin oxidoreductase (PFOR) pathway with a H_2 yield that can be either 2 or 4 $\frac{mol_{H_2}}{mol_{glucose}}$ [3, 35]. Annex B.2.1 details the microbiology and biochemistry of DF.

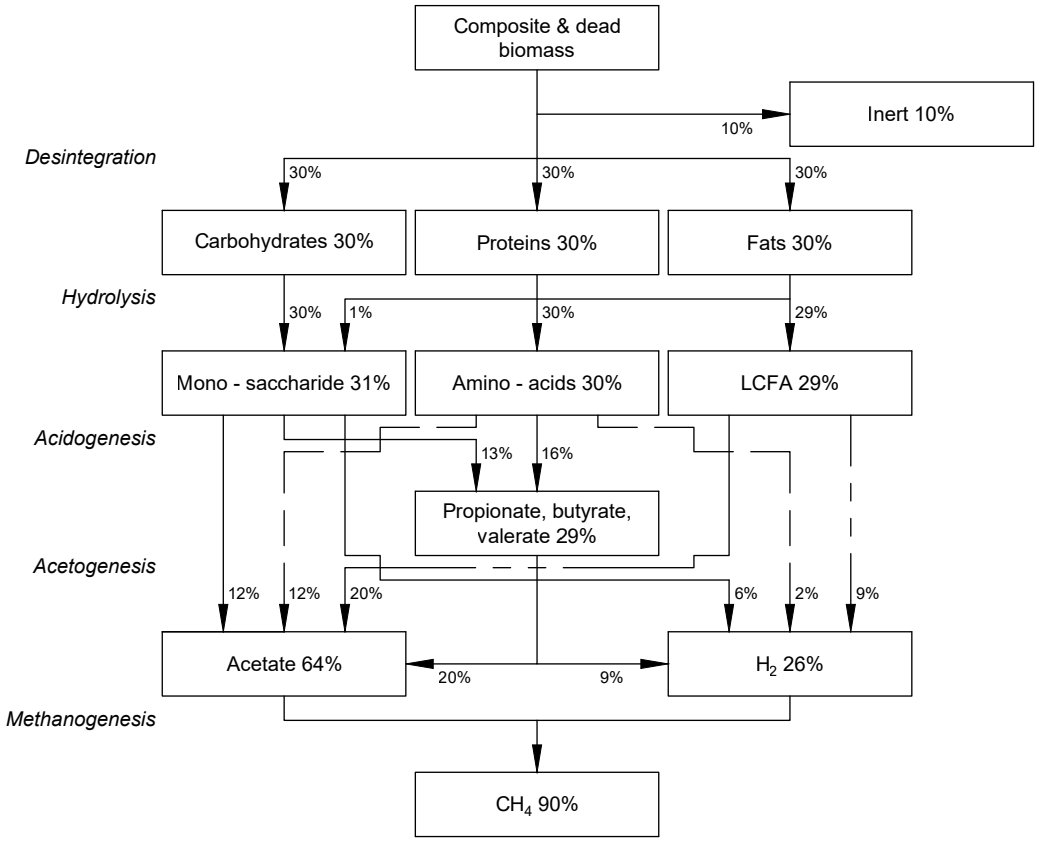

Fig. 1.3: Chemical oxygen demand (COD) flux in anaerobic digestion with DF for a particulate composite comprised of 10 % inerts, and 30 % each of carbohydrates, proteins and lipids (in terms of COD). Propionic acid (10 %), butyric acid (12 %) and valeric acid (7 %) are grouped in the figure for simplicity [37].

Despite its advantages, the main limitation of DF is its low H_2 production yield and rate [33, 38], which are attributed to the simultaneous use of carbon sources for cell biomass generation [3], the thermodynamically favorable formation of organic acids (acetic and butyric acids) [39], and the presence of H_2-consumers that decrease the net production [39]. Hence, the maturity status of DF is still at laboratory scale [34]. Developing an appropriate bioreactor with a mixed culture, low-cost substrates and optimal conditions is crucial to convert DF in an economically feasible process.

1.1.4. Techniques to improve fermentative H_2 production

Fermentative H_2 production can be enhanced through improvements in the bioreactor's design or through model-based approaches. Advances in reactor design for DF has been carried out by numerous experiments. Many have focused on the variation of operational parameters, which are usually: feedstock, temperature, pH, and HRT (see Annex B.2.2). Besides, the reactor configuration is another approach to improve fermentative H_2 production. This has led to systems with more robust and reliable performance that are stable over months, have better resistance to short-term fluctuations in operational parameters, and show improved volume production rates [40].

Reactors can be classified based on the mode of implementation of the fermentation process, i.e., batch, semi-continuous, and continuous. Most studies on DF have been conducted using batch mode due to its simplicity, low-cost design, and ease of control [41], which make it more suitable for initial optimization studies [40]. At an industrial scale, continuous reactors are required due to higher efficiencies; of those, continuous stirred-tank reactors (CSTRs) are the most commonly used [42–44]. However, many other bioreactors with associated acronyms (MBR [45], UASB [44, 46], AFBR [47, 48], ASBR [49, 50], CIGSB [51]) have been investigated [52]. Annex B.2.3 details each bioreactor's working principle, advantages, and limitations. Annex B.2.4 further details the classification of membrane bioreactors, and Annex B.2.5 summarizes DF experiments that used wastewater as substrate.

Modeling is another improvement strategy. Even if experimental studies are required to validate the model accuracy [53, 54], it has the following advantages [53–58]:

1. It is an economical alternative to costly and time-consuming experiments.
2. It can predict the process performance under varying conditions. Thereby, it allows process design, process optimization, and scale-up.
3. Compared to experiments, it is easier to discern the synergistic effects of multiple variables and the existence of varied bacterial species in mixed cultures.
4. Depending on the modeling strategy, it can deliver a good representation of complex processes and thus, facilitate the comprehension of the process and the interactions between factors.

Despite the advantages, process optimization of DF remains limited to experimental studies. Moreover, biological H_2 production models are far less mature than anaerobic digestion and no commercial simulator is available for H_2 [54]. Finally, empirical models remain the most widely used, even though a physical basis is absent [54].

Phenomenological models can improve the reactor design and optimize the involved processes. However, simplifications of the mathematical description may be necessary to treat the complexity of DF. This applies especially when novel bioreactors are designed, such as multi-domain anaerobic membrane bioreactors [59].

1.1.5. Composite bioactive membranes for wastewater-to-H_2 processes

Dark fermentation should be operated under conditions that simultaneously favor the activity of H_2 producers and reduce the activity of H_2 consumers [41]. A design-based solution is cell immobilization of selected microbial species on membranes promoting high cell-density cultivation.

Immobilization also allows cell resistance to inhibitory substrates or products, protection against shear forces, and operation at higher dilution rates, which in turn increases reaction rates and productivity. Ideal isolation techniques also allow to separate H_2 producers from H_2 consumers, favoring net H_2 production.

Moreover, at high partial pressure of H_2, the conversion of substrate to H_2 in dark fermentation decreases [52], and the metabolic flux will tend to other products such as organic acids, ethanol, and butanol [41, 60]. Besides sparging with an inert gas (e.g., N_2 or CO_2) or applying vacuum, membrane technology for gas separation can reduce the H_2 partial pressure [3].

Within wastewater-to-hydrogen systems, multi-domain anaerobic membrane bioreactors allow simultaneous biological production and extraction of the H_2 gas from a wastewater fluid [61–63]. An example is the composite bioactive membrane (CBMem) proposed by Prieto et al. (2016). The researchers isolated H_2-producing acetogens from methanogens through encapsulation with cast poly(vinyl alcohol) in a multi-layer configuration (hollow-fiber membrane/immobilized cells/sealant layer) for simultaneous H_2 production and separation (Fig. 1.4) [63]. It was demonstrated that the CBMem module offers a solution to the microbial competition problem without requiring waste pretreatment. Additionally, by providing a high surface area for gas transfer, this invention is an efficient mechanism for removing the H_2 once it is produced. The module may solve the dual problem of waste disposal and H_2 generation cost-effectively. However, further research is needed to improve scale-up.

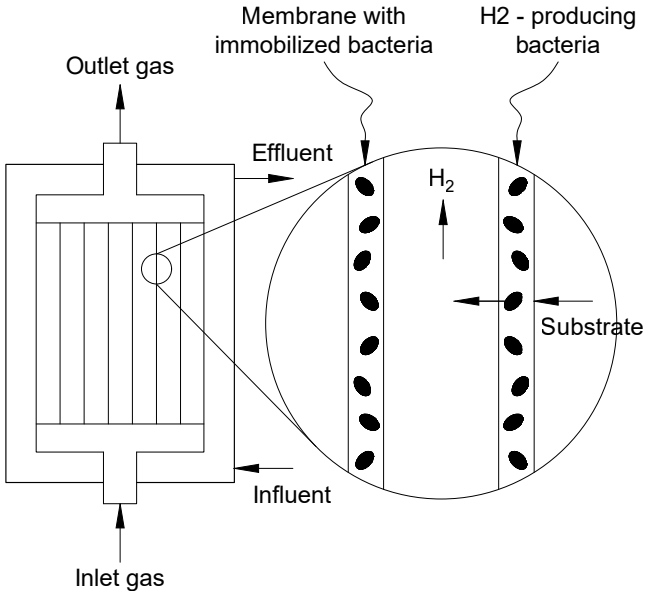

Fig. 1.4: Schema of the CBMem [63].

1.2. Research questions and goals

The main goal of this thesis is to create a phenomenological model of a composite bioactive membrane reactor for process intensification of H_2 from wastewater. More precisely, this study intends to answer the following research questions:

RQ1: What are the critical physical, chemical, and biological processes in a CBMem reactor to sustain a dynamic model of its performance?

RQ2: How does the bioactive layer evolve and influence the H_2 yield, capture efficiency, and lifespan of a CBMem module?

RQ3: What is the impact on the H_2 yield, capture efficiency, and membrane's lifespan when improving the operational conditions and membrane parameters?

To answer each research question and reach the main goal, the following specific goals are proposed:

SG1: To formulate a phenomenological model which integrates relevant biological, kinetic and mass transfer mechanisms involved in the H_2 production in a CBMem reactor.

SG2: To characterize the evolution of the bioactive layer through a model-based approach for the evaluation of H_2 yield, capture efficiency, and lifespan of the CBMem module.

SG3: To propose new operational conditions and membrane parameters to intensify the process based on a sensitivity analysis of the model.

1.3. Scientific contribution

The models proposed in the literature so far only cover parts of the studied system, which may be due to the unexploited CBMem technology. Developing reliable models for membrane bioreactors for H_2 production is critical for reactor design, process intensification, and science-based scale-up. Thus, the thesis' novelty is developing a multi-domain phenomenological model for a CBMem reactor for fermentative H_2 production from wastewater, sensitive to changes in the internal design and operational conditions, namely: spatial distribution, mass transfer and reaction, and cell dynamics.

This research may contribute to a better comprehension of the system's behavior and improve the CBMem technology. Consequently, it could benefit the design of experiments, the construction of next-generation membrane-based bioreactors, and the development of models for similar systems. Finally, it may provide society with a tool to explore wastewater-to-H_2 applications.

1.4. Thesis organization

The thesis consists of nine chapters and Annex sections. Chapter 1 corresponds to an introduction of the work, which includes the motivation, theoretical framework, research questions, and goals. Chapter 2 presents the methodology. Chapter 3 covers the literature review on comprehending and modeling the process mechanisms and phenomena of multi-domain anaerobic membrane bioreactors. Chapters 4 and 5 explain the model formulation and its implementation. The following chapters cover the main results and discussions: Chapter 6 is related to the model calibration and validation in accordance with SG1, Chapter 7 covers the process simulation associated with SG2, and Chapter 8 develops the process intensification based on SG3. Finally, Chapter 9 presents the concluding remarks, challenges, and suggestions for future work.

Chapter 2

Methodology

This chapter presents the thesis methodology to achieve each specific goal. Firstly, the necessary steps to develop the phenomenological model of the CBMem reactor are given. Secondly, the steps for process performance simulation are described. Thirdly, the process intensification strategy is explained.

2.1. SG1: Developing the phenomenological model

Fig. 2.1 shows the steps followed when developing the model, which are explained below.

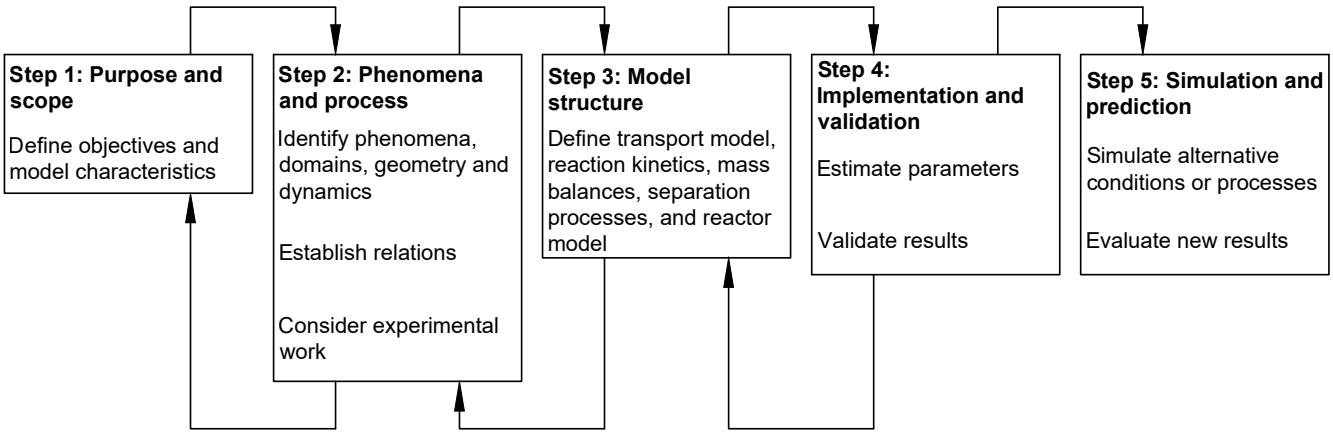

Fig. 2.1: Steps involved in phenomena-based process modeling.

2.1.1. Purpose and scope

Step 1 encompassed the definition of the model's purpose and scope. The model's purpose is related to the thesis goals described in Section 1.2, i.e., it aims to assist process performance analysis by integrating a description of relevant biological, kinetic, and mass transfer mechanisms. Coherently, it was necessary to define the characteristics the model should adopt, which delimit its scope. The information found in the literature and the analysis that was elaborated from it assisted in selecting the relevant phenomena to be modeled. Thus, steps 1 and 2 are iterative.

2.1.2. Phenomena and process

Step 2 involved comprehending the CBMem reactor and its phenomena. First, the system's hierarchy was identified by decomposing the reactor into domains. Then, each phenomenon, e.g., dark fermentation, bioactive layer behavior, and membrane-based gas separation, had to be well-understood and their relations established [64]. Having identified the phenomena, it becomes crucial to elucidate their connection with the spatial domain they inhabit (Fig. 2.2). Overall, step 2 relied on a bibliographic review.

Moreover, to understand how to translate the relations between phenomena into mathematical equations, existing models for fermentative H_2 production, bioactive layer behavior, and whole-cell biocatalytic membrane reactors (BMRs) were investigated by following the steps shown in Fig. C.1 (see Annex C). As observed in Fig. C.2, no BMR model has been reported to address simultaneous fermentative H_2 production and membrane-based gas separation using wastewater. Therefore, the search also comprised an overview of the models that have been proposed, focusing on whole-cell BMRs for wastewater treatment. The search was based on ISI-WoS publications, and it was performed over the title, abstract, and keywords of all publications with the ISI-WoS searching engine. The following logic sentence was used:

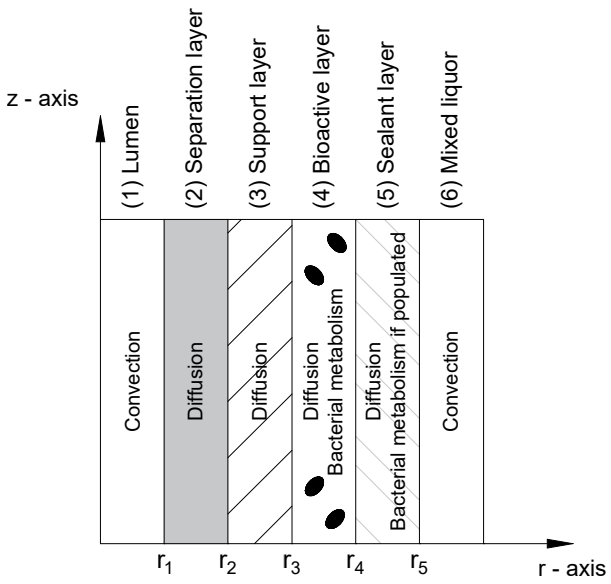

Fig. 2.2: Membrane fiber domains and considered phenomena.

(model OR modeling) AND (mass transfer OR transport OR diffusion) AND (reaction OR degradation OR consumption OR removal OR treatment OR production) AND (biocatalytic OR bioactive OR biological OR biofilm OR immobilized OR encapsulated OR growth) AND cell AND membrane AND wastewater

Thus, 28 articles published between 1993 and 2022 were found. After document screening and full-text review, it was necessary to filter the publications by research focus and topic (Fig. C.1, step 4-6). Six articles passed the filter; these were published between 2006 and 2020 and focus on the modeling of reaction and mass transfer in reactors with biological membranes. Finally, the models were characterized through a review-matrix that defines the reactor, substrate, modeling objective, modeled phenomena, analyzed variables, validation, and the gaps that have not been covered by them to describe the reactor's internal design appropriately (Fig. C.1, step 11).

This comprehensive literature review was summarized and published in the International Journal of Hydrogen Energy, appearing under the paper titled "Biocatalytic membrane reactor modeling for fermentative hydrogen production from wastewater: A review" [59].

2.1.3. Model structure

Step 3 defined the model structure. As shown in Fig. 2.1, this is an iterative exercise after evaluating the model complexity based on the phenomena description and model implementation. State variables (that describe the system's state) and equations (that describe how the state variables change as a function of space and time) were defined [64]. The state variables were chosen following the information they deliver about the process performance, such as substrate consumption, cell proliferation, and H_2 production. These were the available anaerobically degradable substrate (S) measured in terms of the COD, the concentration of the hydrogen product (H_2), and cell (X) concentration. The state variables depended on each other and independent variables, i.e., spatial dimensions and time.

Furthermore, a representative multi-domain fiber model was developed based on submodels for each domain. The model's system of equations resulted by relating the state variables to the independent variables and transport principles, biochemical kinetics, and the law of conservation of mass. Consequently, each domain is represented by a system of ordinary or partial differential equations that describe the rate of change of the species concentration. Moreover, for each differential equation, suitable boundary conditions were proposed. The submodels also involved several parameters that define the system and set the operating conditions. Finally, the multi-domain fiber model was integrated into a reactor model formulation by considering the number of fibers to follow the overall reactor performance [64].

2.1.4. Model implementation and validation

Once the model structure was defined, implementation and validation proceeded. The reactor model was non-linear with coupled equations, while the submodels were intrinsically boundary value problems (BVPs)[2] of two types: (1) the models related to the membrane were expressed as a system of equations of second order ordinary differential equations (ODEs), and (2) the models related to the fluid phases were expressed as a system of equations of second order partial differential equations (PDEs). To simplify the implementation, the finite-difference method was used, i.e., derivatives in the differential equations were approximated using Taylor expansion at evenly spaced grid points (see Annex D).

A suitable scientific programming and numeric computing platform should be considered to solve this system (see Annex E). The open-source software GNU Octave was selected as it allows to structure equations in vectors or matrices and solve ODEs, PDEs, and algebraic equations. In addition, it can use solvers based on numerical methods, and parameter estimation can be easily controlled. The model was implemented in GNU Octave and consists of several different and interconnected scripts, including model functions with the equations to be solved and a script that fosters parameter estimation and simulations (Fig. 2.3).

[2] In BVPs, the goal is to find a solution to a differential equation that satisfies certain specified boundary conditions, e.g., the boundary conditions apply at the beginning and end of the integration interval [65].

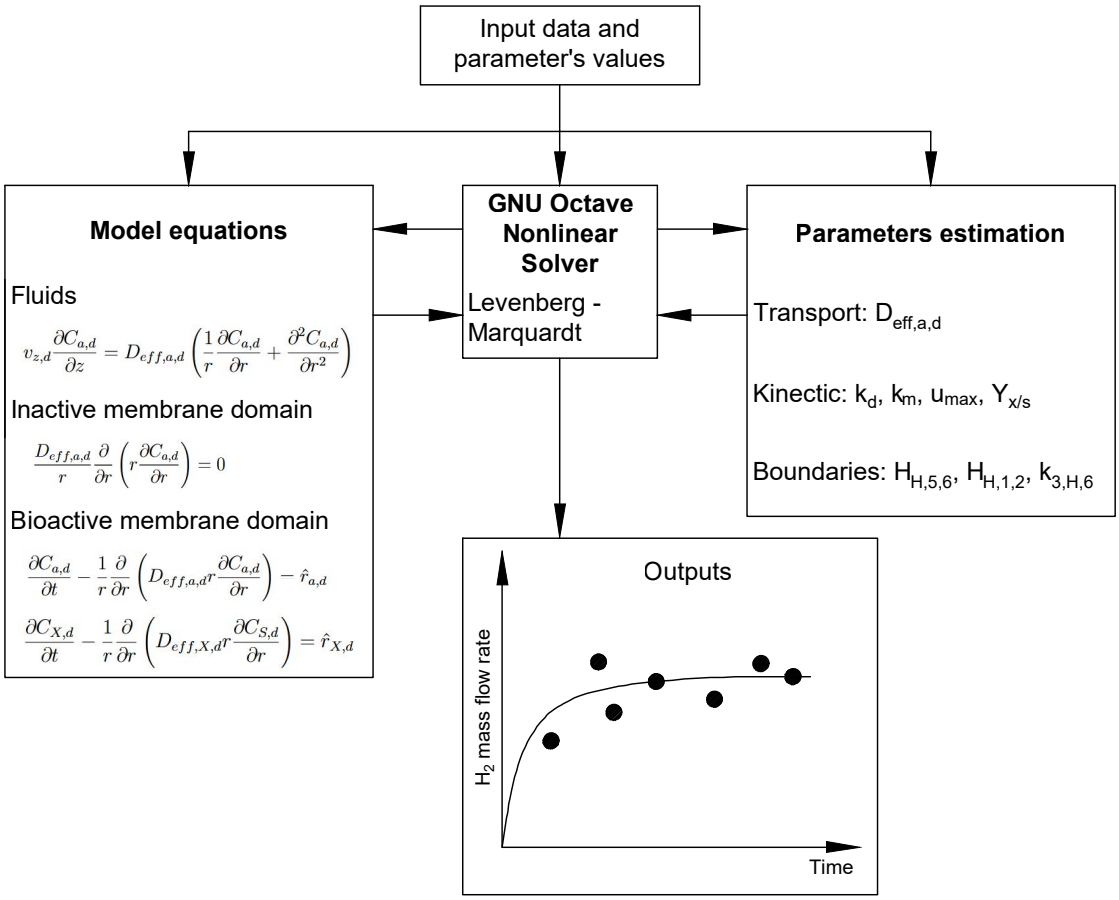

Fig. 2.3: Model implementation and parameter calibration based on data-fitting.

The multi-domain fiber model depends on several parameters. Some were estimated by using values extracted from the literature or laboratory experiments, while others were calibrated. Calibration is highly recommended for parameters specific to the experiment. Due to the uncertainty of a high number of parameters, we decided to conduct calibrations for transport and kinetic parameters for each domain consecutively, i.e., from the most external (mixed liquor side) to the most internal (lumen) domain (Fig. 2.2). Domain coupling allowed the calibrated parameters of an outer domain to be used in the next calibration of the adjacent (and innermost) domain. Due to the lack of experimental data within the domains, the calibrations required proposing verisimilar data to exemplify the expected profiles and tendencies. This was considered for simulations of only three days as a more stabilized operation is expected for this period.

In addition, due to the BVP's unknown values, especially those located at the borders, we decided to develop a solver based on "initial" conditions and model fitting with experimental data[3]. This approach required guessing four parameters: (1) the values related to the hydrogen's concentration ratios at the most external (membrane/ mixed liquor) and (2) at the internal (lumen side/ membrane) interface, (3) a parameter that describe the H_2 concentration's time dependency at the membrane/ mixed liquor interface to ensure dynamic domain coupling, and (4) the maximum specific growth constant rate to allow the adaption of the internal bioactive domains. The membrane is modeled until reaching the lumen side, and the model output is compared with a set

[3] Due to the data, simulations cover one month.

of experimental data. Depending on the difference between modeled and experimental data, the solver iterates.

Data-fitting was implemented in a least-squares sense, using GNU Octave's *leasqr* function, which is based on Levenberg-Marquardt nonlinear regression (see Annex F). That is, the sum of least squares was applied as a cost function and the values of the parameters are varied to minimize the deviation. The calibration's quality depends on the quality of the parameter's initial guess. Thus, different simulations were run to choose the most suitable guess. The optimized parameters were selected by evaluating the parameters' confidence intervals, p-values, and visual inspection of the model's confidence region, compared to the referential data [66]. On the one hand, a student's t-distribution was considered for the confidence intervals, with a confidence level of 95 %. On the other hand, p-values for a two-tailed test were computed using the cumulative distribution function of the t-distribution and a significance level of 0.05.

Experimental data related to a lab-scale bioreactor were extracted from the study conducted by Prieto et al. (2016) (see Annex G). To have enough data points, the experimental data set was extended through interpolation between adjacent points and subject to a random function to add noise. Then, the data was divided into two subsets. The first subset is used for parameter estimation and direct validation, and the other subset is used for cross-validation. Both validations were performed by computing the model's confidence region and visually comparing it with the provided data set [66]. Also, a student's t-distribution was considered for validations, with a confidence level of 95 %.

2.2. SG2: Simulating the process performance

To predict the process performance, the model was improved to compute the H_2 yield and capture efficiency as output. These performance indicators were evaluated by simulating for one month, i.e., the experimental trial's timespan, and a six months operations.

On the one hand, to calculate the H_2 yield (γ_H), Equation (2.1) was used, i.e., the recovered H_2 in the outlet gas flow rate ($F_{H-G,out}$) is normalized to the COD of the reactor's feed ($F_{COD-L,in}$).

$$\gamma_H = \frac{F_{H-G,out}}{F_{COD-L,in}} \tag{2.1}$$

On the other hand, the H_2 capture efficiency (η_H) of the membrane module was calculated as described in Equation (2.2), i.e., the recovered H_2 in the outlet gas flow rate ($F_{H-G,out}$) is normalized to the net H_2 outlet flow rate, measured as the sum of the outlet gas and liquid flow rate ($F_{H-L,out}$).

$$\eta_H = \frac{F_{H-G,out}}{F_{H-G,out} + F_{H-L,out}} \tag{2.2}$$

Finally, the membrane's lifespan was evaluated according to three different criteria:

1. H_2 capture efficiency: According to the membrane's purpose, the lifespan was defined as the moment when the capture efficiency is equal or less than a set operational threshold to avoid detrimental loss of the membrane's functionality. Thresholds were proposed to be of 50 % and 30 % efficiency, as an efficiency of less than 50 % would already show an hampered operation

due to membrane fouling compared to a completely inert membrane.

2. Cell concentration in bioactive domains: According to the bioactive behavior, the lifespan was defined as the moment when the median cell concentration of bioactive domains is greater than or equal to a threshold related to the membrane's maximum attainable cell concentration ($C_{X,max}$). This criteria serves to avoid domain saturation in terms of space and substrate availability. Thresholds were proposed to be 30 % $C_{X,max}$, 50 % $C_{X,max}$, and 70 % $C_{X,max}$.

3. Substrate concentration in bioactive domains: According to a key operational factor, the lifespan was defined as the moment when the median substrate concentration in bioactive domains is equal or less than a threshold related to the COD of the reactor's feed ($C_{S,6,z0}$). This criteria serves to avoid substrate depletion. Thresholds were proposed to be 30 % $C_{S,6,z0}$ and 50 % $C_{S,6,z0}$.

Once the thresholds are surpassed, the membrane's functionality is hampered and replacement should be recommended. Thus, the membrane's lifespan is evaluated for all three criteria and worst scenarios are compared.

2.3. SG3: Proposing operational and design parameters

Sensitivity analysis was performed for selected parameters. This helps to identify the parameters that significantly impact the process performance, recognize predominant phenomena, and improve reactor design and operation. Moreover, a sensitivity analysis gives suggestions for model expansion, contraction, or refinement.

First, parameters of interest were selected by means of their relevance for design and operational improvements. Then, the parameters were varied one at a time to a given value (Table 2.1), and the model was solved for each sensitivity analysis. Finally, the different simulations were compared to the original solution to identify the parameter values that allowed improvements in H_2 yield, capture efficiency, and the membrane's lifespan.

Table 2.1: Sensitivity analysis over selected parameters.

Parameter	**Base value**	**Final value**	Δ [%]
COD in the reactor's	6,920	20,000	198
feed [$\frac{mg}{L}$]		69,200	900
Initial immobilized cell	0.2	0.3	50
mass [mg]		0.4	100
Initial immobilized cell	10.75	16.13	50
layer width [μm]		21.50	100

Chapter 3

Reactor phenomena and models

This chapter identifies the process mechanisms of multi-domain bioreactors for fermentative H_2 production and existing models based on a literature review.

3.1. CBMem reactor and phenomena

The CBMem reactor (Fig. 3.1A) is a cylindrical continuous anaerobic reactor. At its bottom, wastewater is fed with an upward flow. The submerged CBMem module is positioned at the center of the reactor. Due to the outside-in filtration operation [63], the wastewater is fed into the extracapillary space (outside the fibers), flows radially through the membrane, and contacts the bioactive layer. Thus, the substrate (organic molecules) contained within the wastewater is consumed by the cells to produce H_2 biologically. The H_2 molecules then diffuse through the remaining membrane layers and are collected at the lumen side (center of the fiber) by the N_2 sparging gas, which flows co-currently to the wastewater. The gas mixture is collected at the end of the CBMem fiber, whereas the wastewater with reduced organic load leaves the reactor through its upper exit.

The submerged CBMem module consists of a woven mat of 135 parallel fibers. Each fiber has multiple layers that act as a barrier between the liquid and gas streams (Fig. 3.1B and C). The most internal layer is the support and separation layer, a hydrophobic polypropylene hollow-fiber. Another support layer follows, made of poly(dopamine) (PDA), which allows cell immobilization on top of it. Finally, the poly(vinyl alcohol) (PVA) sealant layer allows cell retention [63]. Moreover, according to the film theory, the CBMem module could show further resistance layers to mass transfer adjacent to the fluid/solid interfaces [67].

The studied reactor is heterogeneous; the gas phase (N_2 and H_2) appears at the lumen side. Nevertheless, gas can also be found within the mixed liquor if bubble nucleation occurs due to the local supersaturation of the dissolved gas [54]. No gas phase exists at the headspace of the bioreactor as the wastewater (liquid phase) fills the tank completely. In turn, the solid phase consists of the membrane with biotic factors. However, it may also consist of particulate agglomerations that settle, float or are suspended within the liquid medium [54].

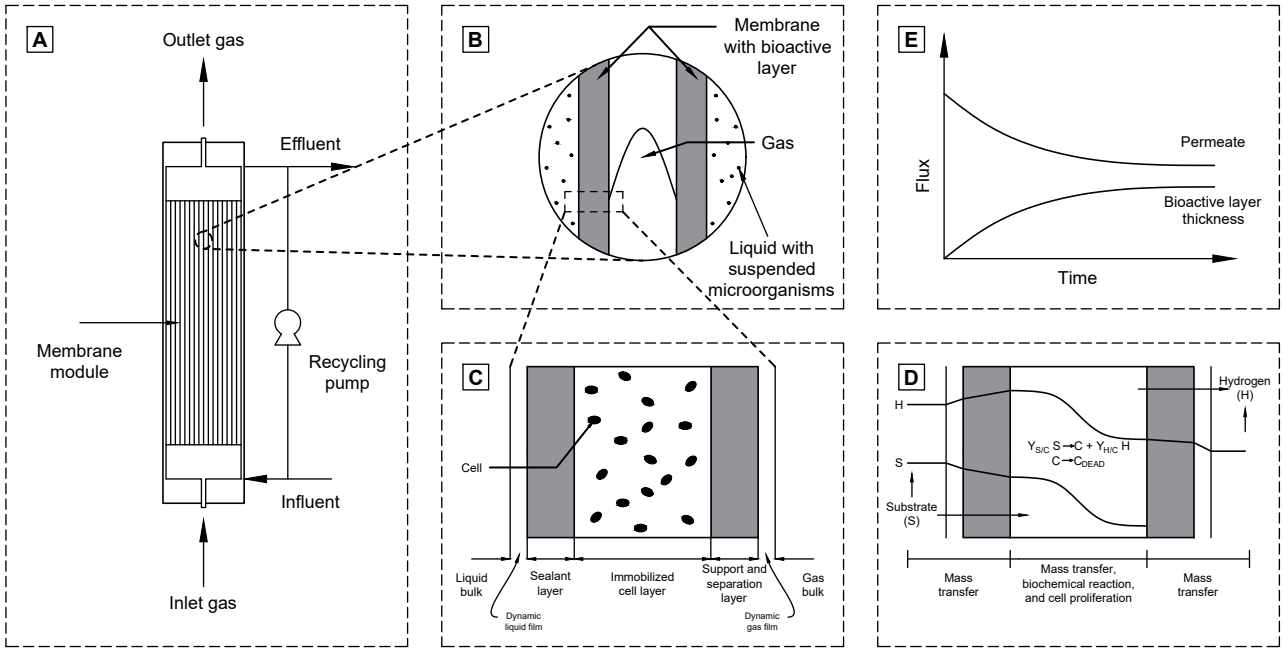

Fig. 3.1: Schematic representation of the modules and phenomena of the CBMem reactor for fermentative H_2 production. A: CBMem reactor with outside-in filtration; B: CBMem fiber; C: Fiber layers; D: Phenomena within layers; E: Dynamics of phenomena.

Besides multiphase operation, the reactor involves several multiscale phenomena. Transport phenomena control the fluid flows in the lumen, membrane, and mixed liquor and affect the movement of energy and species. Naturally, heat transfer occurs inside the reactor; however, the process is held at ambient temperature [3, 63].

Another phenomenon is the mass transfer of some species (Fig. 3.1D) through media (continuous phase), interfaces (gas/liquid, liquid/solid, solid/solid, solid/gas), and cells (dispersed phase) with different rates. Mass transfer can occur by diffusion due to a concentration gradient or convection due to combined diffusion and advection promoted by a fluid flow drag. The separation efficiency of the gases through the membrane depends on its morphological properties (porosity, wall thickness, lumen radius, and matrix structure) [68], which influence the reactor's operational requirements (e.g., transmembrane pressure and feed velocity), and its performance [69]. As the membrane layers have different porosity but are mainly considered porous solids (pore size larger than 1 nm), mass transfer depends on the actual structure and channels. Thereby, transport occurs by a convective flow through the pores [70]. Applying convective velocity is favorable for submerged hollow-fibers to overcome diffusive mass transport [71] and nutrient limitation [72, 73]. Hence, mass transport can be enlarged by the transmembrane pressure difference between the two sides of the membrane, with a lower pressure on the lumen side [74, 75].

Reactions are also essential phenomena. For example, among chemical reactions, acid-base equilibrium occurs within the wastewater [37], and fermentative reactions within the bioactive layer (Fig. 3.1D). Dark fermentation involves substrate consumption through cells, which may require previous substrate hydrolysis to obtain readily degradable sugars. It also involves product formation (H_2, volatile fatty acids, and alcohol) linked to cell metabolism [54]. By using *Clostridium sp.*, H_2 production is defined via the pyruvate ferredoxin oxidoreductase pathway (see Annex B.2.1)

[35]. Inhibition phenomena can also constrain biokinetics due to substrate concentration, pH, dilution effects, or temperature [76].

Cell growth and proliferation occur in the bioactive layer (Fig. 3.1D). As the cells are immobilized into the membrane matrix, further growth can occur within the support [77] and sealant layer [63, 78] or in the extracapillary space to form biofilm. If the sealant layer does not work ideally, cells are released back into the reactor bulk and proliferate on the retentate side [63]. However, since the cells are stationary, their progeny remains near the initial seed, inducing the formation of cell clusters [79]. Proliferation can also be related to multispecies cell culture. Ideally, the microbial seed is prepared to favor the presence of H_2-producing species and reduce the concentration of H_2-consumers (i.e., methanogenic archaea) [63]. However, methanogens could grow in the cell culture and cause undesired substrate competition, H_2 consumption, and CH_4 production.

Further, during the operation of the CBMem reactor, nutrient supply can be limited [72, 80, 81]. As the substrate diffuses through the bioactive layer, it is consumed by the cells, and substrate availability diminishes in the radial direction. This decrease causes uneven cell distribution within the support [82, 83]. Consequently, the membrane presents an uneven distribution of growth rates, i.e., cells near the feed medium proliferate rapidly, whereas cells toward the inner region of the membrane proliferate slowly. In an extreme case, the metabolic activity is confined to the interface between the mixed liquor and the cell-containing support [83]. Moreover, as cell proliferation occurs, the total substrate consumption rate increases; however, the diffusion rates decrease [79], altering mass transfer [69] (Fig. 3.1E) and, consequently, the reaction rates [84]. These effects are also triggered as the substrate concentration in the axial direction changes.

In conclusion, the CBMem reactor has a spatial distribution of different phases, and the phenomena are complex and dynamic. Among the phenomena, mass transfer through the membrane is critical and coupled to cell metabolism. Thus, it affects the overall reactor performance.

3.2. Existing models

Several articles exist on fermentative H_2 production, membrane-based gas separation, biocatalytic layer behavior, or their respective modeling, while review articles studying their combination are absent. Moreover, a relatively small and outdated body of literature is concerned with BMRs[4] [69, 85, 86]. Although some existing reactors share similarities with a BMR for H_2 production from wastewater, their modeling approaches have not been sufficient to describe diffusion and reaction through the membrane's multiple coupling domains. The review published in the International Journal of Hydrogen Energy provides a basis for developing models for multi-domain anaerobic membrane bioreactors for wastewater-to-H_2 to help developers who wish to formulate models sensitive to changes in the internal design and operational conditions, namely: spatial distribution, mass transfer and reaction, and cell dynamics [59].

We identified that models can be classified as unstructured (or structured), nonsegregated (or segregated), and distributed (or nondistributed) models [54]. Unstructured models do not distinguish intracellular and extracellular processes. In turn, nonsegregated models do not consider the heterogeneity of microbial populations. Finally, distributed models can account for transport

[4] A BMR is similar to the CBMem reactor. Its description can be consulted in Annex B.2.4

processes, spatial concentration heterogeneity, and multiphase flows. Fermentative bioreactors are commonly represented as (1) unstructured nonsegregated and nondistributed models, ignoring all heterogeneities; (2) unstructured kinetic models that are generally nondistributed and nonsegregated; and (3) spatially distributed models coupled to unstructured kinetics, usually nonsegregated [54].

Moreover, our work showed that the literature has mainly focused on traditional fermentative bioreactors (e.g., CSTR or batch tests without membrane units) or MBRs, rather than BMRs. MBR models use assumptions and generalizations that are unsuitable for describing the internal design and bioactive layer behavior of BMRs. Compared to traditional fermentative bioreactors, BMRs have clear differences: the presence of immobilized biocatalysts and multiple phases, the spatial distribution, and mass transfer through the membrane [69, 79]. The mass transport parameters and their dependency on the concentration or space coordinate are characteristic of the layer's and biocatalyst's nature [87]. Thus, to understand the mechanisms of a BMR that affect its average performance, a combination of biokinetic and transport models through the membrane is required, e.g., via an unstructured distributed model, including the dynamics of cells.

As an example, Nagy et al. comprehensively described the mathematical modeling of diffusive and convective mass transport through biocatalytic membrane layers [69, 87–89]. The studies considered different cases: with and without biochemical reactions, first-order and zero-order bioreactions, as well as nonlinear Michaelis–Menten reaction kinetics, considering possible variable mass transport parameters, e.g., diffusion coefficient and convective velocity. As a result, the overall mass transfer coefficient for the different cases was defined.

Finally, we developed a review matrix that summarizes the models reported in the literature for BMRs (or similar), considering wastewater as a substrate. We identified that most models do not address the variety and heterogeneity of domains in whole-cell BMRs nor membrane-attached cell population growth, considering assumptions that over-simplify reactor modeling. This explains the few existing studies that discuss the association between concentration distribution and space dimensions.

In summary, the review identifies that up-to-date models of BMRs or submerged MBRs are focused on wastewater treatment, not on simultaneous fermentative H_2 production using wastewater and membrane-based gas separation. Current knowledge for modeling reaction kinetics and mass transfer in MBRs can be a reference for multi-domain anaerobic membrane bioreactor models. However, assumptions such as steady-state conditions and constant substrate concentration are unsuitable. Therefore, these findings suggest that phenomenological modeling can promote a more realistic representation of spatial heterogeneity and process complexity.

Chapter 4

Model formulation

This chapter presents the model formulation. Firstly, the model's scope and limitations are presented, followed by the model structure. Finally, the mathematical description of the models is summarized.

4.1. Scope and limitations

The model to be developed aims to integrate relevant biological, kinetic, and mass transfer mechanisms involved in the H_2 production in a CBMem reactor for process intensification.

The process is shown in Fig. 4.1. The model's scope englobes the wastewater-to-H_2 process and membrane-based H_2 separation within a CBMem reactor.

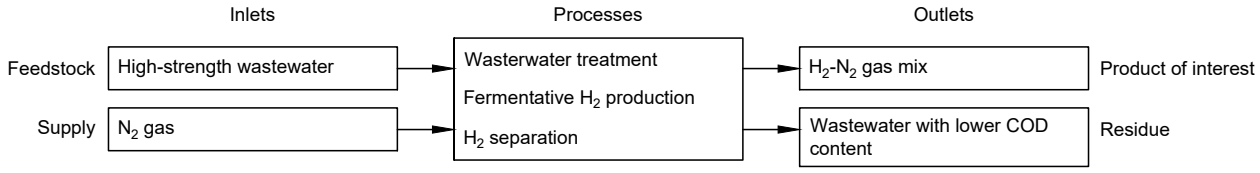

Fig. 4.1: Wastewater-to-H_2 process.

The reactor is cylindrical and can be separated into lower, central, and upper modules (Fig. 4.2). The lower and upper modules are analogous and contain mainly transport phenomena. In turn, the central module contains the CBMem. Considering geometry, the central module can be further segmented; as the CBMem module is a flat surface, it slightly interrupts the cylindrical symmetry of the reactor. In addition, the CBMem module distinguishes 135 fibers put in parallel and which are analogous, except for the ones at the extremes of the CBMem module as they only have an adjacent fiber at one side.

As the CBMem contains the most important phenomena, we decided that the reactor model can be limited to this module, neglecting the geometrical interruptions that were explained before. Furthermore, we considered as sufficient to create a representative multi-domain fiber model, based on submodels for each domain as the fiber model's output can be easily amplified by the number of fibers to create the reactor model and relate the reactor inlets and outlets (Fig. 4.1).

The scope of the multi-domain fiber model includes the representation of the species concentration profiles through the multiple domains. These are: (1) lumen, (2) hollow-fiber support and separation layer, (3) PDA-support layer, (4) bioactive layer, (5) PVA-sealant layer, and (6) mixed liquor that surrounds each fiber (Fig. 4.2). The domains' numeric abbreviation is considered for future modeling treatment.

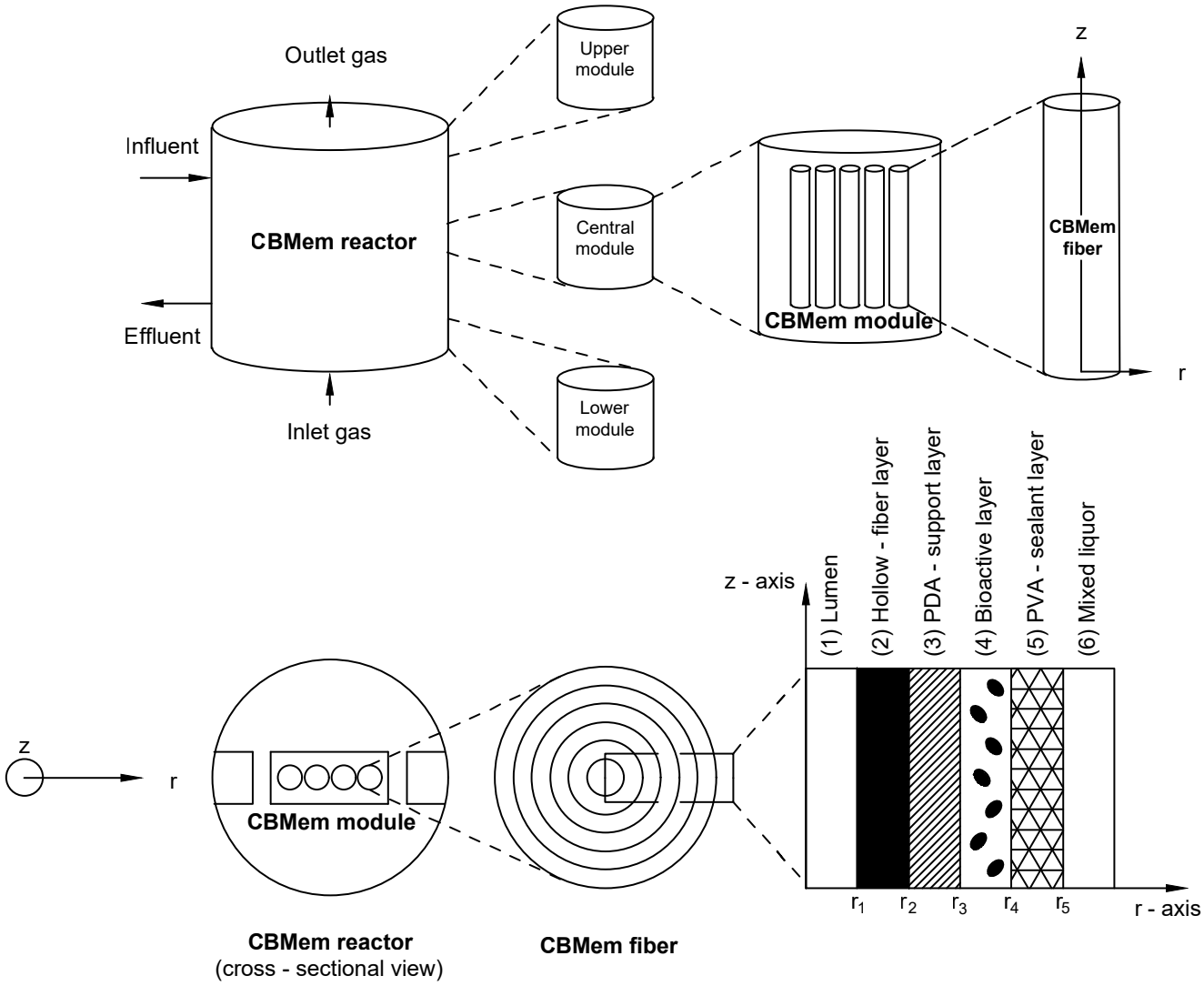

Fig. 4.2: CBMem reactor segmentation with the fiber domains and the model's coordinate system.

Regarding the model's characteristics, we considered the following:

1. Nonsegregated: The model considers the microbial population as homogeneous (only *Clostridium sp.*), assuming that the pretreatment of the microbial seed successfully removes undesired microbial species.

2. Unstructured: the model does not distinguish intra- and extracellular biochemical processes. Moreover, it is assumed that the biological reactions follow Monod-based kinetics as it is simple, widely used, and easy to adapt [76]. Biokinetic model adaption includes inhibition phenomenon due to the H_2 partial pressure sensitivity.

3. Distributed: The model reflects spatial heterogeneity of species and non-ideality. Consequently, mass balances for nutrients, products, and cells are developed for the different reactor domains, considering the diffusion coefficient as a function of space.

4. Dynamic: The model depends on the time variable as the reactor shows cell growth that evolves within the membrane.

5. Implementable: The model must be simple enough to be implemented in the selected software, but without significantly undermining representation and accuracy, i.e., the model ensures spatial distinction of phases, species, phenomena, and dynamics.

In addition, the following considerations were taken:

1. Cell growth: It is assumed that the cells grow only in available and suitable spaces, from the immobilized layer towards the mixed liquor due to nutrient supply. Thus, proliferation occurs within the immobilized bioactive layer and sealant layer. No biofilm formation in the extracapillary space is considered as cell growth within the sealant layer already hampers the membrane's performance, reducing its lifespan.

   Moreover, to describe the uneven cell distribution within the CBMem fibers, the model assumes that after reaching a maximum attainable cell concentration ($C_{X,max}$) that a volume of the bioactive layer can hold, an excess cell concentration is distributed within the adjacent membrane layer toward nutrient supply (approaching the mixed liquor). When the PVA-sealant layer begins to be populated with cells, the excess cell concentration is distributed within this domain and mass balance equations switch to represent the bioactive state. This approach considers a fixed boundary condition between the immobilized and the sealant layer, i.e., the condition does not displace through space. However, the boundary conditions' value changes through time, improving the dynamic representativity of concentrations.

2. Mass transport: In practice, mass transport in the CBMem occurs by convection. On the one hand, we assumed that Fick's law holds for the diffusive mass flux. In fluid and inactive membrane domains, the effective diffusivity is assumed to be constant. However, in bioactive domains, the effective diffusivity changes due to cell growth, which depends on the cell concentration at a specific space coordinate (see Eq. (4.1)) [90]. Consequently, the effective diffusion coefficient (D_{eff}) varies linearly with the cell concentration (C_X) between the diffusion coefficient in the membrane matrix at inert conditions ($D_{eff,M}$) and zero. $C_{X,max}$ is the maximum attainable cell concentration that would be reached if the cells could grow everywhere in the membrane where space is not occupied by the inert material.

$$D_{eff} = D_{eff,M}\left(1 - \frac{C_X}{C_{X,max}}\right) \tag{4.1}$$

   On the other hand, we described convection only in fluid domains through transport models. For the mixed liquor, we adopted a model based on the continuity and momentum conservation equations, which are in function of pressure profiles. In turn, for the lumen side, we assumed a velocity profile equation of a fluid in a straight circular pipe, assuming constant velocity in the axial position. Finally, to reduce model complexity, advection in membrane domains is assumed to be non-existent.

   As for the pressure model, a profile to a fixed decrease is calibrated. This moderates dependence on data and is considered to be admissible as the axial pressure decrease within the

fluids is negligible, especially for the gas phase [63]. For the mixed liquor, the pressure profile is chosen based on the quality of the velocity profiles to secure the physical sense.

3. Domain coupling: To represent the inherent coupling of domains, we used Henry-like equilibrium on the membrane interface. Depending on the domain, we additionally considered the conservation of mass flux.

4.2. Model structure

The CBMem model is a combination of variables, equations, and parameters. The state variables are substrate (S), product (H_2), and cell (X) concentration. These are subject to the spatial and temporal dimensions. According to reactor segmentation, the main dimensions are axial (along the fiber length and abbreviated with a z) and radial (along the fiber width and abbreviated with an r). For fluid domains, the consideration of both spatial dimensions is suitable. For membrane domains, the radial is more significant. Due to the fiber's axis symmetry, the angular coordinate is neglected. Finally, the multi-domain fiber model considered a cylindrical coordinate system, where its origin is set in the center and bottom of the fiber.

Besides the spatial framework, time characterizes the process change. However, the rate is relative; e.g., population dynamics change in a long-term sense (days to weeks) [91], which is not apparent in small-term (minutes to hours). The temporal dimension is especially relevant for bioactive domains. Due to the domain coupling, the domain's state variables are also coupled to those measured in the remaining domains. Therefore, bioactive domains can represent time-dependency through equations, while the inactive domains are subject to the dynamic through the boundary conditions.

As for the state equations, they determine how the state of the system changes as a function of space and time. This involves the above-mentioned state variables and complies with the principle of conservation in mass and momentum balances. Moreover, due to the biological reaction, the state variables (concentration of substrate, H_2, and cells) are mutually dependent. The system of state equations that was obtained resulted in a set of ODEs and PDEs.

The model structure (Fig. 4.3) comprises the multi-domain fiber model, which in turn depends on the coupling of submodels of each membrane domain. The models are explained below.

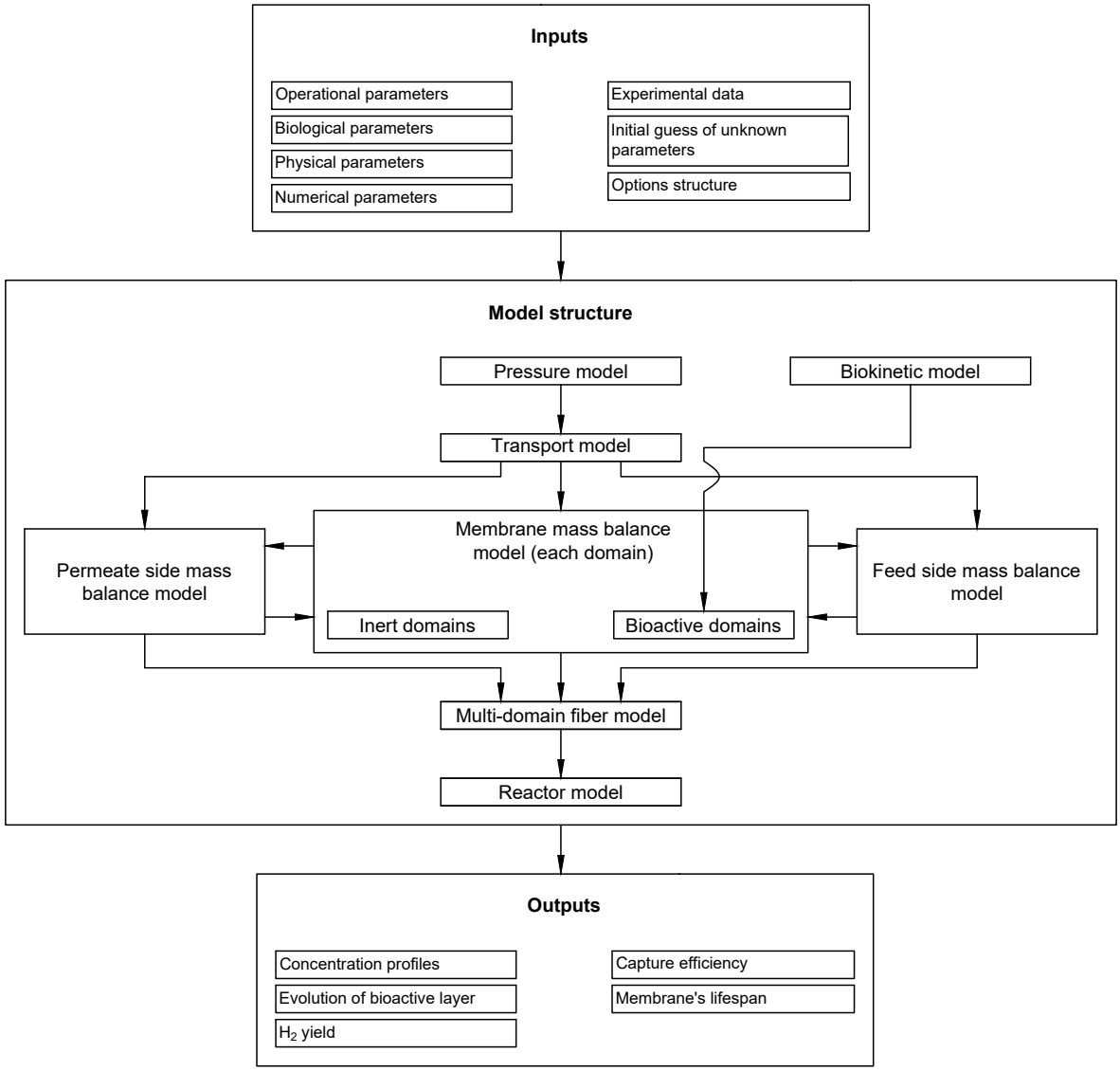

Fig. 4.3: Model structure and communication between sub- and auxiliary models.

1. **Reactor model**: Accounts for net H_2 production and recovery by amplifying the multi-domain fiber model by the number of existing fibers. It also informs about the overall process performance.

2. **Multi-domain fiber model**: Ensures domain coupling and compliance with the process entries at fiber scale. See Annex H to review the detailed modeling strategy for the CBMem fiber.

3. **Domain models**: Describe the concentration profile of each species in the respective domain, based on mass balance. Mass balance equations secure the conservation of mass by accounting for the material that enters and leaves each domain. Concentration gradients are considered as the driving force for diffusion. For fluid domains, the model also depends on the transport model to account for the advective term. Moreover, the mass balances describe the time-based behavior of all chemical species. Finally, the mass balances for bioactive domains define

generation/ consumption terms related to the biokinetic model. See Annex H to review the assumptions for the model of each domain.

In addition, auxiliary models were required, which are the following:

1. **Transport model**: Describe the momentum transfer by obtaining the velocity profiles of a domain, based on the continuity equation, momentum conservation equation, and the pressure models. Annex I.1 shows the calculation memory for the transport models. This includes Annex I.1.1 that illustrates the model development of the radial and axial velocity profiles for the lumen side and Annex I.1.2 for the mixed liquor. For completeness, we included Annex I.1.3 to explain the model development for the radial velocity profile through a membrane, although this term has been neglected in the membrane domain models for the CBMem. In addition, Annex I.2 shows the calculation memory for the pressure models.

2. **Biokinetic model**: Establishes biokinetic laws for cell growth, substrate consumption, and H_2 production. We used Monod-based equations with inhibition phenomena due to the H_2 partial pressure sensitivity. Note that the biokinetic model requires depends on process-specific kinetic parameters. Annex I.3 details the biokinetic model's development.

Finally, the system of equations contained in the model also depends on parameters, which are values representing inherent properties of the system. These are of physical, operational, biological, geometrical, and numerical nature. Parameters can be estimated from laboratory experiments, literature, or calibration. Most parameters for the CBMem modeling were derived from the literature and experimentation, while some were obtained from calibration. Annex K summarizes the parameters' values that were required for modeling.

The following subsections show a summary of the reactor model's partial differential equations, considering the model structure shown in Fig. 4.3 and the domains' numeric abbreviation shown in Fig. 4.2. Moreover, a detailed description of the model development is presented in Annex H. Finally, this study employs finite-differences for the radial, axial, and time axis as a solution strategy for model implementation, which is explained in Chapter 5.

4.2.1. Multi-domain fiber model

In a CBMem fiber, substrate is available in the mixed liquor, moves through the membrane layers, and reacts in the bioactive layer to form the product, while the product moves to the lumen side. This mass transfer-reaction combined process can be described through the multi-domain fiber model, which was developed and implemented for the CBMem's domains and the involved phenomena shown in Figure 2.2.

The main considerations and assumptions used to formulate the multi-domain fiber model are the following:

1. Fick's law holds for the diffusive mass flux.

2. Henry-like equilibrium exists on the membrane interfaces.

3. The biochemical reaction takes place in domains where cells grow [69]. These only grow within the immobilized cell layer and towards the sealant layer-mixed liquor interface due to substrate availability. No biofilm formation is considered.

The multi-domain fiber model comprises submodels based on mass balance for each species in each domain. According to the number of variables that involve derivates, the submodels can be classified into two types: (1) the models related to the fluid domains were systems of equations of second-order partial differential equations, and (2) the models related to the membrane were systems of equations of second-order ordinary differential equations. Moreover, according to the domains' reactivity, the second case can be further classified into inactive and bioactive domain models. The representative equations for these models are explained below.

4.2.1.1. Fluid domain models

The fluid domains are the lumen side (1) and mixed liquor (6). The main assumption used to formulate the fluid models is the following:

1. The flow is steady state [92].

In a fluid domain d (d=$\{1, 6\}$), a species a (a=$\{$S, X, H$\}$) can be transferred through advection in the axial direction (z) or diffusion in the radial direction (r); no further phenomena are present nor are other variables significant. Thus, the mass balance model is defined through Eq. (4.2).

$$v_{z,d}\frac{\partial C_{a,d}}{\partial z} = D_{eff,a,d}\left(\frac{1}{r}\frac{\partial C_{a,d}}{\partial r} + \frac{\partial^2 C_{a,d}}{\partial r^2}\right) \tag{4.2}$$

To solve Eq. (4.2), appropriate boundary conditions are required (Fig. 4.4). These are different if the mixed liquor or lumen side is solved. For the mixed liquor, the first boundary condition is an initial condition for the species concentration at the lowest axial point, which can be a constant concentration or a function. The second boundary condition describes the optimal concentration of the species' distribution profile at the fluid center for all axial positions. The third boundary condition must be related to the membrane interface; however, as this value is unknown, it could be initially guessed as a function of nearby concentrations and time, and then calibrated.

The boundary conditions for the mixed liquor (6) side are:

$$\begin{cases} C_{a,d} = f1_{a,d} & \text{at } z = z_0 \quad \forall r \in \left[r_{d-1}, r_{d-1} + \dfrac{r_{d+1} - r_{d-1}}{2}\right] & \text{(4.3a)} \\ \dfrac{\partial C_{a,d}}{\partial r} = 0 & \text{at } r = r_{d-1} + \dfrac{r_{d+1} - r_{d-1}}{2} \quad \forall z \setminus z_0 & \text{(4.3b)} \\ C_{a,d} = f2_{a,d} & \text{at } r = r_{d-1} \quad \forall z \setminus z_0 & \text{(4.3c)} \end{cases}$$

For the lumen side, the boundary conditions are analogous; however, the third boundary condition would be estimated based on domain coupling, using Henry-like equilibrium on the membrane interface. Thus, the boundary conditions for the lumen (1) side are:

$$\begin{cases} C_{a,d} = f1_{a,d} & \text{at } z = z_0 \quad \forall r < r_d & \text{(4.4a)} \\ \dfrac{\partial C_{a,d}}{\partial r} = 0 & \text{at } r = 0 \quad \forall z \setminus z_0 & \text{(4.4b)} \\ C_{a,d} = H_{a,d,d+1} C_{a,d+1} & \text{at } r = r_d \quad \forall z & \text{(4.4c)} \end{cases}$$

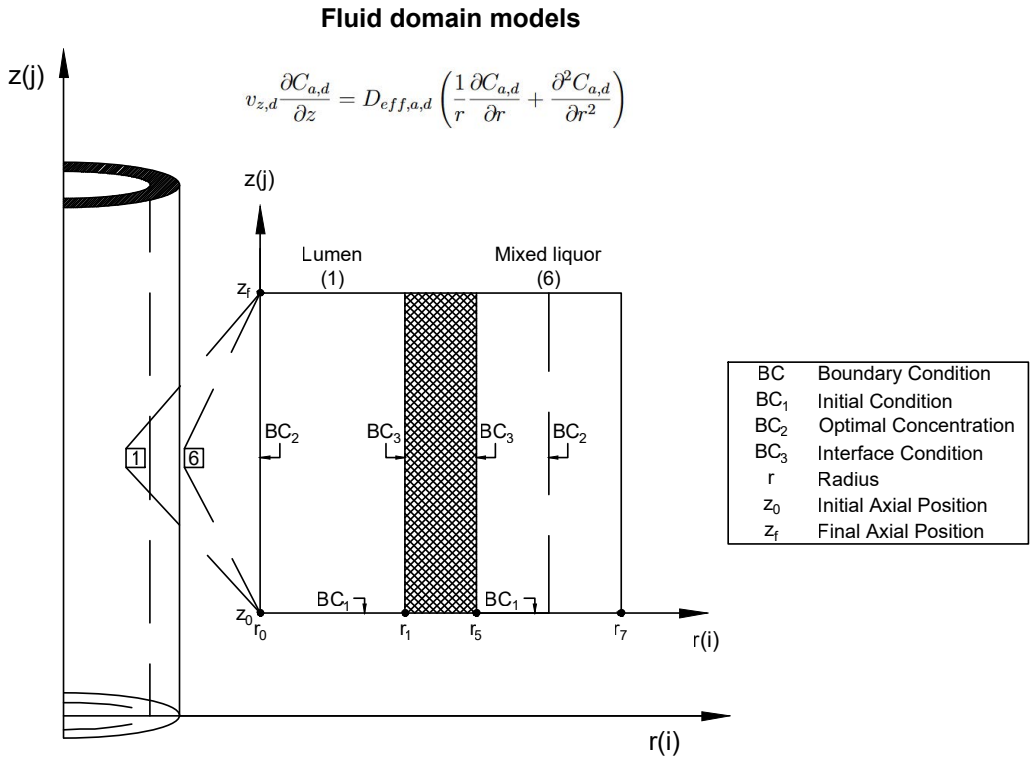

Fig. 4.4: Fluid domain considering its model and respective boundary conditions.

4.2.1.2. Membrane domain models

The membrane domains are the hollow-fiber layer (2), PDA-support layer (3), bioactive layer (4), and PVA-sealant layer (5). The main considerations and assumptions used to formulate the membrane models are the following:

1. Mass transport through the membrane layers occurs by diffusion. Advective transport is neglected [69].

2. There is no axial flow and no axial transport inside the membrane layer [69].

Depending on the presence of cells, the membrane domains can be divided into inactive and bioactive domains. For each, the representative equations and specific assumptions are explained below.

Inactive membrane domains

Inactive domains are the hollow-fiber layer (2), the PDA-support layer (3), and the PVA-sealant layer (5) if it has not been populated with cells. To develop their model, the following additional assumptions were used:

1. Process is steady state.

2. The mass flux is conserved at the interfaces.

In an inactive domain d (d=$\{2, 3, 5\}$), a species a (a=$\{$S, X, H$\}$) can be transferred through diffusion in the radial direction (r); no further phenomena are present nor are other variables significant. Thus, the mass balance model is defined through Eq. (4.5).

$$\frac{D_{eff,a,d}}{r}\frac{\partial}{\partial r}\left(r\frac{\partial C_{a,d}}{\partial r}\right) = 0 \tag{4.5}$$

To solve Eq. (4.5), two boundary conditions are required (Fig. 4.5), e.g., Henry-like equilibrium and conservation of mass flux. Thus, the boundary conditions are:

$$\begin{cases} \dfrac{\partial C_{a,d}}{\partial r} = \dfrac{-N_{a,d}}{D_{eff,a,d}} & \text{at } r = r_d \quad \forall z \qquad (4.6a) \\ C_{a,d} = H_{a,d,d+1} C_{a,d+1} & \text{at } r = r_d \quad \forall z \qquad (4.6b) \end{cases}$$

Where, due to the flux conservation and its definition, considering negligible radial velocity:

$$N_{a,d}(r_d) = N_{a,d+1}(r_d) = -D_{eff,a,d+1}\frac{\partial C_{a,d+1}}{\partial r}(r_d) \tag{4.7}$$

N.b. that the principle of mass conservation is ensured as the flux conservation is applied for the same position at the membrane interface. Thus, the boundary condition of Eq. 4.7 does not show proportions of the radial variable and can be directly applied for the domain border.

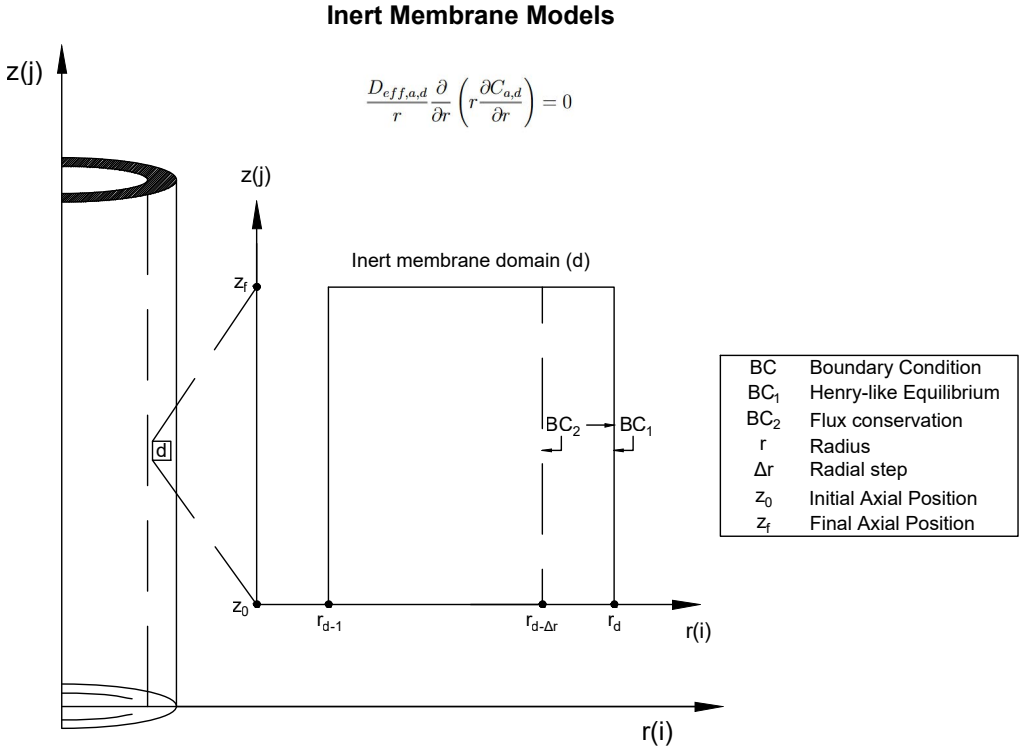

Fig. 4.5: Inactive membrane domain considering its model and respective boundary conditions.

Bioactive membrane domains

Bioactive membrane domains are the immobilized cell layer (4) and the PVA-sealant layer (5) when it transforms into a bioactive state due to cell migration. Their mass balance equations should represent cell dynamics (time-dependence) and reaction kinetics. To develop their model, the following additional assumptions were used:

1. Process is unsteady state [69].
2. Reaction occurs at every position within the bioactive membrane domain [69].
3. The biochemical reaction rate and mass transport parameters (e.g., effective diffusivity) vary as a function of the space coordinate due to changes in cell concentration [69].

In a bioactive domain d (d=$\{4, 5\}$), a species a (a=$\{\mathrm{S}, \mathrm{X}, \mathrm{H}\}$) presents both reaction and transfer phenomena. First, the species can accumulate in time (t). Second, depending on the species and the system's state, a species can be produced or consumed. Third, the species experience diffusion or diffusion-like transfer in the radial direction (r). No further phenomena are developed nor are other variables significant.

The mass balance models for the substrate and hydrogen species (a=$\{\mathrm{S}, \mathrm{H}\}$) in bioactive membrane domains are defined through Eq. (4.8). The biokinetic reaction rate ($\hat{r}_{a,d}$) is detailed in Section 4.2.3, while the effective diffusivity coefficient is described by Eq. (4.1).

$$\frac{\partial C_{a,d}}{\partial t} - \frac{1}{r}\frac{\partial}{\partial r}\left(D_{eff,a,d} r \frac{\partial C_{a,d}}{\partial r}\right) = \hat{r}_{a,d} \tag{4.8}$$

Three boundary conditions are required to solve Eq. (4.8) (Fig. 4.6). First, an initial condition for the species concentration is required, which can be a constant concentration or a function. This must be considered at the beginning of the biological processes in the domain. The second boundary condition describes a coupling condition at the outer membrane interface, e.g., Henry-like equilibrium. The third boundary condition must be related to the inner membrane interface; however, as this value is unknown, it could be guessed as a function of nearby concentrations.

Thus, the boundary conditions are:

$$\begin{cases} C_{a,d} = f1_{a,d} & \forall r \in [r_{d-1}, r_d) \quad \forall z \text{ at } t = t_k & \text{(4.9a)} \\ C_{a,d} = H_{a,d,d+1} C_{a,d+1} & \text{at } r = r_d \quad \forall z \ \forall t & \text{(4.9b)} \\ C_{a,d} = f2_{a,d} & \text{at } r = r_{d-1} \quad \forall z \text{ at } t > t_k & \text{(4.9c)} \end{cases}$$

Cells' mass balance in bioactive domains needs special consideration. Biomass growth and migration are stimulated by substrate availability. Moreover, cells will migrate if there is not enough available space to grow. Thus, the following assumptions were also used:

1. Mass transport of cells is described in diffusive terms stimulated by the substrate gradient.
2. If the cell concentration of a certain moment and position surpasses the maximum cell capacity that the membrane can hold, then the cell concentration is corrected by assuming it to be the maximum cell concentration, while the concentration difference (defined as the "excess cell

concentration", $C_{X,excess}$) migrates to an adjacent position (measured for the next time point) in the direction where the substrate is more available, i.e., approaching the mixed liquor. Therefore, the accumulation term of the cell mass balance will be developed by including $C_{X,excess}$ and a term subject to a binary value (k_{bb}) due to a boolean condition that represents proliferation within a bioactive domain.

3. Excess cell concentration strategy also represents cell migration and proliferation into the adjacent membrane domain that was initially inert. When the concentration of the bioactive layer (domain 4) near the bioactive/sealant border surpasses the maximum cell concentration, then the cell concentration is corrected by assuming it to be the maximum cell concentration, while the concentration difference ($C_{X,excess}$) migrates to domain 5. Migration is defined as the unequal distribution of the excess cell concentration over domain 5, while ensuring mass conservation. That is, the cell mass is distributed over all radial position of domain 5, for the same axial position and time point as those measured during the evaluation of the concentration in domain 4 that activates cell migration and proliferation into the adjacent domain.

The mass balance model for the cell species (X) in domain d related to the bioactive membrane domains (d=$\{4, 5\}$), are defined through Eq. (4.10). The biokinetic reaction rate is detailed in Section 4.2.3, while the effective diffusivity coefficient is described by Eq. (4.1). As mentioned before, the accumulation term will be described through Eq. (4.11) to represent proliferation within a bioactive domain.

$$\frac{\partial C_{X,d}}{\partial t} - \frac{1}{r}\frac{\partial}{\partial r}\left(D_{eff,X,d} r \frac{\partial C_{S,d}}{\partial r}\right) = \hat{r}_{X,d} \tag{4.10}$$

$$\frac{\partial C_{X,d}}{\partial t} \approx \frac{C_{X,d}(i,k+1) - C_{X,d}(i,k) + (C_{X,d}(i-1,k) - C_{X,max})k_{bb}}{\Delta t} \tag{4.11}$$

For the cell mass balance, the boundary conditions are analogous as those for the other species; however, the second boundary condition should consider a function based on nearby concentrations measured from the moment before.

Thus, the boundary conditions are:

$$\begin{cases} C_{X,d} = f1_{X,d} & \forall r \in [r_{d-1}, r_d) \quad \forall z \text{ at } t = t_k & \text{(4.12a)} \\ C_{X,d} = f2_{X,d} & \text{at } r = r_d \quad \forall z \ \forall t & \text{(4.12b)} \\ C_{X,d} = f3_{X,d} & \text{at } r = r_{d-1} \quad \forall z \text{ at } t > t_k & \text{(4.12c)} \end{cases}$$

Note that $t_k = t_0$ applies for the bioactive domain (d=$\{4\}$), while $t_k = t_{crit}$ applies for the PVA-sealant layer (d=$\{5\}$). Moreover, $f1_{X,4}$ should be related to the initial immobilized cell concentration known by design ($C_{X,4,t_0}$), while $f1_{X,5}$ should be based on the concentration at t_{crit} ($C_{X,5,t_{crit}}$), obtained through modeling when the sealant layer begins to be populated with cells.

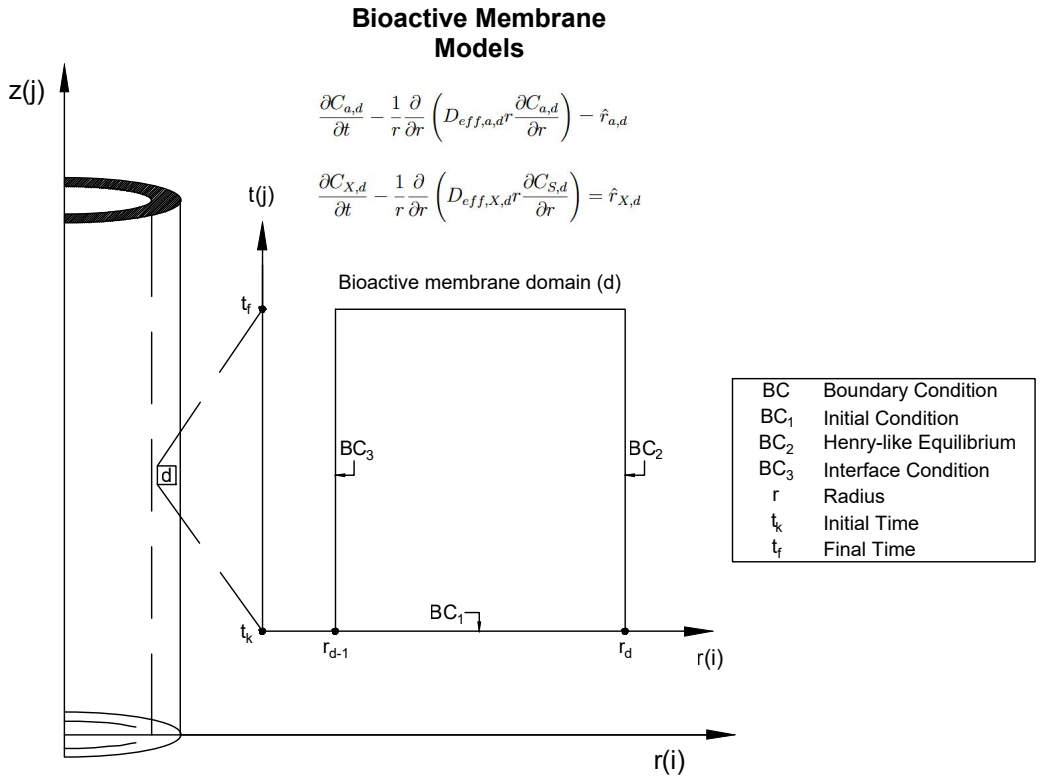

Fig. 4.6: Bioactive membrane domain considering its model and respective boundary conditions.

4.2.2. Transport model

Due to convective flow in the fluid domains, the CBMem's velocity profiles are required for modeling (Fig. 4.7). The axial velocity profile of the lumen side is represented by Eq. (4.13). Similarly, the axial velocity profile of the mixed liquor is represented by Eq. (4.14).

$$v_{z,1} = v_{in}(1 - \frac{r}{r_1})^{k_{v,1}} \tag{4.13}$$

$$v_{z,6} = \frac{\varepsilon}{4\mu_w}\left(\frac{dP_6}{dz} - \rho g\right) \tag{4.14}$$

$$\varepsilon = \frac{(r^2 - r_7^2)ln(r_5) + (r_5^2 - r^2)ln(r_7) + (r_7^2 - r_5^2)ln(r)}{ln(r_5) - ln(r_7)} \tag{4.15}$$

The pressure profiles and their derivatives for fluid domain d are represented by Eqs. (4.16) and (4.17).

$$P_d = P_{d,z_0} + k_{1,P,d}\frac{P_{d,z_f} - P_{d,z_0}}{z_f - z_0}z + k_{2,P,d}z^2 \tag{4.16}$$

$$\frac{dP_d}{dz} = k_{1,P,d}\frac{P_{d,z_f} - P_{d,z_0}}{z_f - z_0} + k_{2,P,d}z \tag{4.17}$$

$k_{v,1}$, $k_{1,P,d}$, and $k_{2,P,d}$ are unknown parameters that need to be calibrated.

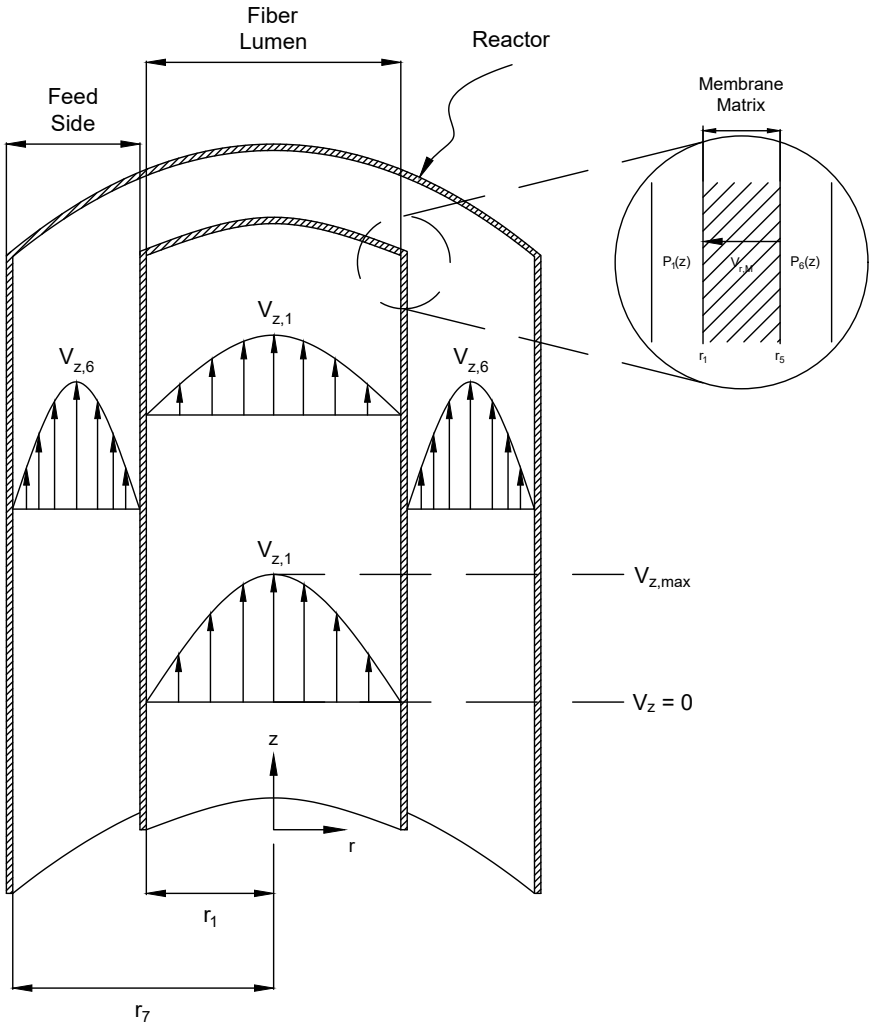

Fig. 4.7: Illustration of velocity profiles within the CBMem fiber.

4.2.3. Biokinetic model

The relation between substrate, cells, and hydrogen is shown in Fig. 4.8. A biokinetic model was formulated to describe the reaction rate of the bioactive domain models. For these, the following main considerations and assumptions were used:

1. Monod-based kinetics can describe the biochemical reactions related to the dark fermentation process [59].
2. As the substrate can be of different substances contained in the wastewater [91], the substrate concentration is measured as COD. Therefore, the reaction has one rate-limiting substrate.
3. Cell culture is held under controlled conditions using *Clostridia sp.* as a single species.
4. The cells are in the exponential phase, i.e., the growth rate is higher than the decay rate.
5. Cell growth is inhibited by its concentration due to space competition; thus, a maximum cell capacity is considered.

6. Product formation is associated with cell population growth. Nongrowth-associated product formation rates are negligible.

7. Non-competitive inhibition function is considered for H_2 regulation [37] and described by a simplified Han-Levenspiel inhibition term in the function of the H_2 saturation concentration [54, 93]. Moreover, another non-competitive inhibition function, described by a modified Monod inhibition term in the function of its critical inhibitory concentration, is considered [54, 94].

Eq. (4.18), (4.19), and (4.20) represent the substrate (S) consumption, net cell (X) growth, and hydrogen (H) production rate measured in domain d, respectively.

$$\hat{r}_{S,d} = -\frac{\mu_{max}}{Y_{X/S}} \frac{C_{S,d} C_{X,d}}{K_S + C_{S,d}} - k_m C_{X,d} \tag{4.18}$$

$$\hat{r}_{X,d} = \left(\mu_{max} \frac{C_{S,d} C_{X,d}}{K_S + C_{S,d}} - k_{dec} C_{X,d} \right) \left(1 - \frac{C_{X,d}}{C_{X,max}} \right) \tag{4.19}$$

$$\hat{r}_{H,d} = \frac{\mu_{max}}{Y_{X/H}} \frac{C_{S,d} C_{X,d}}{K_S + C_{S,d}} \left(1 - \frac{C_{H,d}}{C_{H,sat}} \right)^n \left(\frac{C_{H,crit}}{C_{H,d} + C_{H,crit}} \right) \tag{4.20}$$

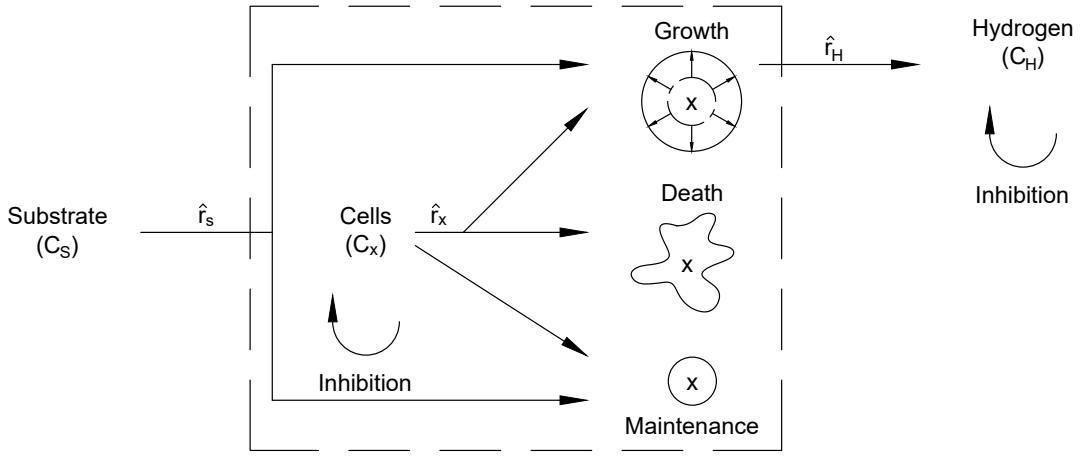

Fig. 4.8: Biological phenomena.

4.2.4. Multi-domain membrane bioreactor model

The multi-domain fiber model allows the expression of the H_2 concentration at different spatial and temporal points. However, to be comparable with experimental data, the H_2 total mass outlet flow rate must be expressed as a function of time.

First, the permeated H_2 concentration at the fibers' outlet for every time point is defined as the average H_2 concentration modeled at the lumen (1) side at the fiber's end. This is described by Eq. (4.21).

$$C_{H,1,out} = \overline{C_{H,1}(z,r,t)} \qquad \forall r \in [r_0, r_1] \quad \forall t \text{ at } z = z_f \tag{4.21}$$

Then, the H_2 mass outlet flow rate is related to the permeated H_2 concentration at the fibers' outlet by considering the number of fibers that compose the CBMem module (Fig. 4.9). For this, the permeated H_2 concentration at the fibers' outlet is multiplied by the sparging gas flow rate that enters the membrane module. Through the inlet gas flow rate, the number of fibers is intrinsically considered. Moreover, this assumes that the mass flow does not change significantly with the permeated product. The H_2 mass outlet flow rate is described by Eq. (4.22).

$$F_{H-G,out} = C_{H,1,out} F_{G,in} \qquad \forall t \tag{4.22}$$

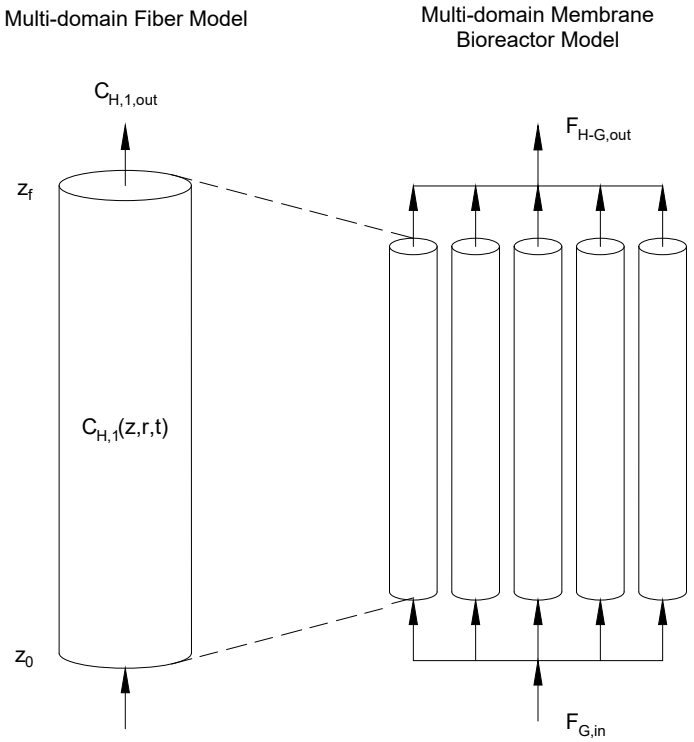

Fig. 4.9: Relationship between the reactor model and multi-domain fiber model to describe the H_2 mass flow rate at the outlet of the CBMem module.

In summary, the model's representative equations and boundary conditions are summarized in Table 4.1.

Table 4.1: Summary of the model equations and boundary conditions to describe the phenomena of a species a in domain d through a multi-domain fiber (Fig. 2.2). The symbols used are defined in Annex A.

Model	**Domain**	**Species**	**Equation**	**Boundary condition**
Multi-domain fiber	NA[a]	S, H, X	System of coupled equations related to submodels	NA[a]
	1	H	$C_{H,d,out} = \overline{C_{H,d}(z,r,t)}$	NA[a]
	1	H	$F_{H-G,out} = C_{H,d,out} F_{G,in}$	NA[a]
Fluid	6	S, H, X	$v_{z,d}\frac{\partial C_{a,d}}{\partial z} = D_{eff,a,d}\left(\frac{1}{r}\frac{\partial C_{a,d}}{\partial r} + \frac{\partial^2 C_{a,d}}{\partial r^2}\right)$	BC1: $C_{a,d} = f1_{a,d} \quad \forall r \in \left[r_{d-1}, r_{d-1} + \frac{r_{d+1}-r_{d-1}}{2}\right]$ *at* $z = z_0$ BC2: $\frac{\partial C_{a,d}}{\partial r} = 0 \quad \forall z \setminus z_0$ *at* $r = r_{d-1} + \frac{r_{d+1}-r_{d-1}}{2}$ BC3: $C_{a,d} = f2_{a,d} \quad \forall z \setminus z_0$ *at* $r = r_{d-1}$
	1	S, H, X	$v_{z,d}\frac{\partial C_{a,d}}{\partial z} = D_{eff,a,d}\left(\frac{1}{r}\frac{\partial C_{a,d}}{\partial r} + \frac{\partial^2 C_{a,d}}{\partial r^2}\right)$	BC1: $C_{a,d} = f1_{a,d} \quad \forall r < r_d$ *at* $z = z_0$ BC2: $\frac{\partial C_{a,d}}{\partial r} = 0 \quad \forall z \setminus z_0$ *at* $r = 0$ BC3: $C_{a,d} = H_{a,d,d+1} C_{a,d+1} \quad \forall z$ *at* $r = r_d$
Inactive membrane	2,3,5	S, H, X	$\frac{D_{eff,a,d}}{r}\frac{\partial}{\partial r}\left(r\frac{\partial C_{a,d}}{\partial r}\right) = 0$	BC1: $\frac{\partial C_{a,d}}{\partial r} = \frac{-N_{a,d}}{D_{eff,a,d}} \quad \forall z$ *at* $r = r_d$ where: $N_{a,d}(r_d) = N_{a,d+1}(r_d) = -D_{eff,a,d+1}\frac{\partial C_{a,d+1}}{\partial r}(r_d)$ BC2: $C_{a,d} = H_{a,d,d+1} C_{a,d+1} \quad \forall z$ *at* $r = r_d$
Bioactive membrane	4,5	S, H	$\frac{\partial C_{a,d}}{\partial t} - \frac{1}{r}\frac{\partial}{\partial r}\left(D_{eff,a,d} r \frac{\partial C_{a,d}}{\partial r}\right) = \hat{r}_{a,d}$	BC1: $C_{a,d} = f1_{a,d} \quad \forall r \in [r_{d-1}, r_d) \; \forall z$ *at* $t = t_k$ BC2: $C_{a,d} = H_{a,d,d+1} C_{a,d+1} \quad \forall z \; \forall t$ *at* $r = r_d$ BC3: $C_{a,d} = f2_{a,d} \quad \forall z$ *at* $r = r_{d-1}$ *at* $t > t_k$
	4,5	X	$\frac{\partial C_{X,d}}{\partial t} - \frac{1}{r}\frac{\partial}{\partial r}\left(D_{eff,X,d} r \frac{\partial C_{S,d}}{\partial r}\right) = \hat{r}_{X,d}$	BC1: $C_{X,d} = f1_{X,d} \quad \forall r \in [r_{d-1}, r_d) \; \forall z$ *at* $t = t_k$ BC2: $C_{X,d} = f2_{X,d} \quad \forall z \; \forall t$ *at* $r = r_d$ BC3: $C_{X,d} = f3_{X,d} \quad \forall z$ *at* $r = r_{d-1}$ *at* $t > t_k$
Biokinetic	4,5	S	$\hat{r}_{S,d} = -\frac{\mu_{max}}{Y_{X/S}}\frac{C_{S,d} C_{X,d}}{K_S + C_{S,d}} - k_m C_{X,d}$	NA[a]
	4,5	H	$\hat{r}_{H,d} = \frac{\mu_{max}}{Y_{X/H}}\frac{C_{S,d} C_{X,d}}{K_S + C_{S,d}}\left(1 - \frac{C_{H,d}}{C_{H,sat}}\right)^n \left(\frac{C_{H,crit}}{C_{H,d} + C_{H,crit}}\right)$	NA[a]
	4,5	X	$\hat{r}_{X,d} = \left(\mu_{max}\frac{C_{S,d} C_{X,d}}{K_S + C_{S,d}} - k_{dec} C_{X,d}\right)\left(1 - \frac{C_{X,d}}{C_{X,max}}\right)$	NA[a]
Transport model	1	NA[a]	$v_{z,d} = v_{in}\left(1 - \frac{r}{r_d}\right)^{k_{v,d}}$	NA[a]
	6	NA[a]	$v_{z,d} = \frac{\varepsilon}{4\mu_w}\left(\frac{dP_d}{dz} - \rho g\right)$ where: $\varepsilon = \frac{(r^2 - r_{d+1}^2)ln(r_{d-1}) + (r_{d-1}^2 - r^2)ln(r_{d+1}) + (r_{d+1}^2 - r_{d-1}^2)ln(r)}{ln(r_{d-1}) - ln(r_{d+1})}$	NA[a]

[a]NA = Not applicable

Chapter 5

Model implementation

This chapter presents the model implementation. First, the implementation strategy is summarized. Second, the multi-domain fiber model in its discretized form is presented. Finally, the model code's structure is explained, highlighting the most relevant scripts that were developed.

5.1. Implementation strategy

The multi-domain membrane bioreactor model is intrinsically composed of coupled boundary value problems of non-linear second-order partial or ordinary differential equations. Furthermore, due to the bioactive domains' reaction rates, the species' equations were coupled. As a consequence of the complex model structure, model implementation has been conducted through several trials to analyze partial results, improve the model, and secure physical consistency, as well as the quality of the final output. The trials allowed to progressively increase the model complexity and improve the solving method. For example, we started to model the domains separately to understand programming requirements, especially for more complex domains (e.g., bioactive domains). Then, the trials advanced until computing the CBMem fiber and reactor model with its coupled domains; however, we coded additional if-statements to switch the domains "on" and "off" and allow the modeling of different domain combinations to ease the practice. The implementation strategy concluded into the steps shown in Fig. 5.1.

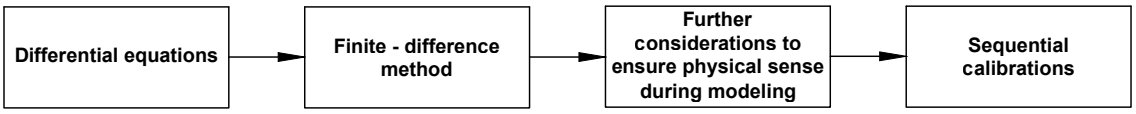

Fig. 5.1: CBMem model implementation strategy.

To solve the model proposed in Section 4.2.1, we employed finite differences in the radial, axial, and time axis as a solution strategy. This approach is particularly useful in modeling phenomena in multi-domain reactors, compared to the high computational costs and time-consuming solving of ODEs. The finite-difference method (see Annex D) applies a local Taylor expansion to describe the concentration difference along the direction of independent variables. Thus, differential equations are approximated using a regular, fine, and structured mesh formed by a square network of lines. This discretization approach is especially recommendable for bioactive domains for dynamic treatment, because of the possibility to model the system as several "short" sequential pseudo-steady state approximations.

As a common practice, we used forward and central difference schemes for first and second-order derivatives, respectively. The forward difference method for first-order derivatives is simple and straightforward, especially when applied at the boundaries. In contrast, the central difference method provides higher accuracy, and is more suitable for second-order derivatives as it captures the behavior of solutions, especially those involving diffusion. However, approximating derivatives using finite difference schemes introduces truncation errors that must be controlled. Moreover, when the current value depends on previous values with existing errors, the overall error can accumulate, potentially leading to larger errors in the final solution if not carefully managed. The approximation of second-order derivatives using the central difference scheme can introduce higher errors due to its nonlinear form. Therefore, multivariate and nonlinear terms can increase the overall error and the risk of instability. Despite the potential of higher error propagation, we concluded that the chosen schemes and their error characteristics were well-managed within the numerical method.

To activate cell migration into the sealant layer, we imposed a lower maximum cell capacity than the initial cell concentration for the bioactive layer (domain 4). Nevertheless, this maximum cell capacity is gradually increased by 10 % if the median of the cell concentration, measured in the bioactive layer, is greater than or equal to 70 % of the current iteration. Thus, this enables the simulation of cell migration phenomenon, while ensuring compliance with the expected maximum cell capacity in both domains.

In addition, depending on the species and domain, initial conditions and some boundary conditions were assumed to follow a function that represents an increasing or decreasing concentration profile to allow solving of the discretized model equations.

Furthermore, we ensured physical consistency during model solving. First, when model solving resulted in negative concentrations, the concentration is corrected by forcing it to be zero. This is applied for mass balance equations and boundary conditions. Second, if the substrate concentration in the bioactive domain reaches zero, the microbial maintenance coefficient rate (k_m) of Eq. (4.18) is imposed to be zero to ensure coherent substrate behaviour. Finally, the cell concentration in bioactive domains is opportunely corrected to respect the maximum cell concentration. This occurs especially after calculating the excess cell concentration to activate cell migration within the bioactive domain or cell proliferation to the adjacent domain. Cell mass conservation is always ensured. A cell sink variable is defined for both domain 4 and 5, which is filled with excess concentration that has not been distributed. Also, the use of the sinks' cell concentration is promoted by adding it in each iteration to the "excess cell concentration" ($C_{X,excess}$) that is being distributed over domain 5 during proliferation.

Finally, the implementation trials also clarified the need for an improved parameter estimation strategy; thus, concluding the decision to conduct parameter calibration for each domain consecutively. For parameter estimation we used the *leasqr* function in GNU Octave, based on the Levenberg-Marquardt nonlinear regression (see Annex F). By analyzing the length of the confidence interval around the point estimate, the parameters' precision were revealed. If the range is narrow, the margin of error is small, i.e., the calibrated parameter is a precise estimate. However, if the interval is wide, the parameter is an imprecise estimate. Also, the parameters' p-values were analyzed to conclude their significance.

5.2. Discretized multi-domain fiber model

The multi-domain fiber model (see Section 4.2.1) was discretized considering the approximation of first and second-order derivatives along the radial direction (positions denoted with i), along the axial direction (positions denoted with j), and along time (moments denoted with k). The discretized fluid and membrane domain models are summarized below. See Annex J for a detailed summary of the model equations and boundary conditions.

5.2.1. Fluid domain models

The fluid domain models (see Eq. (4.2), Section 4.2.1.1) were discretized, using the forward difference along the axial and radial axis and the central difference for the second-order derivative along the radial axis, and afterward rearranged. Eq. (5.1) shows the concentration profiles for a species a (a={S, X, H}) in domain d (d={1, 6}) based on mass balance.

$$C_{a,d}(i,j+1,k) = D_{a,d}\frac{1}{r}\frac{\Delta z}{v_{z,d}}\frac{C_{a,d}(i+1,j,k)-C_{a,d}(i,j,k)}{\Delta r}+ \\ D_{a,d}\frac{\Delta z}{v_{z,d}}\frac{C_{a,d}(i+1,j,k)-2C_{a,d}(i,j,k)+C_{a,d}(i-1,j,k)}{\Delta r^2}+C_{a,d}(i,j,k) \tag{5.1}$$

Fig. 5.2 illustrates the concentration's dependency on the adjacent concentrations, measured in terms of Δz and Δr-distance. Note that the time variable was included for standarization and correct domain coupling.

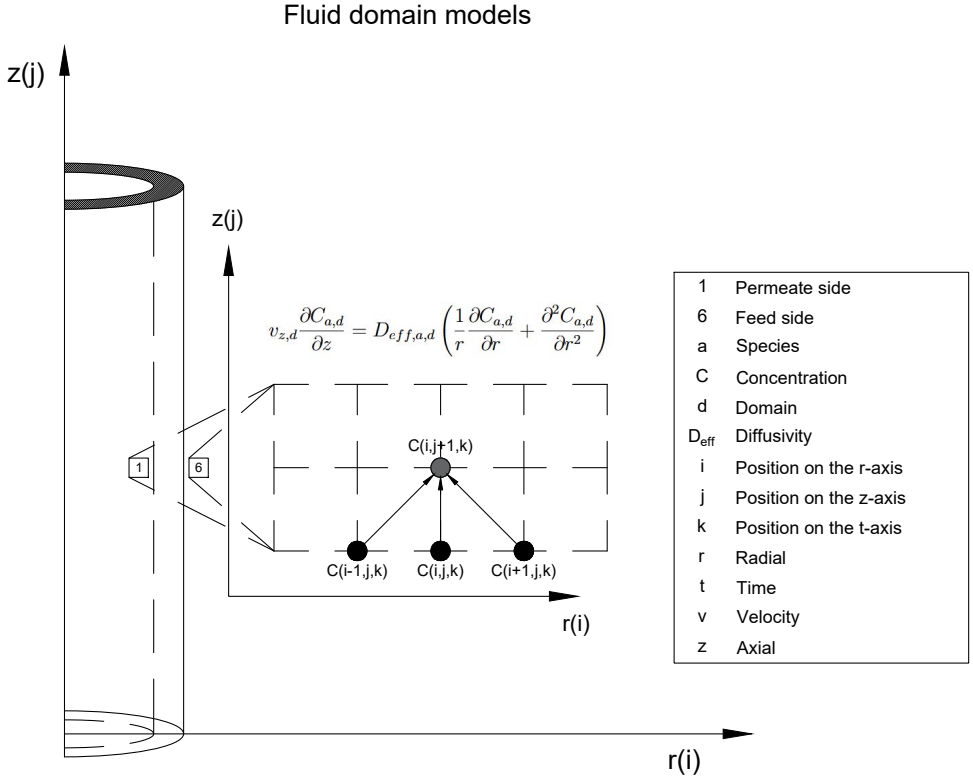

Fig. 5.2: Discretization of the fluid domain model.

5.2.2. Membrane domain models

The membrane domain models (see Section 4.2.1.2) for both inactive and bioactive domains were transformed using the finite-difference method.

Inactive membrane domains

The differential models related to inactive membrane domains express only radial dependency. Thus, they were discretized, using the forward difference along the radial axis and the central difference for the second-order derivative along the radial axis, and afterward rearranged. Eq. (5.2) shows the concentration profile for a species a (a={S, X, H}) in domain d (d={2, 3, 5}) based on mass balance.

$$C_{a,d}(i-1,j,k) = \frac{\Delta r^2}{D_{a,d}}\left(-\frac{D_{a,d}}{r}\frac{C_{a,d}(i+1,j,k)-C_{a,d}(i,j,k)}{\Delta r}\right)+ \\ 2C_{a,d}(i,j,k) - C_{a,d}(i+1,j,k) \tag{5.2}$$

Fig. 5.3 illustrates the concentration's dependency on the adjacent concentrations, measured in terms of Δr-distance. Note that the axial and time variable were included for standarization and correct domain coupling.

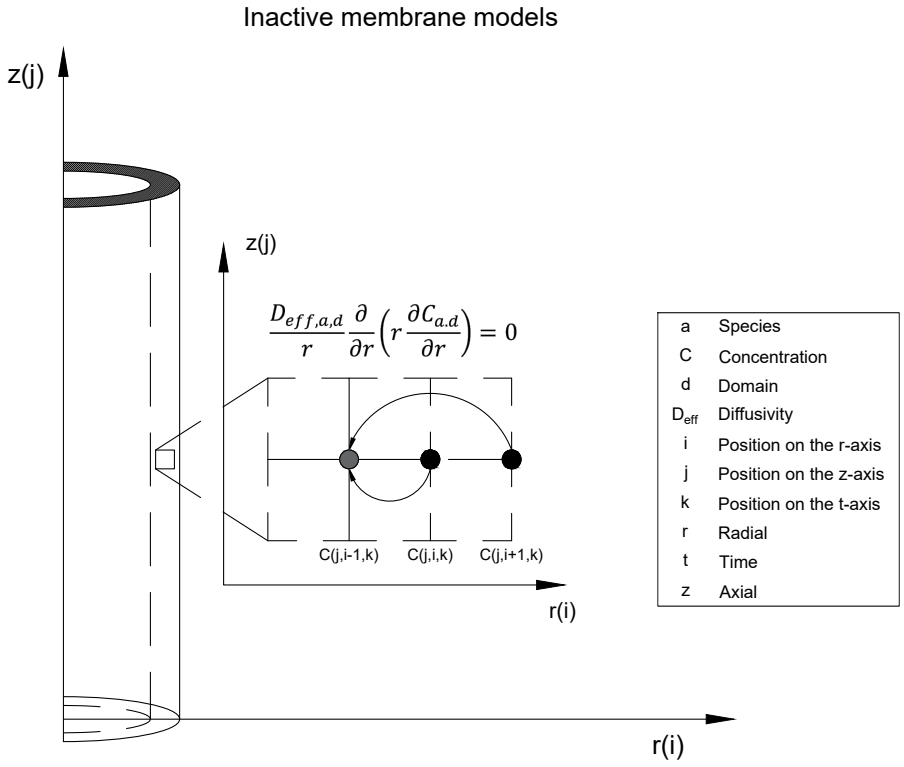

Fig. 5.3: Discretization of the inactive domain models.

Bioactive membrane domains

The models related to bioactive membrane domains do not express axial but time and radial dependence. Thus, they were discretized, using the forward difference along the temporal and

radial axis and the central difference for the second-order derivative along the radial axis, and afterward rearranged. Eqs. (5.3), (5.4), and (5.5) show the concentration profile for each species in a bioactive domain d (d=$\{4, 5\}$) based on mass balance.

$$C_{S,d}(i,j,k+1) = \Delta t \left(k_{1,S} \frac{C_{S,d}(i+1,j,k) - 2C_{S,d}(i,j,k) + C_{S,d}(i-1,j,k)}{\Delta r^2} + k_{2,S} \frac{C_{S,d}(i+1,j,k) - C_{S,d}(i,j,k)}{\Delta r} - k_{3,S} \frac{C_{S,d}(i,j,k)}{K_S + C_{S,d}(i,j,k)} - k_{4,S} \right) + C_{S,d}(i,j,k) \tag{5.3}$$

$$C_{H,d}(i,j,k+1) = \Delta t \left(k_{1,H} \frac{C_{H,d}(i+1,j,k) - 2C_{H,d}(i,j,k) + C_{H,d}(i-1,j,k)}{\Delta r^2} + k_{2,H} \frac{C_{H,d}(i+1,j,k) - C_{H,d}(i,j,k)}{\Delta r} + k_{3,H} \left(1 - \frac{C_{H,d}(i,j,k)}{C_{H,sat}} \right)^n \left(\frac{C_{H,crit}}{C_{H,d} + C_{H,crit}} \right) \right) + C_{H,d}(i,j,k) \tag{5.4}$$

$$C_{X,d}(i,j,k+1) = \Delta t \left(k_{1,X} \frac{C_{S,d}(i+1,j,k) - 2C_{S,d}(i,j,k) + C_{S,d}(i-1,j,k)}{\Delta r^2} + k_{2,X} \frac{C_{S,d}(i+1,j,k) - C_{S,d}(i,j,k)}{\Delta r} + k_{3,X} C_{X,d}(i,j,k) \left(1 - \frac{C_{X,d}(i,j,k)}{C_{X,max}} \right) \right) + (C_{X,d}(i-1,j,k) - C_{X,max}) k_{bb} + C_{X,d}(i,j,k) \tag{5.5}$$

Note that the variables $k_{1,S}$ - $k_{4,S}$, $k_{1,H}$ - $k_{3,H}$, and $k_{1,X}$ - $k_{3,X}$ are defined by Eqs. (5.6)-(5.22).

$$k_{1,S} = D_{S,d} \left(1 - \frac{C_{X,d}(i,j,k)}{C_{X,max}} \right) \tag{5.6}$$

$$k_{2,S} = \frac{D_{S,d}}{r} \left(1 - \frac{C_{X,d}(i,j,k)}{C_{X,max}} \right) - \frac{D_{S,d}}{C_{X,max}} \frac{C_{X,d}(i+1,j,k) - C_{X,d}(i,j,k)}{\Delta r} \tag{5.7}$$

$$k_{3,S} = \frac{\mu_{max} C_{X,d}(i,j,k)}{Y_{X/S}} \tag{5.8}$$

$$k_{4,S} = k_m C_{X,d}(i,j,k) \tag{5.9}$$

$$k_{1,H} = D_{H,d} \left(1 - \frac{C_{X,d}(i,j,k)}{C_{X,max}} \right) \tag{5.10}$$

$$k_{1,S} = D_{S,d} \left(1 - \frac{C_{X,d}(i,j,k)}{C_{X,max}} \right) \tag{5.11}$$

$$k_{2,S} = \frac{D_{S,d}}{r} \left(1 - \frac{C_{X,d}(i,j,k)}{C_{X,max}} \right) - \frac{D_{S,d}}{C_{X,max}} \frac{C_{X,d}(i+1,j,k) - C_{X,d}(i,j,k)}{\Delta r} \tag{5.12}$$

$$k_{3,S} = \frac{\mu_{max} C_{X,d}(i,j,k)}{Y_{X/S}} \tag{5.13}$$

$$k_{4,S} = k_m C_{X,d}(i,j,k) \tag{5.14}$$

$$k_{3,S} = \frac{\mu_{max} C_{X,d}(i,j,k)}{Y_{X/S}} \tag{5.15}$$

$$k_{4,S} = k_m C_{X,d}(i,j,k) \tag{5.16}$$

$$k_{1,H} = D_{H,d}\left(1 - \frac{C_{X,d}(i,j,k)}{C_{X,max}}\right) \tag{5.17}$$

$$k_{2,H} = \frac{D_{H,d}}{r}\left(1 - \frac{C_{X,d}(i,j,k)}{C_{X,max}}\right) - \frac{D_{H,d}}{C_{X,max}} \frac{C_{X,d}(i+1,j,k) - C_{X,d}(i,j,k)}{\Delta r} \tag{5.18}$$

$$k_{3,H} = \frac{\mu_{max}}{Y_{X/H}} \frac{C_{S,d}(i,j,k) C_{X,d}(i,j,k)}{K_S + C_{S,d}(i,j,k)} \tag{5.19}$$

$$k_{1,X} = D_{X,d}\left(1 - \frac{C_{X,d}(i,j,k)}{C_{X,max}}\right) \tag{5.20}$$

$$k_{2,X} = \frac{D_{X,d}}{r}\left(1 - \frac{C_{X,d}(i,j,k)}{C_{X,max}}\right) - \frac{D_{X,d}}{C_{X,max}} \frac{C_{X,d}(i+1,j,k) - C_{X,d}(i,k)}{\Delta r} \tag{5.21}$$

$$k_{3,X} = \mu_{max} \frac{C_{S,d}(i,j,k)}{K_S + C_{S,d}(i,j,k)} - k_{dec} \tag{5.22}$$

Fig. 5.4 illustrates the concentration's dependency on the adjacent concentrations, measured in terms of Δt and Δr-difference. Note that the axial variable was included for standarization and correct domain coupling.

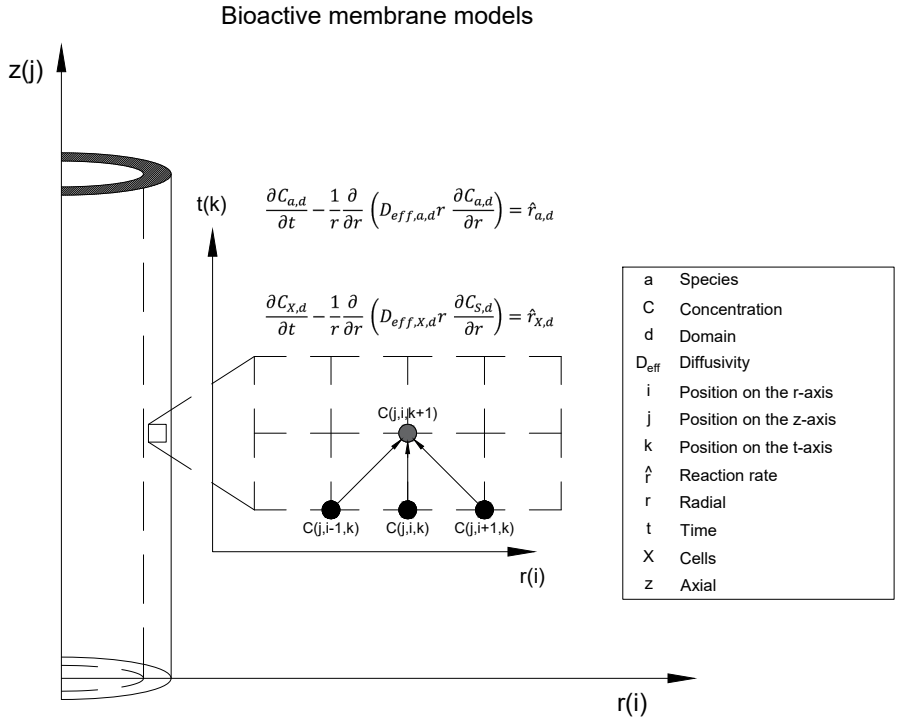

Fig. 5.4: Discretization of the bioactive domain models.

5.3. Implementation in GNU Octave

To implement the model, several parameters were estimated using different information sources. All parameters and assumptions that were considered are reported in Annex K. Then, the model code was structured using interconnected scripts. The most relevant are briefly described below:

1. **Main:** Englobes the main code. Loads data, fits parameters using the *leasqr* function, reports the calibrated parameters and their confidence intervals, generates graphical results, and informs about the overall process performance. According to the needs, this script calls the *CBMem reactor model* script for calibrations or simulations.

2. **CBMem reactor model:** Englobes the model code called for calibration or simulation. Solves the mass balances of each domain, i.e., from the mixed liquor side (domain 6) to the lumen side (domain 1), by calling the respective *Domain d* script while ensuring domain coupling. The model code is controlled through switch-parameters that activate or deactivate the modeling of certain domains. Depending on the needs, the *CBMem reactor model* generates different outputs of interest, such as concentration profiles or the H_2 outlet mass flow rate.

3. **Domain d model:** Englobes the mass balances for domain d to be solved. A script is provided for each domain, except for domain 4 and 5, which were coded jointly in one script due to their interdependence. According to the needs, the *Domain d* script calls auxiliary functions.

4. **Other auxiliary scripts:**

   - Data scripts: Include experimental or verisimilar data. This script is called by the *Main*.
   - Transport model: Englobes the transport code to be solved for calibration of transport parameters. For this, it calls the *Velocity model*.
   - Velocity models: Defines the axial velocity equation to be solved. A script is provided for the mixed liquor and lumen. Depending on the equation, it calls the *Pressure model*.
   - Pressure model: Englobes the pressure model to be solved for the mixed liquor and lumen, delivering the pressure distribution for different z points (axial direction), its first and second derivative.
   - Inequality distribution function: Allows an unequal distribution of excess cell mass over the radial axis of a certain domain, while ensuring mass conservation. The distribution is controlled through a parameter called λ; high values for λ indicate that the excess cell mass is concentrated in the domain's most internal radial positions. This script is called by the *Domain 45 model*.
   - Variance function: Calculates the variance of matrices. This script is called by the *Main* to determine confidence regions.
   - Lifetime functions: Defines the membranes lifetime by evaluating if-clauses. Three different lifetime definitions are provided. One is contingent upon the H_2 capture efficiency, assessed against a minimum acceptable threshold. Another hinges on cell growth within domains 4 (bioactive layer) and 5 (sealant layer), juxtaposed against the maximum cell capacity. The third definition rests on substrate availability within domains 4 and 5, measured against a predetermined maximum acceptable depletion threshold.

The ready-to-use GNU Octave routine for the calibration, simulation, and sensitivity analysis of the CBMem reactor model can be downloaded from the author's cloud (see reference [95]).

Chapter 6

Model calibration and validation

In order to complete the assessment of the first specific goal, the following chapter will show and discuss the main results for model calibration, direct validation, and cross-validation.

6.1. Results and discussion

The CBMem reactor model is based on several parameters, and in general the quality of a model depends on the quality of parameter estimation. Due to the structure of the system of equations, parameter estimation required different information sources. Some parameters were estimated using bibliographic sources, which are summarized in Annex K. Others were calibrated through the Levenberg-Marquardt nonlinear regression in GNU Octave. Model calibrations were implemented for transport models, domain models, and the CBMem model (Fig. 6.1).

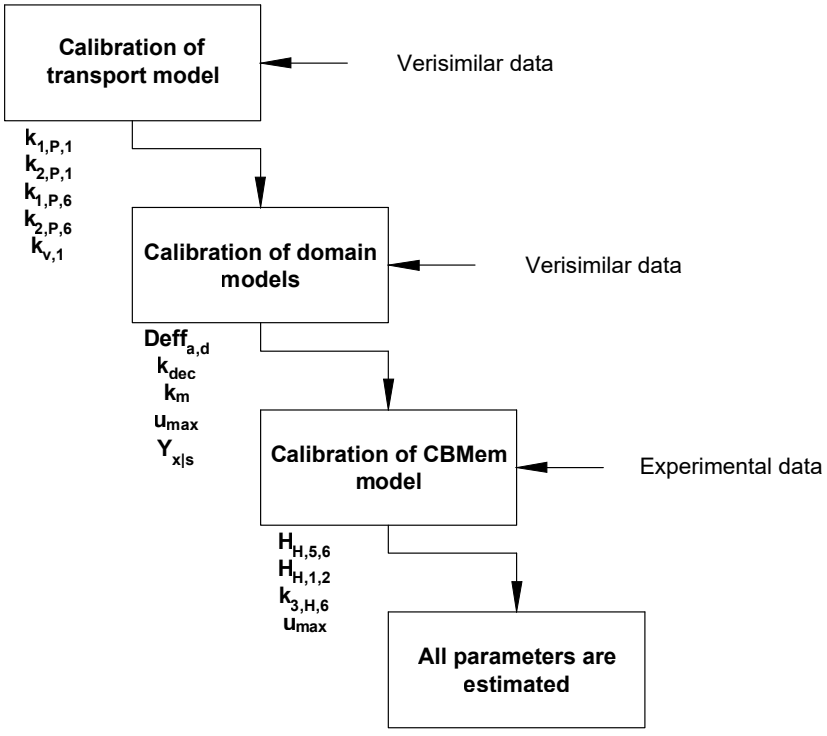

Fig. 6.1: Calibration sequence.

First, transport parameters were calibrated by using verisimilar data to ensure an expected velocity profile that is directly incidential in the mass balance equations of domain 1 and 6. Second, domain calibrations, using verisimilar data and a timespan of 3 days, were conducted in sequence, mainly to estimate diffusive parameters. However, for domain 4 and 5 in their bioactive state, parameter calibration for diffusive and biokinetic parameters was concluded through a manual procedure, i.e., the *leasqr* function was not employed. This decision was taken based on the several unknown parameters, the model sensitivity towards their values, and the unknown concentration profiles.

Third, parameter calibrations for the complete CBMem module, using experimental data that cover 30 days, were performed. When adopting a strategy of simultaneous calibration of parameters for the CBMem reactor model, we observed that the confidence interval through *leasqr* was not obtained. This outcome could be attributed to the model structure and the numerous parameters. On the one hand, the non-linear model structure could create multiple solutions, where local minima compete with global minima. On the other hand, despite the model's physical sense, some parameters could depend on others. This is common in biological models where, for example, the maintenance coefficient (k_m) and the half-saturation constant (K_S) are closely linked [66]. To address this drawback parameter reduction can be implemented. For example, the values of some parameters can be set to calibrate the remaining unknown values, or parameters can be mathematically aggregated.

For the adjustment of the CBMem reactor model, we adopted a three sequential calibrations strategy to estimate boundary-related parameters by fixing the values of some parameters to calibrate others. Thus, estimates can be improved and used for the next calibration. A major advantage of this strategy was that it provided the estimates' confidence interval. After concluding model calibration, cross-validation was conducted.

The main results are presented and discussed below. In addition, the details of the model calibrations are presented in Annex L.

6.1.1. Calibration of the transport model

As shown in Annex L.1, the calibration of the transport model (see Section 4.2.2) resulted to achieve a good fit for the velocity profiles, however with an insignificant change in axial direction. Surprisingly, the pressure profile of the mixed liquor (domain 6) was not able to represent the decrease between inlet and outlet pressure. The calibrations found that the parameters $k_{1,P,1}$ and $k_{1,P,6}$ are the most influential to calibrate the models; but, contradicting values would be required to simultaneously fit the pressure and velocity profiles. In addition, data-fitting revealed that $k_{2,P,1}$ and $k_{2,P,6}$ tend to zero, showing that term z^2 of the pressure model for domain 1 and 6 is negligible.

For the scope of this research, the results related to the pressure profile do not undermine representativeness because of the small reactor scale and the negligible pressure decrease according to experimental observations. Nevertheless, future model improvements should address the axial variation of the pressure model if the radial velocity profile through the membrane is an operational variable of interest to study convective transport.

6.1.2. Calibration of domain models

As reported in Annex L.2, the calibration of membrane domains aimed to estimate the values of diffusion coefficients to ensure the expected tendency of the species' concentration profiles. Visual inspection showed that the modeled concentrations were similar to the proposed referential data, as the latter tend to remain within the confidence regions.

The parameters' confidence intervals revealed mixed results in terms of margin of error. Of the calibrated parameters, $D_{H,2}$, $D_{H,3}$, and $D_{S,5}$ had a difference of less than $\pm 0.1\,\%$ compared with their intervals' limits. As for $D_{H,1}$ and $D_{H,5}$, this difference was less than $\pm 16\,\%$. However, $D_{S,6}$, $D_{H,6}$, and $D_{S,3}$ resulted to have large confidence intervals (more than $\pm 50\,\%$). Of those, $D_{S,3}$ had the largest, indicating a low certainty on this estimate. In addition, the p-value analysis revealed that $D_{H,6}$ and $D_{S,3}$ resulted to be statistically non-significant.

Large confidence intervals can be explained in part by the dispersion of the verisimilar data; thus, a greater data set could be recommended. Another explanation is the *leasqr* configuration, e.g., the considered values of the initial parameters or the limited range for variation through the *options.bound* argument. Similarly, p-values less than the significance level can either indicate that not enough data is provided or the parameters might not be contributing meaningfully to the model. Despite these results for some transport parameters, the verisimilar data that we used was only indicative to ensure the concentration profiles' tendencies and do not necessarily represent reality. Thus, the outcome is of low importance.

In addition, all calibrated parameters were significantly different compared to those reported in the bibliography. This difference can be explained by the numeric steps that we decided to use for modeling, which force the diffusive parameters to remain in a certain range to avoid model instability. Hence, the calibrated diffusion coefficients should not be associated to their physical meaning of species diffusion in the respective material. Furthermore, several calibrated diffusion coefficients required to be of a smaller order of magnitude compared to expected values, which could create difficulties to observe the influence of transport phenomena on the overall process.

As for the bioactive domains, they could adequately represent biological phenomena and the relation between species. Especially the substrate and cell concentration profiles within space and time showed a good response. However, it can be seen from the data in Table 6.1 that a significant change of several biological parameters, compared to their bibliographic values, was required. These were the biomass decay constant (k_{dec}), the microbial maintenance coefficient (k_m), the maximum specific growth constant (μ_{max}), and the yield of biomass on substrate ($Y_{X/S}$).

Table 6.1: Biological parameters after manual calibration of bioactive domains.

Parameter	**Calibrated value**	**Bibliographic value**[a]
k_{dec}, Biomass decay constant $\left[\frac{1}{s}\right]$	3.000e-07	9.259e-06
k_m, Microbial maintenance coefficient $\left[\frac{kg_{COD}}{kg_{cells}\,s}\right]$	1.013e-09	3.125e-04
μ_{max}, Maximum specific growth rate $\left[\frac{1}{s}\right]$	1.500e-06	4.630e-05
$Y_{X/S}$, Yield of biomass on substrate $\left[\frac{kg_{cells}}{kg_{COD}}\right]$	15.000e+02	15.000e-02

[a]Reference values were obtained from studies using ADM1-based models, structured kinetic models for ideal reactors [37, 96].

Interestingly, we observed that the model stability was highly dependent on the substrate con-

centration behavior and availability. The μ_{max} was calibrated, concluding a value that is 3 % the reported value in bibliography. This allowed to observe cell growth. However, as μ_{max} influences directly on the substrate consumption rate, we also decided to calibrate the $Y_{X/S}$. To avoid substrate depletion, $Y_{X/S}$ changed by being 10,000 times its reference value. This difference is a rather counterintuitive outcome as yields are based on the stoichiometry of the biochemical reactions and should be, thus, similar to the reported in bibliography. Nevertheless, assuming sufficient available substrate concentration within the bioactive domains is particularly useful in studying the model's capacity to represent biological phenomena in time. Finally, k_m and k_{dec} also changed because of their defined dependency on μ_{max} and $Y_{X/S}$ and their involvement in the same biokinetic equations.

A note of caution is due here since the bibliographic values of biological parameters are usually determined through models that could have another structure. As discussed in Boese-Cortés et al. (2019) [59], fermentative bioreactors have been commonly represented as unstructured nonsegregated and nondistributed models, ignoring all heterogeneities, or unstructured kinetic models. The former involve empirical and statistical equations that are able to fit experimental data by linear o nonlinear regression even if they do not establish a physical analysis. The latter involve semiempirical equations that are based on conventional biokinetics applied at the reactor-scale; however, such kinetic models are not necessarily a true phenomenological description, as usually an ideal (perfectly mixed homogeneous) bioreactor is assumed and generalized expressions are employed.

In summary, the results suggest that calibration of membrane domains, especially bioactive domains, is difficult to conduct when not sufficient, reliable, and diverse data is available. We also observed that the selection of the numerical steps is incidental on the parameters' value to ensure model stability. Therefore, the calibrated biological and transport parameters must be interpreted with caution as these are subject to the model structure.

The calibration results also indicate that the substrate concentration in the wastewater feed stream (6.92 $\frac{g}{L}$) of the experimental set-up (see Annex G) is not sufficient for wastewater-to-H_2 operations. By assuming sufficient substrate concentration within the bioactive domains, the calibrated parameters do not allow to represent accurately the substrate concentration profiles of the case study. Nevertheless, we conclude that the model is capable of representing biological behavior and, thus, used the calibrated parameters for further analysis.

6.1.3. Calibration of CBMem

The most relevant calibrations were applied over the complete CBMem modeling to estimate parameters subject to different domains. Parameters that directly influence the H_2 profile were selected, including those related to the boundary conditions and biological activity.

We conducted three consecutive calibrations. First, Henry-like equilibrium coefficients for the H_2 at the sealant layer/mixed liquor ($H_{H,5,6}$) and the lumen side/support layer interface ($H_{H,1,2}$) were calibrated. These are represented through Eqs.(6.1) and (6.2). Second, the mixed liquor side's parameter $k_{3,H,6}$, that describes the dynamics of H_2 at the border (Eq. (6.3)) was adjusted to allow dynamic domain coupling with internal occurring phenomena. Third, the maximum specific growth rate (μ_{max}), represented through Eq. (6.4) (used in the mass balance equations for both domain 4 and 5 which are interdependent with the other species' mass balances), was adjusted for a flexible calibration that adapts to the internal biological phenomena. All three parameter estimations were

conducted by considering the fit of the H_2 outlet mass flow rate to experimental data.

$$C_{H,d} = H_{H,5,6} C_{H,6} \quad \text{at } r = r_5 \quad \forall z \; \forall t \tag{6.1}$$

$$C_{H,1} = H_{H,1,2} C_{H,2} \quad \text{at } r = r_1 \quad \forall z \; \forall t \tag{6.2}$$

$$\begin{aligned} C_{H,6} = \frac{1}{3} \left(k_{1,H,6} C_{H,6}(j+1, i+1, k) + k_{2,H,6} C_{H,6}(j, i, k) + \right. \\ \left. k_{3,H,6} t + C_{H,6}(j+1, i, k-1) \right) \quad \text{at } r = r_5 \quad \forall z \setminus z_0 \end{aligned} \tag{6.3}$$

$$\hat{r}_{H,d} = \frac{\mu_{max}}{Y_{X/H}} \frac{C_{S,d} C_{X,d}}{K_S + C_{S,d}} \left(1 - \frac{C_{H,d}}{C_{H,sat}} \right)^n \left(\frac{C_{H,crit}}{C_{H,d} + C_{H,crit}} \right) \tag{6.4}$$

Tables L.17 - L.19 of Annex L.3 show the input and output arguments of each CBMem model calibration. For all three calibrations, convergence was achieved after one iteration, changing the parameters' value from their initial guess, except for $k_{3,H,6}$. Moreover, Table 6.2 summarizes the comparisons of the estimates with respect to their confidence intervals.

When comparing the calibrated values with their confidence interval, it can be seen that the difference from the adjusted value of $H_{H,5,6}$ with respect to its limits is of $\pm 5\,\%$, indicating a high confidence on the estimated parameter. Contrarily, the difference for $H_{H,1,2}$ is of $\pm 72\,\%$; thus, this estimate has a significant margin of error. The uncertainty on $H_{H,1,2}$ can be due to the high variance of the experimental data used for calibration that can be derived from measurement errors. Finally, the difference for $k_{3,H,6}$ and μ_{max}, compared to their confidence intervals' limit, were $\pm 6\,\%$ and $\pm 0.3\,\%$, respectively. These findings show that the last two calibrations allowed certainty inherent in their estimates. Besides the analysis of the confidence intervals, the parameters' p-value was obtained and showed to be in all cases less than the significance level, suggesting that the calibrated parameters are significant and likely to have a meaningful impact on the model's outcome.

Table 6.2: Parameters calibrated to experimental data.

Parameter	**Calibrated value**	**Confidence interval**	**P-value**
$H_{H,5,6}$, Equilibrium distribution coefficient of hydrogen between domain 5 and 6 [−]	9.999e-01	[9.512e-01 10.488e-01]	0
$H_{H,1,2}$, Equilibrium distribution coefficient of hydrogen between domain 1 and 2 [−]	10.574e-01	[2.989e-01 18.158e-01]	8.582e-03
$k_{3,H,6}$, H_2 boundary condition parameter for dynamic representation at the membrane/ mixed liquor border $[\frac{kg}{m^3 s}]$	9.999e-12	[9.4294e-12 1.057e-11]	0
μ_{max}, Maximum specific growth rate $\left[\frac{1}{s}\right]$	1.480e-06	[1.476e-06 1.484e-06]	0

Note that no comparison with bibliographic values was reported because of the process and model-specific parameters. As for equilibrium distribution coefficients, these are highly dependent on the involved species and media, and no suitable reference could be found in the literature. In turn, $k_{3,H,6}$ is a specific model parameter to mathematically describe a boundary condition at the membrane/mixed liquor interface, whose experimental measurement is not common. The μ_{max} is also a highly specific. Despite the fact that the calibrated value resulted to be $3.2\,\%$ the reported

value in bibliography [37, 96], this comparison is not sufficiently substantiated as the calibrated μ_{max} is related to the modeling of cell growth within a membrane, while commonly reported μ_{max} values are estimated through unstructured kinetic models for dark fermentation in ideal reactors.

After all calibrations, the parameters were used to plot the modeled H_2 outlet mass flow along with the experimental data against time, being the plot for the last calibration of most importance (Fig. 6.2). Visual inspection for direct validation showed that the modeled permeated H_2 is similar to the experimental data as the latter remained within the confidence region, indicating a good fit. Only the second experimental data point resulted to be an outlier. This data point was zero when the CBMem reactor operated for 24 hours, which could be due to the acclimatization of microorganisms. In turn, the model considers an exponential cell growth from the start.

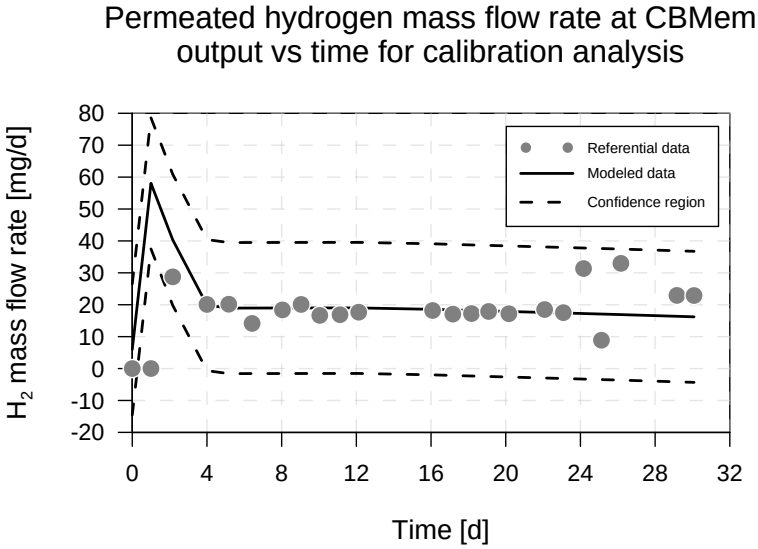

Fig. 6.2: Calibration of the CBMem model using the calibrated parameters of Table 6.2.

What stands out in Fig. 6.2 is the modeled peak at 24 hours. This could be attributed to the H_2 concentration profile behavior within domain 4 that has been observed for the first temporal points (during the 3 day simulation), which showed a significant increased in form of a peak (see Annex L.2.2, Fig. L.11). It seems possible that these tendencies are due to the imposed boundary conditions and the model sensitivity towards concentration differences. Nevertheless, the formation of a peak at the outlet is also observed in the experimental data set (Fig. G.3). Once the modeled peak is stabilized, Fig. 6.2 showed a slight trend of decreasing the permeated H_2, which agreed with the expected outcome.

Overall, these results indicate that the CBMem calibration allowed a good fit with the experimental data. Nevertheless, a calibrated model needs to be validated to ensure its representation capacity.

6.1.4. Validation

The calibrated parameters were afterwards used for cross-validation. Fig. 6.3 compares the modeled data with the second set of experimental data. With the help of the confidence region, a good fit could be observed. The model allowed to follow the data points, except for two at the

initial moments. As we used the same independent data points for the graphical output, the modeled profile did not show the initial condition at $t = 0$. Thus, instead of observing a peak (as seen during direct validation in Fig. 6.2), the modeled H_2 mass flow rate expressed a decreasing tendency, which was more notorious at the beginning of the simulation and stabilized around day 3 onwards.

Furthermore, due to the nature of the "experimental data" set (created through interpolation with noise addition), caution must be applied, as the findings might not be sufficient to ensure validation. The availability of sufficient experimental data at different operating conditions is an important issue for future research.

Despite the above mentioned limitations, we conclude that the model is suitable to represent the CBMem reactor from day 3. The next chapter, therefore, moves on to discuss the process simulation by observing the species' behavior through the CBMem and evaluating the performance.

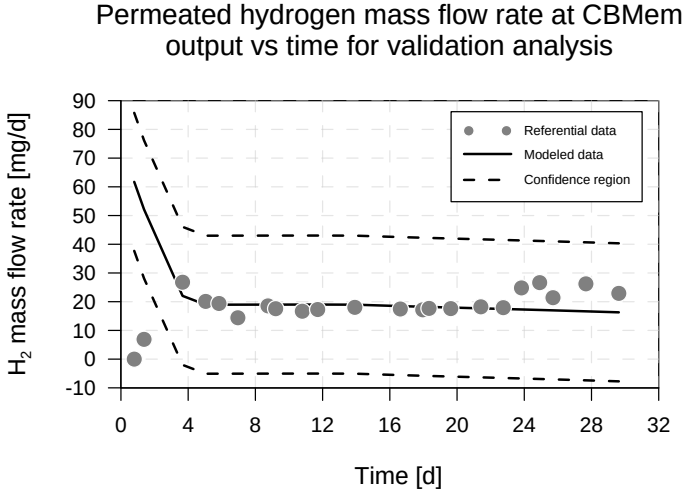

Fig. 6.3: Cross-validation of the CBMem model using the calibrated parameters.

6.2. Chapter conclusions

In the previous sections, a phenomenological model was developed for a multi-domain membrane bioreactor for H_2 production and separation from wastewater. The model integrates biological, kinetic, and mass transfer mechanisms, assessing the importance of internal design and operational conditions. It employs coupled second-order PDEs or ODEs based on mass balances to follow concentration profiles of cells, substrate, and H_2 in each domain. Biological reaction, advection, and diffusion are tailored to specific domains. The model accounts for effects of cell growth on the mass transfer and substrate- and space-driven cell migration. Representative equations with their boundary conditions were defined for fluids, inactive, and bioactive membrane domains, and their mathematical integration was ensured.

As a solution strategy, the CBMem reactor model was transformed using the finite-difference method for implementation in GNU Octave. Parameter estimation using both bibliographic sources and calibration was required. Due to the small data set, several unknown values, and the need to ensure expected concentration profiles, sequential parameter calibrations based on Levenberg-

Marquardt nonlinear regression were conducted. Finally, data-fitting to experimental observations was performed to estimate parameters that influence the CBMem operation for H_2 production and recovery, and cross-validation followed.

Despite the challenges derived from limited data and parameter estimation, good fits were observed based on the confidence region. Although several assumptions were taken, a conservative approach was maintained. The strongest assumptions are related with the domain-specific condition of variables in time, the adopted linear equation to describe the effective diffusion coefficient, and transport phenomena in membrane domains. Each of those assumptions are explained below.

As the model is based on equations that are domain-specific, we defined a model structure that combines domains with different state conditions (steady and unsteady). This modeling strategy makes the implementation more flexible as only the equations for unsteady-state domains, i.e., bioactive layers, depend explicitly on the time step, while steady-state (inactive) domains are time-dependent through their boundary conditions based on concentration variations. The model's temporal resolution is dominated by the unsteady-state domains, influencing the dimensions of the concentration matrices but also the numerical stability of the entire system. Therefore, the bioactive domains must be carefully modeled and calibrated. Despite this, the strategy enables flexibility in terms of spatial (radial) resolution for each domain, which can decrease computational costs.

The second assumption, that adopts Eq. (4.1) for the effective diffusion coefficient, allows to represent variation of mass transfer due to cell growth in space and time. It is a simple method that is representative for both inert and bioactive conditions, assuming that cells are impermeable and consequently reduce available volume for diffusion in the membrane matrix. Although other equations can be suggested [59], the function is less dependent on diffusive parameters as it would only require estimations of the molecular diffusivity in the inert support phase, which can be easily conducted through experiments. The adopted transport model influences the formation of concentration gradients in space with the possibility of reaching complete depletion of substrate or the accumulation of the hydrogen product due to diffusive resistance. Thus, the use of linear functions can adequately describe the interacting processes of biological membranes and process variables.

The third assumption that is considered to be of most importance is assuming only diffusive phenomena, and not the combined effect with advection, in membrane domains. Although the some membrane layers had pore size larger than 1 nm that can allow a convective flow through the pores [70], the assumption allowed a more simplified model, while representing the most critical phenomena. Due to its dense and porous structure, the membrane restricts bulk fluid flow, and the movement of substrates and products through the membrane is dominated by diffusion. Nevertheless, applying convective velocity can be an operational parameter of interest as it is favorable for submerged hollow-fibers to overcome diffusive mass transport [71] and nutrient limitation [72, 73].

In conclusion, the developed phenomenological model integrates key phenomena and domain-specific conditions for H_2 production in a CBMem reactor, capturing its dynamic behavior to provide insights into performance. Moreover, due to its modular-structure, the model is easily adaptable to different membrane designs for further exploration. Overall, when adequately calibrated and validated, the model could serve as a powerful tool not only for understanding the wastewater-to-H_2 process but also for driving innovation for process intensification.

Chapter 7

Process simulation

To assess the second specific goal, this chapter presents and discusses the main results related to process simulations for phenomena and performance analysis. Thus, the chapter will respond to the research question on how does the bioactive layer evolve and influence performance indicators.

7.1. Results and discussion

The calibrated parameters were used for subsequent simulations considering a 1 month and 6 month timespan to analyze the concentration profiles within the membrane and the evolution of the bioactive layer behavior. In addition, the CBMem reactor performance is evaluated in terms of the H_2 yield, H_2 capture efficiency, and membrane lifespan.

7.1.1. Simulations for 1 month

7.1.1.1. Concentration profiles through the CBMem

As shown in Fig. 7.1, the substrate, H_2, and cell concentration profiles for the CBMem were obtained. The graph was plotted for domain 1 to 5 to ease visual analysis; in addition, the concentrations were plotted for three different times: day 0, day 15, and day 30.

As shown in Fig. 7.1A, the substrate concentration profile decreased from the membrane/mixed liquor interface towards the membrane. The concentration was relatively stable within domain 5, presenting values around 5.52 $\frac{g}{L}$. At day 15 and 30, the concentration further decreased when it reaches domain 4. The observed decrease in the substrate concentration is attributed to the substrate consumption by the cells. Substrate consumption was more pronounced at more advanced times. Finally, the concentration profile turned to be zero once it reached the hollow fiber, which is consistent to the layer's selectivity and hydrophobia.

Moreover, Fig. 7.1B presents the H_2 concentration profile through the CBMem. Overall, the H_2 concentration moved between values close to zero and 1.6 $\frac{mg}{L}$. H_2 concentration decreased smoothly from the membrane/mixed liquor interface into the membrane. Approximately at the middle of domain 5, this tendency was inverted for times higher than day 0, resulting in a graph that had a convex behavior within the sealant layer. Once domain 4 was reached, the H_2 concentration changed its profile. At day 0, the concentration decreased in domain 4, 3, and 2. In turn, at day 15 and 30, H_2 concentration increased, which can be explained in part by the biological H_2 production

from the immobilized cells. Then, the concentration decreased in domain 3 and 2. Due to the adopted Henry-like equilibrium distribution coefficient, the H_2 concentration showed a slight increase at the lumen/membrane interface, compared to the concentration expressed at the membrane side. This tendency reflects the hydrogen's affinity towards the gas phase.

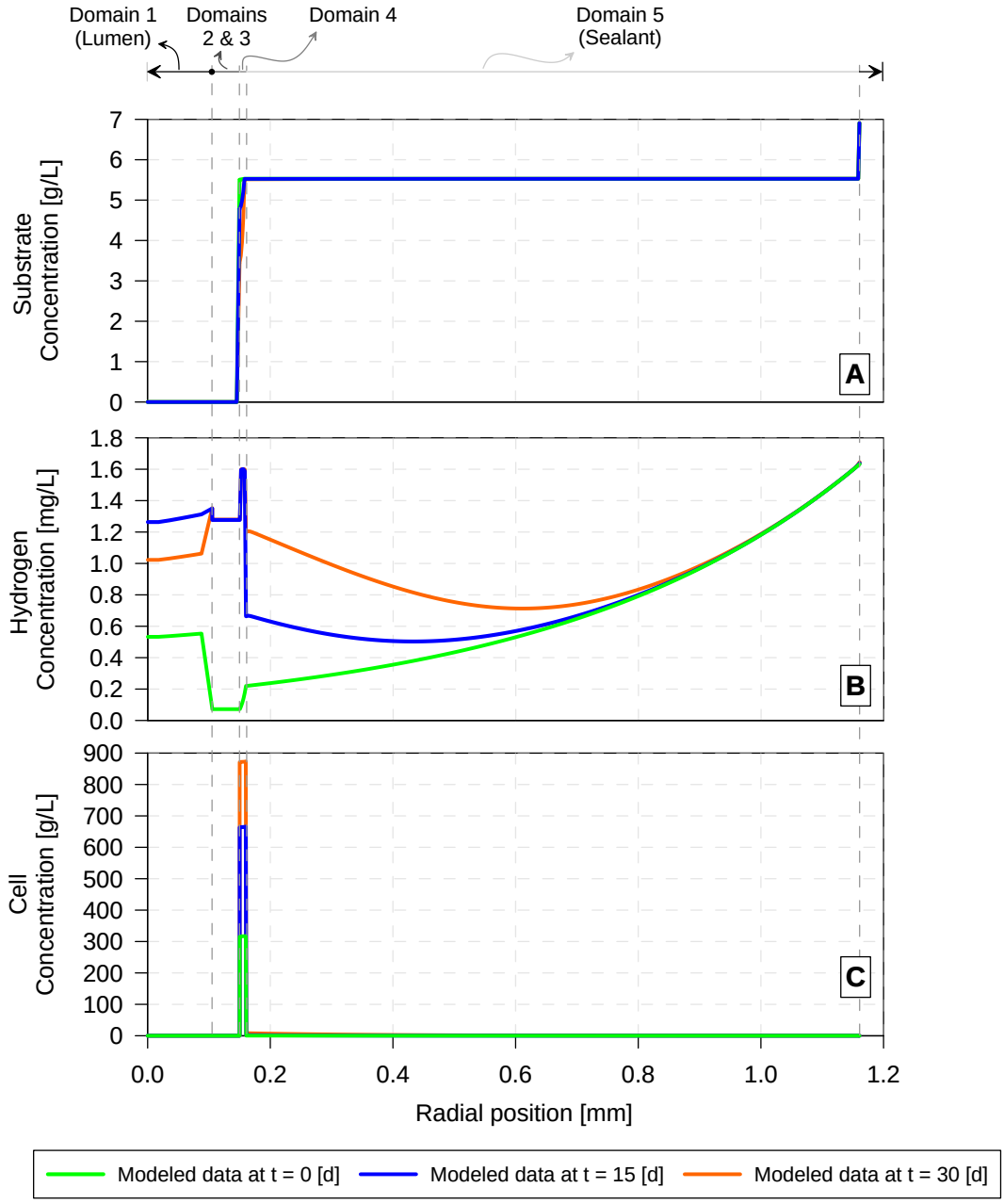

Fig. 7.1: Species concentration profiles in the CBMem during a one month operation.

For all times, the H_2 concentration profile decreased within domain 1. This agrees with the use of the sparging gas to sweep the H_2 towards the outlet. The most striking result to emerge from the data was that H_2 concentration in the lumen was above zero at day 0. A likely cause is that the discretized model required initial conditions: internal domains are related (coupled) to the H_2 concentration at the mixed liquor defined from day 0, and the increase observed from domain 2 (hollow-fiber) to 1 (lumen) is due to the Henry-like equilibrium distribution. Thus, we prioritized

long-term representation over the reactor start-up and membrane acclimatization. This result suggests that day 0 should be considered as the day with an already significant H_2 production. In addition to the previous observation, we noticed that the H_2 concentration at day 15 is higher than day 30. This might be attributed to the observed H_2 peak presented at initial moments, which the discretized model tends to stabilize in longer times.

Lastly, the concentration profile, represented in Fig. 7.1C, showed cell presence within domain 4, and their expected growth in time. A deeper examination of the bioactive behavior is provided in the next section, supported by visually distinctive concentration profiles for domain 4 and 5.

7.1.1.2. Evolution of the bioactive layer

To improve the analysis of the bioactive layers, we plotted the species concentration for domain 4 and 5 at the three different times (Fig. 7.2). Regarding domain 5, all three species showed a curved concentration profile. Overall, the substrate concentration decreased as it entered the membrane, as well as time passed (Fig. 7.2A). An unanticipated tendency was the one expressed modestly close to the membrane/mixed liquor border. However, this might be related to the boundary condition and its use during the discretized mass balance model solving.

The H_2 concentration in domain 5 showed its decrease as this species entered the membrane (Fig. 7.2B). Furthermore, it can be clearly observed how the convex profile was formed as time passed, resulting in an increase of the H_2 concentration towards the interface that separates the domains 4 and 5. This intriguing tendency reflects the profile's adaption to the H_2 increase within domain 4, demonstrating that the model ensures domain coupling. Moreover, back diffusion of H_2 from domain 4 to domain 5 could contribute.

The model also showed that the cell concentration profile is higher at the domain 4/5 interface, decreasing from this position towards the mixed liquor (Fig. 7.2C). This result is consistent with cell migration phenomena. Thus, cells began to migrate from the initially immobilized cell layer towards the sealant layer, stimulated by space and substrate limitations. The model also proved that the cell concentration grew in time. For example, while the initial concentration at the left border was less than 0.5 $\frac{g}{L}$, the concentration was above 8 $\frac{g}{L}$ at day 30.

As for domain 4, a similar substrate concentration tendency was observed (Fig. 7.2D). When comparing with the behavior in domain 5, domain 4 showed that substrate consumption was notoriously more pronounced in space (considering that this is a small layer) and time. Also, the substrate decrease in domain 4 showed a convex form, which differs with the concave behavior in domain 5. The substrate decreasing tendencies are directly related to the high cell concentration profile within the domain.

However, the H_2 concentration profiles at initial conditions was distinctive from those at day 15 and 30 (Fig. 7.2E). Due to the model structure, the former resulted from a defined model profile; we proposed a decreasing tendency from the most right border towards the membrane's inside. In turn, the concentrations at longer times expressed an increase from the most right border, a relatively stable profile at the domain's center, and a decrease at the most left border. The stable profile segment showed having reached the critical H_2 concentration that enhances production inhibition. This also affirms diffusion restrictions in the material. As for the pronounced tendencies

at the borders, being the profile expressed, it might be attributed to the influence of the boundary conditions on the mass balance equation. The model structure depends on spatially adjacent concentrations, as well as those expressed at the moment before. These observations suggest that the boundary conditions have to be carefully chosen to obtain a smooth concentration profile.

Finally, as shown in Fig. 7.2F, the cell concentrations in domain 4 showed a relatively stable profile through the immobilized cell layer. However, we confirmed that the modeled profile had an increasing tendency towards the domain 4/5 interface, stimulated by the nutrient supply. Moreover, the concentration profile was maintained through time, but increased its value. Initial cell concentration (around 317 $\frac{g}{L}$) increased to around 660 $\frac{g}{L}$ at day 15, and 872 $\frac{g}{L}$ at day 30. Thus, it can be observed that the cell concentrations at day 15 is higher than half the concentration difference between day 0 and 30. These finding agrees with the expected exponential cell growth. In summary, cell growth can be clearly observed in a one month period, approaching the maximum attainable cell concentration ($950\frac{g}{L}$)

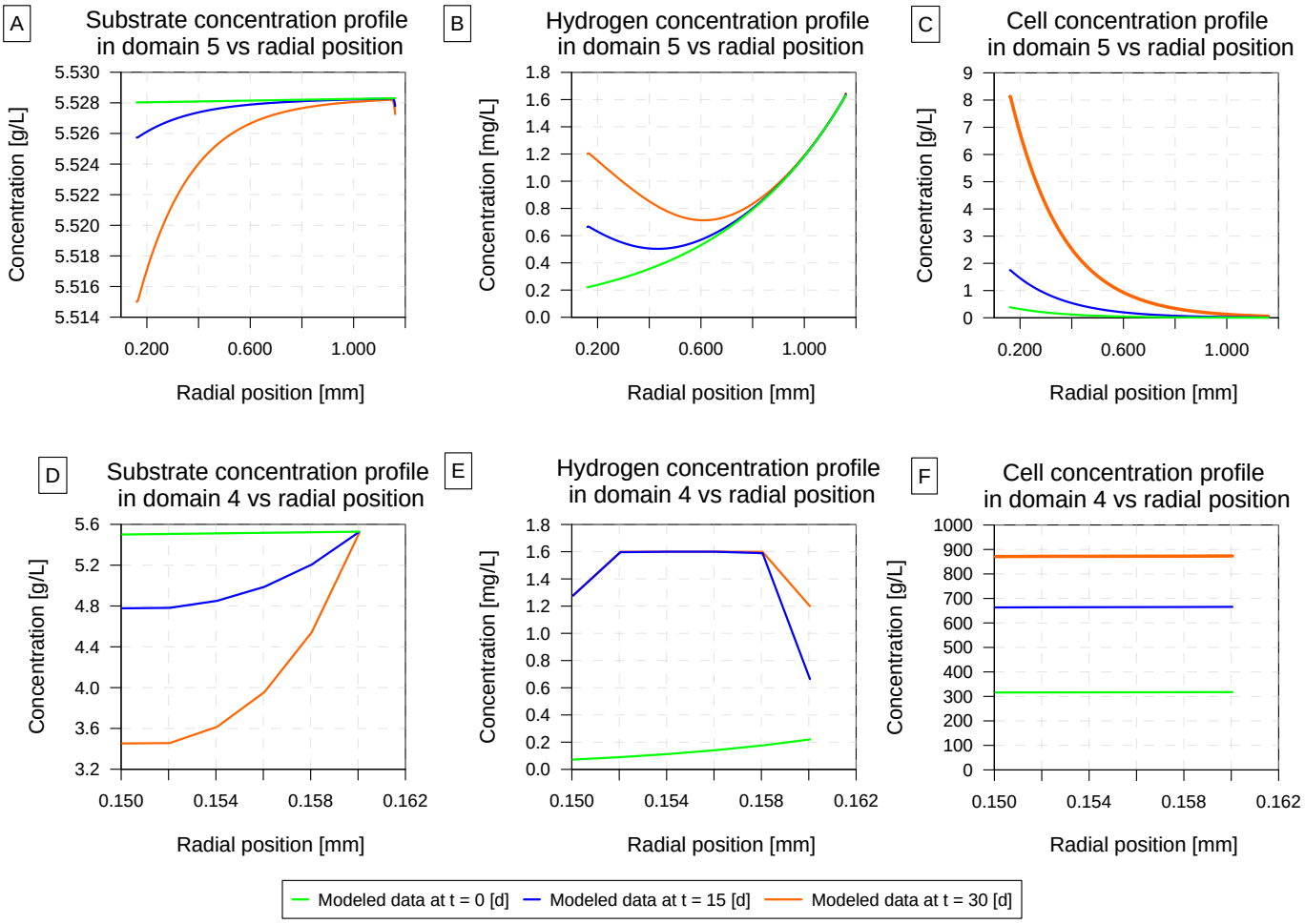

Fig. 7.2: Species concentration profiles in bioactive layers (domain 4 and 5) during a one month operation.

7.1.1.3. Reactor performance

Both the H_2 yield and capture efficiency showed an analogous tendency as the permeated H_2 mass flow outlet rate (Fig. 7.3A and B, repectively). A peak was observed for initial moments, reaching 28.4 % and 90.9 % for the yield and capture efficiency, respectively. This is consistent with

the recovered H_2 mass flow behavior (Fig. 6.2). From around day 3 onwards, decreasing but more stable tendencies followed.

From Table 7.1, we saw that the CBMem reached an average H_2 yield and capture efficiency of 9.8 $\frac{ml}{g\,COD}$ and 75.8 %. These results are similar to the unpublished data from Prieto et al. (2016) [63], which reported an average H_2 yield of 15 % and an average H_2 capture efficiency of 84 %.

According to the proposed membrane lifetime definitions, we observed that the CBMem simulation did not reach its lifespan within 1 month. Therefore, a continued reactor operation can be suggested and simulations were conducted for a six month period.

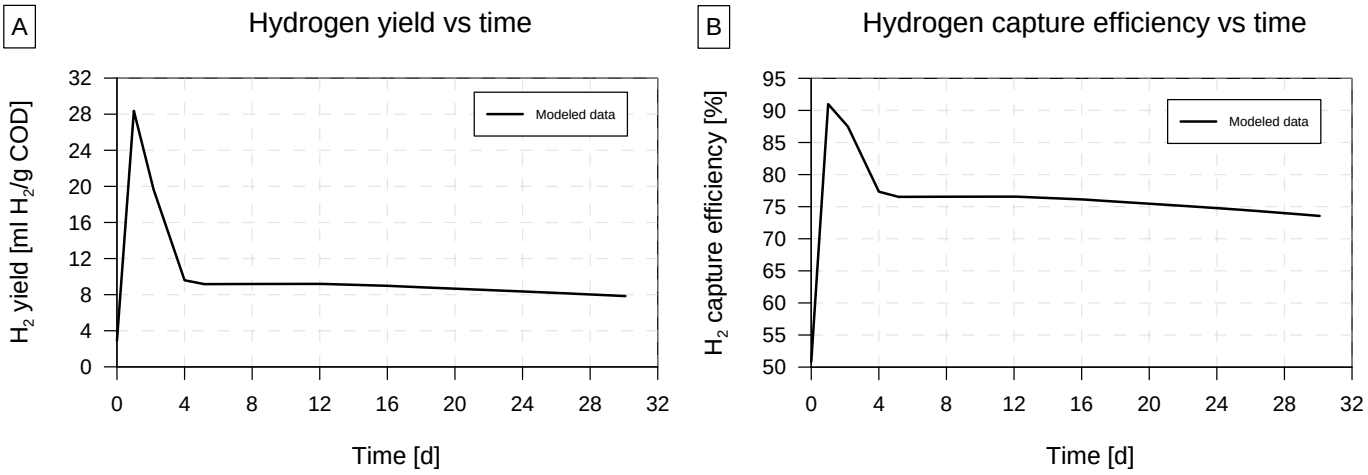

Fig. 7.3: CBMem's hydrogen yield and capture efficiency during a one month operation.

Table 7.1: CBMem's performance parameters, including yield and capture efficiency, after a one month operation.

Performance parameter	**Value**
H_2 yield $[\frac{ml\,H_2}{g\,COD}]$	9.84±4.84
H_2 capture efficiency [%]	75.76 ±6.78

7.1.2. Simulations for 6 months

The following subsections examine the simulation results for a CBMem operation of six months.

7.1.2.1. Concentration profiles through the CBMem

After simulating for a six months operation, the H_2 outlet and the species' concentration profiles through CBMem were obtained. Fig. 7.4 shows the recover permeated H_2. A H_2 peak is marked at the beginning (0.25 days). From around day 4 the profile stabilized and followed afterwards a smooth decreasing curve, whose slope began to reduce after a longer operation (around day 75 onwards) to stabilize again. It is somewhat surprising that the H_2 peak reached a higher value (74 $\frac{mg}{d}$) than the peak during the calibration exercise (58 $\frac{mg}{d}$, Fig. 6.2), although model steps and parameters were not changed.

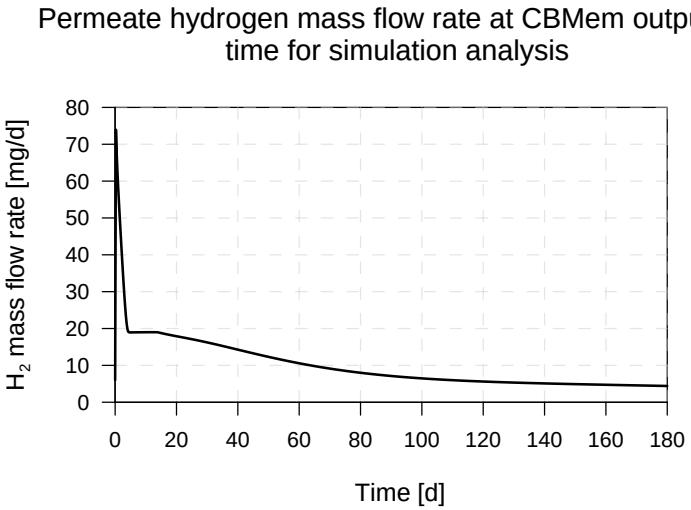

Fig. 7.4: CBMem's hydrogen mass flow rate at the gas outlet during a six months operation.

Fig. 7.5 shows the concentration profiles for each species from domain 1 and 5. Also in this case, the concentration profiles were plotted for three different times: day 0, day 90, and day 180.

As shown in Fig. 7.5A, the substrate concentration decreased during its transport through the membrane (from domain 5 to 1). During the initial time (day 0) the concentration within domain 5 was stable, until reaching domain 4, where it abruptly decreased. At day 90, substrate concentration was notorious within domain 5, causing a concave and decreasing profile. Another finding that stands out is that at day 180, the substrate concentration already tended to zero within domain 5. This indicated a rapid substrate consumption, because of a high presence of cells. Finally, no substrate concentration was observed within domains 3, 2, and 1, which was coherent to the defined modeling conditions considering cell growth towards the feed.

According to Fig. 7.5B, a decreasing H_2 profile for day 0 was obtained, which is due to the modeled initial condition subject to the H_2 concentration in the mixed liquor and its diffusion through the membrane. One interesting finding was that this profile differs with those observed for day 90 and 180: already at day 90 the H_2 concentration reached values close to 1.6 $\frac{mg}{L}$, corresponding to the H_2 saturation concentration. The concentration magnitude was maintained until reaching day 180. Thus, risk of product inhibition is clearly identified.

Furthermore, all three H_2 concentration profiles decreased when entering domain 4, were relatively stable within domain 3 and 2, and decreased in domain 1. Overall, the H_2 concentration was higher at day 90, than 180, which was notorious since domain 4. This difference could be explained due to the beginning of cell decay in longer operations subject to substrate depletion; thus, growth-associated product formation is reduced.

Moreover, H_2 concentration within domain 1 was higher at day 0, than for the other simulations. As explained before, the initial modeled profile (at $t = 0$) is a defined condition subject to the H_2 in the mixed liquor. Moreover, the model at initial simulation times was sensitive to the considered boundary conditions and stabilization occurred for later time points. Thus, the model is representative for operations that already completed the start-up phase. What stands out is that the H_2 concentration in the lumen after a six-month operations reached values close to zero

(around 5e-03 $\frac{mg}{L}$), while at day 90 the concentrations were around 0.2 $\frac{mg}{L}$. This result reflects the expected CBMem loss of H_2 recovery in time.

Also, the concentration profile for cells, presented in Fig. 7.5C, showed cells in domain 4 and its growth in domain 5. At day 90, the cell concentration within domain 4 is already close to the maximum cell capacity; thus, cells were stimulated to migrate into domain 5. After 180 days, the concentration within domain 5 had increased close to the maximum capacity, while the concentrations within domain 4 decreased. This decrease can be explained due to the substrate depletion.

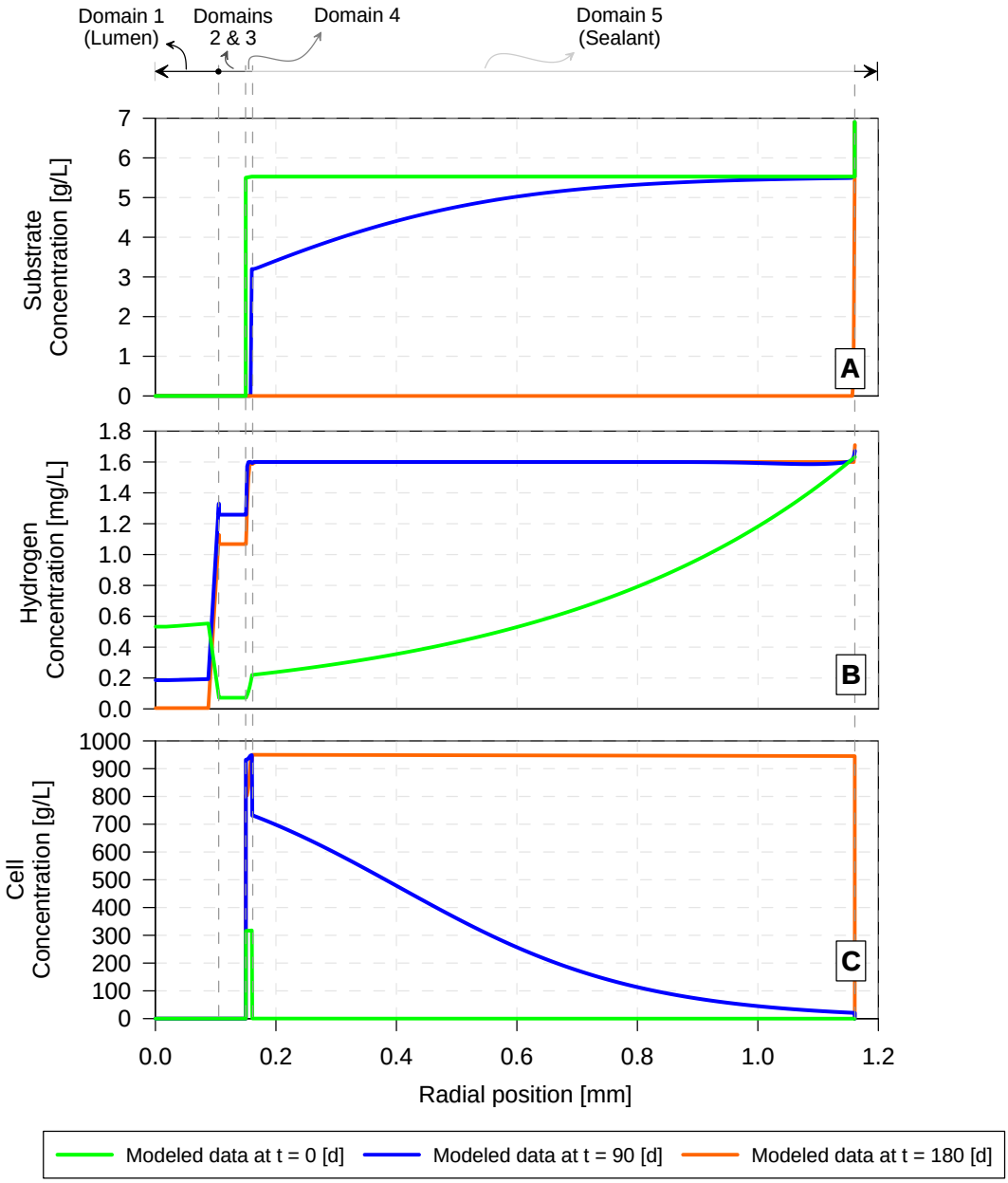

Fig. 7.5: Species concentration profiles in the CBMem during a six months operation.

7.1.2.2. Evolution of the bioactive layer

A six month simulation can deliver interesting findings for the analysis of bioactive layers' evolution. Fig. 7.6 presents the species' concentrations for domain 4 and 5 at the three different times (day 0, 90, and 180). More detailed figures, with plots for nine different times, are presented in Annex L.4.

As described before, the substrate concentration within domain 5 decreased in space and time (Fig. 7.6A), caused by cell-associated substrate consumption. At day 180, complete substrate depletion was observed. For the same moment, a high cell concentration was registered. Thus, we conclude that the model is capable to represent correctly the nexus between substrate utilization and cell maintenance and growth. However, substrate depletion is an undesired condition as the cells will not have enough nutrients for their metabolism. Thus, cell decay and uneven cell distribution would follow, i.e., cells would tend to grow closer to the membrane/mixed liquor interface. In consequence, CBMem operations would be hampered.

According to Fig. 7.6B, the H_2 concentration showed its decrease at day 0 as this species entered the membrane. However, H_2 concentration increased within time, reaching a stable profile, but close to its saturation concentration. H_2 saturation was considered within the inhibition term for the H_2 production rate; thus, no higher concentrations were modeled. This finding indicates that longer reactor operations, e.g., of around 3 months or more, must promote transport phenomena to successfully recover the produced H_2 within the membrane. Therefore, by applying a drag force, produced from a pressure difference, diffusive transport limitation could be overcome.

As for the cells' behavior in domain 5, the model showed that the cells grew in time; from values close to zero at day 0 to almost the maximum cell concentration at day 180 (Fig. 7.6C). For example, at day 90, we could see excess cell concentration being distributed within domain 5, favoring higher concentrations closer to the domain 4/5 interface (left side of the graph) caused by cell migration. Finally, a six month operation showed that the domain reached almost its maximum capacity of attainable cells. Thus, we could expect that the CBMem loses its function. Moreover, cells would probably begin to grow an additional biofilm layer on the membrane and be released into the reactor bulk.

As for domain 4, substrate depletion was already observed from day 90 due to the high cell concentration within this layer (Fig. 7.6D). Thus, the lack of nutrients can explain the preference of cells to migrate into domain 5.

The H_2 concentration in domain 4 (Fig. 7.6E) showed a distinctive behavior for longer times, compared to day 0, which has already been explained in previous sections (see Section 7.1.1.2). In addition, the H_2 concentration decreased from day 90 onwards; however, H_2 concentration could still be observed at day 190, which is related to the remaining cells in this domain.

Finally, Fig. 7.6F shows that the cell concentration increased from their initially immobilized concentration (around 317 $\frac{g}{L}$) to values close to the maximum concentration (950 $\frac{g}{L}$), measured at day 90. However, at day 180, a decrease of the cell concentration was observed. This can be explained due to the substrate depletion and cell migration into domain 5. Consistent with this cause, the cell profile showed higher concentration values close to the border that separates domain 4 with 5 (right side of the graph).

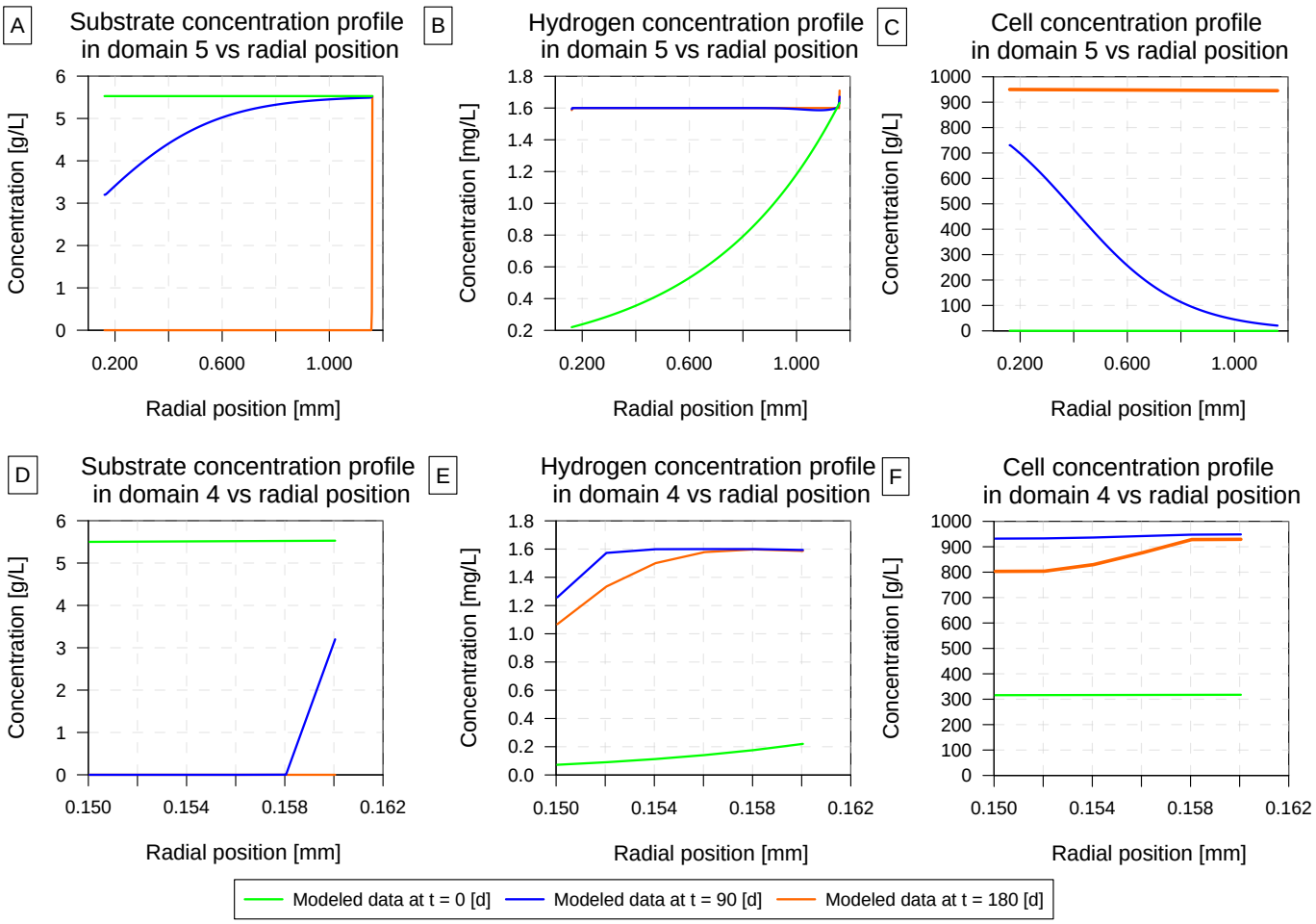

Fig. 7.6: Species concentration profiles in bioactive layers (domain 4 and 5) during a six months operation.

7.1.2.3. Reactor performance

The six month simulation showed a similar tendency for the H_2 yield and capture efficiency in time (Fig. 7.7A and B). Both graphs showed a peak at initial moments, reaching 36 % and 93 % for the yield and capture efficiency, respectively. Since day 4, decreasing but more stable tendencies followed. Both performance indicators showed a more pronounced decrease until day 100 onwards.

From Table 7.2, we can see that the CBMem reached an average value of the H_2 yield and capture efficiency of 4.8 $\frac{ml}{g\,COD}$ and 58.0 %. When comparing these results with a one month operation (yield of 9.8 $\frac{ml}{g\,COD}$ and 75.8 %, respectively), we can conclude that simulations of longer CBMem operations showed an important decrease in the performance indicators, which is directly related to taking the mean of the time-dependent variables.

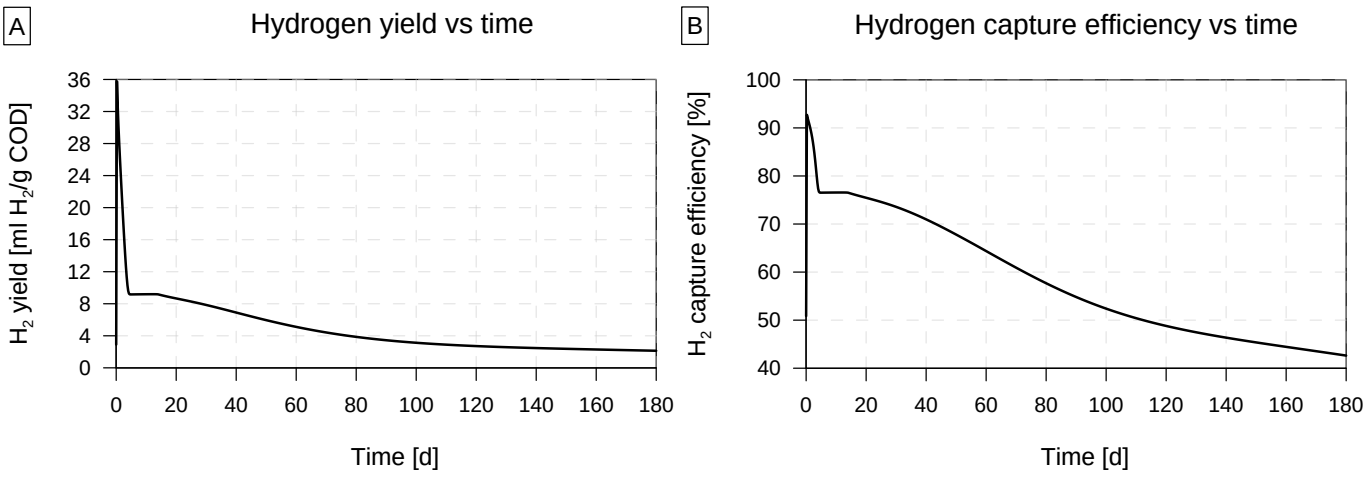

Fig. 7.7: CBMem's hydrogen yield and capture efficiency during a six months operation.

Table 7.2: CBMem's performance parameters, including yield and capture efficiency, after a six months operation.

Performance parameter	**Value**
H_2 yield $[\frac{ml\,H_2}{g\,COD}]$	4.79±3.53
H_2 capture efficiency [%]	58.00 ±12.19

According to the proposed membrane lifetime definitions, we observed that the CBMem simulation reached its lifespan before completing the sixth month. Table 7.3 shows the lifespan results based on the proposed criteria.

The worst case scenario would occur in 112.5 days (3.75 months), when the H_2 capture efficiency criteria is less or equal to 50 %. Operations for longer times would already be affected due to membrane fouling, and membrane replacement would be required. It is worth noting that within a six month operation, the capture efficiency would not be less than 30 %. However, when projecting the decreasing tendency shown in Fig. 7.7, this threshold is expected to be reached for operations of around 8 months.

However, by limiting CBMem's lifespan definition to the comparison of the cell concentration in the bioactive domains with the maximum attainable cell concentration capacity, the CBMem lifespan would be between 144 days (4.8 months) and 159 days (5.3 months). This criteria represents directly membrane deterioration due to excessive cell growth, which would hamper H_2 diffusion and recovery.

Although substrate depletion criteria could be a reversible factor for membrane lifespan, it is interesting for improving the operating conditions but also for indirectly measuring cell growth and diffusive limitations of nutrients into the membrane. With the calibrated parameters, the COD concentration within the inlet wastewater would not be sufficient for continued cell growth and metabolism. When we consider a substrate depletion of 50 % as a CBMem threshold criteria, the COD content in the wastewater feed should be increased around day 127.5 (4.25 months).

Finally, very little was found in the literature on the question of the lifespan of biological membranes for wastewater-to-energy. Nevertheless, the study conducted by Juntawang et al. (2017)

was useful as it focused on assessing performance and fouling of entrapped cells-based-anaerobic membrane bioreactor using phosphorylated polyvinil alcohol for wastewater treatment. The experiment concluded that the soluble COD removal remained high throughout the operation time between day 30 - 120 after steady state (30 days were related to a startup period); however, average periods to reach fouling were 11 days, suggesting the need for chemical cleaning. In conclusion, our work also addresses a literature gap by providing a phenomenological model that enhances our understanding of membrane lifespan in membrane bioreactors with immobilized cells [97].

Table 7.3: CBMem lifespan analysis according to different criteria.

Criteria	**Threshold**	**Life [days]**
H_2 capture efficiency	$\leq 50\,\%$	112.5
	$\leq 30\,\%$	NA[a]
Cell concentration in bioactive domains	$\geq 30\,\%\ C_{X,max}$ [b]	144
	$\geq 50\,\%\ C_{X,max}$ [b]	148
	$\geq 70\,\%\ C_{X,max}$ [b]	159
Substrate concentration in bioactive domains	$\leq 50\,\%\ C_{S,6,z_0}$ [c]	127.5
	$\leq 30\,\%\ C_{S,6,z_0}$ [c]	148.5

[a]NA = Not available; [b]$C_{X,max} = 950\ \frac{g}{L}$; [c]$C_{S,6,z_0} = 6.92\ \frac{g}{L}$

7.2. Chapter conclusions

In this chapter, the model was used to perform simulations of a one month and six month operation to characterize the phenomena through the CBMem. Especially, the evolution of the bioactive layer was assessed and the H_2 yield, capture efficiency, and membrane lifespan were evaluated.

The simulations confirmed the model's capacity to represent biological phenomena dynamics, including substrate consumption, cell growth and migration, and H_2 production, as well as their mutual effect on the species concentrations. Moreover, the simulations showed risk of substrate depleition, H_2 production inhibition due to its own concentration, and cell growth approaching the maximum attainable cell capacity that, at the same time, strengthens cell migration.

After a one month simulation, the average H_2 yield and capture efficiency were 9.8 $\frac{ml}{gCOD}$ and 75.8 %, respectively. These decreased to 4.8 $\frac{ml}{gCOD}$ and 58.0 % after six months. Finally, the membrane's lifespan was obtained to be less than four months considering the worst case scenario that observed a low H_2 capture efficiency.

While acknowledging the specificity of concentration profiles and performance indicators derived from the calibrated model, it's important to underscore the model's potential in providing useful insights on the process phenomena. These insights not only aid in estimating reactor performance but also inform decisions regarding membrane replacement. With further sensitivity analysis, the extension of the membrane function could be further studied, enhancing operational efficiency and cost-effectiveness. In conclusion, the application of a high-quality calibrated multi-domain membrane bioreactor model can significantly advance the field of model-based design, leading to improvements in wastewater-to-H_2 bioreactors.

Chapter 8

Process intensification through a sensitivity analysis

To assess the third specific goal, this chapter presents and discusses the main results related to the process intensification based on sensitivity analysis. For this, performance indicators will be studied when changing operational conditions and membrane parameters.

8.1. Results and discussion

The calibrated and validated CBMem model was used for simulations considering a six month timespan to analyze the effect of operation and membrane parameters on performance. For this, we studied the increase of COD content in the wastewater feed stream, the increase of initially immobilized cell mass, and the increase of the bioactive layer width. The CBMem reactor performance is evaluated in terms of the H_2 yield, H_2 capture efficiency, and the CBMem's lifespan.

8.1.1. Sensitivity analysis on COD

Sensitivity analysis was conducted on COD change of the wastewater. For this, we compared the following COD values: 6,920 $\frac{mg}{L}$, related to the COD content of the experimental study; 20,000 $\frac{mg}{L}$, related to common used high-strength wastewater in experimental trials for dark fermentation; and a 10-times increase of the COD content, i.e., 69,200 $\frac{mg}{L}$, which is close to the highest values that have been reported in the literature (see Annex B.2.5).

Fig. 8.1 shows the results of the sensitivity analysis of the H_2 yield on the COD content. We observed that higher COD values induced a decrease of the H_2 yield. First, when using a COD content of 6,920 $\frac{mg}{L}$, the model concluded a H_2 yield of 4.8 $\frac{ml\,H_2}{g\,COD}$. This value decreased to 1.9 $\frac{ml\,H_2}{g\,COD}$ for wastewater with a COD of 20,000 $\frac{mg}{L}$. Finally, when the feed had 69,200 $\frac{mg}{L}$ of COD, the modeled H_2 yield would be 0.7 $\frac{ml\,H_2}{g\,COD}$. According to the yield's definition (Eq. (2.1)), this tendency means that the COD content is not usefully utilized to produce H_2. This outcome is contrary to the expected, as a higher COD content indirectly signals higher amounts of organic compounds to be utilized. However, the H_2 behavior in a six month operations approached the saturation concentration. Thus, we can conclude that inhibition phenomena was already observed and an increase of COD content would not favor H_2 production. Moreover, higher CODs trigger inhibition phenomena earlier. In summary, higher COD content would favor cell growth and consequent H_2

productivity only if inhibition phenomena is diminished. Therefore, we recommend operations with enhanced transport, e.g., through combined advection and diffusion.

In turn, Fig. 8.2 shows the results of the sensitivity analysis of the H_2 capture efficiency on the COD content. Higher COD values showed an increase of the capture efficiency. For example, the COD content of 6,920 $\frac{mg}{L}$ produced an efficiency of 58.0 %. This value increased to 61.8 % and 67.5 % for wastewater with a COD of 20,000 $\frac{mg}{L}$ and 69,200 $\frac{mg}{L}$, respectively. According to the yield's definition (Eq. (2.2)), this tendency means that more H_2 was recovered in the gas stream within time. This behavior can be explained as higher COD content enhanced the production of H_2 within the bioactive domains to the maximum; thus, higher H_2 concentrations in the gas lumen were modeled in time.

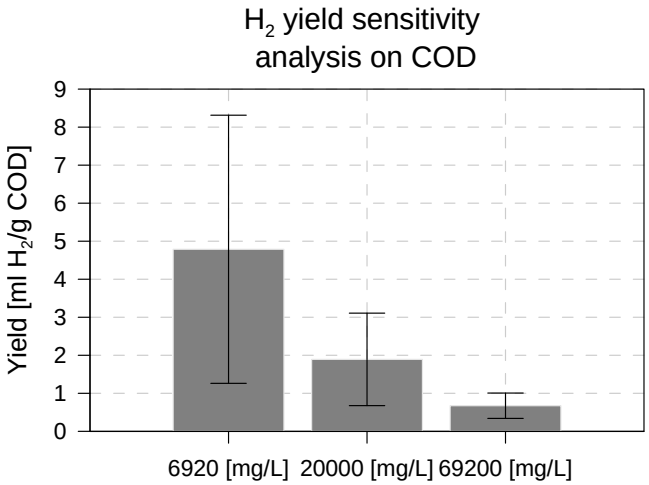

Fig. 8.1: Sensitivity analysis of H_2 yield on COD content.

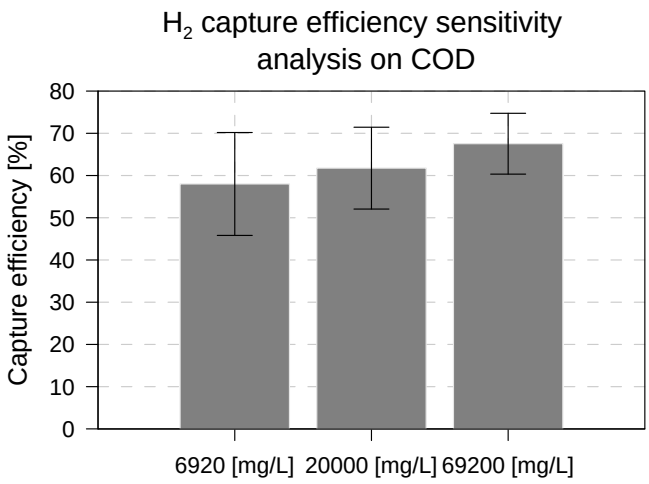

Fig. 8.2: Sensitivity analysis of H_2 capture efficiency on COD content.

According to the proposed membrane lifetime definitions, we observed that in all three cases the CBMem simulation reached its lifespan before completing the sixth month. Table 8.1 shows the lifespan results based on the proposed definitions and sensitivity analysis.

When operating with a COD content of 6,920 $\frac{mg}{L}$, the worst case scenario would occur in 112.5 days (3.75 months), i.e., when the H_2 capture efficiency criteria is less or equal to 50 %. In turn, the CBMem's lifespan is favored when operating with higher COD contents. For a COD content of 20,000 $\frac{mg}{L}$, the worst case lifespan increased to 139 days, limited to the same criteria as before. Finally, for the case of 69,200 $\frac{mg}{L}$ COD, the lifespan was 142.5 days due to cell growth within the bioactive domains according to the criteria of having reached at least 30 % of the maximum attainable cell concentration. In turn, this case did not show any risk of reduced capture efficiency within a six month operation.

By limiting the CBMem's lifespan definition to the comparison of the cell concentration in the bioactive domains with the maximum attainable cell concentration capacity, the CBMem lifespan was modeled to be between 144 - 159 days (for 6,920 $\frac{mg}{L}$), 143 - 158 days (for 20,000 $\frac{mg}{L}$), and 142.5 - 157.5 days (for 69,200 $\frac{mg}{L}$). In other words, the membrane deterioration due to excessive cell growth decreases insignificantly with higher COD contents.

Finally, when analyzing substrate depletion criteria, the model showed that substrate can be a

limiting operation factor for experiments with COD contents of 6,920 $\frac{mg}{L}$ and 20,000 $\frac{mg}{L}$ (Table 8.1, threshold of 50 %$C_{S,6,z_0}$). Nevertheless, it can be concluded that higher COD contents coherently allowed longer operations by delaying complete substrate utilization.

In summary, according to the created CBMem model and the used definitions, wastewater streams with higher COD content would favor the H_2 capture efficiency, but not the H_2 yield. This discrepancy indicates that operations with a higher COD content risk H_2 production inhibition and therefore, must enhance H_2 transfer towards the gas phase. Despite the fact that higher CODs can favor the CBMem's lifespan according to the H_2 capture efficiency criteria, it would not significantly improve the lifespan when considering the cell growth criteria, which is the most certain indicator for the proposed model.

Table 8.1: CBMem lifespan analysis according to different criteria.

Criteria	**Threshold**	**Life [days] when COD=6,920 [$\frac{mg}{L}$]**	**Life [days] when COD=20,000 [$\frac{mg}{L}$]**	**Life [days] when COD=69,200 [$\frac{mg}{L}$]**
H_2 capture	$\leq 50\,\%$	112.5	139	NA[a]
efficiency	$\leq 30\,\%$	NA[a]	NA[a]	NA[a]
Cell concentration in	$\geq 30\,\%\ C_{X,max}$ [b]	144	143	142.5
bioactive domains	$\geq 50\,\%\ C_{X,max}$ [b]	148	144.8	144.3
	$\geq 70\,\%\ C_{X,max}$ [b]	159	158	157.5
Substrate concentration	$\leq 50\,\% C_{S,6,z_0}$ [c]	127.5	156	NA[a]
in bioactive domains	$\leq 30\,\% C_{S,6,z_0}$ [c]	148.5	NA[a]	NA[a]

[a]NA = Not available; [b]$C_{X,max} = 950\ \frac{g}{L}$; [c]$C_{S,6,z_0} = 6.92\ \frac{g}{L}$

8.1.2. Sensitivity analysis on initial immobilized cell mass and width

Further sensitivity analyses on design parameters, i.e., on immobilized cell mass and layer width, were performed. As both parameters describe the condition of initial cell concentration within domain 4, these are linearly dependent. Thus, this section will focus on the effect of changing cell mass. Changes of the cell layer width will also be referenced; however, as the modeling strategy assumed constant domain widths (not moving boundaries), this parameter could be less strategic to analyse. Nevertheless, the results of the sensitivity analysis on this parameter are further detailed in Annex L.5.

Sensitivity analysis on the change of initial immobilized cell mass was performed, comparing three cases: 0.2 mg, 0.3 mg, and 0.4 mg. Fig. 8.3 shows the results of the sensitivity analysis of the H_2 yield on immobilized cell mass. We observed that higher cell masses produced higher yields. For example, 4.8 $\frac{ml\,H_2}{g\,COD}$ grew to 5.4 $\frac{ml\,H_2}{g\,COD}$ when increasing the cell mass from 0.2 mg to 0.3 mg. By further raising the mass to 0.4 mg, the yield was 6.1 $\frac{ml\,H_2}{g\,COD}$, i.e., an increase in 27 % compared to the base case yield.

A similar effect was observed for the H_2 capture efficiency. Fig. 8.4 shows the efficiency's continual growth from 57.6 % to 61.1 % and 64.6 % for 0.3 mg and 0.4 mg, respectively. Thus, the highest mass showed the most favorable condition, with an efficiency increase in 12 % compared to the base case.

The response of these performance indicators to the initial immobilized cell mass can be explained by cell growth-associated product formation. Higher initial cell mass is directly related to an increase in cell concentration distributed within the bioactive domains. Thus, the overall cell growth rate and, proportionally, the H_2 production rate are intensified.

A similar tendency was observed when studying the effect of initial cell layer width (see Annex L.5). Although an increase of this design parameter would reduce the initial cell concentration that is distributed through domain 4, cells would have more space to grow and production would be amplified. Therefore, increases in layer width concluded an increase in the performance parameters. What was interesting about this sensitivity analysis was that the chosen cases of layer width improved H_2 recovery compared to the cases of initial cell mass. For example, the yield increase in 65 % compared to the base case yield when expanding the width 200 % (from 10.75 [μm] to 21.50 [μm]). Similarly, the capture efficiency resulted to be 70.9 %, i.e., an increase in 23 % compared to the base case.

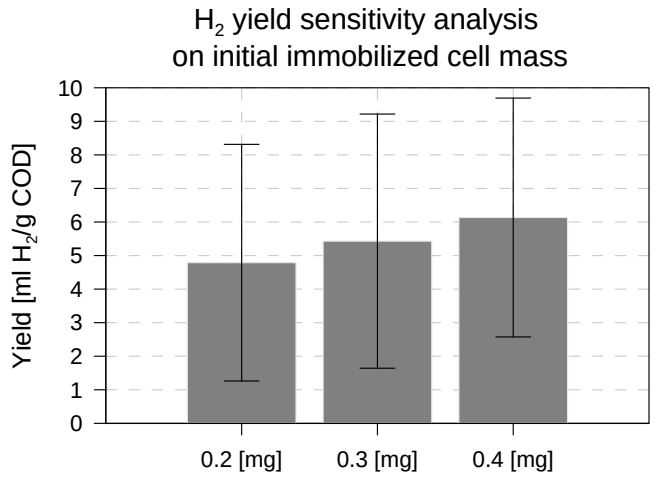

Fig. 8.3: Sensitivity analysis of H_2 yield on immobilized cell mass.

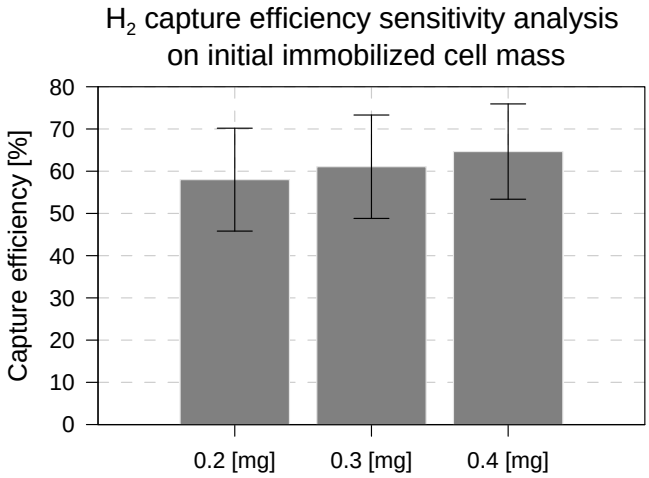

Fig. 8.4: Sensitivity analysis of H_2 capture efficiency on immobilized cell mass.

Moreover, Table 8.3 shows the lifespan results based on the proposed definitions and sensitivity analysis of cell mass. We observed that in all three analysis the CBMem simulation reached its lifespan. Only the H_2 capture efficiency criteria with a threshold of 30 % was not met in any case.

The base case that used 0.2 mg of cells concluded its worst scenario for day 112.5 (3.75 months). When simulating a CBMem designed with initially 0.3 mg of cells, the lowest lifespan was of 66.3 days (2.2 months), limited to the cell concentration criteria with a 30 % threshold. Lastly, the membrane life when immobilizing 0.4 mg of cells was minimum 56.3 days (1.9 months), due to the same criteria as in the previous case. In consequence, based on a worst scenarios, higher cell mass reduces the CBMem lifespan as an increase in 100 % cell mass would shorten the life in 50 %.

On the one hand, by only considering the lifespan based on the H_2 capture efficiency criteria, the lifespan increased with higher cell masses: from 112.5 days (for 0.2 mg) to 131.3 days (for 0.3 mg) and, finally, to 151.3 days (for 0.4 mg). This also accords with our previous observations for performance indicators.

On the other hand, when analyzing the cell concentration in bioactive domains criteria, the

CBMem lifespan was modeled to be between 144 - 159 days (for 0.2 mg), 66.3 - 91 days (for 0.3 mg), and 56.3 - 81 days (for 0.4 mg). In other words, the membrane deterioration due to excessive cell growth is intensified with a higher immobilized cell mass.

Finally, when analyzing substrate depletion criteria, lifespan reduction was observed for higher cell masses. The observed correlation can be explained by the proportional substrate consumption in function of cell concentration.

These results suggest that initial immobilized cell mass controls a positive feedback on the H_2 yield and H_2 efficiency, because of enhanced cell growth and, thus, growth-associated product formation. However, trade-off relations between cell growth and risk of substrate depletion was concluded after the lifespan analysis. For this reason, the more encapsulated cells, the more soluble substrate will be required, thus it is recommended to increase the COD content of the feed wastewater or improve the hydraulic retention time. Moreover, cell growth poses a risk of membrane deterioration through bacterial fouling, requiring replacement and thereby escalating process costs.

Similar tendencies were observed when increasing the cell layer width (see Annex L.5). higher widths showed decreases in the membrane's life according to worst scenario. However, these decreases were not that much pronounced as those observed during cell mass sensitivity analysis. For example, the model anticipated that the CBMem lifespan could be of 102.8 days (3.4 months), when having a 200 % increase of the layer width. In addition, when analyzing the H_2 capture efficiency criteria, the membrane would not risk its lifespan during a six month operation. Despite the positive impact on H_2 recovery, the trade-off relation between cell growth-associated H_2 performance indicators and biological-based membrane deterioration remains.

Table 8.2: CBMem lifespan analysis according to different criteria.

Criteria	**Threshold**	**Life [days] when $m_{X,0}$=0.2 $[mg]$**	**Life [days] when $m_{X,0}$=0.3 $[mg]$**	**Life [days] when $m_{X,0}$=0.4 $[mg]$**
H_2 capture	$\leq 50\,\%$	112.5	131.3	151.3
efficiency	$\leq 30\,\%$	NA[a]	NA[a]	NA[a]
Cell concentration in	$\geq 30\,\%$ $C_{X,max}$ [b]	144	66.3	56.3
bioactive domains	$\geq 50\,\%$ $C_{X,max}$ [b]	148	78.8	68.8
	$\geq 70\,\%$ $C_{X,max}$ [b]	159	91	81
Substrate concentration	$\leq 50\,\% C_{S,6,z_0}$ [c]	127.5	84	74.8
in bioactive domains	$\leq 30\,\% C_{S,6,z_0}$ [c]	148.5	98	88.8

[a] NA = Not available; [b] $C_{X,max} = 950\ \frac{g}{L}$; [c] $C_{S,6,z_0} = 6.92\ \frac{g}{L}$

8.2. Chapter conclusions

The results in this chapter provided important insights into the sensitivity analysis of operation and design parameters to study the CBMem's performance and lifespan for wastewater-to-H_2 production and separation.

The change of COD as an operating condition showed that higher COD values could favor the H_2 capture efficiency. However, it would not improve the H_2 yield due to the risk of reaching production inhibition. Moreover, COD would not significantly improve the membrane's lifespan.

Regarding the increases of design parameters, such as the initial immobilized cell mass or layer width, these indicated improvements in both the H_2 yield and capture efficiency. Yet, these scenarios produced a trade-off relation with enhanced cell growth, and the process would risk the occurrence of substrate depletion and membrane deterioration.

The limitation of the conducted sensitivity analysis was based on model calibration as the parameters did not allow to represent hampered transport phenomena due to cell growth as expected. Thus, the membrane's lifespan based on H_2 efficiency criteria may be overestimated. Nevertheless, lifespan criteria based on cell growth showed to be particularly useful.

In spite of the before mentioned limitation, the study certainly adds to our understanding of the capability of phenomenological models to intensify biological H_2 production and separation in membrane bioreactors. Phenomena-based modeling provided a better comprehension of the effect of bioactive layer evolution on the H_2 yield, efficiency, and CBMem lifespan. Thus, suitable recommendations for reactor operations or designs could be provided, such as COD control or the frequency of membrane replacement. These model-based benefits can directly improve technology decisions towards scale-up.

Finally, additional research is needed to determine the combination of operational and design parameters that are technically modifiable to optimize the process. This could be assessed through optimization models, which are mathematical tools that include variables, constraints, and a set of objective functions to select the best alternative within possible options. For example, the single-objective optimization of a CBMem could study the maximization of H_2 capture efficiency by varying the COD content and immobilized cell layer width. Furthermore, multi-objective optimization could be explored, which are composed of a set of objective functions which are appropriate to study trade-off relations. As an example, the optimization of both process performance and costs due to membrane replacement could be carried out. Finally, post-optimal sensitivity or multi-scenario analysis could usefully determine the effect of parameters on the results. In conclusion, the current study provides a useful reference for further developing phenomenological models for optimized wastewater treatment and energy recovery.

Chapter 9

Concluding remarks

Wastewater-to-hydrogen has emerged as an attractive process system because of its capacity to produce a valuable energy carrier from renewable sources by adopting biological water reuse technology. However, the system's drawback is their hampered performance if a high partial pressure of hydrogen (H_2) exists inside the reactor, which reduces the conversion of substrate to H_2 and produces undesired metabolic products. To overcome this operating challenge, membrane technology for simultaneous cell immobilization and gas separation has been developed as a solution.

Improvements in the bioreactors' design and operation can be studied through a model-based approach. Despite being cost-effective, H_2 production models are undeveloped, and simple empirical equations remain the most widely used, even though a physical basis in those is absent. In turn, a phenomenological description can deliver a better comprehension of complex, dynamic, and heterogeneous systems, especially when novel bioreactors are designed, such as the composite bioactive membrane (CBMem) for wastewater-to-H_2.

The main focus of the present work was to create a phenomenological model of a CBMem reactor for process intensification of H_2 from wastewater. This goal has been accomplished with the following partial results:

A set of equations was developed for the phenomenological description of a multi-domain membrane bioreactor for H_2 production from wastewater, which consists of a system of coupled second-order partial or ordinary differential equations based on mass balances. These were related to biochemical kinetics and mass transfer to follow the concentration profiles of cells, substrate, and H_2 in each domain. The effects of cell growth on the mass transfer and cell migration stimulated by space limitation and substrate gradient were also included. The representative model equations with their boundary conditions were listed for fluids, inactive, and bioactive membrane domains. Then, the model was structured in a modular and coupled way through a multi-domain fiber representation, which also ensured process dynamics induced by the evolution of the bioactive layers. Finally, a reactor model was developed to account for net H_2 production and process performance based on the multi-domain fiber model.

The created phenomenological model was implemented for a CBMem reactor in its discretized form in GNU Octave. Sequential parameter calibrations for the different models were conducted based on the Levenberg-Marquardt nonlinear regression. For the CBMem reactor model data-fitting to experimental observations was performed and cross-validation followed. Overall, good

fits were observed based on the model's confidence region and the calibrated parameters of the CBMem reactor model were of a high confidence.

Due to the model's extensive structure with several unknown parameters, calibration and validation demonstrated the importance of providing sufficient experimental data at different operating conditions. Moreover, the calibration analysis have extended our knowledge of the importance of good estimations on process-specific parameters. Biokinetic and mass transfer parameter estimations of bioactive domains must be ensured to coherently describe the reaction rates and mass transfer performance. Crucial parameters are the diffusivity coefficient of substrate and product, the maximum specific growth rate, microbial maintenance coefficient, and yields.

Despite being limited to the calibrated parameters and selected modeling steps, which ensured model stability while diminishing the representation of the magnitude of diffusion phenomena, the study successfully demonstrates the model's capability to accurately following the H_2 mass flow rate at the reactor's gas outlet based on intrinsic phenomena description. The results highlight the model's robustness in capturing key aspects of H_2 dynamics within the CBMem.

The calibrated model was applied for simulations of a one month and six month operation to characterize the evolution of the bioactive layer and evaluate performance indicators in terms of H_2 yield, capture efficiency, and CBMem lifespan. Simulations confirmed the model's capacity to represent biological phenomena dynamics, including substrate consumption, cell growth, cell migration, and H_2 production, as well as their mutual effect on the species' concentrations. The study also evidenced the model's utility to identify operational risks, such as substrate depletion, H_2 inhibition, and excessive cell growth approaching the membrane's maximum capacity. Moreover, the model emerged as predictor of the performance indicators. The insights gained from this modeling tool may be of assistance for a comprehensive assessment of the performance dependency on the interplay between mass transfer and biological phenomena.

Based on the sensitivity analysis of operation and design parameters, the study found that higher COD values could favor the H_2 capture efficiency, but without improving the H_2 yield due to product inhibition nor membrane's lifespan due to growth behavior of large biomass. The analysis also showed that increases of initial immobilized cell mass or layer width could improve process performance, while reducing the membrane's lifespan due to enhanced cell growth. Overall, we identified that changes in operation and design parameters compared to the base scenario (COD content of 6,920 $\frac{mg}{L}$, initial cell mass layer width of 0.2 mg, and a width of domain 4 of 10.75 μm) would not be recommended if the intention is to extend the CBMem's lifespan. However, as a trade-off relation between lifespan and H_2 performance parameters was observed, process intensification should be further analyzed.

The model that we have developed therefore assists in evaluating the effect of changing the membrane design or operational conditions. Further, it could also prove to be useful in expanding our understanding of enhanced mass transfer on reactor performance, either by construction change, by change of the membrane structure, thickness, or by the need of the transmembrane pressure.

Despite the several advantages of the proposed phenomenological model for the CBMem reactor, its granularity also introduces the challenge in terms of data requirement for its calibration. The level of detail that has been adopted may not be strictly necessary for addressing key questions about

the process. For example, simpler models that consider a reactor composition of less domains, spatial variation only in the radial axis, or homogeneous conditions in the fluids could offer sufficient insights into the critical phenomena and reactor performance, being computationally less intensive.

In conclusion, the findings suggest that the created model has in general a good capacity to represent wastewater-to-H_2 process in the CBMem, achieving the thesis goal. Despite of a structure based on a vast number of parameters, the model relies on physical, chemical, and biological principles which improve the confidence of model predictions when calibration with experimental data are ensured. Thus, the model lays a solid base line for further exploration and refinement to contribute to the understanding of the process in a cost-effective way. Moreover, its modularity allows it to be easily adaptable to different membrane designs.

This project is the first comprehensive investigation of developing a phenomenological model of a multi-domain membrane bioreactor for H_2 production and separation from wastewater and can be a useful reference for developing further modeling tools for assisted decision making on next-generation biological membrane designs.

Future studies should ensure model calibration and validation based on an extensive experimental data set at different operating conditions, e.g., tracing both H_2 recovery at the lumen side and COD removal at the mixed liquor side at different fluid flows and organic loads. To ease model implementation, future work could search for appropriate combinations of modeling steps from a stability analysis, while using realistic parameter values.

Furthermore, the model could also be modified to consider improvements in its formulation: for example, by expressing the advective term in the membrane domain's mass balance equations based on the Darcy's law. This adaption would allow the analysis of convective transport to overcome diffusive limitations for enhanced reactor performance. For this, improved representation of axial variation in the pressure profile model would be required.

There is also abundant room for further progress exploring model representation of biological structures. For example, the modeling of a mixed culture could shed light on the microbial competition problem and the potential of using low-cost, but complex, organic sources derived from waste biomass, without the need for pretreatment. Improvements could also include other biochemical reactions in the model, such as undesired production of metabolites.

Finally, a greater focus on optimization models could produce interesting findings that account for the selection of the most favorable design and operational configuration based on conflict objectives, such as process performance and costs over time. This strategy would also ease model implementation as it ensures maintenance of physical sense by applying restrictions. Therefore, further research in this field is strongly recommended and would provide a powerful tool for multiple-criteria decision-making.

Bibliography

[1] U.S. Energy Information Administration. 2021. Sources of energy. [Online] <https://www.eia.gov/energyexplained/what-is-energy/sources-of-energy.php>.

[2] U.S. Energy Information Administration. 2021. Use of energy. [Online] <https://www.eia.gov/energyexplained/use-of-energy/>.

[3] Sudheer et al. 2020. Bio-Hydrogen: Technology Developments in Microbial Fuel Cells and Their Future Prospects. In: KUMAR N (ed.), Biotechnology for Biofuels: A Sustainable Green Energy Solution, Springer. 61–94.

[4] Rambhujun et al., 2020. Renewable hydrogen for the chemical industry. MRS Energy Sustainability, 7(33).

[5] U.S. Energy Information Administration. 2019. International Energy Outlook 2019. [Online] <https://www.eia.gov/outlooks/ieo/pdf/ieo2019.pdf>.

[6] U.S. Energy Information Administration. 2021. Greenhouse gases. [Online] <https://www.eia.gov/energyexplained/energy-and-the-environment/greenhouse-gases.php>.

[7] Krishnan et al. 2022. The net-zero transition - What it would cost, what it could bring. [Online] <https://www.mckinsey.com/business-functions/sustainability/our-insights/the-net-zero-transition-what-it-would-cost-what-it-could-bring#>.

[8] International Energy Agency. 2020. Total energy supply (TES) by source, World 1990-2018. [Online] <https://www.iea.org/data-and-statistics/data-browser?country=WORLD&fuel=Energysupply&indicator=TPESbySource>.

[9] International Energy Agency. 2020. Total final consumption (TFC) by sector, World 1990-2018. [Online] <https://www.iea.org/data-and-statistics/data-browser?country=WORLD&fuel=Energyconsumption&indicator=TFCShareBySector>.

[10] International Energy Agency. 2021. Energy-related CO2 emissions by sector, World 1990-2018. [Online] <https://www.iea.org/data-and-statistics/data-browser?country=WORLD&fuel=CO2emissions&indicator=CO2BySector>.

[11] International Energy Agency. 2021. Energy-related CO2 emissions by source World 1990-2018. [Online] <https://www.iea.org/data-and-statistics/data-browser?country=WORLD&fuel=CO2emissions&indicator=CO2BySource>.

[12] U.S. Energy Information Administration. 2021. What is energy? [Online] <https://www.eia.gov/energyexplained/what-is-energy/>.

[13] Singla et al., 2021. Hydrogen fuel and fuel cell technology for cleaner future: a review. Environmental Science and Pollution Research, 28(13): 15607–15626.

[14] Office of Energy Efficiency & Renewable Energy. 2021. Hydrogen Storage. [Online] <https://www.energy.gov/eere/fuelcells/hydrogen-storage>.

[15] International Energy Agency. 2020. Global demand for pure hydrogen 1975-2018. [Online] <https://www.iea.org/data-and-statistics/charts/global-demand-for-pure-hydrogen-1975-2018>.

[16] International Energy Agency. 2019. The Future of Hydrogen. [Online] <https://www.iea.org/reports/the-future-of-hydrogen>.

[17] Burek et al., 2016. Water Futures and Solution - Fast Track Initiative (Final Report). Iiasa working paper,

IIASA, Laxenburg, Austria. [Online] <http://pure.iiasa.ac.at/id/eprint/13008/>.

[18] 2030 Water Resources Group, 2009. Charting Our Water Future. Tech. rep. [Online] <https://www.mckinsey.com/~/media/mckinsey/dotcom/client_service/sustainability/pdfs/chartingourwaterfuture/charting_our_water_future_full_report_.ashx>.

[19] United Nations Educational, Scientific and Cultural Organization. 2021. The United Nations World Water Development Report 2021 Valuing Water. [Online] <https://www.unwater.org/publications/un-world-water-development-report-2021/>.

[20] IRENA. 2022. Geopolitics of the Energy Transformation: The Hydrogen Factor. [Online] <https://www.irena.org/-/media/Files/IRENA/Agency/Publication/2022/Jan/IRENA_Geopolitics_Hydrogen_2022.pdf>.

[21] U.S. Department of Energy, 2017. Biofuels and Bioproducts from Wet and Gaseous Waste Streams: Challenges and Opportunities. Tech. rep. [Online] <https://www.energy.gov/sites/default/files/2017/09/f36/biofuels_and_bioproducts_from_wet_and_gaseous_waste_streams_full_report.pdf>.

[22] Perl, J. 2016. Sustainability Engineering Design Resolution Roadmap: Where Do We Go from Here? In: Sustainability Engineering: A Design Guide for the Chemical Process Industry, Springer International Publishing. 177–185.

[23] Scarlat et al. 2019. Chapter Ten - Future Role of Bioenergy. In: LAGO C (ed.), The Role of Bioenergy in the Bioeconomy, Academic Press. 435–547.

[24] International Energy Agency, 2021. Hydrogen in Latin America. techreport, IEA, Paris. [Online] <https://www.iea.org/reports/hydrogen-in-latin-america>.

[25] U.S. Energy Information Administration. 2021. Hydrogen explained. [Online] <https://www.eia.gov/energyexplained/hydrogen/>.

[26] Turner, J., 2004. Sustainable Hydrogen Production. Science, 305(5686): 972–974.

[27] IEA Statistics OECD. 2014. Electricity production from oil, gas and coal sources (% of total). [Online] <https://data.worldbank.org/indicator/EG.ELC.FOSL.ZS>.

[28] Hydrogen Council. 2021. Hydrogen decarbonization pathways: A life-cycle assessment. [Online] <https://hydrogencouncil.com/wp-content/uploads/2021/01/Hydrogen-Council-Report_Decarbonization-Pathways_Part-1-Lifecycle-Assessment.pdf>.

[29] Pham et al. 2018. Chapter 4 - Hydrogen Production From Biogas Reforming: An Overview of Steam Reforming, Dry Reforming, Dual Reforming, and Tri-Reforming of Methane. In: Azzaro-Pantel (ed.), Hydrogen Supply Chains, Academic Press. 111–166.

[30] Saratale et al. 2019. Chapter 10 - Biohydrogen Production From Renewable Biomass Resources. In: PANDEY et al. (ed.), Biohydrogen (Second Edition), Elsevier. 247–277.

[31] Cardeña et al. 2019. Chapter 7 - Microbial Electrolysis Cell for Biohydrogen Production. In: PANDEY et al. (ed.), Biohydrogen (Second Edition), Elsevier. 159–185.

[32] Varanasi et al. 2019. Chapter 5.7 - Biohydrogen Production Using Microbial Electrolysis Cell: Recent Advances and Future Prospects. In: VENKATA S, VARJANI S, and PANDEY A (ed.), Microbial Electrochemical Technology, Elsevier. 843–869.

[33] Chandrasekhar et al., 2015. Biohydrogen Production: Strategies to Improve Process Efficiency through Microbial Routes. 16(4): 8266–8293.

[34] Holladay et al., 2009. An overview of hydrogen production technologies. Catalysis Today, 139(4): 244–260.

[35] Tapia-Venegas et al., 2015. Biohydrogen production by dark fermentation: scaling-up and technologies integration for a sustainable system. 14(4): 761–785.

[36] Gopalakrishnan et al. 2019. Chapter 4 - Dark-Fermentative Biohydrogen Production. In: Biohydrogen (Second Edition), Elsevier. 79–122.

[37] Batstone et al., 2002. The IWA Anaerobic Digestion Model No 1 (ADM1). Water Science and Technology, 45(10): 65–73.

[38] Yildiz, M. and Kibar, M. 2021. Green Hydrogen Synthesis Methods. In: INAMUDDIN et al. (ed.), Advances in Green Synthesis: Avenues and Sustainability, Springer International Publishing. 247–255.

[39] Bundhoo, Z., 2017. Coupling dark fermentation with biochemical or bioelectrochemical systems for enhanced bio-energy production: A review. International Journal of Hydrogen Energy, 42(43): 26667–26686.

[40] Hallenbeck P. and Ghosh D, 2009. Advances in fermentative biohydrogen production: the way forward? Trends in Biotechnology, 27(5): 287–297.

[41] Abo-Hashesh M. and Hallenbeck, P. 2012. Fermentative Hydrogen Production. In: HALLENBECK P. (ed.), Microbial Technologies in Advanced Biofuels Production, Springer US. 77–92.

[42] Ren et al. Assessing optimal fermentation type for bio-hydrogen production in continuous-flow acidogenic reactors. Bioresource Technology, 98(9): 1774–1780.

[43] Azbar et al., 2009. Continuous fermentative hydrogen production from cheese whey wastewater under thermophilic anaerobic conditions. International Journal of Hydrogen Energy, 34(17): 7441–7447.

[44] Jung et al., 2010. Continuous fermentative hydrogen production from coffee drink manufacturing wastewater by applying UASB reactor. International Journal of Hydrogen Energy, 35(24): 13370–13378.

[45] Oh et al., Jul. 2004. Biological hydrogen production using a membrane bioreactor. Biotechnology and Bioengineering, 87(1): 119–127.

[46] Yang et al., 2006. Continuous bio-hydrogen production from citric acid wastewater via facultative anaerobic bacteria. International Journal of Hydrogen Energy, 31(10): 1306–1313.

[47] Zhang et al., 2007. Biohydrogen production in a granular activated carbon anaerobic fluidized bed reactor. International Journal of Hydrogen Energy, 32(2): 185–191.

[48] Rosa et al., 2014. Hydrogen production from cheese whey with ethanol-type fermentation: Effect of hydraulic retention time on the microbial community composition. Bioresource Technology, 161: 10–19.

[49] O-Thong et al., 2007. Improvement of biohydrogen production and treatment efficiency on palm oil mill effluent with nutrient supplementation at thermophilic condition using an anaerobic sequencing batch reactor. Enzyme and Microbial Technology, 41(5): 583–590.

[50] Venkata S., Lalit V., and Sarma P., 2007. Anaerobic biohydrogen production from dairy wastewater treatment in sequencing batch reactor (AnSBR): Effect of organic loading rate. Enzyme and Microbial Technology, 41(4): 506–515.

[51] Lee et al., 2006. Improving biohydrogen production in a carrier-induced granular sludge bed by altering physical configuration and agitation pattern of the bioreactor. International Journal of Hydrogen Energy, 31(12): 1648–1657.

[52] Łukajtis et al., 2018. Hydrogen production from biomass using dark fermentation. Renewable and Sustainable Energy Reviews, 91: 665–694.

[53] Rahimpour et al., 2017. Palladium membranes applications in reaction systems for hydrogen separation and purification: A review. Chemical Engineering and Processing: Process Intensification, 121: 24–49.

[54] Chezeau et al. 2019. Chapter 19 - Modeling and Simulation of the Biohydrogen Production Processes. In: PANDEY et al. (ed.), Biohydrogen (Second Edition), Elsevier. 445–483.

[55] Feng et al., 2021. CFD modeling of the perovskite hollow fiber membrane modules for oxygen separation. Chemical Engineering Science, 230: 116214.

[56] Gao et al., 2019. Modelling mass and heat transfers of Permeate Gap Membrane Distillation using hollow fibre membrane. Desalination, 467: 196–209.

[57] Kancherla et al., 2021. Modeling and simulation for design and analysis of membrane-based separation processes. Computers Chemical Engineering, 148: 107258.

[58] Gadhamshetty et al., 2010. Modeling dark fermentation for biohydrogen production: ADM1-based model vs. Gompertz model. International Journal of Hydrogen Energy, 35(2): 479–490.

[59] Boese-Cortés I., Díaz-Alvarado F., and Prieto, A., 2023. Biocatalytic membrane reactor modeling for fermentative hydrogen production from wastewater: A review. 48(35): 13024–13043.

[60] Ghimire et al., 2015. Dark fermentation of complex waste biomass for biohydrogen production by pretreated thermophilic anaerobic digestate. Journal of Environmental Management, 152: 43–48.

[61] Novak P., Arnold W., and Surdo E. 2017. Membranes for wastewater-generated energy and gas.

[62] Novak P., Arnold W., and Aksan, A. 2018. System and membrane for wastewater-generated energy and gas.

[63] Prieto et al., 2016. Performance of a composite bioactive membrane for H2 production and capture from high strength wastewater. Environmental Science: Water Research and Technology, 2(5): 848–857.

[64] Kleinstreuer C. and Poweigha T. 1984, Modeling and simulation of bioreactor process dynamics. In: Bioprocess Parameter Control, 91–146. Springer Berlin Heidelberg.

[65] The MathWorks Inc. Solving Boundary Value Problems. [Online] <https://www.mathworks.com/help/matlab/math/boundary-value-problems.html>.

[66] Björkmalm, J. 2019. Design of kinetic models for assessment of critical aspects in bioprocess development: A case study of biohydrogen. Phd thesis, Lund, Lund University, Faculty of Engineering.

[67] Luis P. 2018. Chapter 5 - Membrane contactors. In: Fundamental Modelling of Membrane Systems, Elsevier. 153–208.

[68] Valappil et al., 2021. Current and future trends in polymer membrane-based gas separation technology: A comprehensive review. Journal of Industrial and Engineering Chemistry, 98: 103–129.

[69] Nagy E. 2012. Chapter 9 - Membrane Bioreactor. In: Basic Equations of the Mass Transport through a Membrane Layer, Elsevier. 213–247.

[70] Nagy E. 2012. Chapter 1 - On Mass Transport Through a Membrane Layer. In: Basic Equations of the Mass Transport through a Membrane Layer, Elsevier. 1–34.

[71] Nakajima et al., 1989. Forced-flow bioreactor for sucrose inversion using ceramic membrane activated by silanization. Biotechnology and Bioengineering, 33(7): 856–861.

[72] Piret J. and Cooney C., 1991. Model of oxygen transport limitations in hollow fiber bioreactors. Biotechnology and Bioengineering, 37(1): 80–92.

[73] Sardonini C. and Dibiasio D., 1992. An investigation of the diffusion-limited growth of animal cells around single hollow fibers. Biotechnology and Bioengineering, 40(10): 1233–1242.

[74] Jalilnejad E., Sadeghpour P., Ghasemzadeh K., 2019. Advances in MBR Technology, Amsterdam, Elsevier.

[75] da Silva et al., 2017. Hydrogen: Trends, production and characterization of the main process worldwide. International Journal of Hydrogen Energy, 42(4): 2018–2033.

[76] Wang J. and Wan W., 2009. Kinetic models for fermentative hydrogen production: A review. International Journal of Hydrogen Energy, 34(8): 3313–3323.

[77] Zellner et al., 1993. Biofilm formation on polypropylene during start-up of anaerobic fixed-bed reactors. Biofouling, 6(4): 345–361.

[78] Krasňan et al., 2018. Intensified crude glycerol conversion to butanol by immobilized Clostridium pasteurianum. Biochemical Engineering Journal, 134: 114–119.

[79] Riley M., Muzzio F., and Reyes S., 1999. Experimental and modeling studies of diffusion in immobilized cell systems. Applied Biochemistry and Biotechnology, 80(2): 151–188.

[80] Belfort G., 1989. Membranes and bioreactors: A technical challenge in biotechnology. Biotechnology and Bioengineering, 33(8): 1047–1066.

[81] Calabrò V., Curcio S., and Iorio G., 2002. A theoretical analysis of transport phenomena in a hollow fiber membrane bioreactor with immobilized biocatalyst. Journal of Membrane Science, 206(1): 217–241.

[82] Radovich J., 1985. Mass transfer effects in fermentations using immobilized whole cells. Enzyme and Microbial Technology, 7(1): 2–10.

[83] Lazar A., 1991. Immobilization of animal cells in fixed bed bioreactors. Biotechnology Advances, 9(3): 411–424.

[84] Schonberg J. and Belfort, G., 1987. Enhanced Nutrient Transport in Hollow Fiber Perfusion Bioreactors: A Theoretical Analysis. Biotechnology Progress, 3(2): 80–89.

[85] Sheldon M. and Small H., 2005. Immobilisation and biofilm development of Phanerochaete chrysosporium on polysulphone and ceramic membranes. Journal of Membrane Science, 263(1): 30–37.

[86] Chung T., Wu, P., and Juang, R., 2005. Use of microporous hollow fibers for improved biodegradation of high-strength phenol solutions. Journal of Membrane Science, 258(1): 55–63.

[87] Nagy E., 2009, Mathematical Modeling of Biochemical Membrane Reactors.

[88] Nagy E., 2009. Basic equations of mass transfer through biocatalytic membrane layer. 4(3): 270–278.

[89] Nagy E. and Kulcsár E., 2009. Mass transport through biocatalytic membrane reactor. Desalination, 245(1): 422–436.

[90] de Gooijer C., Wijffels R., and Tramper J., 1991. Growth and substrate consumption of Nitrobacter agilis cells immobilized in carrageenan: Part 1. Dynamic modeling. Biotechnology and Bioengineering, 38(3): 224–231.

[91] Wik T., 2003. Trickling Filters and Biofilm Reactor Modelling. Reviews in Environmental Science and Biotechnology, 2(2): 193–212.

[92] Kelsey L, Pillarella M., and Zydney A., 1990. Theoretical analysis of convective flow profiels in a hollow-fiber membrane bioreactor. Chemical Engineering Science, 45(11): 3211–3220.

[93] Han K. and Levenspiel O., 1988. Extended monod kinetics for substrate, product, and cell inhibition. Biotechnology and Bioengineering, 32(4): 430–447.

[94] Nath K. and Das D., 2011. Modeling and optimization of fermentative hydrogen production. Bioresource Technology, 102(18): 8569–8581.

[95] Boese-Cortés I. Dropbox to access CBMem phenomenological model. [Online] <https://www.dropbox.com/scl/fo/c0xcr1addms4oc3agqie8/ALYsivCbOgMZk9HiumjwYoI?rlkey=nlois2evs77xue8fmzd7gdjem&st=9azcbdb8&dl=0>.

[96] Baquerizo G. 2014. Mathematical modeling and simulation of hydrogen production by dark fermentation using an ADM1-based model. 127–164.

[97] Juntawang C., Rongsayamanont C., and Khan E., 2017. Entrapped cells-based-anaerobic membrane bioreactor treating domestic wastewater: Performances, fouling, and bacterial community structure. Chemosphere, 187: 147–155.

[98] Granados-Fernández et al., 2020. Biomass catalytic gasification performance over unsupported Ni-Ce catalyst for high-yield hydrogen production. Biofuels, Bioproducts and Biorefining, 14(1): 20–29.

[99] Arregi et al., 2018. Evaluation of thermochemical routes for hydrogen production from biomass: A review. Energy Conversion and Management, 165: 696–719.

[100] Formica M., Frigo S., and Gabbrielli R., 2016. Development of a new steady state zero-dimensional simulation model for woody biomass gasification in a full scale plant. Energy Conversion and Management, 120: 358–369.

[101] Cao et al., 2020. Biorenewable hydrogen production through biomass gasification: A review and future prospects. Environmental Research, 186: 109547.

[102] Dou et al., 2019. Hydrogen production from the thermochemical conversion of biomass: issues and challenges. Sustainable Energy Fuels, 3(2): 314–342.

[103] Mahidhara et al., 2019. Biological hydrogen production: molecular and electrolytic perspectives. World Journal of Microbiology and Biotechnology, 35(8): 116.

[104] Saghir et al. 2018. Recent Trends in Gasification Based Waste-to-Energy.

[105] Balat M., 2008. Hydrogen-Rich Gas Production from Biomass via Pyrolysis and Gasification Processes and Effects of Catalyst on Hydrogen Yield. Energy Sources Part A: Recovery, Utilization, and Environmental Effects, 30(6): 552–564.

[106] Anca-Couce A., 2016. Reaction mechanisms and multi-scale modelling of lignocellulosic biomass pyrolysis. Progress in Energy and Combustion Science, 53: 41–79.

[107] Xu Z. and Yang S. 2007. Chapter 21 - Biological Production of Hydrogen from Renewable Resources. In:

YANG S. (ed.), Bioprocessing for Value-Added Products from Renewable Resources, Elsevier. 527–557.

[108] Mohanraj et al. 2019. Chapter 17 - Metabolic Engineering and Molecular Biotechnology of Biohydrogen Production. In: pande (ed.), Biohydrogen (Second Edition), Elsevier. 413–434.

[109] Nikolaidis P. and Poullikkas A., 2017. A comparative overview of hydrogen production processes. Renewable and Sustainable Energy Reviews, 67: 597–611.

[110] Hirose et al., 2018. Electrochemically active bacteria sense electrode potentials for regulating catabolic pathways. Nature Communications, 9(1): 1083.

[111] Hirose et al., 2019. Understanding and engineering electrochemically active bacteria for sustainable biotechnology. Bioresources and Bioprocessing, 6(1): 10.

[112] Kadier et al., 2016. A comprehensive review of microbial electrolysis cells (MEC) reactor designs and configurations for sustainable hydrogen gas production. Alexandria Engineering Journal, 55(1): 427–443.

[113] Ghosh et al., 2017. Hydrogen from food processing wastes via photofermentation using Purple Non-sulfur Bacteria (PNSB) - A review. Energy Conversion and Management, 141: 299–314.

[114] Hawkes et al., 2002. Sustainable fermentative hydrogen production: challenges for process optimisation. International Journal of Hydrogen Energy, 27(11-12): 1339–1347.

[115] Wang H., Paul D., and Chung T., 2013. Surface modification of polyimide membranes by diethylenetriamine (DETA) vapor for H2 purification and moisture effect on gas permeation. Journal of Membrane Science, 430: 223–233.

[116] Chang, S., Li, J.Z., Liu, F., 2011. Evaluation of different pretreatment methods for preparing hydrogen-producing seed inocula from waste activated sludge. Renewable Energy, 36(5): 1517–1522.

[117] Saady N., 2013. Homoacetogenesis during hydrogen production by mixed cultures dark fermentation: Unresolved challenge. International Journal of Hydrogen Energy, 38(30): 13172–13191.

[118] Siriwongrungson V., Zeng R., and Angelidaki I., 2007. Homoacetogenesis as the alternative pathway for H2 sink during thermophilic anaerobic degradation of butyrate under suppressed methanogenesis. Water Research, 41(18): 4204–4210.

[119] Wong Y., Wu T., and Juan J., 2014. A review of sustainable hydrogen production using seed sludge via dark fermentation. Renewable and Sustainable Energy Reviews, 34: 471–482.

[120] Wang et al., 2003. Producing hydrogen from wastewater sludge by Clostridium bifermentans. Journal of Biotechnology, 102(1): 83–92.

[121] Cai M., Liu J., and WeiY., 2004. Enhanced Biohydrogen Production from Sewage Sludge with Alkaline Pretreatment. Environmental Science and Technology, 38(11): 3195–3202.

[122] Niu et al., 2010. Characteristics of fermentative hydrogen production with Klebsiella pneumoniae ECU-15 isolated from anaerobic sewage sludge. International Journal of Hydrogen Energy, 35(1): 71–80.

[123] Zhang H., Bruns M., and Logan B., 2006. Biological hydrogen production by Clostridium acetobutylicum in an unsaturated flow reactor. Water Research, 40(4): 728–734.

[124] Zeidan A. and van Niel E., 2010. A quantitative analysis of hydrogen production efficiency of the extreme thermophile Caldicellulosiruptor owensensis OLT. International Journal of Hydrogen Energy, 35(3): 1128–1137.

[125] Hawkes et al., 2007. Continuous dark fermentative hydrogen production by mesophilic microflora: Principles and progress. International Journal of Hydrogen Energy, 32(2): 172–184.

[126] Li C. and Fang H., 2007. Fermentative Hydrogen Production From Wastewater and Solid Wastes by Mixed Cultures. Critical Reviews in Environmental Science and Technology, 37(1): 1–39.

[127] Kapdan I. and Kargi F., 2006. Bio-hydrogen production from waste materials. Enzyme and Microbial Technology, 38(5): 569–582.

[128] Guo et al., 2010. Hydrogen production from agricultural waste by dark fermentation: A review. International Journal of Hydrogen Energy, 35(19): 10660–10673.

[129] Ntaikou I., Antonopoulou G., and Lyberatos G., 2010. Biohydrogen Production from Biomass and

Wastes via Dark Fermentation: A Review. Waste and Biomass Valorization, 1(1): 21–39.

[130] Ghimire et al., 2015. A review on dark fermentative biohydrogen production from organic biomass: Process parameters and use of by-products. Applied Energy, 144: 73–95.

[131] Chen et al., 2012. Thermophilic dark fermentation of untreated rice straw using mixed cultures for hydrogen production. International Journal of Hydrogen Energy, 37(20): 15540–15546.

[132] Valdez-Vazquez et al., 2005. Semi-continuous solid substrate anaerobic reactors for H2 production from organic waste: Mesophilic versus thermophilic regime. International Journal of Hydrogen Energy, 30(13): 1383–1391.

[133] Zhang et al., 2007. Enhanced biohydrogen production from cornstalk wastes with acidification pretreatment by mixed anaerobic cultures. Biomass and Bioenergy, 31(4): 250–254.

[134] Nissilä et al., 2011. Thermophilic hydrogen production from cellulose with rumen fluid enrichment cultures: Effects of different heat treatments. International Journal of Hydrogen Energy, 36(2): 1482–1490.

[135] Tawfik A. and El-Qelish M., 2012. Continuous hydrogen production from co-digestion of municipal food waste and kitchen wastewater in mesophilic anaerobic baffled reactor. Bioresource Technology, 114: 270–274.

[136] Show et al., 2012. Biohydrogen production: Current perspectives and the way forward. International Journal of Hydrogen Energy, 37(20): 15616–15631.

[137] Elbeshbishy E., 2011. Enhancement of Biohydrogen and Biomethane Production from Wastes Using Ultrasonication. Electronic Thesis and Dissertation Repository, 322.

[138] Varrone et al., 2013. Enrichment of activated sludge for enhanced hydrogen production from crude glycerol. International Journal of Hydrogen Energy, 38(3): 1319–1331.

[139] Venkata G. and Venkata S., 2014. Deoiled algal cake as feedstock for dark fermentative biohydrogen production: An integrated biorefinery approach. International Journal of Hydrogen Energy, 39(18): 9573–9579.

[140] Panagiotopoulos et al., 2013. Biodiesel and biohydrogen production from cotton-seed cake in a biorefinery concept. Bioresource Technology, 136: 78–86.

[141] Show K., Lee D., and Chang J., 2011. Bioreactor and process design for biohydrogen production. Bioresource Technology, 102(18): 8524–8533.

[142] Hay et al., 2013. Biohydrogen production through photo fermentation or dark fermentation using waste as a substrate: Overview, economics, and future prospects of hydrogen usage. Biofuels, Bioproducts and Biorefining, 7(3): 334–352.

[143] Levin D., Pitt L., and Love M., 2004. Biohydrogen production: prospects and limitations to practical application. International Journal of Hydrogen Energy, 29(2): 173–185.

[144] Shin H., Youn J., and Kim S., 2004. Hydrogen production from food waste in anaerobic mesophilic and thermophilic acidogenesis. International Journal of Hydrogen Energy, 29(13): 1355–1363.

[145] Jung et al., 2011. Bioreactor design for continuous dark fermentative hydrogen production. Bioresource Technology, 102(18): 8612–8620.

[146] Lay J., Li Y., and Noike T., 1997. Influences of pH and moisture content on the methane production in high-solids sludge digestion. Water Research, 31(6): 1518–1524.

[147] Deublein D. and Steinhauser A., 2011. Biogas from waste and renewable resources: an introduction, John Wiley Sons.

[148] Bowles K. and Ellefson L., 1985. Effects of butanol on Clostridium acetobutylicum. Applied and Environmental Microbiology, 50(5): 1165–1170.

[149] Bakonyi et al., 2014. Review on the start-up experiences of continuous fermentative hydrogen producing bioreactors. Renewable and Sustainable Energy Reviews, 40: 806–813.

[150] Liu et al., 2014. Hydrogen production via catalytic pyrolysis of biomass in a two-stage fixed bed reactor system. International Journal of Hydrogen Energy, 39(25): 13128–13135.

[151] Davila-Vazquez et al., 2008. Fermentative biohydrogen production: trends and perspectives. Reviews in

Environmental Science and Bio/Technology, 7(1): 27–45.

[152] Sivagurunathan et al., 2016. A critical review on issues and overcoming strategies for the enhancement of dark fermentative hydrogen production in continuous systems. International Journal of Hydrogen Energy, 41(6): 3820–3836.

[153] Chen et al., 2008. Fermentative hydrogen production at high sulfate concentration. International Journal of Hydrogen Energy, 33(5): 1573–1578.

[154] Wu S., Lin C., and Chang J., 2003. Hydrogen Production with Immobilized Sewage Sludge in Three-Phase Fluidized-Bed Bioreactors. Biotechnology Progress, 19(3): 828–832.

[155] Tapia-Venegas et al., 2013. Bio-hydrogen production during acidogenic fermentation in a multistage stirred tank reactor. International Journal of Hydrogen Energy, 38(5): 2185–2190.

[156] Zahedi et al., 2013. Hydrogen production from the organic fraction of municipal solid waste in anaerobic thermophilic acidogenesis: Influence of organic loading rate and microbial content of the solid waste. Bioresource Technology, 129: 85–91.

[157] Massanet-Nicolau et al., 2010. Production of hydrogen from sewage biosolids in a continuously fed bioreactor: Effect of hydraulic retention time and sparging. International Journal of Hydrogen Energy, 35(2): 469–478.

[158] Ottaviano et al., 2017. Continuous thermophilic hydrogen production from cheese whey powder solution in an anaerobic fluidized bed reactor: Effect of hydraulic retention time and initial substrate concentration. International Journal of Hydrogen Energy, 42(8): 4848–4860.

[159] Liu et al., 2016. Fermentative hydrogen production potential from washing wastewater of beverage production process. International Journal of Hydrogen Energy, 41(7): 4466–4473.

[160] Veeravalli et al., 2014. Fermentative H2 production using a switchgrass steam exploded liquor fed to mixed anaerobic cultures: Effect of hydraulic retention time, linoleic acid and nitrogen sparging. International Journal of Hydrogen Energy, 39(19): 9994–10002.

[161] Chen Y., Yin Y., and Wang J., 2021. Recent advance in inhibition of dark fermentative hydrogen production. International Journal of Hydrogen Energy, 46(7): 5053–5073.

[162] Noblecourt et al., 2017. High hydrogen production rate in a submerged membrane anaerobic bioreactor. International Journal of Hydrogen Energy, 42(39): 24656–24666.

[163] Dreschke et al., 2019. Influence of liquid-phase hydrogen on dark fermentation by Thermotoga neapolitana. Renewable Energy, 140: 354–360.

[164] Beckers et al., 2015. Investigation of the links between mass transfer conditions, dissolved hydrogen concentration and biohydrogen production by the pure strain Clostridium butyricum CWBI1009. Biochemical Engineering Journal, 98: 18–28.

[165] André et al., 1990. Liquid-to-Gas Mass Transfer in Anaerobic Processes: Inevitable Transfer Limitations of Methane and Hydrogen in the Biomethanation Process. Applied and Environmental Microbiology, 56(6): 1636–1644.

[166] Chou et al., 2008. Pilot study of the influence of stirring and pH on anaerobes converting high-solid organic wastes to hydrogen. International Journal of Hydrogen Energy, 33(5): 1550–1558.

[167] Mizuno et al., 2000. Enhancement of hydrogen production from glucose by nitrogen gas sparging. Bioresource Technology, 73(1): 59–65.

[168] Kim et al., 2006. Effect of gas sparging on continuous fermentative hydrogen production. International Journal of Hydrogen Energy, 31(15): 2158–2169.

[169] Lee et al., 2012. Enhancing the performance of dark fermentative hydrogen production using a reduced pressure fermentation strategy. International Journal of Hydrogen Energy, 37(20): 15556–15562.

[170] Mandal B., Nath K., and Das D., 2006. Improvement of Biohydrogen Production Under Decreased Partial Pressure of H2 by Enterobacter cloacae. Biotechnology Letters, 28(11): 831–835.

[171] Nielsen et al., 2001. Hydrogen production from organic waste. International Journal of Hydrogen Energy, 26(6): 547–550.

[172] Teplyakov et al., 2002. Lab-scale bioreactor integrated with active membrane system for hydrogen production: experience and prospects. International Journal of Hydrogen Energy, 27(11): 1149–1155.

[173] van Niel E. 2016. Biological Processes for Hydrogen Production. In: R. Hatti-Kaul, G. Mamo, B. Mattiasson (eds.), Anaerobes in Biotechnology, Springer International Publishing. 155–193.

[174] Pawar et al., 2013. Biohydrogen production from wheat straw hydrolysate using Caldicellulosiruptor saccharolyticus followed by biogas production in a two-step uncoupled process. International Journal of Hydrogen Energy, 38(22): 9121–9130.

[175] Balachandar et al. 2013. Chapter 6 - Biohydrogen Production from Organic Wastes by Dark Fermentation. In: Biohydrogen, Elsevier. 103–144.

[176] Lin et al., 2007. Integration of fermentative hydrogen process and fuel cell for on-line electricity generation. International Journal of Hydrogen Energy, 32(7): 802–808.

[177] Show et al., 2007. Production of hydrogen in a granular sludge-based anaerobic continuous stirred tank reactor. International Journal of Hydrogen Energy, 32(18): 4744–4753.

[178] Chang J., Lee K., and Lin P., 2002. Biohydrogen production with fixed-bed bioreactors. International Journal of Hydrogen Energy, 27(11): 1167–1174.

[179] Zhang et al., 2008. The role of acid incubation in rapid immobilization of hydrogen-producing culture in anaerobic upflow column reactors. International Journal of Hydrogen Energy, 33(19): 5151–5160.

[180] Chen, S.Y., Chu, C.Y., Cheng, M.j., Lin, C.Y., 2009. The Autonomous House: A Bio-Hydrogen Based Energy Self-Sufficient Approach. International Journal of Environmental Research and Public Health, 6(4).

[181] Busch, J. 2009. Modeling and model-based control of membrane bioreactors. phdthesis, Mönchengladbach, Rheinisch-Westfälischen Technischen Hochschule Aachen, Fakultät für Maschinenwesen.

[182] Giorno L. and Drioli E., 2000. Biocatalytic membrane reactors: applications and perspectives. Trends in Biotechnology, 18(8): 339–349.

[183] Nicolella C., Pavasant P., and Livingston A., 2000. Substrate counterdiffusion and reaction in membrane-attached biofilms: mathematical analysis of rate limiting mechanisms. Chemical Engineering Science, 55(8): 1385–1398.

[184] González-Brambila M., Monroy O., and López-Isunza F., 2006. Experimental and theoretical study of membrane-aerated biofilm reactor behavior under different modes of oxygen supply for the treatment of synthetic wastewater. Chemical Engineering Science, 61(16): 5268–5281.

[185] Merkey B., Rittmann B., Chopp D., 2009. Modeling how soluble microbial products (SMP) support heterotrophic bacteria in autotroph-based biofilms. Journal of Theoretical Biology, 259(4): 670–683.

[186] Wang Q. and Zhang T., 2010. Review of mathematical models for biofilms. Solid State Communications, 150(21): 1009–1022.

[187] Kim M., Lee D., and Kim D., 2011. Continuous hydrogen production from tofu processing waste using anaerobic mixed microflora under thermophilic conditions. International Journal of Hydrogen Energy, 36(14): 8712–8718.

[188] Lee et al., 2014. Effect of organic loading rate on continuous hydrogen production from food waste in submerged anaerobic membrane bioreactor. International Journal of Hydrogen Energy, 39(30): 16863–16871.

[189] Bakonyi et al., 2018. A review of the innovative gas separation membrane bioreactor with mechanisms for integrated production and purification of biohydrogen. Bioresource Technology, 270: 643–655.

[190] Jabbari et al. 2019. Recent Progresses in Application of Membrane Bioreactors in Production of Biohydrogen.

[191] Helmi A. and Gallucci F. 2020. Latest Developments in Membrane (Bio)Reactors.

[192] Mahboubi et al., 2016. Reverse membrane bioreactor: Introduction to a new technology for biofuel production. Biotechnology Advances, 34(5): 954–975.

[193] Charcosset C., 2006. Membrane processes in biotechnology: An overview. Biotechnology Advances, 24(5): 482–492.

[194] Rios G., Belleville M., and Paolucci-Jeanjean D., 2007. Membrane engineering in biotechnology: quo vamus? Trends in Biotechnology, 25(6): 242–246.

[195] Renaudie et al., 2021. Biohydrogen production in a continuous liquid/gas hollow fiber membrane bioreactor: Efficient retention of hydrogen producing bacteria via granule and biofilm formation. Bioresource Technology, 319: 124203.

[196] Vees C., Neuendorf C., and Pflügl S., 2020. Towards continuous industrial bioprocessing with solventogenic and acetogenic clostridia: challenges, progress and perspectives. Journal of Industrial Microbiology and Biotechnology, 47(9-10): 753–787.

[197] Fernandes et al., 2010. Potential to produce biohydrogen from various wastewaters. Energy for Sustainable Development, 14(2): 143–148.

[198] Vatsala T., Raj S., and Manimaran A., 2008. A pilot-scale study of biohydrogen production from distillery effluent using defined bacterial co-culture. International Journal of Hydrogen Energy, 33(20): 5404–5415.

[199] Tang et al., 2008. Biohydrogen production from cattle wastewater by enriched anaerobic mixed consortia: Influence of fermentation temperature and pH. Journal of Bioscience and Bioengineering, 106(1): 80–87.

[200] Ngo T., Kim M., and Sim S., 2011. High-yield biohydrogen production from biodiesel manufacturing waste by Thermotoga neapolitana. International Journal of Hydrogen Energy, 36(10): 5836–5842.

[201] Yu et al., 2002. Hydrogen production from rice winery wastewater in an upflow anaerobic reactor by using mixed anaerobic cultures. International Journal of Hydrogen Energy, 27(11): 1359–1365.

[202] Sivaramakrishna et al., 2009. Biological hydrogen production from probiotic wastewater as substrate by selectively enriched anaerobic mixed microflora. Renewable Energy, 34(3): 937–940.

[203] Ferchichi et al., 2005. Influence of initial pH on hydrogen production from cheese whey. Journal of Biotechnology, 120(4): 402–409.

[204] Van Ginkel S., Oh S., and Logan B., 2005. Biohydrogen gas production from food processing and domestic wastewaters. International Journal of Hydrogen Energy, 30(15): 1535–1542.

[205] Shi et al., 2010. Optimization of conditions for hydrogen production from brewery wastewater by anaerobic sludge using desirability function approach. Renewable Energy, 35(7): 1493–1498.

[206] Mangayil R., Karp M., and Santala V., 2012. Bioconversion of crude glycerol from biodiesel production to hydrogen. International Journal of Hydrogen Energy, 37(17): 12198–12204.

[207] Venkata et al., 2007. Biohydrogen production from chemical wastewater as substrate by selectively enriched anaerobic mixed consortia: Influence of fermentation pH and substrate composition. International Journal of Hydrogen Energy, 32(13): 2286–2295.

[208] Tai et al., 2010. Biological hydrogen production from phenol-containing wastewater using Clostridium butyricum. International Journal of Hydrogen Energy, 35(24): 13345–13349.

[209] Azbar et al., 2009. Comparative Evaluation of Bio-Hydrogen Production From Cheese Whey Wastewater Under Thermophilic and Mesophilic Anaerobic Conditions. International Journal of Green Energy, 6(2): 192–200.

[210] Chu C., Tung L., and Lin C., 2013. Effect of substrate concentration and pH on biohydrogen production kinetics from food industry wastewater by mixed culture. International Journal of Hydrogen Energy, 38(35): 15849–15855.

[211] Reungsang A., Sittijunda S., and O-thong S., 2013. Bio-hydrogen production from glycerol by immobilized Enterobacter aerogenes ATCC 13048 on heat-treated UASB granules as affected by organic loading rate. International Journal of Hydrogen Energy, 38(17): 6970–6979.

[212] Sittijunda S. and Pattra S., 2016. Evaluation of different pretreatment methods to prepare an inoculum for bio-hydrogen production from cassava starch wastewater. Asia Pac J Sci Technol, 21(2): 81–92.

[213] Kuzmin D. Finite Difference Method. Institute of Applied Mathematics University of Dortmund [Lecture Slides from Introduction to Computational Fluid Dynamics.]. [Online] <http://www.mathematik.tu-dortmund.de/~kuzmin/cfdintro/lecture4.pdf>.

[214] The MathWorks Inc. Solve Stiff ODEs. [Online] <https://www.mathworks.com/help/matlab/math/solve-stiff-odes.html>.

[215] GNU Octave. Matlab-compatible solvers. [Online] <https://docs.octave.org/latest/Matlab_002dcompatible-solvers.html>.

[216] GNU Octave. GNU Octave (version 8.2.0). [Online] <https://docs.octave.org/latest/>.

[217] Bard Y., 1974. Nonlinear Parameter Estimation, Academic Press.

[218] Octave Sourceforge. leasqr. [Online] <https://octave.sourceforge.io/optim/function/leasqr.html>.

[219] Klatt C. and LaPara T., 2003. Aerobic biological treatment of synthetic municipal wastewater in membrane-coupled bioreactors. Biotechnology and Bioengineering, 82(3): 313–320.

[220] Raunkjær K., Hvitved-Jacobsen T., and Nielsen P., 1994. Measurement of pools of protein, carbohydrate and lipid in domestic wastewater. Water Research, 28(2): 251–262.

[221] 3M. 3M™ Liqui-Cel™ MM Series Membrane Contactor. [Online] <https://www.3m.com/3M/en_US/p/d/b5005009013/>.

[222] Ma et al., 2003. Evaluation of polyethylene hollow-fiber membranes for hydrogen delivery to support reductive dechlorination in a soil column. Water Research, 37(12): 2905–2918.

[223] Villanueva García, I., 2020. Estudio de prefactibilidad de un reactor anaeróbico de membranas para generación de hidrógeno en riles vitivinícolas - caso Concha y Toro. Bachelor's thesis, Santiago, Chile, University of Chile.

[224] American Public Health Association. 2018. 2540 SOLIDS. No. 0 In Standard Methods for the Examination of Water and Wastewater, American Public Health Association.

[225] Nagy E. 2012. Chapter 7 - Transport of Fluid Phase in a Capillary Membrane. In: Basic Equations of the Mass Transport through a Membrane Layer, Elsevier. 177–192.

[226] Bird R., Stewart W., and Lightfoot E., 1960. Transport phenomena, New York, John Wiley & Sons, Inc., vol. 7.

[227] Qin Y. and Cabral J., 1998. Lumen mass transfer in hollow-fiber membrane processes with nonlinear boundary conditions. AIChE journal, 44(4): 836–848.

[228] Aschmoneit et al. 2020. 4 - Computational fluid dynamics modeling of forward osmosis processes. In: Current Trends and Future Developments on (Bio-) Membranes, Elsevier. 85–111.

[229] Bruining W., 1989. A general description of flows and pressures in hollow fiber membrane modules. Chemical Engineering Science, 44(6): 1441–1447.

[230] Brotherton J. and Chau P., 1990. Modeling analysis of an intercalated-spiral alternate-dead-ended hollow fiber bioreactor for mammalian cell cultures. Biotechnology and Bioengineering, 35(4): 375–394.

[231] Berman A., 1953. Laminar Flow in Channels with Porous Walls. Journal of Applied Physics, 24(9): 1232–1235.

[232] Mondor M. and Moresoli C., 1999. Theoretical analysis of the influence of the axial variation of the transmembrane pressure in cross-flow filtration of rigid spheres. Journal of Membrane Science, 152(1): 71–87.

[233] Godongwana B., Sheldon M., and Solomons D., 2007. Momentum transfer inside a vertically orientated capillary membrane bioreactor. Journal of Membrane Science, 303(1): 86–99.

[234] Atangana A. 2018. Chapter 2 - Principle of Groundwater Flow. In: Fractional Operators with Constant and Variable Order with Application to Geo-Hydrology, Academic Press. 15–47.

[235] Labecki M., Piret J., and Bowen B., 1995. Two-dimensional analysis of fluid flow in hollow-fibre modules. Chemical Engineering Science, 50(21): 3369–3384.

[236] Shores T. 2007. Matrix Algebra. In: Applied Linear Algebra and Matrix Analysis, Springer. 55–144.

[237] Mu Y., Wang G., and Yu H., 2006. Kinetic modeling of batch hydrogen production process by mixed anaerobic cultures. Bioresource Technology, 97(11): 1302–1307.

[238] Ntaikou et al., 2008. Hydrogen production from sugars and sweet sorghum biomass using Ruminococcus

albus. International Journal of Hydrogen Energy, 33(4): 1153–1163.

[239] Standards Unit, Microbiology Services, P. 2016. UK Standards for Microbiology Investigations - Identification of Clostridium species. [Online] <https://assets.publishing.service.gov.uk/government/uploads/system/uploads/attachment_data/file/504183/ID_8i4.1.pdf>.

[240] Egilmez H., Morozov A., and Galyov E., 2021. Modelling the spatiotemporal complexity of interactions between pathogenic bacteria and a phage with a temperature-dependent life cycle switch. Scientific reports, 11: 4382.

[241] Sander R., 2015. Compilation of Henry's law constants (version 4.0) for water as solvent. Atmospheric Chemistry and Physics, 15(8): 4399–4981.

[242] Wijffels et al., 1991. Growth and substrate consumption of Nitrobacter agilis cells immobilized in carrageenan: Part 2. Model evaluation. 38(3): 232–240.

[243] van Niel E., Claassen P., and Stams A., Feb. 2003. Substrate and product inhibition of hydrogen production by the extreme thermophile, Caldicellulosiruptor saccharolyticus. Biotechnology and Bioengineering, 81(3): 255–262.

[244] Cengel Y., 2007. Heat and Mass Transfer (a Practical Approach), McGraw-Hill Education. 3rd edn.

[245] Wik T. 1999. On Modeling the Dynamics of Fixed Biofilm Reactors with focus on nitrifying trickling filters. Phd thesis, Goeteborg, Chalmers University of Technology, School of Electrical and Computer Engineering.

[246] Martin K., Picioreanu C., and Nerenberg R., 2013. Multidimensional modeling of biofilm development and fluid dynamics in a hydrogen-based, membrane biofilm reactor (MBfR). Water Research, 47(13): 4739–4751.

[247] Haynes W., 2012. CRC Handbook of Chemistry and Physi, CRC Press.

[248] Suhaimi H. 2015. Glucose diffusivity in tissue engineering membranes and scaffolds: implications for hollow fibre membrane bioreactor. Phd thesis, Loughborough, Loughborough University, Aeronautical, Automotive, Chemical and Materials Engineering.

[249] Puspita D. and Darminto D., 2013. Measurement of Hydrogen Diffusion through PVA Hydrogel using Magnetic Resonance Imaging Method in Comparison with Consistency Assessment using Digital Penetrometer. Jurnal Fisika dan Aplikasinya, 9: 86.

[250] Horn H. and Morgenroth E., 2006. Transport of oxygen, sodium chloride, and sodium nitrate in biofilms. Chemical Engineering Science, 61(5): 1347–1356.

[251] Desai, N., Shaik, V.A., Ardekani, A.M. Hydrodynamic Interaction Enhances Colonization of Sinking Nutrient Sources by Motile Microorganisms. 10.

[252] San Marchi C. and Somerday B. 2012. Technical Reference for Hydrogen Compatibility of Materials. [Online] <https://h2tools.org/sites/default/files/SAND2012_7321.pdf>.

Annexes

Annex A

Nomenclature

This chapter presents a list of the symbols and acronyms and of subscripts and superscripts used in this work.

Symbols and acronyms

a	Species
A	Area
ADP	Adenosine diphosphate
$AFBR$	Anaerobic fluidized-bed reactor
$AGSBR$	Agitated granular sludge bed reactor
$ASBR$	Anaerobic sequencing batch reactor
$Asm.$	Assumption
atm	Atmosphere
ATP	Adenosine triphosphate
BC	Boundary condition
BMR	Biocatalytic membrane reactor
BOD	Biochemical oxygen demand
BVP	Boundary value problem
χ	Variable
C	Concentration or Celsius
$C_2H_4O_2$	Acetic Acid
$C_6H_{12}O_6$	Glucose
$CaCO_3$	Calcium carbonate
$CBMem$	Composite bioactive membrane
CH_4	Methane
CI	Confidence interval
$CIGSB$	Carrier-induced granular sludge bed
CO	Carbon monoxide
CO_2	Carbon dioxide
CoA	Coenzyme A
COD	Chemical oxygen demand
$corp$	Correlation matrix of parameters
$covp$	Covariance matrix of parameters
$covr$	Diagonal of covariance matrix of residuals
$CSABR$	Continuously stirred anaerobic bioreactor
$CSTR$	Continuous stirred-tank reactor
cvg	Convergence
δ	Perturbation
Δ	Difference, step size, or width
d	Domain or day
D	Diffusion coefficient
DAQ	Data acquisition
DF	Dark fermentation
$dFdp$	Partial derivative function
$DGGE$	Denaturing gradient gel electrophoresis
$diag$	Diagonal
dp	Fractional parameter increment
Dp	Pore size
ϵ	Porosity
η_H	H_2 capture efficiency
e^-	Electron
$E.$	Escherichia
$Eq.$	Equation
$\forall$	For all
f	Function or computed values
F	Flow rate or function
Fe	Iron
f_d	Ratio between the diffusion coefficient in biofilm and water
Fd	Ferredoxin
$Fig.$	Figure
γ_H	H_2 yield
g	Standard acceleration of gravity or gram
h	Hour
H	Hydrogen, height, or equilibrium distribution coefficient
H^+	Proton
H_2	Hydrogen
H_2O	Water
HC	Hydrocarbon
HPG	H_2-producing granules

HRT	Hydraulic retention time
$\in$	In
i	Radial position
I	Inhibition
ID	Inner diameter
IEA	International energy agency
$ISI - WoS$	Institute for scientific information - web of science
$iter$	Iteration
j	Axial position
J	Joule, Jacobian matrix, or flux
k	Constant, variable, or time point
$k0$	Initial parameter vector
$kopt$	Optimized parameter vector
κ	Permeability constant of the fiber's membrane layer (Darcy permeability)
kg	Kilogram
λ	Damping factor, cell redistribution parameter, or variable
L	Litre or fiber length
ln	Natural logarithm
μ	Dynamic viscosity
μL	Microliter
μm	Micrometre
m	Meter or constant
M	Membrane
Ma	Flow's Mach number
MBR	Membrane bioreactor
MEC	Microbial electrolysis cell
mg	Milligram
MJ	Million joules
ml	Milliliter
$MLSS$	Mixed liquor suspended solids
Mt	Million tons
$Mtoe$	Million tons of oil equivalent
n	Constant, degree of inhibition constant, or molar composition
N	Number or total mass flux (diffusive and convective)
$N0$	Zero mass flux
N_2	Nitrogen
NA	Not available
NAD	Nicotinamide adenine dinucleotide
$NADH$	Reduced form of NAD
NH_3	Ammonia
Ni	Nickel
$niter$	Maximum iterations
nm	Nanometer
NOx	Nitrogen oxides
O_2	Oxygen
OD	Outer diameter
ODE	Ordinary differential equation
ox	Oxidized
p	Parameter
P	Pressure
P_i	Phosphorus
PCR	Polymerase chain reaction
PDA	Poly(dopamine)
PDE	Partial differential equations
Pe	Peclet number
PEM	Polymer electrolyte membrane
PFL	Pyruvate formate lyase
$PFOR$	Pyruvate ferredoxin oxidoreductase
pH	Potential of hydrogen
pin	Vector of initial parameters
PM	Particulate matter
PVA	Poly (vinyl alcohol)
$pval$	P-value
$PVTMS$	Poly(vinyl trimethylsilane)
q	Darcy flux
Q	Flow rate
$\hat{r}$	Reaction rate
ρ	Density
$r2$	Coefficient of multiple determination
red	Reduced
RQ	Research question
r	Radial space coordinate
r_i	Residual i
s	Second
S	Substrate
SG	Specific goal
SO_2	Sulfur dioxide
$sp.$	Species
$stdresid$	Standarized residuals
$stol$	Scalar tolerance
STR	Sludge retention time
θ	Tangential space coordinate or parameter
t	Time coordinate or ton
T	Temperature or transpose
TES	Total energy supply
TFC	Total final consumption
tol	Tolerance
u	Variable
$UASB$	Upflow anaerobic sludge blanket
ε	Variable
φ	Variable
v	Velocity or volume
V	Volume
VFA	Volatile fatty acid
vol	Volume
w	Weight
wt	Weight
$WWTP$	Wastewater treatment plant
x	Variable
x_i	Observed independent data i
X	Cell
y	Matrix of observed values
y_i	Observed dependent data i
Y	Yield
z	Axial space coordinate
Z	Confidence region matrix

Subscripts and superscripts

0	Initial, inlet, or zero
1	Domain 1 (lumen side) or first
2	Domain 2 (hollow-fiber) or second
3	Domain 3 (PDA) or third
4	Domain 4 (initially immobilized cell layer) or forth
5	Domain 5 (PVA)
57	Center between membrane border and bioreactor wall
6	Domain 6 (Mixed liquor)
7	Bioreactor
a	Species
ax	Axial
bb	Binary value related to a boolean condition that represents proliferation
bib	Bibliography
$COD-L$	COD content in the feed wastewater
$crit$	Critical
d	Domain
D	Diffusivity
dec	Decay
eff	Effective
$excess$	Excess
f	Final or fiber
g	Gas or growth
G	Gas
H	Hydrogen
$H-G$	H_2 in the gas
$H-L$	H_2 in the liquid
i	Inlet or affluent
in	Inlet
IP	Product inhibition
k	Constant or time point $k = 0$ for domain 4 or $k = crit$ for domain 5
L	Liquid
m	Maintenance
M	Membrane or membrane matrix (at inert conditions)
max	Maximum
o	Out
out	Outlet
P	Pressure, product, or production
pts	Points
r	Radial or recycle
rad	Radial
$rand$	Random
S	Substrate or half-saturation
sat	Saturation
θ	Tangential
t	Time
tot	Total
v	Velocity
w	Wastewater
X	Cells
X/P	Biomass on product
X/S	Biomass on substrate
X/H	Biomass on hydrogen
z	Axial position

Annex B

H_2 from biomass and dark fermentation

This chapter presents the different processes for H_2 production from biomass, their advantages and disadvantages. Additionally, the dark fermentation process and the relevance of several operational conditions are explained. Finally, the chapter refers to the different reactor configurations that have been tested in literature and summarizes their characteristics and limitations.

B.1. H_2 from biomass

Currently, biomass covers 14 % of the total primary global energy consumption [98]. It can be used to produce H_2, as it has a H_2 content of 5 to 7 wt %. In addition, waste biomass rather than virgin sources should be employed to avoid the concern of land use [99]. Thermochemical and biochemical processes are the two main routes to produce H_2 from biomass [100, 101]. The former includes gasification, pyrolisis, steam reforming, and supercritical gasification (Table B.1) [102, 103]. Compared to biological routes, thermochemical methods are more flexible and simpler as there is no need for additional chemicals; however, they use heat and pressure [104], which increase costs and carbon footprint.

Table B.1: Thermochemical methods for H_2 production from biomass

Biomass process	**Reaction**	**Conditions**	**Ref.**
Gasification	Biomass $\longrightarrow H_2 + CO_2 + CO + N_2$	700 - 1,200 °C. Require gasification agents (O_2, CO_2, steam and air)	[98, 99]
Pyrolisis	Biomass $\longrightarrow H_2 + CO_2 + CO +$ HC[a] gases	300 - 650 °C. Lower H_2 yield of around 18 vol %	[99, 105, 106]
Steam reforming	$C_nH_m + nH_2O \longrightarrow nCO + (\frac{m}{2} + n)H_2$	H_2 content in syngas varies with operation conditions (T, steam-to-biomass ratio, catalysts)	[99]

[a] HC = Hydrocarbon

Biochemical processes can be categorized as bioelectrochemical systems, biophotolysis (direct and indirect), photofermentation, and dark fermentation [107–109].

Bioelectrochemical systems

Bioelectrochemical systems, such as microbial electrolysis cells (MEC), have been used to grow electrochemically active microorganisms under electrochemical interactions with electrodes to catalyze and oxidize organic matter so that CO_2, electrons and protons can be obtained [31, 110, 111].

In this system, electrons are transferred to the anode, while protons cross a membrane to reach the cathode, combine, and release H_2 [112]. To initiate the cathodic proton reduction, MEC requires an external power supply [38]. Electrochemical reactions are represented in Eqs. (B.1) and (B.2). An anode reaction is given for acetate oxidation.

$$\text{Oxidation (anode)} \qquad C_2H_4O_2 + 2H_2O \longrightarrow 2CO_2 + 8H^+ + 8e^- \tag{B.1}$$

$$\text{Reduction (cathode)} \qquad 8H^+ + 8e^- \longrightarrow 4H_2 \tag{B.2}$$

Biophotolysis

H_2 production from biomass can also be light-driven. Biophotolysis is a photochemical reaction series that is triggered by the absorption of light energy, which in turn is converted into chemical energy [38]. Water is split to produce H_2 by green algae or cyanobacteria under anaerobic conditions. During direct biophotolysis by green algae, O_2 is generated (Eq. (B.3)). However, the reversible hydrogenase is sensitive to O_2, and thus, H_2 production can be inhibited. Indirect biophotolysis by cyanobacteria can overcome this limitation through temporally or spatially separated O_2 and H_2 evolution (Eqs. (B.4) and (B.5)) [38].

$$\text{Direct biophotolysis} \qquad 2H_2O \xrightarrow{\text{Light energy}} 2H_2 + O_2 \tag{B.3}$$

$$\text{Indirect biophotolysis} \qquad 6H_2O + 6CO_2 \xrightarrow{\text{Light energy}} C_6H_{12}O_6 + 6O_2 \tag{B.4}$$

$$C_6H_{12}O_6 + 6H_2O \xrightarrow{\text{Light energy}} 12H_2 + 6CO_2 \tag{B.5}$$

Photofermentation

Another light-driven process is photofermentation: organic acids are converted into H_2 and CO_2 by photosynthetic (purple and green) bacteria. However, depending on nitrogen concentration, the pathway differs; under nitrogen-limited conditions more H_2 can be produced with the same energy demand (Eqs. (B.6) vs. (B.7)) [38, 113].

$$\text{N}_2\text{ limited} \qquad 2H^+ + 2e^- + 4ATP \longrightarrow H_2 + 4ADP + 4P_i \tag{B.6}$$

$$\text{N}_2\text{-excess} \qquad N_2 + 8H^+ + 8e^- + 16ATP \longrightarrow 2NH_3 + H_2 + 16ADP + 16P_i \tag{B.7}$$

Dark fermentation

In a light-independent process, namely dark fermentation (DF), organic substrates are converted into H_2 in anaerobic conditions by anaerobic or facultative bacteria. Glucose, as model substrate, is converted into pyruvate through glycolisis; then the metabolic pathway differs according to the type of bacteria and their enzymes [3]. In terms of efficiency, DF could compete with the methods listed in Table 1.1, and in comparison to photofermentation and photolysis, it occurs at a higher rate. However, the main disadvantage of DF is its low yield of H_2 on substrates due to the formation of various by-products [33].

Table B.2 summarizes and compares the biological processes for H_2 production from biomass.

Table B.2: Comparison of the different biological processes to produce H_2 from biomass. Adapted from [4, 33, 109].

Process	**Reactions**	**Key enzymes**	**Energy conversion efficiency [%]**	**Advantages**	**Disadvantages**
Biophotolysis	Direct: $2H_2O$+light energy$\longrightarrow$ $2H_2$+O_2 Indirect: $6H_2O$+$6CO_2$+light energy$\longrightarrow$ $C_6H_{12}O_6$+$6CO_2$ $C_6H_{12}O_6$+$2H_2O\longrightarrow$ $4H_2$+$2CH_3COOH$+$2CO_2$	Nitrogenase or hydrogenase	10	CO_2-consumed O_2 as only byproduct Operation under mild conditions	Requires external light source Low H_2 rates and yields Need for large reactor volume O_2 sensitivity High raw material cost
Photofermentation	$C_6H_{12}O_6$+$6H_2O$+light energy$\longrightarrow$ $12H_2$+$6CO_2$ Nitrogen-deficient process: CH_3COOH+$2H_2O$+light energy$\longrightarrow$ $2H_2$+$2CO_2$	Nitrogenase, hydrogenase	0.1	CO_2-neutral Contributes to waste recycling	Light-dependent Low H_2 rates and yields Low conversion efficiency Need for large reactor volume O_2 sensitivity
Dark fermentation	$C_6H_{12}O_6$+$6H_2O\longrightarrow$ $12H_2$+$6CO_2$	Hydrogenase	60-80	CO_2-neutral Simple Light-independent Contributes to waste recycling No O_2 limitation	Fatty acids removal Low H_2 rates and yields Low conversion efficiency Need for large reactor volume Need for separation of gas mixture

B.2. Dark fermentation process

The following section explains the microbiology and biochemistry of the fermentative H_2 production and summarizes the influence of operational conditions and reactor designs on the process performance.

B.2.1. Microbiology and biochemistry

Inoculum

H_2 production can be performed with both pure and mixed cultures. Pure cultures are of single bacterial strain and are advantageous for investigations because of their consistent results, and ease of establishing optimized conditions and reproducing the process [35]. For this type of fermentative culture, *Clostridium* and *Enterobacter* are the most widely used [41]. Mixed cultures have technical advantages; H_2 can be produced from a complex organic or carbon source derived from waste biomass, without the need for pretreatment, thanks to the synergies between microorganisms. This may considerably decrease costs for large-scale production [3, 35, 36]. Mixed cultures are also more adaptable to variation in environmental parameters, which is ideal for industrial applications [36]. The inoculum can be isolated from various sources, such as sludge from anaerobic digesters or active sludge reactors, which contain H_2-producing microorganisms [35].

H_2-producing bacteria can be strict and facultative anaerobes. On the one hand, strict anaerobic bacteria are advantageous due to higher yield of H_2, but their drawbacks are their sensitivity to inhibition by oxygen, and their need for specific nutrients and control of sporulation in unfavorable conditions during reactor operation [114]. Mostly *Clostridia* species have been cultured to produce H_2, but this production occurs during log phase, and once the culture has reached the stationary phase, the metabolic flux will shift towards the accumulation of organic compounds [3]. On the other hand, facultative bacteria are easier to cultivate and maintain under laboratory conditions. Moreover, they can sustain higher H_2 partial pressure build up during H_2 production [36]. To conclude, each type of H_2-producing bacteria has advantages and disadvantages that have to be considered for the fermentation process.

Mixed cultures can also contain H_2-consuming or non-hydrogen-producing species. H_2 consumers can be hydrogenotrophic methanogenic archaea, homoacetogenic bacteria, or nitrate- and sulfate-reducers [35]. Under low concentrations of nitrate or sulfate, the main H_2 consumers are homoacetogenic bacteria and methanogenic archaea [115, 116]. Homoacetogenic bacteria are obligate anaerobes and seem to modify their metabolism under stress conditions. They use H_2/CO_2 as the sole source of carbon and energy [117, 118], grow rapidly, might form spores, and could have the same optimum pH as H_2 producers [115]. Regarding methanogenic archaea, pretreatments, which include interventions on the inoculum or the fermentative culture, can reduce their presence [119]. Thermal shock or acid/ base addition induces microorganism's incapability to form spores, whereas biokinetic control with low HRT in a continuous system induces low generation times [35]. In addition, ultrasonication and supplementation with organic compounds have been investigated as pretreatment methods [120, 121]. Inoculum pretreatment can also affect the H_2-producing microorganisms. For example, thermal shock appears to be favorable to the presence of *Clostridium sp.* [122–124]. For large-scale applications, energy costs and the technical complexity of the pretreatment should be evaluated [125].

Otherwise, non-H_2-producing species can synthesize reducing agents (i.e., lactate and propionate) and compete for substrate with H_2-producing microorganisms. By-products that minimize the production of H_2 can be eliminated or decreased using operational conditions that disfavor their metabolic pathways [117].

To determine the evolution of the community structure, microbial analysis methods, such as PCR coupled with DGGE, are convenient [41].

Metabolic pathways

Regeneration of a cell's energy occurs through metabolic reactions. Under anaerobic conditions, the Krebs cycle is blocked. Therefore, the extra reductants are utilized for the formation of reduced end metabolites such as volatile fatty acid (acetic acid, butyric acid or lactic acid) and alcohol (ethanol or butanol). H_2 is produced for maintenance of the cell's redox potential [36].

The metabolic pathway initiates with glucose consumption for regeneration of ATP, which leads to pyruvate production via glycolysis. Pyruvate may enter into two different pathways that lead to the production of H_2: the PFL or PFOR pathway (Fig. B.1) [3]. In the case of facultative anaerobes, for instance, *E. coli*, the production of H_2 is via the PFL pathway, in which pyruvate oxidizes to acetyl CoA and formate (Eq. (B.8)). This reaction is catalyzed by pyruvate formate lyase. Afterward, formate is converted into H_2 and CO_2 by formate hydrogen lyase (Eq. (B.9)) [3, 36].

$$\text{Pyruvate} + \text{CoA} \longrightarrow \text{Acetyl CoA} + \text{Formate} \tag{B.8}$$

$$\text{Formate} \longrightarrow H_2 + CO_2 \tag{B.9}$$

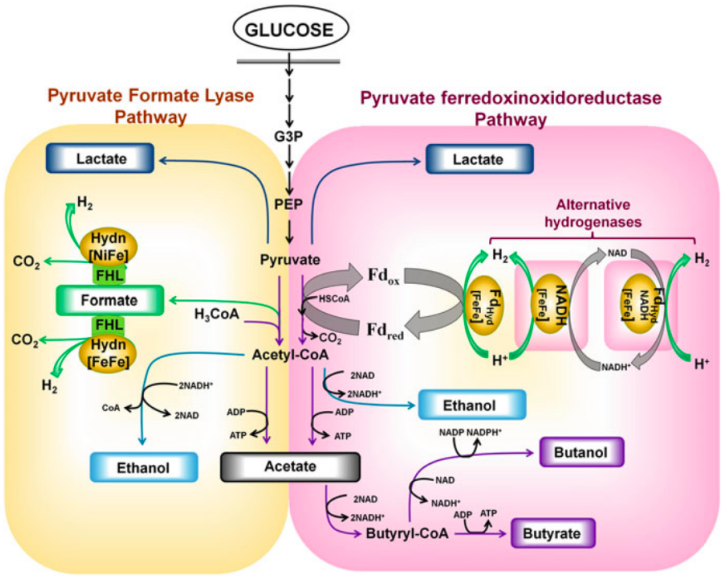

Fig. B.1: PFL and PFOR pathways used by fermentative species for the production of hydrogen from glucose. Reproduced from Sudheer et al. (2020) [3].

Depending on the microorganism involved, the H_2 production using formate hydrogen lyase occurs through formate-dependent [Fe-Fe] hydrogenase or [Ni-Fe] hydrogenase, and in most cases it will not use the NADH produced during glycolysis. Hence, various reduced carbon compounds (ethanol or lactate) will be formed upon oxidizing the NAD, which limits the yield to a maximum of 2 $\frac{mol_{H_2}}{mol_{glucose}}$ [3, 35].

In the case of strict anaerobes, such as *Clostridium sp.*, the production of H_2 is via the PFOR pathway, in which pyruvate oxidizes to acetyl CoA and CO_2 by pyruvate ferredoxin oxidoreductase. This reaction requires ferredoxin reduction (Eq. (B.10)). Then [Fe-Fe] hydrogenase oxidizes the reduced ferredoxin and produces H_2 (Eq. (B.11)), whereas acetyl CoA produces acetate and one ATP molecule [3, 36].

$$\text{Pyruvate} + \text{CoA} + 2\text{Fd(ox)} \longrightarrow \text{Acetyl CoA} + 2\text{Fd(red)} + CO_2 \tag{B.10}$$

$$2H^+ + \text{Fd(red)} \longrightarrow H_2 + \text{Fd(ox)} \tag{B.11}$$

Under special conditions of partial pressure inside the reactor, the NADH generated during glycolysis can be re-oxidized to produce additional H_2 molecules through NADH-dependent (NADH-[Fe-Fe]) and NADH-Fd_{red} dependent (NADH-Fd_{red}-[Fe-Fe]) hydrogenase. Thus, the H_2 yield can be either 2 or 4 $\frac{mol_{H_2}}{mol_{glucose}}$ [3, 35].

For the lactate pathway, pyruvate oxidizes into lactate. No H_2 is produced if the end metabolite of the pathway is lactic acid, ethanol, or propionate. Besides, some facultative anaerobes carry out anaerobic respiration by utilizing nitrate or fumarate as terminal electron acceptors, preventing H_2 production. Therefore, the culture medium should not contain these electron acceptors [36].

B.2.2. Operating conditions

Feedstock

The fermentative pathways depend on the substrates [126]. This way, the substrate plays a significant role in H_2 yield, production rate, and process economy. These depend mainly on the substrate's carbohydrate content, availability, and biodegradability [127–129]. Simple monosaccharides, such as glucose, xylose, ribose; and disaccharides, such as sucrose and lactose, are readily biodegradable [3]. However, these are expensive and the costs of fuel production at a large scale can triple [35]. DF offers the use of complex substrates from industrial waste or wastewaters, which enables the production of H_2 and VFAs within organic waste treatment [130].

Because of the highly abundant and degradable material content, the following waste carbon resources have been considered: organic municipal waste originated from households or restaurants, food processing plant residues or sewage sludge [131–135], agricultural residues as lignocellulosic biomasses, effluents from livestock farms and aquatic plants [127, 136], and wastewater streams from renewable energy industry [137–140].

However, not all feedstocks are ideal; some require pretreatment. The long polymer chains of complex substrates need to be broken down to obtain sugars that can be easily assimilated, accelerating the fermentation process and improving H_2 yields [52, 141, 142]. Other wastes, such

as municipal sewage sludge, contain methano-bacteria; thus, pretreatment is required to diminish their presence [120, 121].

Temperature

One of the operating parameters that affects the growth rate of bacteria and the conversion efficiency of the substrates to H_2 is temperature. According to temperature ranges suitable for growth conditions, bacterial species can be classified as psychrophiles (0–25°C), mesophiles (25–40°C), thermophiles (40–65°C), extreme thermophiles (65–80°C), or hyperthermophiles (>80°C) [143]. Since DF is mediated through specific enzymes, their activity depends on the temperature, which can take an optimum value. Temperatures that are lower or higher than optimal decrease enzymatic activity. Therefore, optimal temperature depends on the type of microorganism and the kind of substrate used during fermentation.

Successful DF processes depend on the temperature range and operating costs. Both the mesophilic and thermophilic range can be suitable [126]. Under mesophilic conditions, readily biodegradable substrates seem to be converted most efficiently [130]. In turn, thermophilic conditions favor H_2 production due to the increment in system entropy [36], and they enhance the activity of enzymes responsible for hydrolysis of complex substrates [128, 132, 144]. However, higher temperatures in mixed cultures can result in the impoverishment of bacterial strains' diversity. The latter produces a less complete degradation of substrates, which is detrimental to the fermentation of waste [145]. In addition, temperature affects the economic aspects of the process. More energy is required when operating at higher temperatures, which means higher operating costs [3]. In conclusion, the choice of the operating temperature has to consider the process goals.

pH

All the metabolic processes are based on the enzyme activity of a particular reaction at a specific pH. Enzymes, such as hydrogenases, are active in a certain pH range and reach their maximum activity at the optimum pH value [146]. Moreover, pH affects the growth of microbes. In mixed cultures, lower pH values favor the production of H_2 and inhibit methanogens from consuming it. However, H_2 production is accompanied by the accumulation of organic acids, which will lower the medium's pH and inhibit the activity of the enzymes responsible for H_2 synthesis [147]. Thus, pH control for its maintenance at a constant, and optimal level is important.

The optimal pH level that has to be maintained varies depending on the strain or source of mixed cultures, substrate, and mode of fermentation system used [3]. In general, the optimum pH for DF ranges from 5 to 7, which is favorable for bacterial growth [126]. pH lower than 5 is not advised due to the formation of acidic metabolites [36, 148].

Hydraulic retention times

H_2 production at an industrial scale requires semi-continuous and continuous processes, which operate with the hydraulic retention time (HRT). HRT influences the reactor design and also the process performance. It is defined as the average length of time that a substrate remains in the reactor [52]. On the one hand, short HRTs reduce reactor size and cost [125]. On the other hand, HRT is a key factor for the selection of microorganisms based on their growth rate [36], affecting

H_2 productivity. Usually, HRT is adjusted from long to short intervals to allow the acclimatization of microorganisms to new environments and to prevent the bacteria of interest from being washed away [52]. Moreover, the HRT shift leads to dynamical changes in the microbial population, thus affecting the process [149]. As the specific growth rate of methane-producing bacteria is low (0.017-0.020 h^{-1}) when compared with H_2-producing bacteria (0.172 h^{-1}) [36, 150], short HRTs can remove the slowly growing methanogens of mixed consortia. Therefore, it can lead to an enriched culture with H_2 producers and achieve a higher productivity [36].

HRT also affects the growth phase and metabolism of species. The HRT should be established to maintain the H_2-producing bacteria in the exponential phase, as they produce H_2 and VFAs, whereas during steady state phase alcohol is synthesized [151, 152]. Regarding the H_2 production rate, it increases over a certain range of HRT values until reaching the optimal value; then it decreases at higher HRTs [153]. The optimal HRT value depends on the biodegradability of the substrate used [130]. If the substrate contains simple carbohydrates, then optimal HRT is usually several hours: 2 h [154], 4 h [153], or 12 h [155]. Instead, for complex and waste substrates it is more variable [48, 156–160].

H_2 partial pressure

The partial pressure of H_2 is another relevant parameter. H_2 production by hydrogenases is a reversible process. Hence, and according to Le Chatelier's principle, at high partial pressure of H_2 in the reactor, the conversion of substrate to H_2 decreases [36, 52, 161]. This effect is different depending on the hydrogenase reduction pathway involved. H_2 production from reduced ferredoxin is much more favorable than H_2 production from NADH, so the former is less sensitive to this effect [41]. Also, as H_2 partial pressure increases, the metabolic flux shifts towards other products, such as organic acids, ethanol, and butanol [41, 130]. In consequence, H_2 has to be removed as it is formed to maintain a high and constant production rate.

The threshold inhibitory partial pressure of H_2 is 10^{-3} atm [162]. However, critical supersaturation phenomena can occur [163]; therefore, the concentration of the H_2 gas in the liquid phase can be 7-80 times the equilibrium conditions [164, 165]. Methods to reduce the partial pressure of H_2 involve stirring the medium during fermentation [166] or sparging the fermentation mixture with an inert gas, usually N_2 [157, 167] or CO_2. Even though the latter is more effective compared with N_2 sparging [168], the product dilutes with the sparging gas and H_2 separation becomes time and cost-consuming. Thus, removing the gaseous phase from the reactor by applying vacuum can be beneficial [169, 170]. Alternatively, membranes that are highly selective for H_2 can be used. Metallic membranes, such as a palladium-silver membrane [171], and polymer membranes, such as PVTMS [172], have been employed. However, a disadvantage of using membranes consists of the formation and development of biofilms, which may favor the growth of methanogenic bacteria [128] and accelerate the need for membrane replacement [3].

B.2.3. Reactor configuration

Besides reactor operation, reactor types and configurations have been tested for H_2 production. According to the literature, Table B.3 shows the reactors that have been used for fermentative single-stage systems; each has its principles, advantages, and limitations. Multistage reactor systems configurations have also been employed. These are commonly two-stage systems; DF occurs in the first stage, while in the second stage, the by-products from DF can be converted into energy,

e.g., conversion to H_2 by employing energy in the form of either light or electricity [173], or reduction to CH_4 through anaerobic digestion [174]. Another type of two-stage system consists of separate hydrolysis and fermentation processes to achieve higher conversion and yield [52]. This hybrid production process could make the DF sustainable and economically feasible [173].

Table B.3: Comparison of different reactor configurations.

Reactor	**Main characteristics and advantages**	**Limitations**	**Ref.**
CSTR	Continuous feedstock and effluent flow Simple construction Easy operation Effective homogeneous mixing Cell growth controlled by HRT VSS: 1,000 - 4,000 $\frac{mg\ VSS}{L}$	Sensitive to fluctuating operating conditions Limited H_2 production rate Risk of cell washout at lower HRT Recommended cell recycling or retention	[41, 126, 175–177]
MBR	Cell retention through membrane High and constant biomass concentration Independent selection of HRT and STR Better control of process parameters than CSTR	Membrane fouling High operating costs	[45, 52, 126]
Fixed-bed reactors	Cell retention through carrier material Low turbulence	High mass transfer resistance Low substrate concentration Recommended recirculation flow	[36, 178]
UASB	Experience in waste(water) treatment and H_2 production at lab- and pilot-scale 0.2 - 2 mm HPG are formed HPG resistant to wash out HPG resistant to toxic conditions Mixing occurs through gas bubbles formation High H_2 production efficiency High cell concentration Stable conditions Possible operation at short HRTs	Long initiation time for HPG formation HPG sensitivity to channeling effects Poor substrate-biomass contact	[36, 52, 145]
AFBR	Cell retention through granules or biofilm with solid surface Mixing occurs through feed gas Good heat and mass transfer Suitable for higher hydraulic loading Possible operation at short HRTs	High energy consumption	[47, 52, 179]
ASBR	Sequencing batch operation Experience in waste(water) treatment and H_2 production Ease of control Efficient COD removal and H_2 production Cycle duration and pH as the most influencing parameters	Reduced performance in overloaded systems	[36, 180]
CIGSB, AGSBR or CSABR	Formation of self-flocculating granular sludge or matrix Enhanced cell retention Effective H_2 production	Inefficient mixing Low stability of functional granules Low mass transfer	[36]

B.2.4. Membrane bioreactor classification

Membranes can be used as a barrier between two streams in liquid or vapor phases. Their filtration process leads to the physical separation of particles, macromolecules, or dissolved molecules from fluids. However, their performance decreases with time due to membrane fouling. Moreover, energy consumption and membrane replacement influence economic feasibility [181]. MBRs have

been widely used in wastewater treatment [182], and some have even been characterized as environmentally friendly and less energy intensive than traditional reactors [183–186]. The application of MBRs for H_2 production has also been considered [187, 188] and reviewed [35, 189, 190].

MBRs can be classified according to microbial structure, membrane location, and biocatalyst configuration [69, 190, 191]. First, according to the microbial structure, MBRs can be aerobic and anaerobic, of which the latter is suitable for dark fermentation [35]. Second, considering the membrane location in the bioreactor system, the MBR can be classified into sidestream (Fig. B.2A) and submerged (or immersed) configurations (Fig. B.2B or C) [192]. With respect to the biocatalyst configuration, MBRs can be divided into two main categories: (1) sidestream systems where a bioreactor, e.g., a continuous stirred tank reactor (CSTR), with freely-moving biocatalysts is combined with an external membrane module used as a separation unit, and (2) systems in which the membrane acts simultaneously as a support for the immobilized biocatalysts and as a separation unit in an immersed configuration. The second category, defined as biocatalytic membrane reactors (BMRs) [69], can be further subdivided into enzymatic BMRs (Fig. B.2D) [193, 194] or whole-cell BMRs [85, 86]. It is worth pointing out that these types of reactors should be strictly called bioactive membrane reactors as catalysts do not, by definition, undergo a permanent chemical change and should, therefore, not be used to explain cells. Finally, whole-cell BMRs require cell immobilization, which can occur by forming a biofilm above the membrane module (Fig. B.2E) [195], or through the entrapment of cells [196] (Fig. B.2F).

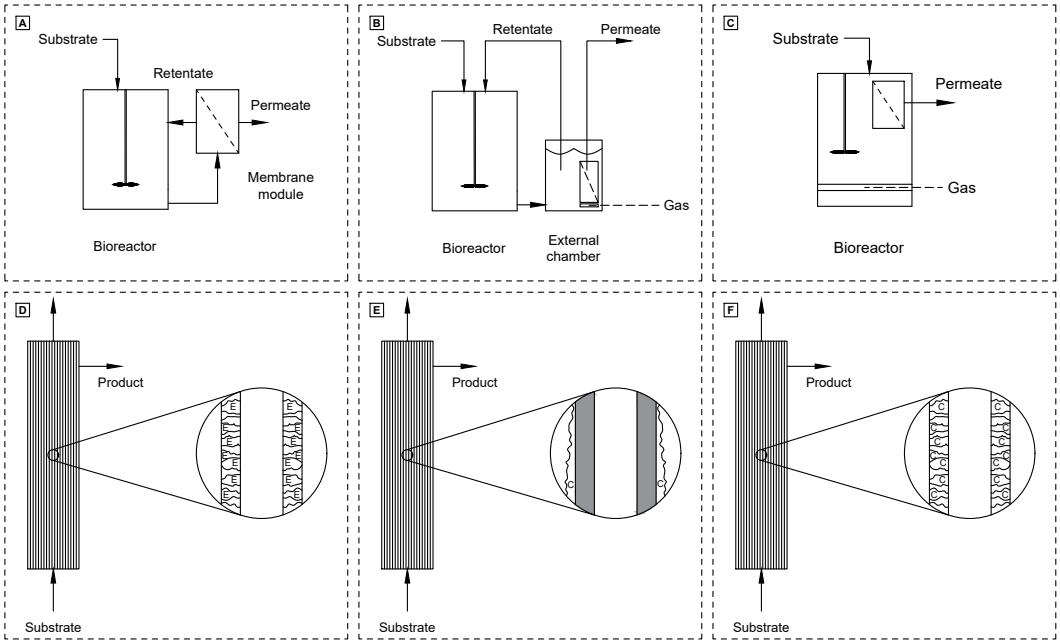

Fig. B.2: Configuration of different MBRs. A: Sidestream MBR; B: Submerged MBR with an external chamber; C: Submerged MBR with membrane module within the bioreactor; D: Enzymatic BMR; E: Whole-cell BMR with natural immobilization (biofilm); F: Whole-cell BMR with artificial immobilization.

B.2.5. Wastewater-to-H_2 experiments

Several dark fermentation experiments have been held by using wastewater as substrate. These are summarized in Table B.4.

Table B.4: Hydrogen production from complex wastewater substrate.

Substrate	**Substrate concentration** [$\frac{gCOD}{L}$]	**Inoculum**	**Reactor configuration**	**H_2 yield** [$\frac{mmol\,H_2}{gCOD}$]	**Ref.**
Vinasse	0.25	H_2-producers from a packed-bed reactor	Batch	24.970	[197]
Cheese whey	40.00	Anaerobic digest sludge with heat pretreatment	CSTR	22.000	[43]
Distillery effluent	101.00	Co-culture with *C. freundii, E. aerogens,* and *R. palustris*	Batch	14.371[a]	[198]
Cattle	2.65	Sewage sludge	Batch	13.052[b]	[199]
Crude glycerol	5.01	*Thermotoga neapolitana*	Batch	12.188[c]	[200]
Palm oil mill effluent	70.00 - 90.00	*Thermoanaerobacterium*-rich sludge	ASBR	11.663[a]	[49]
Rice winery	34.00	Mixed bacterial flora from WWTP	Similar to UASB	11.142[a]	[201]
Probiotic	9.48	Mixed anaerobic consortia	Batch	9.372[a]	[202]
Cheese whey	46.45	*C. saccharoper butylacetonicum*	Batch	7.032[d]	[203]
Confectionery processing	0.60	Soil	Batch	6.956[b]	[204]
Coffee drink	20.00	Anaerobic digest sludge	UASB	6.717[a]	[44]
Brewery	6.05	Anaerobic sludge	Batch	6.121[b]	[205]
Domestic sewage	0.25	H_2-producers from a packed-bed reactor	Batch	6.010	[197]
Potato processing	21.00	Soil	Batch	5.728[b]	[204]
Crude glycerol	0.25	H_2-producers from a packed-bed reactor	Batch	6.030	[197]
Crude glycerol	1.00	Activated sludge	Batch	4.911	[206]
Citric acid	18.00	Facultative anaerobic enrichment cultures (predominantly *C. pasteurianum*)	UASB	4.374	[46]
Apple processing	9.00	Soil	Batch	4.092[b]	[204]
Coffee drink	20.00	Anaerobic digest sludge	CSTR	1.666[a]	[44]
Chemical and domestic sewage	2.75	Anaerobic mixed microflora	Batch	1.250	[207]
Phenol-containing	7.20 - 7.80	*C. butyricum*	Batch	7.289[a]	[208]
Cattle	2.65	Mixed wastewater sludge, cow dung compost, chicken manure compost, and river sludge	Batch	13.052[c]	[199]
Cheese whey	11.26	Mixed cultures (anaerobic bacteria from UASB)	Batch	8.100	[209]
Brewery	64.20	Mixed cultures (from activated sludge)	Batch	10.413[a]	[210]
Waste glycerol	NA[e]	Mixed cultures (containing immobilized *E. aerogenes* ATCC 13048)	USAB	1.446[c]	[211]
Cassava starch	25.00	Mixed cultures (granules and sediment from UASB)	Batch	8.227[a]	[212]
Cheese whey	5.00	Mixed cultures from sludge	AFBR	3.151[d]	[48]
Beverage	10.39	Mixed cultures from WWTP	CSABR	1.562[a]	[159]
Beverage	10.13	Mixed cultures WWTP	CSABR	4.790[a]	[159]
Coffee drink	20.00	Anaerobic digest sludge with heat pretreatment	UASB	4.998[a]	[44]

[a] 192.06 [$\frac{gCOD}{mol hexose}$].
[b] $\frac{V}{mol}$ = 24.44 [$\frac{L}{mol}$] at 25°C and 1 atm.
[c] 224 [$\frac{gCOD}{mol\,glycerol}$].
[d] 1.122 [$\frac{gCOD}{g\,lactose}$].
[e] NA = Not available.

Annex C

Literature review methodology

Fig. C.1 shows the steps that were followed during the literature review on existing models for fermentative H_2 production, bioactive layer behavior, and whole-cell biocatalytic membrane reactors. Fig. C.2 provides the number of studies conducted so far on the modeling of different membrane bioreactors. The data represents the related literature concerning the membrane bioreactor classification described in Annex B.2.4, which was collected by using the ISI Web of Science (ISI-WoS) Core Collection with the ISI-WoS searching engine.

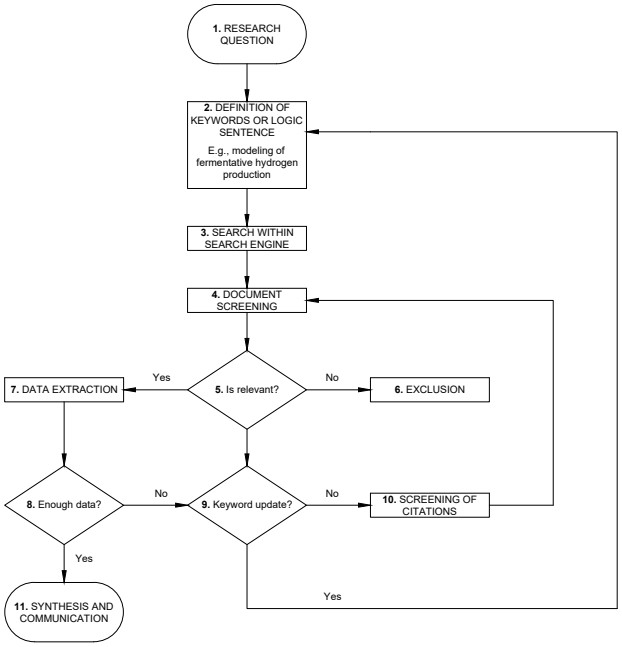

Fig. C.1: Methodology employed for the search of modeling strategies for fermentative H_2 production.

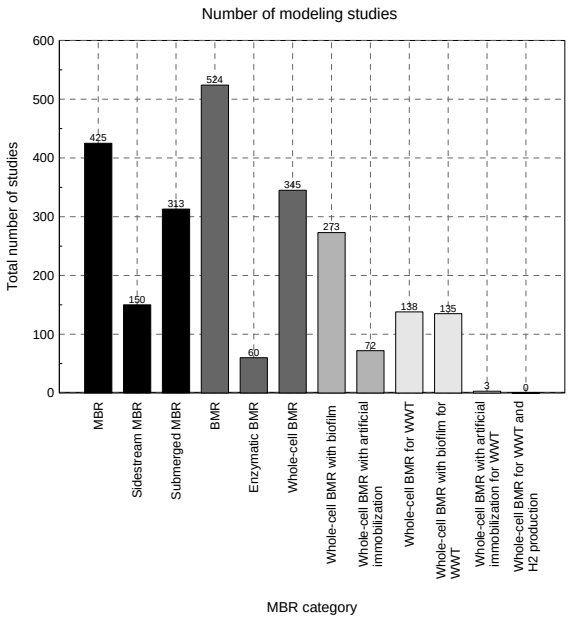

Fig. C.2: Studies on modeling of different MBRs.

Annex D

Finite-difference method

The finite-difference method is a numerical technique for solving differential equations by approximating derivatives with finite differences. It is based on the application of a local Taylor expansion to approximate partial differential equations by using a regular, fine, and structured mesh formed by a square network of lines. Considering the definition of a first-order derivative:

$$\frac{\partial u}{\partial x}(x) = \lim_{\Delta x \to 0} \frac{u(x+\Delta x) - u(x)}{\Delta x} \approx \frac{u_{i+1} - u_i}{\Delta x} \qquad \text{Forward difference} \qquad \text{(D.1)}$$

$$\frac{\partial u}{\partial x}(x) = \lim_{\Delta x \to 0} \frac{u(x) - u(x-\Delta x)}{\Delta x} \approx \frac{u_i - u_{i-1}}{\Delta x} \qquad \text{Backward difference} \qquad \text{(D.2)}$$

$$\frac{\partial u}{\partial x}(x) = \lim_{\Delta x \to 0} \frac{u(x+\Delta x) - u(x-\Delta x)}{2\Delta x} \approx \frac{u_{i+1} - u_{i-1}}{2\Delta x} \qquad \text{Central difference} \qquad \text{(D.3)}$$

That is, the slope of a curve at a certain point $u(x)$ (its derivative) is approximated by the slope calculated from two points that distance from each other (in terms of Δx) (Fig. D.1), being these differences applied to each node of the discretized mesh.

The approximation of second-order derivatives considering a central difference scheme is shown in Eq. (D.4).

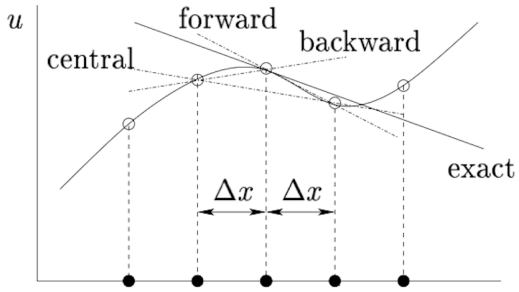

Fig. D.1: Finite-difference method for first order derivatives [213].

$$\left(\frac{\partial^2 u}{\partial x^2}\right)_i = \lim_{\Delta x \to 0} \frac{\left(\frac{\partial u}{\partial x}\right)_{i+1/2} - \left(\frac{\partial u}{\partial x}\right)_{i-1/2}}{\Delta x} \approx \frac{\frac{u_{i+1}-u_i}{\Delta x} - \frac{u_i - u_{i-1}}{\Delta x}}{\Delta x} \approx \frac{u_{i+1} - 2u_i + u_{i-1}}{(\Delta x)^2} \qquad \text{(D.4)}$$

Annex E

Softwares and PDE solvers

Process programming requires suitable programming and computing software. Among the alternatives are MATLAB® or GNU Octave. Their programming language allows them to create scripts, functions, and classes, and to visualize and explore data. Moreover, they can express matrix and array mathematics directly. Finally, both allow numerical computation and can thus solve ODEs, PDEs, and algebraic equations.

Solver examples based on numerical methods are BVP or ODE solvers. BVPs can be solved with MATLAB® BVP solvers bvp4c and bvp5c. bvp4c is a finite-difference code that implements the 3-stage Lobatto IIIa formula, where the collocation polynomial provides a C^1-continuous solution that is fourth-order accurate uniformly in the interval of integration [65]. bvp5c is similar to bvp4c but implements the 4-stage Lobatto IIIa formula, and the solution is fifth-order accurate uniformly in the interval of integration. bvp5c solves the algebraic equations directly and augments the system with trivial differential equations for unknown parameters, whereas bvp4c uses analytical condensation and handles unknown parameters directly [65]. So far, Octave does not provide bvp4c or bvp5c. Moreover, the disadvantage of using BVP solvers is that a guess for the required solution of the differential equations must be provided. Its quality is critical for the solver's performance and successful computation. Considering the model structure, this would be the case for each domain of the CBMem and each species.

Regarding ODEs, MATLAB® offers ODE solvers based on the problem type, i.e., stiff or nonstiff problems. Stiffness occurs when there is a difference in scaling within the problem (drastic variation). Nonstiff solvers are ODE23 or ODE45. ODE23 and ODE45 are automatic step-size Runge-Kutta-Fehlberg integration methods. ODE23 uses a second and third-order pair of formulas for medium accuracy, while ODE45 uses a fourth and fifth-order pair for higher accuracy. Thus, ODE45 usually takes fewer integration steps and gives a solution more rapidly. However, ODE23 may be more efficient at crude tolerances and in the presence of moderate stiffness. Both ODE23 and ODE45 are also available in Octave.

Stiff problems are common in process modeling. Thus, solvers such as ODE15s or ODE23s are recommended. On the one hand, ODE15s integrates a system of stiff ODEs using a variable step and variable order method based on backward difference formulas. On the other hand, ODE23s uses a modified second-order Rosenbrock method. The former performs best for most stiff problems while the latter can be more efficient if the problem permits a crude error tolerance or when the problems have solutions that change rapidly [214]. Both are also provided in Octave [215, 216].

Annex F

Levenberg-Marquardt nonlinear regression

Among different available methods, Levenberg-Marquardt is a popular algorithm to solve nonlinear least-squares problems effectively due to its ability to converge from a wide range of initial guess values of parameters. The problem's objective is to minimize the difference between a set of experimental or verisimilar data and the data generated by the model function. That is, given a set of observed data (x_i, y_i), the method optimizes the parameter θ of a model function $f(x_i, \theta)$ to minimize the sum of the squares of the deviations. The objective function of the least-square problems is then formulated as follows [217]:

$$F(\theta) = \frac{1}{2}\sum_{i=1}^{n} r_i(x)^2 \tag{F.1}$$

where n is the number of data points considered, $r_i(x) = (f(x_i, \theta) - y_i)^2$ is called a residual, and y_i is y component of the data point at x_i. If the function is nonlinear in the model parameters vector $\theta = [\theta_1, \theta_2, ..., \theta_m]^T$, where m is the number of parameters, then minimization of the objective function is carried out iteratively [217].

The Levenberg-Marquardt algorithm starts with an initial guess for the parameters vector θ. In each iteration step, perturbation $\delta\theta$ of parameters is calculated and next iteration proceeds with a new estimate, $\theta + \delta\theta$. The following search scheme is used to update the parameter [217]:

$$(J_K^T J_k + \lambda diag(J_K^T J_k))\delta\theta_k = -J_K^T r_k \tag{F.2}$$

$$\theta^{k+1} = \theta^k + \delta\theta^k \tag{F.3}$$

where J is the Jacobian matrix of residuals, and λ a damping factor.

GNU Octave's *leasqr* function has the structure shown in Eq. (F.4) [218].

$$\begin{aligned}[f, p, cvg, iter, corp, covp, covr, stdresid, Z, r2] = \\ leasqr(x, y, pin, F, stol, niter, wt, dp, dFdp, options)\end{aligned} \tag{F.4}$$

On the one hand, its input arguments are the following:

- x: Vector or matrix of independent variables.

- y: Vector or matrix of observed values.
- *pin*: Vector of initial parameters to be adjusted by leasqr.
- F: Name of function or function handle.
- *stol*: Scalar tolerance on fractional improvement in scalar sum of squares.
- *niter*: Maximum number of iterations.
- *wt*: Statistical weights.
- *dp*: Fractional increment of p for numerical partial derivatives. $dp(j) > 0$ means central difference on j-th parameter $p(j)$, while $dp(j) = 0$ holds $p(j)$ fixed, i.e., leasqr won't change initial guess: $pin(j)$.
- *dFdp*: Name of partial derivative function in quotes or function handle. Set to $'dfdp'$ for a slow but general partial derivatives function.
- *options*: Structure with multiple options, such as *bound*, which is a two-column-matrix, one row for each parameter in *pin*. Each row contains a minimal and maximal value for each parameter.

On the other hand, the output arguments of the *leasqr* function are the following:

- f: Column vector of values computed: f = F(x,p).
- p: Column vector trial or final parameters, i.e, the solution.
- *cvg*: Scalar: = 1 if convergence, = 0 otherwise.
- *iter*: Scalar number of iterations used.
- *corp*: Correlation matrix for parameters.
- *covp*: Covariance matrix of the parameters.
- *covr*: Diagonal of the covariance matrix of the residuals.
- *stdresid*: Standardized residuals.
- Z: Matrix that defines confidence region.
- $r2$: Coefficient of multiple determination in its intercept form.

Annex G

Experimental data collection

This chapter presents the experiment's methodology based on Prieto et al. (2016) [63] and subsequent laboratory experiments. Firstly, the construction of the reactor is explained. Secondly, its operation and the necessary measurements are detailed. Finally, the data sets are characterized.

G.1. Reactor construction

Feedstock

Synthetic wastewater was prepared as feedstock as described by Klara and LaPara (2003) [219] and contained starch, gelatin, and polyoxyethylene-sorbitan monooleate to simulate the polysaccharide, protein, and lipid components of municipal wastewater [220].

At first, the media contained the following composition (per liter of deionized water) [219]: 150 mg gelatin, 70 mg starch, 120 mg polyoxyethylene-sorbitan monooleate, 10 mg yeast extract, 10 mg casamino acids, 150 mg ammonium chloride, 100 mg sodium bicarbonate, 25 mg sodium phosphate, 30 mg potassium phosphate, 40 mg magnesium chloride, 60 mg calcium chloride, and 0,1 mL SL7 trace mineral solution. As this media had a low COD of 400 $\frac{mg}{L}$, it was modified to obtain high-strength wastewater with a COD content of 6.92 $\frac{g}{L}$.

Microbial seed

For the fabrication of the CBMem's bioactive layer, an acetogenic seed culture was required. A sample of municipal anaerobic sludge was heat-treated at 80 °C for 40 minutes to favor the presence of *Clostridium sp.* and reduce the presence of methanogenic archaea [122–124]. Afterward, the species were isolated: serum bottles were prepared to contain 100 mL of synthetic wastewater and sparged with N_2 gas to achieve anaerobic conditions. Subsequently, 2 mL of the heat-treated seed were inoculated in serum bottles and incubated at 37 °C for 24 hours. Then, biological H_2 production was verified by extracting 1 mL of the gas formed in the headspace with a syringe and analyzing the sample with gas chromatography. This isolation procedure was repeated 2 to 3 times.

Finally, the serum bottles were washed twice with deionized water and the culture was concentrated through centrifugation. The obtained pellet was resuspended with 10 mL of synthetic water and the culture was used as inoculum for the bioactive layer of the CBMem module. Besides, a stock culture was maintained at ambient temperature for other iterations.

CBMem module construction

The composite membrane module was composed of a gas transfer layer, a support layer, an immobilized bioactive layer, and a sealant layer. As shown in Fig. G.1, the gas transfer layer consisted of a woven mat of 12 cm×12 cm and 135 microporous hydrophobic polypropylene hollow-fibers (210 μm ID, 300 μm OD, model 3M™ X50 Hollow Fiber) [221]. The nominal pore size of the hollow-fibers was approximately 0.03 μm [221, 222], and the porosity was 40 % [221]. The bioactive layer consisted of the acetogenic seed culture cast on a PDA support layer. An additional PVA layer followed to act as a sealing coat to prevent the release of cells into the reactor bulk.

For the encapsulation using PDA, a 2 $\frac{g}{L}$ solution was prepared by dissolving dopamine hydrochloride (H8502-25G, Sigma Aldrich, St. Louis, MO) in 10 [mM] Tris solution. The pH of the solution was adjusted to 8.5 using 0.1 normal HCl. The bare hollow-fibers were submerged in PDA solution to obtain a thin film of less than 50 [nm] that provided an adhesive surface for the cells [63]. The concentrated seed culture was sprayed onto each side of the PDA-coated surface. Then, the layer was air-dryed in a fume hood before it was dip-coated with an 8.3 % (w/v) aqueous solution of PVA (Elvanol 71-30 DuPont; Wilmington, DE). Finally, the coated fibers were potted into silicone tubes, which acted as a manifold to distribute gas through the fibers, and the tubes were sealed with silicone adhesive to avoid leakage, resulting in a woven mat with an active surface of 12 cm (width)×6 cm (height).

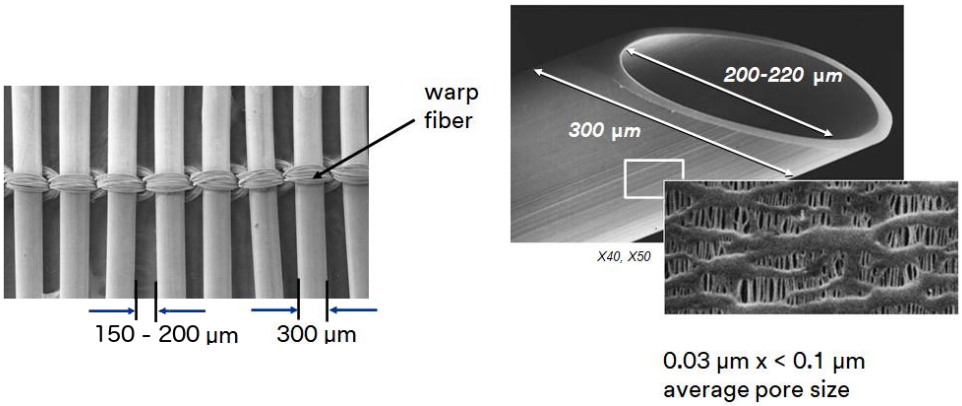

Fig. G.1: Detail of model 3M™ X50 Hollow Fiber. Provided by 3M [221].

CBMem reactor construction

The experimental set-up consisted of a 5.3 L cylindrical acrylic tank that acted as a continuous flow-through anaerobic reactor. It contained the submerged CBMem module, which was positioned at the center of the reactor; each silicone tube of the CBMem module was fixed with plastic strings to a plastic tube to avoid the membrane's deformation.

The CBMem module acted as an outside-in filtration module. The silicone tubes of the module were plumbed into a gas line using plastic fittings for the feed of the sweep gas. The gas flow rate (Qg_i) that was measured daily and controlled manually with a gas flow meter and a needle valve. The sweep gas consisted of compressed ultra-high pure N_2 that flew continuously through the module to recover the biologically produced gas and alleviate any potential pressure build-up inside the membrane that might be detrimental to long-term operation.

In addition, a double-head peristaltic pump (Masterflex, ColePalmer, Vernon Hills, IL) was installed to continuously feed the reactor with the feedstock solution.

The configuration of the reactor is represented in Fig. G.2. The nomenclature used can be consulted in Annex A.

To achieve the monitoring of the reactor, the following devices were installed:

1. DAQ system: It consisted of a remote monitoring system for the on-line measurements and register of data. The interface (HOBO RX3000 online sensors, ONSET Computer Corporation, CapeCod, MA) was connected to a computer through the HOBOware software (ONSET Computer Corporation, CapeCod, MA). The system received on-line data from the connected sensors every 1 minute and saved the data every 10 minutes [223].

2. Thermometer: A thermometer was located inside the reactor and connected to the DAQ to monitor the temperature of fermentation.

3. pH meter: A pH meter was used to measure and control of the pH in three points: affluent and effluent mixed liquor flow, and inside the reactor.

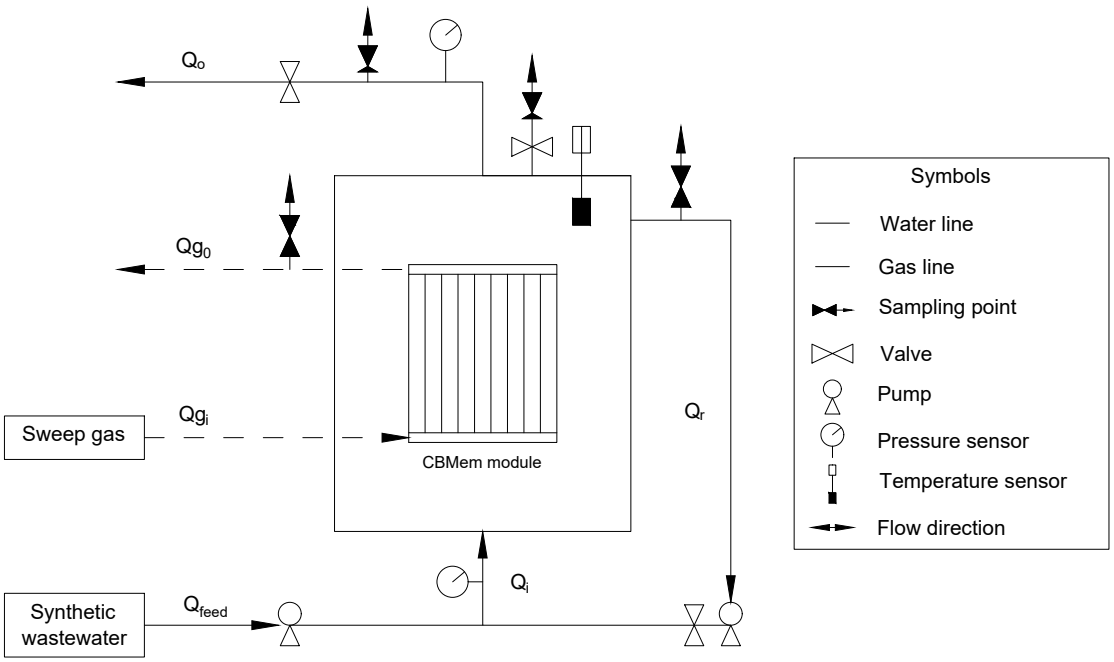

Fig. G.2: Schema of the reactor.

G.2. Reactor operation

Operating conditions

The experiment is defined in Table G.1.

Table G.1: Summary of the process' operating conditions.

Equipment	Parameter	Symbol	Value	Unit	Justification	Ref.
Membrane	Hollow-fiber layer: Internal diameter	ID_2	210	μm	Manufacturer	[221]
	Hollow-fiber layer: Outside diameter	OD_2	300	μm	Manufacturer	[221]
	Hollow-fiber layer: pore size	Dp_2	0.03	μm	Manufacturer	[221]
	Hollow-fiber layer: porosity	ϵ_2	40	%	Manufacturer	[221]
	PDA support layer: Thickness	Δr_3	$50{\cdot}10^{-3}$	μm	Construction	[63]
	PVA sealant layer: Thickness	Δr_5	1	mm	Construction	[63]
	Effective fiber length	L	6	cm	Design criteria	NA[a]
	Number of fibers	N_f	135	-	Design criteria	NA[a]
Reactor	Volume	V	5.346	L	Design criteria	NA[a]
	Diameter	D_7	6.5	cm	Design criteria	NA[a]
	Height	H	25	cm	Design criteria	NA[a]
	Membrane height position	z_0	6.5	cm	Design criteria	NA[a]
Experiment	Affluent mixed liquor flow	Q_i	3	$\frac{L}{d}$	Design criteria	NA[a]
	Recycle flow	Q_r	518.40	$\frac{L}{d}$	Design criteria	NA[a]
	Gas feed flow	Qg_i	14.40	$\frac{L}{d}$	Design criteria	NA[a]
	Temperature	T	25.60	°C	Design criteria	NA[a]
	Pressure of the reactor	P	1	atm	Design criteria	NA[a]
	Pressure of the gas feed	Pg_i	0.34	atm	Design criteria	NA[a]
	Pressure of the affluent mixed liquor	P_i	13.26	atm	Design criteria	NA[a]
	Tank pressure	P	10.60	atm	Design criteria	NA[a]
	pH	pH	5 - 6	-	Design criteria	NA[a]
	COD content in feed flow	$C_{COD,Qi}$	6.92	$\frac{g}{L}$	Design criteria	NA[a]
	Molar composition of N_2 in Qg_i	n_{N_2}	99.99	[%]	Manufacturer	NA[a]

[a]Not applicable.

Measurements and analytical methods

During the start-up, some indicators had to be verified for the correct construction and stable performance. These are the following: (1) the system does not present leakages, (2) the reactor operates correctly with the proposed conditions, (3) hydrogen production data can be obtained, and (4) COD removal data can be obtained. Once the start-up was ensured, the experimental measurements were taken using analytical methods and online monitoring. Table G.2 summarizes the set of measurements.

Table G.2: Summary of the measurements through analytical methods or online monitoring.

Analytical methods	**On-line monitoring**
MLSS, COD, pH, total gas composition, off-gas composition off-gas volume, total gas volume	Q_i, Q_r, P, T

Regarding the analytical methods, the MLSS was measured daily according to Standard Method 2540 [224]. Moreover, COD values of the affluent and effluent flow were measured daily on diluted samples using Hach HR COD digestion vials (Hack Company, Loveland, CO) [63]. Further, samples of the CBMem off-gas and total gas were taken daily and its composition (H_2) was analyzed using gas chromatography (Autosystem XL, Perkin Elmer, Massachusetts, United States) equipped with a thermal conductivity detector and a molecular column (Sieve 13 $\times$). For this, a 5 mL sample of the effluent was taken with a gas-tight syringe. Air (1 mL) was injected into the syringe and the air/liquid mixture was shaken and allowed to equilibrate for approximately 10 minutes. Then, a 100 μL sample of the headspace was taken with a locking gas-tight syringe and injected for gas chromatography measurement. This last step was repeated for the measurement of the off-gas composition. In addition, the flow of the produced CBMem's off-gas and total gas were measured daily using a volume displacement system, i.e., two water-filled test tubes with tubing connected to the gas line. The water volume evicted by the effect of air allowed the measurement of the volume of biogas produced. Finally, influent and effluent pH were monitored daily and the reactor's pH was adjusted to 5 to 6 using $CaCO_3$.

For the online monitoring of the affluent mixed liquor flow, Q_i, and the recycle flow, Q_r, the peristaltic pumps were calibrated and the flows were defined to supply 3 $[\frac{L}{d}]$ and 518.40 $[\frac{L}{d}]$, respectively.

G.3. Experimental data sets for modeling

When the model was implemented, the expected laboratory trials that involved the CBMem configuration of interest (Fig. 2.2) were not finished within the framework of the research project. Thus, we considered experimental data from a previous study [63] that used the same CBMem configuration and similar operating conditions. The experimental data is shown in Fig. G.3 and summarized in Table G.3.

To have enough data points, the set shown in Table G.3 was extended for both columns by using Eq. (G.1), where x_2 is related to the set of points measured after x_1. The *rand* function returns a random scalar drawn from the uniform distribution in the interval (0,1). Thus, x_{rand} is between x_1 and x_2.

$$x_{rand} = x_1 + (x_2 - x_1) * rand \tag{G.1}$$

After obtaining the extended experimental data set by using Eq. (G.1), it was separated into two data sets. This was carried out by choosing every other day data to create the second set. Finally, Table G.3 was considered as the data set for calibration, while Table G.4 was used for validation.

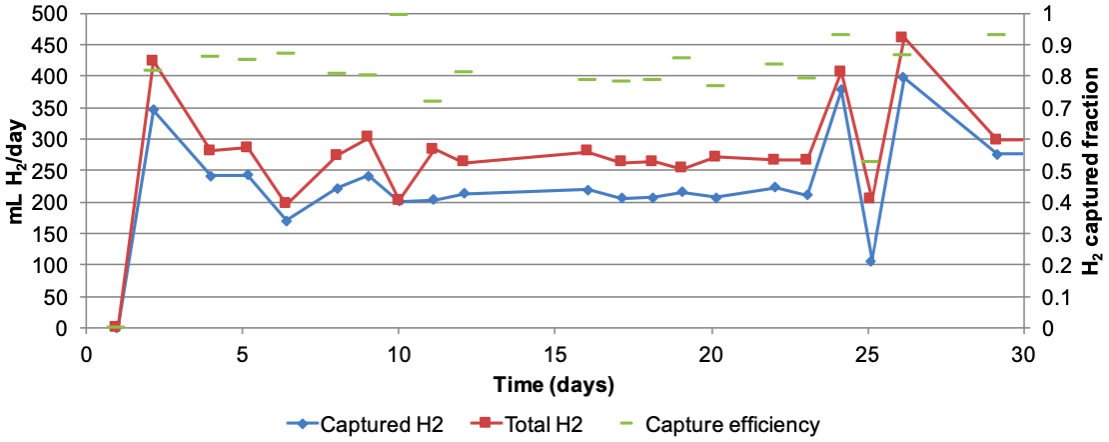

Fig. G.3: CBMem performance for H_2 production and capture from synthetic wastewater (unpublished data) [63].

Table G.3: Unpublished data from Prieto et al. (2016) [63], used for calibration.

Time [h]	H_2 captured in gas effluent $[\frac{mL\,H_2}{d}]$
0	0.000
24	0.000
52	346.262
96	242.085
124	242.941
154	170.401
193	221.447
217	242.118
241	200.803
267	203.367
291	212.815
386	219.226
412	205.549
436	207.649
458	215.583
484	206.998
530	222.813
554	211.095
580	377.649
603	106.980
628	397.191
700	276.189
722	275.803

Table G.4: Experimental data with noise for validation.

Time [h]	H_2 captured in gas effluent $[\frac{mL\,H_2}{d}]$
19	0.000
33	82.976
88	322.724
121	242.178
140	233.486
167	173.536
210	223.331
221	211.531
259	200.916
281	208.113
334	217.272
399	210.346
431	206.926
440	212.917
471	211.994
514	219.490
546	215.907
572	298.789
598	320.947
617	257.752
664	315.859
711	275.891

Annex H

Multi-domain fiber model development

This chapter presents a detailed procedure to obtain the CBMem fiber model, highlighting model strategy and assumptions.

H.1. Domain coupling and dynamic treatment

The membrane reactor has a multi-layer configuration, where domains are placed parallel, and separated by interfaces. Each domain has its respective mass balance equations, which are intrinsically boundary value problems. For solving the membrane completely, the values at the interfaces should be known. However, several are unknown in practice. Moreover, domain coupling results by relating the boundary conditions from one domain with data (e.g., concentration profiles), e.g., an adjacent domain that has been solved before. In general, coupling can be done by assuming equilibrium-like behavior or conservation of mass flux for the transferred species.

The domains that involve known data are those that are connected with the reactor's inlet and outlet flows. In a CBMem, the mixed liquor and lumen gas side could provide some relevant operating parameters and experimental data.

Model computing is in practice a linear strategy. For example, based on the code, the solver would "begin" in one domain (e.g., at the mixed liquor), solve the domain's mass balance equations, and then continue with the domain that is adjacent to the previous one (e.g., the PVA sealant layer) due to the provided functions that relate both domains at the interface. However, some parameters of those functions are not known. Thus, we propose that the modeling strategy for multi-domain membranes involves an "initial value problem". First, values for the border's unknown parameters need to be guessed. Then, the solver models each domain until reaching the domain where the modeled data (that depends on the initial guesses) can be compared with realistic or experimental data. Finally, membrane solving can be repeated through iterations based on data-fitting and improved guessed values until reaching a stopping criterion (e.g., fulfillment of error threshold).

The modeling results in concentration profiles of each species in each domain that are expressed in function of independent variables, e.g., radial position (r), axial (z) position, and time (k). However, not all mass balance equations, in their differential form, must express their dependence on all three independent variables. For example, some mass balances assumed a steady state; thus, the equations do not express the time variable. However, other domains' equations, i.e., the

bioactive domains, do depend on time. Because of the domain coupling through its borders, the domains respond to all three independent variables. Therefore, the coding of the mass balance must ensure expressing the concentrations' dependency on those, which is easily implemented when using the finite-difference form.

Time dependence for this reactor is important as the process system evolves continuously over time and can change abruptly due to some slight variation of parameters. Therefore, we considered an unsteady state for the bioactive domains. However, Monod-type rates create a non-linear model and, in consequence, instability. Therefore, the implementation strategy based on discretization is convenient to manage the computational difficulties. Consequently, the computing considers sequential pseudo-steady state approximation for "small" discrete time intervals such that concentration evolution is simulated as a step chart. This results in equations relating the value of the concentration at time $t+1$ to its value at time t. Thus, the model can be solved through iteration by starting with the initial condition at $t = t_0$.

H.2. Component mass balance for each domain

Fig. H.1 illustrates the general component movements in the fully open system. The substrate is available on the mixed liquor side, moves through the membrane layers, and reacts in the bioactive layer to form the products. These, in turn, move to the lumen side. The mass transfer-reaction combined phenomenon can be described through mass balance models, which are mathematical descriptions of the conservation of mass by accounting for the mass entering a system, leaving it, and changing due to reaction (i.e., generation of products or consumption of substrate to produce the products).

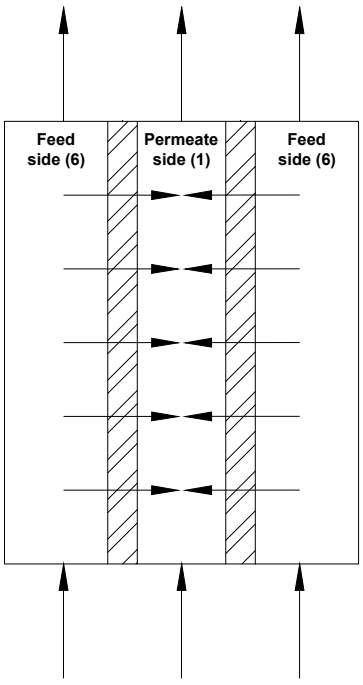

Fig. H.1: Schematic representations of the component flows in a fiber of the open CBMem reactor.

Mass balance equations for the substrate (S), product (H), and cells (X) have to be given for all domains of the CBMem fiber, namely the lumen side, mixed liquor side, and each membrane layer. The following assumptions are considered for the modeling:

1. Fick's law holds for the diffusive mass flux.
2. The velocity profiles are invariant in space [225].
3. The biochemical reaction takes place in sections where cells grow [69].
4. The reaction does not affect the velocity profiles in the system [69].

5. Cells only grow within the immobilized cell layer and towards the sealant layer-mixed liquor interface due to substrate availability.

6. No biofilm formation is considered.

7. The biochemical processes are isothermal [69].

8. The hollow-fiber support layer is only permeable to H_2.

The explanation for each assumption is provided below:

A1 It is a common assumption to develop the general equation of mass transfer [225]. Fick's law allows us to relate the diffusive flux to the gradient of the concentration, so that it expresses that the species move from a region of high concentration to a region of low concentration, with a magnitude that is proportional to the concentration gradient.

A2 It is a common assumption to develop the general equation of mass transfer to simplify the model [225]. Thus, the derivation of the velocity is not required.

A3 It induces the need for mass balances with reaction rates in the regions where cells grow [69].

A4 It is a common assumption to develop the general equation of mass transfer and simplify the model [225]. Thus, the derivation of the velocity is not required.

A5 In non-ideal conditions, cell growth could occur in other domains, besides the membrane. For example, the sealant layer could be defective and cells could be released back into the mixed liquor before or during the operation. Also, due to the source of wastewater supply, cells could be contained within the feed flow. Moreover, cells usually grow in clusters and can migrate in different directions. However, their migration is stimulated by the substrate supply. Therefore, this assumption is considered for model simplification and is sufficient as the model focuses on membrane evolution.

A6 Considering the model's goal, it is enough to simulate until the membrane's lifetime has been reached (when it loses the ability to diffuse the nutrients and the product). Considering previous studies, this already occurs without observing biofilm formation [63].

A7 Heat transfer is low as the reactor operates at ambient temperature. Thus, heat balance is not needed [69].

A8 This assumption is based on the hollow-fiber characteristics. Therefore, no substrate nor cells are expected to be present on the lumen side.

The general equation of mass transfer of a species a is shown in Eq. (H.1).

$$\begin{Bmatrix}\text{Rate of mass}\\ \text{accumulation}\\ \text{of a}\end{Bmatrix} = \begin{Bmatrix}\text{Net mass}\\ \text{inflow rate}\\ \text{of a}\end{Bmatrix} - \begin{Bmatrix}\text{Net mass}\\ \text{outflow}\\ \text{rate of a}\end{Bmatrix} + \begin{Bmatrix}\text{Mass generation/}\\ \text{consumption rate}\\ \text{of a}\end{Bmatrix} \tag{H.1}$$

Considering Asm. (2), the mass balance is represented by Eq. (H.2) [226].

$$\frac{\partial C_a}{\partial t} + v\nabla C_a + \nabla J - \hat{r}_a = 0 \tag{H.2}$$

$$J = -\nabla D C_a \tag{H.3}$$

Note that $\hat{r}_a$ is the generation/ consumption term, whose value is positive if the species a is produced, or negative if it is consumed.

Combining Eq. (H.2) and Eq. (H.3), the following equation is obtained:

$$\frac{\partial C_a}{\partial t} + v\nabla C_a - \nabla^2 D C_a - \hat{r}_a = 0 \tag{H.4}$$

Considering the ∇-operator in cylindrical coordinates [226] and that the diffusivity isotropic and constant[5], Eq. (H.2) can be rewritten as follows:

$$\frac{\partial C_a}{\partial t} + \left[v_r \frac{\partial C_a}{\partial r} + \frac{v_\theta}{r}\frac{\partial C_a}{\partial \theta} + v_z \frac{\partial C_a}{\partial z} \right] - D\left[\frac{1}{r}\frac{\partial}{\partial r}\left(r\frac{\partial C_a}{\partial r} \right) + \frac{1}{r^2}\frac{\partial^2 C_a}{\partial \theta^2} + \frac{\partial^2 C_a}{\partial z^2} \right] - \hat{r}_a = 0 \tag{H.5}$$

The previous equation is the base for the development of mass balances of each species in each domain, which are summarized in Table H.1. The following sections will focus on highlighting the assumptions of each domain to comprehend the construction of these model equations.

Table H.1: Mass balance equations for a species a in domain d. The symbols used are defined in Annex A.

Model	**Domain**	**Species**	**Equation**
Fluid	6	S, H, X	$v_{z,d}\frac{\partial C_{a,d}}{\partial z} = D_{eff,a,d}\left(\frac{1}{r}\frac{\partial C_{a,d}}{\partial r} + \frac{\partial^2 C_{a,d}}{\partial r^2}\right)$
	1	S, H, X	$v_{z,d}\frac{\partial C_{a,d}}{\partial z} = D_{eff,a,d}\left(\frac{1}{r}\frac{\partial C_{a,d}}{\partial r} + \frac{\partial^2 C_{a,d}}{\partial r^2}\right)$
Inactive membrane	2,3,5	S, H, X	$\frac{D_{eff,a,d}}{r}\frac{\partial}{\partial r}\left(r\frac{\partial C_{a,d}}{\partial r}\right) = 0$
Bioactive membrane	4,5	S, H	$\frac{\partial C_{a,d}}{\partial t} - \frac{1}{r}\frac{\partial}{\partial r}\left(D_{eff,a,d} r \frac{\partial C_{a,d}}{\partial r}\right) = \hat{r}_{a,d}$
	4,5	X	$\frac{\partial C_{X,d}}{\partial t} - \frac{1}{r}\frac{\partial}{\partial r}\left(D_{eff,X,d} r \frac{\partial C_{S,d}}{\partial r}\right) = \hat{r}_{X,d}$

Assumptions for the lumen side

The following assumptions are taken for the lumen (domain 1):

1. The flow in the lumen side is steady state [92].
2. The flow is laminar, and the entrance effects can be ignored [92].
3. The flow is axisymmetric, i.e., the substrate flows only in axial and radial directions.
4. No reaction occurs at the lumen side.
5. The axial diffusion terms can be neglected [72, 227].
6. The radial convective term can be neglected [227].
7. The inlet sparging gas only contains ultrapure nitrogen.
8. Effective diffusivity is isotropic and constant [225].

[5] This assumption depends on the domain. In this case, it is only considered for illustrative purposes of the mathematical operator. Moreover, Eq. (H.5) is widely used.

9. Henry-like equilibrium exists on the membrane interfaces.

The explanation for each assumption is provided below:

A1 The reactor is a continuous-flow reactor and the membrane is located at the reactor's center, where dead volume is not perceived. Thus, the mass balance equation does not express the accumulation term, and time dependence through this term is neglected. Nevertheless, the domain model will be sensitive to temporal changes through its coupling with other domain models at the membrane/mixed liquor interface.

A2 The fluid flow is held at a low rate, which sustains laminar flow [63]. Moreover, neglecting entrance effects is a common assumption to simplify model development [92].

A3 This assumption is due to the cylindrical reactor shape. The influence of the CBMem module on the flow is neglected for simplifications.

A4 As explained before, due to the reactor's design criteria and its operation, cells should exclusively be present in the membrane domains. However, non-ideal conditions could produce cells in the mixed liquor. Therefore, by assuming that the cells are absent, no metabolic-related reaction occurs. Other reactions are neglected.

A5 This is based on the axial Peclet number ($Pe_{ax} = \frac{v_z L}{D}$). If $\mathrm{Pe}_{ax} \in [10,\ 4.5{\cdot}10^4]$, the axial diffusion term is negligible [225, 227]. The resistance to the flow of packed cells, membrane fouling, and protein concentration polarization could decrease the velocity, thus the Peclet number is expressed as upper bound [227].

A6 This is based on the radial Peclet number ($Pe_{rad} = \frac{v_r r_1}{D}$). If $Pe_{rad} \in [10^{-5},\ 1]$, the radial concentration gradient is low and, accordingly, the momentum equation of the transverse velocity can be neglected [225]. This Peclet number is also expressed as upper bound [227].

A7 According to the manufacturer, the N_2 sparging gas is ultrapure and has very low traces of other molecules. Thus, these traces can be neglected.

A8 The diffusivity coefficient is invariant in space as no medium change, e.g., through cell growth, is expected. It is a common assumption to develop the general equation of mass transfer to simplify the model [225]. So, the derivation of the diffusion coefficient is not required.

A9 This is considered to estimate a relation between the species' concentrations of two adjacent domains to provide a boundary condition.

Assumptions for the mixed liquor

For the mixed liquor (domain 6), analogous assumptions and explanations apply as those shown for the lumen side, except for Asm. (7) as no sparging gas is supplied into the mixed liquor. Note that due to the general component mass balance's assumptions, especially Asm. (3) and (5), no reaction occurs on the mixed liquor side.

Assumptions for the membrane's hollow-fiber layer

The following assumptions are taken for the hollow-fiber (domain 2):

1. Process is steady state.

2. Mass transport through the membrane layers occurs by diffusion. Advective transport is neglected [69].

3. The flow is axisymmetric.

4. There is no axial flow and no axial component transport inside the membrane layer [69].

5. Henry-like equilibrium exists on the membrane interfaces.

6. No reaction occurs within this domain [69].

7. The mass flux is conserved at the interfaces.

8. Effective diffusivity is isotropic and constant [225].

The explanation for each assumption is provided below:

A1 This is a strong assumption as membrane layers can retain and accumulate substances [69]. However, this allows the elimination of the accumulation term from the mass balance equation, and time dependence through this term is neglected. Nevertheless, the domain model will be sensitive to temporal changes through its coupling with other domain models at the membrane layer's borders.

A2 This is a strong assumption as the membrane is expected to be classified as a porous solid (pore size larger than 1 nm). For example, the most dense layer, which is the hollow-fiber layer, has a nominal pore size of 0.03 μm [221, 222]. Therefore, mass transfer depends on the actual structure and channels and transport occurs by a convective flow through the pores [70]. However, the assumption is taken for model simplification.

A3 This assumption is due to the cylindrical fiber shape.

A4 This is considered as the operating conditions allow the main drag force to move in the radial direction, being axial transport negligible [69].

A5 This is considered to estimate a relation between the species' concentrations of two adjacent domains to provide a boundary condition.

A6 As explained before, due to the reactor's design criteria and its operation, cells should exclusively be present in the immobilized layer or, eventually, in the PVA-sealant layer. Moreover, the hollow fiber's characteristics do not offer appropriate conditions for cell growth. Therefore, when cells are absent, no metabolic-related reaction occurs. Other reactions are neglected.

A7 It is a common assumption to develop mass balance equations [225]. This assumption is considered to estimate a relation between the species' concentration gradients of two adjacent domains to provide another boundary condition.

A8 The diffusivity coefficient is invariant in space as no medium relevant change, e.g., through cell growth, is expected. It is a common assumption to develop the general equation of mass transfer to simplify the model [225]. So, the derivation of the diffusion coefficient is not required.

Assumptions for the membrane's (PDA) support layer

The mass balance for the membrane's support layer (domain 3) considers analogous assumptions and explanations to those applicable for the hollow-fiber. Unlike the hollow-fiber layer, the PDA support layer is permeable to both hydrogen and substrate.

Assumptions for the membrane's immobilized cell layer

The following section details the assumptions for the membrane's immobilized cell layer (domain 4). Note that these are analogous to the assumptions applicable for the hollow-fiber, except for Asm. (1), (6), (7), and (8). Instead, the following assumptions are taken:

1. The process is unsteady state [69].
2. Reaction occurs at every position within the immobilized cell layer based on cell metabolism [69].
3. The biochemical reaction rate and effective diffusivity can vary as a function of the space coordinate [69].
4. Mass transport is described in diffusive terms stimulated by the substrate gradient.
5. If the cell concentration of a certain moment and position surpasses the maximum cell capacity that the membrane can hold, then the cell concentration is corrected by assuming it to be the maximum cell concentration, while the concentration difference (defined as the "excess cell concentration", $C_{X,excess}$) migrates to an adjacent position (measured for the next time point) in the direction where the substrate is more available (approaching the mixed liquor). Therefore, the accumulation term of the cell mass balance will be developed by including $C_{X,excess}$ and a term subject to a binary value (k_{bb}) due to a boolean condition that represents proliferation.
6. Excess cell concentration strategy also represents cell migration and proliferation within the adjacent membrane domain that was initially inert. When the concentration of the bioactive layer (domain 4) near the bioactive/sealant border surpasses the maximum cell concentration, then the cell concentration is corrected by assuming it to be the maximum cell concentration, while the concentration difference (defined as the "excess cell concentration", $C_{X,excess}$) migrates to domain 5. Migration is defined as the unequal distribution of the excess cell concentration over domain 5, while ensuring mass conservation. I.e., the cell mass is distributed over all radial position of domain 5, for the same axial position and time point as those measured during the evaluation of the concentration in domain 4 that activates cell migration and proliferation.

The explanation for each assumption is provided below:

A1 Mass is changing with time due to cell growth and metabolism. This allows a good representation of the dynamic bioactive layer behavior.

A2 This is because the immobilized cell layer contains cells that consume substrate to produce hydrogen.

A3 Reaction rates and transport parameters change due to changes in the cell concentration related to growth [90].

A4 This assumption is to represent the expected cell growth behavior. Cells will tend to grow in the direction where substrate is more available.

A5 This assumption allows to represent cell migration phenomena. Thus, the cell mass balance will include a term with a binary value (k_{bb}) due to a boolean condition that represents proliferation.

A6 This assumption allows to represent cell migration and proliferation phenomena to other membrane domains (in this case, domain 5).

Assumptions for the membrane's sealant layer

To represent the dynamic behavior of the PVA-sealant layer (domain 5) due to possible cell growth, different modeling strategies can be proposed. First, if migration begins to occur from the immobilized bioactive layer into the PVA-sealant layer, the model can consider that a certain concentration of cells (an "excess" concentration), measured in a certain coordinate, can migrate to nearby positions. When this occurs, then the domain switches into a bioactive state (considering a respective change of the mass balance models).

An analogous alternative is that the "excess" cell concentration is distributed within the complete PVA domain and the latter switches into a bioactive state. For this case, it could be also logical to measure the "excess" cell concentration in the function of the whole immobilized bioactive layer volume.

Moreover, a combination of alternative 1 and 2 could be applied, considering cell distribution in the adjacent domain at the beginning of its bioactive state and migration to nearby positions from this moment onwards.

Another alternative can consider that, if the PVA layer begins to be populated, the PVA layer can be subdivided into two domains with moving boundaries, i.e., one to represent a new and growing bioactive layer (next to the immobilized cell layer) and a decreasing inert fraction (next to the mixed liquor) until space is completely populated with cells. This strategy considers the respective mass balance model according to the domain's active or inactive state. The new bioactive layer's volume could be determined by using a relationship similar to the solution dilution equation, and "excess" cell concentration could be homogeneously distributed within this volume. Then, the criterion that compares the biomass concentration with the maximum cell capacity is used iteratively to describe that excess cell concentration grows in an adjacent volume fraction, thus, allowing to simulate the moving boundary layer. Instead of modeling several newly formed domains, each with fixed boundary conditions, this alternative considers a new bioactive layers that can be jointly modeled with the initially immobilized cell layer and having only one single bioactive layer with a moving boundary condition at r_4.

Based on phenomenological representativeness and model simplicity, we decided to use the combination of the first and second strategy to describe the cell migration behavior.

The assumptions for the mass balance equations depend on the sealant layer's condition. During initial operation, the sealant layer is in an inactive state (no cells are present and no reaction occurs). After longer periods of operation, cells begin to grow within the sealant layer,

being this moment defined as t_{crit} [63, 78].

The following assumptions are taken:

1. The assumptions considered for the hollow-fiber layer will be valid during the initial operation (between t_0 and t_{crit}).
2. After t_{crit}, the layer will switch into an active state (metabolic-related reactions occur). Thus, the assumptions considered for the immobilized cell layer will be valid during longer operation periods.
3. The modeling considers cell growth breakthrough (t_{crit}) when cells begin to not only grow within the immobilized cell layer but also the sealant layer [63, 78]. t_{crit} is the moment when cell concentration within the immobilized cell layer volume near the membrane interface (immobilized layer/ PVA-sealant layer) surpasses the maximum cell capacity for the first time. Then, the excess cell concentration will be added to an adjacent position (measured for the next time point) of the PVA layer (a similar approach to the one described for the immobilized cell layer).

The explanation for each assumption is provided below:

A1 This assumption is to facilitate the management of dynamic behavior for modeling purposes. As initially designed, the PVA-sealant layer should not have inoculated cells. Therefore, it acts as an inert.

A2 This assumption is to facilitate the management of dynamic behavior for modeling purposes. The PVA-sealant layer's characteristics are appropriate for cell growth.

A3 This assumption is to facilitate the management of dynamic behavior for modeling purposes. Consequently, mass balance equations within the model change to represent bioactive phenomena. Moreover, it can be of interest to know when the PVA-sealant layer begins to be populated with cells.

Annex I

Auxiliary models

This annex presents the detailed procedure to obtain the transport model.

I.1. Transport model

Mass transfer, flow phenomena, and pressure drop data are of major importance for bioreactor applications. The following calculation memory explains the procedure to obtain the transport model for the lumen side, mixed liquor, and multi-layer membrane.

Assumptions:

1. The mass transfer does not significantly affect the flow conditions through the membrane [69].
2. Each fiber's outer border can be represented as a square, neglecting the triangular voids between the fiber and square (Fig. I.1).
3. The CBMem fiber model can be described by the equations related to zone 2, independent of the θ-coordinate.

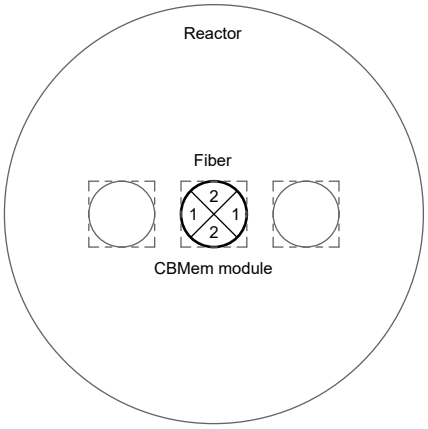

Fig. I.1: Schematic representations of the parallel array of the fibers and defined zones

The explanation for each assumption is provided below:

A1 This is a common assumption for model development. Considering the operating conditions, the mass transfer can be treated separately from the momentum transfer [69].

A2 Zone definition is for model simplification. Zone 1 defines the region adjacent to another fiber, whereas zone 2 defines the region that does not have a fiber next to it.

A3 This is because zone 2 is more incident in fluid flows.

I.1.1. Transport model for the lumen side

The following section details the transport model development for the lumen side (Fig. I.2). N.b. that the numeric abbreviation for the lumen side is (1); therefore, it will be used as a subscript to relate a variable or parameter to this domain.

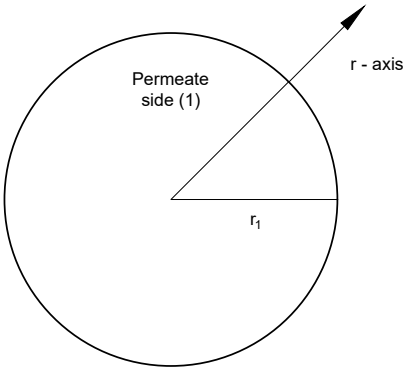

Fig. I.2: Schematic representations of the lumen side.

Assumptions

The model follows these assumptions:

1. The flow in the lumen side is in steady state [92].
2. The flow is incompressible and viscous [228].
3. The system is isothermal.
4. The flow is laminar and the entrance effects can be ignored [92].
5. The flow is axisymmetric, i.e., the substrate flows only in axial and radial directions.
6. Newtonian fluid: density and viscosity are constant.
7. The effect of gravity is negligible for gases.
8. The inertial terms are negligible [229, 230].
9. Axial stress effects are negligible [92].

The explanation for each assumption is provided below:

A1 The reactor is a continuous-flow reactor and the membrane is located at the reactor's center, where dead volume is not perceived. Moreover, the reactor is controlled to maintain the operating conditions constant. Thus, the pressure equation does not express the accumulation term, and time dependence through this term is neglected.

A2 Substantial density fluctuations are important for gas flow at high velocities. Therefore, Asm. (2) is only suitable for fluid flow velocities that are small compared to the speed of sound of the respective phase [228], i.e., Ma < 0.3. In the case of the CBMem reactor, this condition is fulfilled (Ma is less than 0.036).

A3 Heat transfer is low as the reactor operates at ambient temperature. Thus, the temperature will not affect pressure [69].

A4 The fluid flow is held at a low rate, which sustains laminar flow [63]. Moreover, neglecting entrance effects is a common assumption to simplify model development [92].

A5 This assumption is due to the cylindrical reactor shape. The influence of the CBMem module on the flow is neglected for simplifications.

A6 This is a common assumption for model simplification. Moreover, no substantial changes in density or viscosity are expected.

A7 This assumption is self-explanatory.

A8 This assumption is valid if the radial Reynolds number is much less than 1 [231]. This condition is satisfied in almost all hollow-fiber bioreactor applications [92].

A9 This assumption considers that the axial stress terms ($\frac{\partial^2 v_z}{\partial z^2}$) are not as important as shear stresses and are negligible when the ratio of the hollow-fiber ($\frac{r_1}{L}$) is less than 10^{-2}, which is valid for most viscous flows [92]. In the case of the CBMem reactor, this condition is fulfilled (the ratio is $1.75{\cdot}10^{-3}$).

Model development

On the one hand, the equation of continuity (conservation of mass) in a cylindrical coordinate system [226], is shown in Eq. (I.1).

$$\frac{\partial \rho}{\partial t} = -\left[\frac{1}{r}\frac{\partial}{\partial r}(r\rho v_r) + \frac{1}{r}\frac{\partial}{\partial \theta}(\rho v_\theta) + \frac{\partial}{\partial z}(\rho v_z)\right] \tag{I.1}$$

Considering Asm. (1)-(5) the equation is simplified into Eq. (I.2).

$$\frac{1}{r}\frac{\partial}{\partial r}(r v_r) + \frac{\partial v_z}{\partial z} = 0 \tag{I.2}$$

On the other hand, considering cylindrical coordinates and Asm. (6), the momentum conservation equation can be written as shown in Eqs. (I.3), (I.4) and (I.5) for the r-, θ and z-coordinate, respectively [226].

$$\begin{aligned}\rho\left(\frac{\partial v_r}{\partial t} + v_r\frac{\partial v_r}{\partial r} + \frac{v_\theta}{r}\frac{\partial v_r}{\partial \theta} + v_z\frac{\partial v_r}{\partial z} - \frac{v_\theta^2}{r}\right) = &-\frac{\partial P}{\partial r} + \mu\left[\frac{\partial}{\partial r}\left(\frac{1}{r}\frac{\partial}{\partial r}(r v_r)\right) + \frac{1}{r^2}\frac{\partial^2 v_r}{\partial \theta^2}\right.\\ &\left.+\frac{\partial^2 v_r}{\partial z^2} - \frac{2}{r^2}\frac{\partial v_\theta}{\partial \theta}\right] + \rho g_r\end{aligned} \tag{I.3}$$

$$\begin{aligned}\rho\left(\frac{\partial v_\theta}{\partial t} + v_r\frac{\partial v_\theta}{\partial r} + \frac{v_\theta}{r}\frac{\partial v_\theta}{\partial \theta} + v_z\frac{\partial v_\theta}{\partial z} + \frac{v_r v_\theta}{r}\right) = &-\frac{1}{r}\frac{\partial P}{\partial \theta} + \mu\left[\frac{\partial}{\partial r}\left(\frac{1}{r}\frac{\partial}{\partial r}(r v_\theta)\right) + \frac{1}{r^2}\frac{\partial^2 v_\theta}{\partial \theta^2}\right.\\ &\left.+\frac{\partial^2 v_\theta}{\partial z^2} + \frac{2}{r^2}\frac{\partial v_r}{\partial \theta}\right] + \rho g_\theta\end{aligned} \tag{I.4}$$

$$\begin{aligned}\rho\left(\frac{\partial v_z}{\partial t} + v_r\frac{\partial v_z}{\partial r} + \frac{v_\theta}{r}\frac{\partial v_z}{\partial \theta} + v_z\frac{\partial v_z}{\partial z}\right) = &-\frac{\partial P}{\partial z} + \mu\left[\frac{1}{r}\frac{\partial}{\partial r}\left(r\frac{\partial v_z}{\partial r}\right) + \frac{1}{r^2}\frac{\partial^2 v_z}{\partial \theta^2} + \frac{\partial^2 v_z}{\partial z^2}\right]\\ &+\rho g_z\end{aligned} \tag{I.5}$$

Considering Asm. (1)-(5), the momentum conservation equation for the r- and z-coordinate can be written as shown in Eqs. (I.6) and (I.7), respectively.

$$\rho\left(v_r\frac{\partial v_r}{\partial r} + v_z\frac{\partial v_r}{\partial z}\right) = -\frac{\partial P}{\partial r} + \mu\left[\frac{1}{r}\frac{\partial}{\partial r}\left(r\frac{\partial v_r}{\partial r}\right) - \frac{v_r}{r^2} + \frac{\partial^2 v_r}{\partial z^2}\right] + \rho g_r \tag{I.6}$$

$$\rho\left(v_r\frac{\partial v_z}{\partial r} + v_z\frac{\partial v_z}{\partial z}\right) = -\frac{\partial P}{\partial z} + \mu\left[\frac{1}{r}\frac{\partial}{\partial r}\left(r\frac{\partial v_z}{\partial r}\right) + \frac{\partial^2 v_z}{\partial z^2}\right] + \rho g_z \tag{I.7}$$

Note that the previous expressions consider the following equivalence:

$$\frac{\partial}{\partial r}\left(\frac{1}{r}\frac{\partial}{\partial r}(rv_r)\right) = \frac{1}{r}\frac{\partial}{\partial r}\left(r\frac{\partial v_r}{\partial r}\right) - \frac{v_r}{r^2} \tag{I.8}$$

The momentum conservation equation can further be simplified by considering Asm. (7)-(9). This results in Eq. (I.9).

$$\mu\left[\frac{1}{r}\frac{\partial}{\partial r}\left(r\frac{\partial v_z}{\partial r}\right)\right] = \frac{\partial P}{\partial z} \tag{I.9}$$

The axial convective velocity can be determined from Eq. (I.9). Its general solution is:

$$v_{z,1} = \frac{r^2}{4\mu}\frac{dP_1}{dz} + k_1 ln(r) + k_2 \tag{I.10}$$

The boundary conditions to be used are [232]:

$$\begin{cases} \dfrac{\partial v_z}{\partial r} = 0 & \text{at } r = 0 \quad \text{(I.11a)} \\ v_z = 0 & \text{at } r = r_1 \quad \text{(I.11b)} \end{cases}$$

Consequently, the following axial flow rate for the lumen side (gas phase) is obtained [226]:

$$v_{z,1} = -\frac{r_1^2}{4\mu_g}\left(1 - \frac{r^2}{r_1^2}\right)\frac{dP_1}{dz} \tag{I.12}$$

To obtain the radial velocity profiles, Eq. (I.12) has to be differentiated as a function of z.

$$\frac{d}{dz}(v_{z,1}) = -\frac{r_1^2}{4\mu}\left(1 - \frac{r^2}{r_1^2}\right)\frac{d^2P_1}{dz^2} \tag{I.13}$$

By substituting the expression in the continuity equation (Eq. (I.2)), the following equation is obtained:

$$\frac{1}{r}\frac{\partial}{\partial r}(rv_r) - \frac{r_1^2}{4\mu}\left[1 - \left(\frac{r}{r_1}\right)^2\right]\frac{d^2P_1}{dz^2} = 0 \tag{I.14}$$

The general solution is:

$$v_{r,1} = \frac{k_1}{r} - \frac{r(r^2 - 2r_1^2)}{16\mu}\frac{d^2P_1}{dz^2} \tag{I.15}$$

Due to the symmetry, the boundary condition to be used is:

$$\{v_r = 0 \quad \text{at } r = 0 \tag{I.16}$$

Then, the radial lumen velocity (gas phase) will be as:

$$v_{r,1} = -\frac{r(r^2 - 2r_1^2)}{16\mu_g}\frac{d^2P_1}{dz^2} \tag{I.17}$$

Another option for the velocity profile in the lumen is to assume constant velocity regarding the axial position. For this, the equation of a velocity profile of a fluid in a straight circular pipe can be considered. The parameter $k_{v,1}$ can be adjusted to respond to the expected profile for a laminar o turbulent flow.

$$v_{z,1} = v_{in}(1 - \frac{r}{r_1})^{k_{v,1}} \tag{I.18}$$

I.1.2. Transport model for the mixed liquor

The following section details the development of the transport model for the mixed liquor (Fig. I.3). N.b. that the numeric abbreviation for the mixed liquor is (6); therefore, it will be used as a subscript to relate a variable or parameter to this domain.

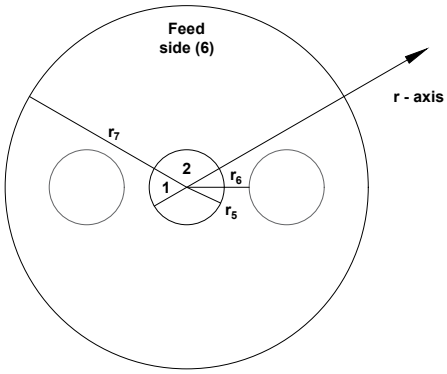

Fig. I.3: Schematic representations of the mixed liquor side.

Assumptions

The mixed liquor model considers the same assumptions of the lumen side model (see section I.1.1), except for Asm. (7), as this is not suitable for liquids in a vertically oriented bioreactor; the effect of the hydrostatic pressure change (in this case $P_{tot} = P - \rho g z$ with $g = 9.807[\frac{m^2}{s}]$) has to be taken into account [233].

Model development

Equally to the lumen side model, the simplified continuity equation is obtained (Eq. (I.19)).

$$\frac{1}{r}\frac{\partial}{\partial r}(rv_r) + \frac{\partial v_z}{\partial z} = 0 \tag{I.19}$$

The momentum equation, considering the gravitational effect, results in Eq. (I.20).

$$\mu\left[\frac{1}{r}\frac{\partial}{\partial r}\left(r\frac{\partial v_z}{\partial r}\right)\right] = \frac{\partial P}{\partial z} - \rho g \tag{I.20}$$

The axial convective velocity can be determined from Eq. (I.20). Its general solution is:

$$v_{z,6} = \frac{r^2}{4\mu}\left(\frac{dP_6}{dz} - \rho g\right) + k_1 ln(r) + k_2 \tag{I.21}$$

The boundary conditions to be used are:

$$\begin{cases} v_z = 0 & \text{at } r = r_5 \quad \text{(I.22a)} \\ v_z = 0 & \text{at } r = r_7 \quad \text{(I.22b)} \end{cases}$$

Consequently, the following axial flow rate for the mixed liquor is obtained:

$$v_{z,6} = \frac{\varepsilon}{4\mu_w}\left(\frac{dP_6}{dz} - \rho g\right) \tag{I.23}$$

$$\varepsilon = \frac{(r^2 - r_7^2)ln(r_5) + (r_5^2 - r^2)ln(r_7) + (r_7^2 - r_5^2)ln(r)}{ln(r_5) - ln(r_7)} \tag{I.24}$$

To obtain the radial velocity profiles, Eq. (I.23) has to be differentiated as a function of z.

$$\frac{d}{dz}(v_{z,6}) = \frac{\varepsilon}{4\mu_w}\frac{d^2P_6}{dz^2} \tag{I.25}$$

By substituting the expression in the continuity equation (Eq. (I.19)), the following equation is obtained:

$$\frac{1}{r}\frac{\partial}{\partial r}(rv_r) + \frac{\varepsilon}{4\mu_w}\frac{d^2P_6}{dz^2} = 0 \tag{I.26}$$

The general solution is: The general solution is:

$$\begin{aligned} v_{r,6} = &-r\frac{ln(r_5)r^2 - 2ln(r_5)r_7^2 - ln(r_7)r^2 + 2ln(r_7)r_5^2 + r_5^2 - r_7^2}{16\mu[ln(r_5) - ln(r_7)]}\frac{d^2P_6}{dz^2} \\ &- r\frac{2ln(r)r_7^2 - 2ln(r)r_5^2}{16\mu[ln(r_5) - ln(r_7)]}\frac{d^2P_6}{dz^2} + \frac{k_1}{r} \end{aligned} \tag{I.27}$$

Due to the symmetry, the boundary condition to be used is:

$$\{v_r = 0 \quad \text{at } r = r_5 + \frac{(r_7 - r_5)}{2} \tag{I.28}$$

Then, the radial mixed liquor velocity (liquid phase) will be as:

$$v_{r,6} = -\frac{\zeta}{16\mu_w r}\frac{d^2P_6}{dz^2} \tag{I.29}$$

$$\begin{aligned} \zeta = &\frac{1}{ln(r_7) - ln(r_5)}\left(\frac{r_5 + r_7}{2}\right)^2\left[ln(r_5)\left(\frac{r_5 + r_7}{2}\right)^2 - 2ln(r_5)r_7^2 - ln(r_7)\left(\frac{r_5 + r_7}{2}\right)^2\right. \\ &\left.+2ln(r_7)r_5^2 - 2ln\left(\frac{r_5 + r_7}{2}\right)r_5^2 + 2ln\left(\frac{r_5 + r_7}{2}\right)r_7^2 + r_5^2 - r_7^2\right] \\ &- \frac{r^2}{ln(r_7) - ln(r_5)}\left[ln(r_5)r^2 - 2r_7^2ln(r_5) - r^2ln(r_7) + 2r_5^2ln(r_7) - 2r_5^2ln(r)\right. \\ &\left.+2r_7^2ln(r) + r_5^2 - r_7^2\right] \end{aligned} \tag{I.30}$$

I.1.3. Transport model for the multi-layer membrane

The following section details the development of the transport model for the multi-layer membrane (Fig. I.4). N.b. that the abbreviation for the membrane is (M); therefore, it will be used as a subscript to relate a variable or parameter to this domain.

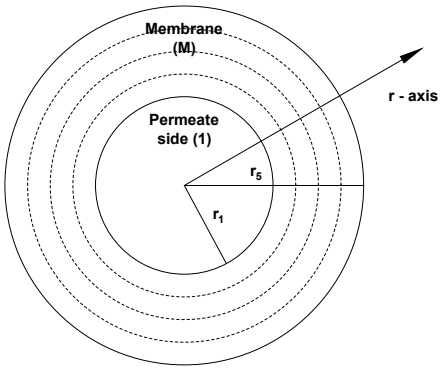

Fig. I.4: Schematic representations of the membrane.

Assumptions

The model follows these assumptions:

1. The membrane is relatively impermeable, i.e., it is the main resistance to flow [69].
2. Axial pressure gradient within the membrane is negligible compared to the radial pressure gradient [69].
3. The radial pressure drop in the membrane matrix is very small compared to that in the membrane's skin. Thus, $P_M(z) \approx P_6(z)$ (subscript "6" denotes the mixed liquor).
4. The mixed liquor pressure (P_6) is greater than the lumen pressure (P_1).
5. Darcy's law for the membrane flow can be applied [69].
6. The fluid viscosity in Darcy's law is equal to the viscosity of water and remains constant during the process, neglecting the influence of other species on its value.

The explanation for each assumption is provided below:

A1 This is true for membrane separations that involve low convective velocity in radial direction.

A2 This phenomenon is usually observed in membrane-based separation processes [69].

A3 This is because the pores in the ultrathin skin are several orders of magnitude smaller than those in the spongy matrix [69].

A4 This is due to the membrane operation [63].

A5 This is a common consideration for flow modeling through membranes as it describes the flux dependency on pressure drop [69].

A6 This assumption is to assimilate water characteristics to the wastewater feed. It is expected that the feed has similar properties.

Model development

Considering Asm. (1) and (2), the axial velocity profile is negligible, i.e.:

$$v_{z,M} = 0 \tag{I.31}$$

Considering Asm. (1), the continuity equation to be solved is shown in Eq. (I.32).

$$\frac{1}{r}\frac{\partial}{\partial r}\left(rv_r\right) = 0 \tag{I.32}$$

The flow through the membrane is proportional to the transmembrane pressure drop and inversely proportional to the fluid viscosity [69]. Thus, considering Asm. (2), (3), and (6), Darcy's law can be applied, which is defined by Eq. (I.33). N.b. the flow will occur from high pressure towards low pressure, opposite the direction of the increasing pressure gradient, hence the negative sign [234].

$$q_M = -\frac{\kappa}{\mu_w}\frac{dP_M}{dr} \tag{I.33}$$

The radial convective velocity in the membrane is related to the Darcy flux by the porosity (Eq. (I.34)).

$$v_M = -\frac{\kappa}{\epsilon\mu_w}\frac{dP_M}{dr} \tag{I.34}$$

Then, combining Eqs. (I.32) and (I.34), Eq. (I.35) is obtained.

$$\frac{1}{r}\frac{d}{dr}\left(r\frac{dP_M}{dr}\right) = 0 \tag{I.35}$$

The general solution of Eq. (I.35) is:

$$P_M = k_1 + k_2 ln(r) \tag{I.36}$$

Due to Asm. (3), the boundary conditions to be used are [69]:

$$\begin{cases} P_M = P_1 & \text{at } r = r_1 \quad \text{(I.37a)} \\ P_M = P_6 & \text{at } r = r_5 \quad \text{(I.37b)} \end{cases}$$

Consequently, the following membrane pressure is obtained:

$$P_M(r,z) = \frac{P_6 ln(r_1) - P_1 ln(r_5) + (P_1 - P_6) ln(r)}{ln(r_1) - ln(r_5)} \tag{I.38}$$

To obtain the radial velocity profile, Eq. (I.38) has to be differentiated as a function of r.

$$\frac{dP_M}{dr} = \frac{P_1 - P_6}{ln(r_1) - ln(r_5)}\frac{1}{r} \tag{I.39}$$

By substituting the obtained expression in Eq. (I.34), the radial convective velocity distribution within the membrane is obtained (Eq. (I.40)). By assuming that $P_6 > P_1$ (Asm. (4)) and considering that $r_5 > r_1$, the negative sign of Eq. (I.34) indicates that the flow will be in the negative r direction (from higher to lower pressure) [234].

$$v_M(r,z) = -\frac{\kappa}{\epsilon\mu_w}\frac{P_1 - P_6}{ln(r_1) - ln(r_5)}\frac{1}{r} \tag{I.40}$$

I.2. Pressure model

The following section details the model development of the axial pressure gradient for the lumen and mixed liquor side so that the transport model for the CBMem fiber can be described completely. N.b. that the numeric abbreviations for the lumen and mixed liquor are (1) and (6), respectively; therefore, they will be used as subscripts to relate a variable or parameter to the domains.

There are two possible model strategies for the axial pressure gradient:

1. To develop a model based on theory.
2. To impose a model based on the quality of the velocity profiles.

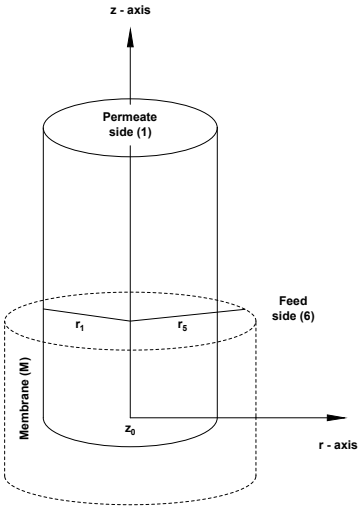

Fig. I.5: Schematic representations of a CBMem fiber, focusing on z-axis.

This section explains both strategies for illustrative purposes. The first strategy relies on the boundary conditions shown in Eq. (I.41a) and (I.41b). Note that the sense of velocities has to be consistent.

$$\begin{cases} v_{r,M} = v_{r,1} \quad \text{at } r = r_1 & \text{(I.41a)} \\ -v_{r,6} = v_{r,M}\dfrac{r_1}{r_5} \quad \text{at } r = r_5 & \text{(I.41b)} \end{cases}$$

With these, the expressions for $\frac{d^2P_1}{dz^2}$ and $\frac{d^2P_6}{dz^2}$ can be obtained. Then, the equation found for $\frac{d^2P_1}{dz^2}$ can be differentiated twice and the equation found for $\frac{d^2P_6}{dz^2}$ can be rewritten as a function of $\frac{d^2P_1}{dz^2}$. The combination of the resulting equations delivers a fourth-order differential equation for the lumen side [92] as shown below:

$$\frac{d^4P_1}{dz^4} - \lambda^2\frac{d^2P_1}{dz^2} = 0 \tag{I.42}$$

$$\lambda = \sqrt{-\frac{16\kappa}{r_1^4\epsilon}\frac{1}{ln(r_1)-ln(r_5)}\left(1 - r_1^4\frac{r_1}{r_5}\frac{1}{\chi}\right)} \tag{I.43}$$

$$\begin{aligned}\chi = \frac{1}{ln(r_7)-ln(r_5)}\left(\frac{r_5+r_7}{2}\right)^2\Bigg[&ln(r_5)\left(\frac{r_5+r_7}{2}\right)^2 - 2ln(r_5)r_7^2 - ln(r_7)\left(\frac{r_5+r_7}{2}\right)^2 \\ &+2ln(r_7)r_5^2 - 2ln\left(\frac{r_5+r_7}{2}\right)r_5^2 + 2ln\left(\frac{r_5+r_7}{2}\right)r_7^2 + r_5^2 - r_7^2\Bigg] \\ &- \frac{r_5^2}{ln(r_7)-ln(r_5)}\left[-ln(r_5)r_5^2 + r_5^2ln(r_7) + r_5^2 - r_7^2\right]\end{aligned} \tag{I.44}$$

The general solution of Eq. (I.42) is:

$$P_1 = k_1 + k_2 z + k_3 e^{\lambda z} + k_4 e^{-\lambda z} \tag{I.45}$$

By differentiating Eq. (I.45) twice, the following equations are obtained:

$$\frac{dP_1}{dz} = k_2 + k_3 \lambda e^{\lambda z} - k_4 \lambda e^{-\lambda z} \tag{I.46}$$

$$\frac{d^2 P_1}{dz^2} = k_3 \lambda^2 e^{\lambda z} + k_4 \lambda^2 e^{-\lambda z} \tag{I.47}$$

By substituting the resulting expression as well as Eq. (I.45) in the expressions of $\frac{d^2 P_1}{dz^2}$ (found with the boundary condition), the pressure gradient in the mixed liquor can also be given:

$$P_6 = k_1 + k_2 z + \varphi k_3 e^{\lambda z} + \varphi k_4 e^{-\lambda z} \tag{I.48}$$

$$\varphi = 1 + \frac{r_1^4 \epsilon}{16\kappa} \left[ln(r_1) - ln(r_5) \right] \lambda^2 \tag{I.49}$$

Its differential equations are represented by the following equations:

$$\frac{dP_6}{dz} = k_2 + \varphi \lambda k_3 e^{\lambda z} - \varphi \lambda k_4 e^{-\lambda z} \tag{I.50}$$

$$\frac{d^2 P_6}{dz^2} = \varphi \lambda^2 k_3 e^{\lambda z} + \varphi \lambda^2 k_4 e^{-\lambda z} \tag{I.51}$$

To determine the integration constants, four boundary conditions are required. These are specific to the flow configuration of the hollow-fibers [235], and their use results in a system of four linear equations and four unknowns (k_1, k_2, k_3, k_4), which can be solved using Cramer's rules [236]. However, it is not easy to find suitable boundary conditions. Moreover, the pressure model supports the transport model, which in turn aids the component mass balance. The latter is of most importance to accurately describe the species' concentration distribution. In addition, as observed in previous experimentation [63], the pressure decrease within the fluids is negligible. Thus, the second proposed strategy is chosen to simplify the pressures' modeling without undermining representativeness.

Assumptions

The model follows these assumptions:

1. The pressure models can be described as a modified linear equation in the function of the entry and outlet pressures of the fluid domain and the fiber length, and an additional term in the function of the square of the axial position to allow an expression for the second derivative of the pressure model, which is required to express the radial velocity profiles.

2. The unknown parameters will be calibrated based on the quality of the velocity profiles.

Model development

Through Asm. (1) and (2), the pressure profiles and their derivatives for the lumen side are represented by Eqs. (I.52)-(I.54). Analogously, Eqs. (I.55)-(I.57) apply for the mixed liquor.

$$P_1 = P_{1,z0} + k_{1,P1}\frac{P_{1,zf} - P_{1,z0}}{z_f - z_0}z + k_{2,P1}z^2 \tag{I.52}$$

$$\frac{dP_1}{dz} = k_{1,P1}\frac{P_{1,zf} - P_{1,z0}}{z_f - z_0} + k_{2,P1}z \tag{I.53}$$

$$\frac{d^2P_1}{dz^2} = k_{2,P1} \tag{I.54}$$

$$P_6 = P_{6,z0} + k_{1,P6}\frac{P_{6,zf} - P_{6,z0}}{z_f - z_0}z + k_{2,P6}z^2 \tag{I.55}$$

$$\frac{dP_6}{dz} = k_{1,P6}\frac{P_{6,zf} - P_{6,z0}}{z_f - z_0} + k_{2,P6}z \tag{I.56}$$

$$\frac{d^2P_6}{dz^2} = k_{2,P6} \tag{I.57}$$

I.3. Biokinetic model development

This annex details the biokinetic model that is used as an auxiliary model to describe the mass balance of the CBMem's bioactive layers.

Assumptions

The following assumptions are taken:

1. Cell culture is held under controlled conditions using *Clostridia sp.* as single species.
2. Monod-based kinetics can describe the biochemical reactions related to the dark fermentation process [59].
3. Nongrowth-associated product formation rates is negligible.
4. The cells are in the exponential phase, i.e., the growth rate is higher than the decay rate. Moreover, product formation is associated with cell population growth.
5. The substrate concentration is measured as COD. It is also assumed that the reaction has one rate-limiting substrate.
6. Non-competitive inhibition function is considered for H_2 regulation [37] and described by a simplified Han-Levenspiel inhibition term in the function of the H_2 saturation concentration [54, 93].
7. Another non-competitive inhibition function is considered to regulate H_2 concentration and described by a modified Monod inhibition term in the function of its critical inhibitory concentration [54, 94].
8. Cell growth is inhibited by its concentration due to space competition; thus, a maximum cell capacity is considered.
9. Besides the H_2 partial pressure, no other inhibition phenomena due to other species (e.g., products or substrates) exist.

The explanation for each assumption is provided below:

A1 Even though other species can exist in the cell culture, this is being avoided due to pretreatment (see Annex G). However, this assumption could be strong if ideal conditions are not met during cell immobilization or feed supply [63].

A2 Monod-based kinetics are widely used for bioreactor modeling as they can fit most experimental data. They have even been used to define the reaction rates of the dark fermentation process. Moreover, Monod model is simple and easy to adapt [59]. However, it does not have physicochemical support to describe cell growth as it is an adaption of the Michaelis-Menten mechanism, which has been developed for enzymatic systems.

A3 This assumption is considered to simplify the species considered in the model. The relevant species involve hydrogen, cells, and substrate [63].

A4 It is preferable to maintain the *Clostridia sp.* in the exponential phase [52]. This is because H_2 and VFA production are maximal during the exponential growth phase. In turn, alcohol production occurs mainly at the stationary growth phase [151]. The control of the HRT allows the maintenance of cells at a certain growth phase (see Annex B.2.2).

A5 As the substrate can be of different substances contained in the wastewater [91], the substrate concentration can be measured as COD[6].

A6 This consideration has been used in other studies to represent inhibition phenomena during dark fermentation [37, 54, 93]. This allows for a decrease in the H_2 production rate when the H_2 concentration approaches the saturation concentration. This maintains the coherence of concentration magnitudes as saturation is observed on the mixed liquor side.

A7 This consideration has been used in other studies to represent inhibition phenomena during dark fermentation [54, 94]. This allows for a decrease in the H_2 production rate when the H_2 concentration approaches the critical value.

A8 This allows simulating the cell growth phenomena and its requirements. The maximum cell capacity has also been described in other studies to model the effective diffusivity.

A9 This is to simplify cell metabolism representation for the CBMem modeling. However, other by-products could inhibit hydrogen production.

Model development

The reaction kinetics for the exponential phase are expressed as:

$$Y_{S/X}S \rightarrow X + Y_{P/X}P \tag{I.58}$$

$$X \rightarrow X_{dead} \tag{I.59}$$

$$S \rightarrow M \tag{I.60}$$

[6] The biochemical oxygen demand (BOD) would be an appropriate unit as it represents the amount of oxygen microorganisms require to break down organic materials [91]. However, the chemical oxygen demand (COD), which represents the amount of oxygen required to break down the organic material via oxidation, is widely used as a wastewater characterization measure in concentrated streams and for upstream and gas utilization industries [37].

Monod kinetics involve the expressions shown in Eqs. (I.61) and (I.62) for substrate consumption and cell growth [54, 69, 76, 230, 237] [59]. Moreover, using Asm. (3), Eq. (I.63) can be used to describe the growth-associated H_2 production rate. Considering single substrate (Asm. 5) and a single microorganism (Asm. 1), the specific rates highlight that substrate uptake leads to growth, maintenance, and product formation [54].

$$\hat{r}_S = -\frac{\hat{r}_{Xg}}{Y_{X/S}} - k_m C_X \tag{I.61}$$

$$\hat{r}_{Xg} = \mu_{max} \frac{C_S C_X}{K_S + C_S} \tag{I.62}$$

$$\hat{r}_P = \frac{\hat{r}_{Xg}}{Y_{X/P}} \tag{I.63}$$

Moreover, as described in Annex B.2.2, the partial pressure can inhibit the H_2 production. By considering Asm. (7), (6), and (9), Eq. (I.63) should consider inhibition phenomena as shown in Eq. (I.64):

$$\hat{r}_{IP} = \hat{r}_P I_P \tag{I.64}$$

$$I_P = \left(1 - \frac{C_P}{C_{P,sat}}\right)^n \left(\frac{C_{P,crit}}{C_P + C_{H,crit}}\right) \tag{I.65}$$

In addition, to accurately describe cell mass balance, the net production rate, shown in Eq. (I.66), has to be considered, which includes both growth (Eq. (I.62)) and decay rates (Eq. (I.67)) [94, 238].

$$\hat{r}_X = \hat{r}_{Xg} - \hat{r}_{dec} \tag{I.66}$$

$$\hat{r}_{dec} = k_{dec} C_X \tag{I.67}$$

Also, by considering Asm. (8), Eq. (I.66) should consider inhibition phenomena as shown in Eq. (I.68):

$$\hat{r}_{IX} = \hat{r}_X I_X \tag{I.68}$$

$$I_X = \left(1 - \frac{C_{X,d}}{C_{X,max}}\right) \tag{I.69}$$

In summary, the following reaction rates are suitable to describe the generation/ consumption term of the mass balances:

$$\hat{r}_S = -\frac{\mu_{max}}{Y_{X/S}} \cdot \frac{C_S C_X}{K_S + C_S} - k_m C_X \tag{I.70}$$

$$\hat{r}_X = \left(\mu_{max} \frac{C_S C_X}{K_S + C_S} - k_{dec} C_X\right) \left(1 - \frac{C_{X,d}}{C_{X,max}}\right) \tag{I.71}$$

$$\hat{r}_H = \frac{\mu_{max}}{Y_{X/H}} \frac{C_S C_X}{K_S + C_S} \left(1 - \frac{C_H}{C_{H,sat}}\right)^n \left(\frac{C_{H,crit}}{C_H + C_{H,crit}}\right) \tag{I.72}$$

Where, due to Asm. (5), S represents COD. Note that the units of the yield coefficients of biomass on substrate ($Y_{X/S}$) and biomass on product ($Y_{X/H}$) are [g cells/g substrate] and [g cells/g hydrogen], respectively.

Annex J

Discretized multi-domain fiber model

This annex presents the discretized model used for implementation. Table J.1 shows a summary of the discretized model equations and boundary conditions to describe the fluid domains and inactive membrane domains, while Table J.2 presents the same information for the bioactive membrane domains.

Table J.1: Summary of the model equations and boundary conditions to describe the inactive membrane and fluid domains of the multi-domain fiber model.

Model	Domain	Species	Discretized equation	Discretized boundary condition
Fluid phase	6	S	$C_{S,6}(i,j+1,k) = D_{S,6}\frac{1}{r}\frac{\Delta z}{v_{z,6}}\frac{C_{S,6}(i+1,j,k)-C_{S,6}(i,j,k)}{\Delta r} + D_{S,6}\frac{\Delta z}{v_{z,6}}\frac{C_{S,6}(i+1,j,k)-2C_{S,6}(i,j,k)+C_{S,6}(i-1,j,k)}{\Delta r^2} + C_{S,6}(i,j,k)$	BC1 $C_{S,6}(i,j,k) = C_{S,6,0} \quad \forall r \in \left[r_{d-1}+\frac{r_{d+1}-r_{d-1}}{2}-\Delta r, r_{d-1}+\frac{r_{d+1}-r_{d-1}}{2}\right]$ *at* $z = z_0$
				$C_{S,6}(i,j,k) = C_{S,6}(i+1,j,k) + \frac{C_{S,6}(i+1,j,k)}{k0_{S,6}} \quad \forall r \in \left[r_{d-1}, r_{d-1}+\frac{r_{d+1}-r_{d-1}}{2}-2\Delta r\right]$ *at* $z = z_0$
				BC2 $C_{S,6}(i,j,k) = C_{S,6}(i-1,j,k) \quad \forall z \setminus z_0$ *at* $r = r_{d-1}+\frac{r_{d+1}-r_{d-1}}{2}$
				BC3 $C_{S,6}(i,j) = k1_{S,6}C_{S,6}(i+1,j,k) + k2_{S,6}C_{S,6}(i,j-1,k) \quad \forall z \setminus z_0$ *at* $r = r_{d-1}$ *and* $t = t_0$
				$C_{S,6}(i,j) = \frac{1}{3}(k1_{S,6}C_{S,6}(i+1,j,k) + k2_{S,6}C_{S,6}(i,j-1,k) + (k3_{S,6}t + C_{S,6}(i,j,k-1))) \quad \forall z \setminus z_0, \forall t \setminus t_0$ *at* $r = r_{d-1}$
		H	$C_{H,6}(i,j+1,k) = D_{H,6}\frac{1}{r}\frac{\Delta z}{v_{z,6}}\frac{C_{H,6}(i+1,j,k)-C_{H,6}(i,j,k)}{\Delta r} + D_{H,6}\frac{\Delta z}{v_{z,6}}\frac{C_{H,6}(i+1,j,k)-2C_{H,6}(i,j,k)+C_{H,6}(i-1,j,k)}{\Delta r^2} + C_{H,6}(i,j,k)$	BC1 $C_{H,6}(i,j,k) = C_{H,6,0} \quad \forall r \in \left[r_{d-1}+\frac{r_{d+1}-r_{d-1}}{2}-\Delta r, r_{d-1}+\frac{r_{d+1}-r_{d-1}}{2}\right]$ *at* $z = z_0$
				$C_{H,6}(i,j,k) = C_{H,6}(i+1,j,k) + \frac{C_{H,6}(i+1,j,k)}{k0_{H,6}} \quad \forall r \in \left[r_{d-1}, r_{d-1}+\frac{r_{d+1}-r_{d-1}}{2}-2\Delta r\right]$ *at* $z = z_0$
				BC2 $C_{H,6}(i,j,k) = C_{H,6}(i-1,j,k) \quad \forall z \setminus z_0$ *at* $r = r_{d-1}+\frac{r_{d+1}-r_{d-1}}{2}$
				BC3 $C_{H,6}(i,j) = k1_{H6}C_{H,6}(i+1,j,k) + k2_{H,6}C_{H,6}(i,j-1,k) \quad \forall z \setminus z_0$ *at* $r = r_{d-1}$ *and* $t = t_0$
				$C_{H,6}(i,j) = \frac{1}{3}(k1_{H,6}C_{H,6}(i+1,j,k) + k2_{H,6}C_{H,6}(i,j-1,k) + (k3_{H,6}t + C_{H,6}(i,j,k-1))) \quad \forall z \setminus z_0, \forall t \setminus t_0$ *at* $r = r_{d-1}$
		X	$C_{X,6}(i,j+1,k) = D_{X,6}\frac{1}{r}\frac{\Delta z}{v_{z,6}}\frac{C_{X,6}(i+1,j,k)-C_{X,6}(i,j,k)}{\Delta r} + D_{X,6}\frac{\Delta z}{v_{z,6}}\frac{C_{X,6}(i+1,j,k)-2C_{X,6}(i,j,k)+C_{X,6}(i-1,j,k)}{\Delta r^2} + C_{X,6}(i,j,k)$	BC1 $C_{X,6}(i,j,k) = f_0 \quad \forall r \in \left[r_{d-1}, r_{d-1}+\frac{r_{d+1}-r_{d-1}}{2}\right]$ *at* $z = z_0$
				BC2 $C_{X,6}(i,j,k) = C_{X,6}(i-1,j,k) \quad \forall z \setminus z_0$ *at* $r = r_{d-1}+\frac{r_{d+1}-r_{d-1}}{2}$
				BC3 $C_{X,6}(i,j) = f_0 \quad \forall z \setminus z_0, \forall t$ *at* $r = r_{d-1}$
	1	S	$C_{S,1}(i,j+1,k) = D_{S,1}\frac{1}{r}\frac{\Delta z}{v_{z,1}}\frac{C_{S,1}(i+1,j,k)-C_{S,1}(i,j,k)}{\Delta r} + D_{S,1}\frac{\Delta z}{v_{z,1}}\frac{C_{S,1}(i+1,j,k)-2C_{S,1}(i,j,k)+C_{S,1}(i-1,j,k)}{\Delta r^2} + C_{S,1}(i,j,k)$	BC1 $C_{S,1}(i,j,k) = H_0C_{S,2}(1,j,k) \quad \forall z, \forall t$ *at* $r = r_d$
				BC2 $C_{S,1}(i,j,k) = f_0 \quad \forall t \ \forall r \in [0, r_d-\Delta r]$ *, at* $z = z_0$
				BC3 $C_{S,1}(i,j,k) = C_{S,1}(i+1,j,k) \quad \forall z \setminus z_0, \forall t$ *at* $r = r_0$
		H	$C_{H,1}(i,j+1,k) = D_{H,1}\frac{1}{r}\frac{\Delta z}{v_{z,1}}\frac{C_{H,1}(i+1,j,k)-C_{H,1}(i,j,k)}{\Delta r} + D_{H,1}\frac{\Delta z}{v_{z,1}}\frac{C_{H,1}(i+1,j,k)-2C_{H,1}(i,j,k)+C_{H,1}(i-1,j,k)}{\Delta r^2} + C_{H,1}(i,j,k)$	BC1 $C_{H,1}(i,j,k) = H_{1,2}C_{H,2}(1,j,k) \quad \forall z, \forall t$ *at* $r = r_d$
				BC2 $C_{H,1}(i,j,k) = C_{H,1}(i+1,j,k) - \frac{C_{H,1}(i+1,j,k)}{k0_{H,1}} \quad \forall t \ \forall r \in [0, r_d-\Delta r]$ *, at* $z = z_0$
				BC3 $C_{H,1}(i,j,k) = C_{H,1}(i+1,j,k) \quad \forall z \setminus z_0, \forall t$ *at* $r = r_0$
		X	$C_{X,1}(i,j+1,k) = D_{X,1}\frac{1}{r}\frac{\Delta z}{v_{z,1}}\frac{C_{X,1}(i+1,j,k)-C_{X,1}(i,j,k)}{\Delta r} + D_{X,1}\frac{\Delta z}{v_{z,1}}\frac{C_{X,1}(i+1,j,k)-2C_{X,1}(i,j,k)+C_{X,1}(i-1,j,k)}{\Delta r^2} + C_{X,1}(i,j,k)$	BC1 $C_{X,1}(i,j,k) = H_0C_{X,2}(1,j,k) \quad \forall z, \forall t$ *at* $r = r_d$
				BC2 $C_{X,1}(i,j,k) = f_0 \quad \forall t \ \forall r \in [0, r_d-\Delta r]$ *, at* $z = z_0$
				BC3 $C_{X,1}(i,j,k) = C_{X,1}(i+1,j,k) \quad \forall z \setminus z_0, \forall t$ *at* $r = r_0$
Inactive membrane	5	S	$C_{S,5}(i-1,j,k) = \frac{\Delta r^2}{D_{S,5}}\left(-\frac{D_{S,5}}{r}\frac{C_{S,5}(i+1,j,k)-C_{S,5}(i,j,k)}{\Delta r}\right) + 2C_{S,5}(i,j,k) - C_{S,5}(i+1,j,k)$	BC1 $C_{S,5}(i,j,k) = H_{S,5,6}C_{S,6}(1,j,k) \quad \forall z, \forall t$ *at* $r = r_d$
				BC2 $C_{S,5}(i,j,k) = C_{S,5}(i+1,j,k) - \Delta r\left(\frac{-N_{S,5}(i+1,j,k)}{D_{eff,S,5}}\right) \quad \forall z, \forall t$ *at* $r = r_d - \Delta r$
		H	$C_{H,5}(i-1,j,k) = \frac{\Delta r^2}{D_{H,5}}\left(-\frac{D_{H,5}}{r}\frac{C_{H,5}(i+1,j,k)-C_{H,5}(i,j,k)}{\Delta r}\right) + 2C_{H,5}(i,j,k) - C_{H,5}(i+1,j,k)$	BC1 $C_{H,5}(i,j,k) = H_{H,5,6}C_{H,6}(1,j,k) \quad \forall z, \forall t$ *at* $r = r_d$
				BC2 $C_{H,5}(i,j,k) = C_{H,5}(i+1,j,k) - \Delta r\left(\frac{-N_{H,5}(i+1,j,k)}{D_{eff,H,5}}\right) \quad \forall z, \forall t$ *at* $r = r_d - \Delta r$
		X	$C_{X,5}(i-1,j,k) = \frac{\Delta r^2}{D_{X,5}}\left(-\frac{D_{X,5}}{r}\frac{C_{X,5}(i+1,j,k)-C_{X,5}(i,j,k)}{\Delta r}\right) + 2C_{X,5}(i,j,k) - C_{X,5}(i+1,j,k)$	BC1 $C_{X,5}(i,j,k) = H_0C_{X,6}(1,j,k) \quad \forall z, \forall t$ *at* $r = r_d$
				BC2 $C_{X,5}(i,j,k) = C_{X,5}(i+1,j,k) - \Delta r\left(\frac{-N_0(i+1,j,k)}{D_{eff,X,5}}\right) \quad \forall z, \forall t$ *at* $r = r_d - \Delta r$
	3	S	$C_{S,3}(i-1,j,k) = \frac{\Delta r^2}{D_{S,3}}\left(-\frac{D_{S,3}}{r}\frac{C_{S,3}(i+1,j,k)-C_{S,3}(i,j,k)}{\Delta r}\right) + 2C_{S,3}(i,j,k) - C_{S,3}(i+1,j,k)$	BC1 $C_{S,3}(i,j,k) = H_{3,4}C_{S,4}(1,j,k) \quad \forall z, \forall t$ *at* $r = r_d$
				BC2 $C_{S,3}(i,j,k) = C_{S,3}(i+1,j,k) - \Delta r\left(\frac{-N_{S,3}(i+1,j,k)}{D_{eff,S,3}}\right) \quad \forall z, \forall t$ *at* $r = r_d - \Delta r$
		H	$C_{H,3}(i-1,j,k) = \frac{\Delta r^2}{D_{H,3}}\left(-\frac{D_{H,3}}{r}\frac{C_{H,3}(i+1,j,k)-C_{H,3}(i,j,k)}{\Delta r}\right) + 2C_{H,3}(i,j,k) - C_{H,3}(i+1,j,k)$	BC1 $C_{H,3}(i,j,k) = H_{3,4}C_{H,4}(1,j,k) \quad \forall z, \forall t$ *at* $r = r_d$
				BC2 $C_{H,3}(i,j,k) = C_{H,3}(i+1,j,k) - \Delta r\left(\frac{-N_{H,3}(i+1,j,k)}{D_{eff,H,3}}\right) \quad \forall z, \forall t$ *at* $r = r_d - \Delta r$
		X	$C_{X,3}(i-1,j,k) = \frac{\Delta r^2}{D_{X,3}}\left(-\frac{D_{X,3}}{r}\frac{C_{X,3}(i+1,j,k)-C_{X,3}(i,j,k)}{\Delta r}\right) + 2C_{X,3}(i,j,k) - C_{X,3}(i+1,j,k)$	BC1 $C_{X,3}(i,j,k) = H_0C_{X,4}(1,j,k) \quad \forall z, \forall t$ *at* $r = r_d$
				BC2 $C_{X,3}(i,j,k) = C_{X,3}(i+1,j,k) - \Delta r\left(\frac{-N_0(i+1,j,k)}{D_{eff,X,3}}\right) \quad \forall z, \forall t$ *at* $r = r_d - \Delta r$
	2	S	$C_{S,2}(i-1,j,k) = \frac{\Delta r^2}{D_{S,2}}\left(-\frac{D_{S,2}}{r}\frac{C_{S,2}(i+1,j,k)-C_{S,2}(i,j,k)}{\Delta r}\right) + 2C_{S,2}(i,j,k) - C_{S,2}(i+1,j,k)$	BC1 $C_{S,2}(i,j,k) = H_0C_{S,3}(1,j,k) \quad \forall z, \forall t$ *at* $r = r_d$
				BC2 $C_{S,2}(i,j,k) = C_{S,2}(i+1,j,k) - \Delta r\left(\frac{-N_0(i+1,j,k)}{D_{eff,S,2}}\right) \quad \forall z, \forall t$ *at* $r = r_d - \Delta r$
		H	$C_{H,2}(i-1,j,k) = \frac{\Delta r^2}{D_{H,2}}\left(-\frac{D_{H,2}}{r}\frac{C_{H,2}(i+1,j,k)-C_{H,2}(i,j,k)}{\Delta r}\right) + 2C_{H,2}(i,j,k) - C_{H,2}(i+1,j,k)$	BC1 $C_{H,2}(i,j,k) = H_{2,3}C_{H,3}(1,j,k) \quad \forall z, \forall t$ *at* $r = r_d$
				BC2 $C_{H,2}(i,j,k) = C_{H,2}(i+1,j,k) - \Delta r\left(\frac{-N_{H,2}(i+1,j,k)}{D_{eff,H,2}}\right) \quad \forall z, \forall t$ *at* $r = r_d - \Delta r$
		X	$C_{X,2}(i-1,j,k) = \frac{\Delta r^2}{D_{X,2}}\left(-\frac{D_{X,2}}{r}\frac{C_{X,2}(i+1,j,k)-C_{X,2}(i,j,k)}{\Delta r}\right) + 2C_{X,2}(i,j,k) - C_{X,2}(i+1,j,k)$	BC1 $C_{X,2}(i,j,k) = H_0C_{X,3}(1,j,k) \quad \forall z, \forall t$ *at* $r = r_d$
				BC2 $C_{X,2}(i,j,k) = C_{X,2}(i+1,j,k) - \Delta r\left(\frac{-N_0(i+1,j,k)}{D_{eff,X,2}}\right) \quad \forall z, \forall t$ *at* $r = r_d - \Delta r$

Table J.2: Summary of the model equations and boundary conditions to describe the bioactive membrane domains of the multi-domain fiber model.

Model	Domain	Species	Discretized equation	Discretized boundary condition
Bioactive membrane	5	S	$C_{S,5}(i,j,k+1) = \Delta t(k_{1,S}\frac{C_{S,5}(i+1,j,k)-2C_{S,5}(i,j,k)+C_{S,5}(i-1,j,k)}{\Delta r^2} + k_{2,S}\frac{C_{S,5}(i+1,j,k)-C_{S,5}(i,j,k)}{\Delta r} - k_{3,S}\frac{C_{S,5}(i,j,k)}{K_S+C_{S,5}(i,j,k)} - k_{4,S}) + C_{S,5}(i,j,k)$ $k_{1,S} = D_{S,5}\left(1-\frac{C_{X,5}(i,j,k)}{C_{X,max}}\right)$ $k_{2,S} = \frac{D_{S,5}}{r}\left(1-\frac{C_{X,5}(i,j,k)}{C_{X,max}}\right) - \frac{D_{S,5}}{C_{X,max}}\frac{C_{X,5}(i+1,j,k)-C_{X,5}(i,j,k)}{\Delta r}$ $k_{3,S} = \frac{\mu_{max}C_{X,5}(i,j,k)}{Y_{X/S}}$ $k_{4,S} = k_m C_{X,5}(i,j,k)$	BC1 $C_{S,5}(i,j,k) = H_{S,5,6}C_{S,6}(1,j,k) \quad \forall z\ , \forall t\ at\ r = r_5$ BC2 $C_{S,5}(i,j,k) = C_{S,5}(i+1,j,k) - \frac{C_{S,5}(i+1,j,k)}{k0_{S,5}} \quad \forall z\ \forall r \in [r_4, r_5 - \Delta r]\ at\ t = t_{crit}$ BC3 $C_{S,5}(i,j,k) = C_{S,5}(i+1,j,k) - \frac{C_{S,5}(i+1,j,k)}{k0_{S,5}} \quad \forall z\ , \forall t \setminus t_{crit}\ at\ r = r_4$
		H	$C_{H,5}(i,j,k+1) = \Delta t(k_{1,H}\frac{C_{H,5}(i+1,j,k)-2C_{H,5}(i,j,k)+C_{H,5}(i-1,j,k)}{\Delta r^2} + k_{2,H}\frac{C_{H,5}(i+1,j,k)-C_{H,5}(i,j,k)}{\Delta r} + k_{3,H}\left(1-\frac{C_{H,5}(i,j,k)}{C_{H,sat}}\right)^n\left(\frac{C_{H,crit}}{C_{H,5}+C_{H,crit}}\right)) + C_{H,5}(i,j,k)$ $k_{1,H} = D_{H,5}\left(1-\frac{C_{X,5}(i,j,k)}{C_{X,max}}\right)$ $k_{2,H} = \frac{D_{H,5}}{r}\left(1-\frac{C_{X,5}(i,j,k)}{C_{X,max}}\right) - \frac{D_{H,5}}{C_{X,max}}\frac{C_{X,5}(i+1,j,k)-C_{X,5}(i,j,k)}{\Delta r}$ $k_{3,H} = \frac{\mu_{max}}{Y_{X/H}}\frac{C_{S,5}(i,j,k)C_{X,5}(i,j,k)}{K_S+C_{S,5}(i,j,k)}$	BC1 $C_{H,5}(i,j,k) = H_{H,5,6}C_{H,6}(1,j,k) \quad \forall z\ , \forall t\ at\ r = r_5$ BC2 $C_{H,5}(i,j,k) = C_{H,5}(i+1,j,k) - \frac{C_{H,5}(i+1,j,k)}{k0_{H,5}} \quad \forall z\ \forall r \in [r_4, r_5 - \Delta r]\ at\ t = t_{crit}$ BC3 $C_{H,5}(i,j,k) = C_{H,5}(i+1,j,k) - \frac{C_{H,5}(i+1,j,k)}{k0_{H,5}} \quad \forall z\ , \forall t \setminus t_{crit}\ at\ r = r_4$
		X	$C_{X,5}(i,j,k+1) = \Delta t(k_{1,X}\frac{C_{S,5}(i+1,j,k)-2C_{S,5}(i,j,k)+C_{S,5}(i-1,j,k)}{\Delta r^2} + k_{2,X}\frac{C_{S,5}(i+1,j,k)-C_{S,5}(i,j,k)}{\Delta r} + k_{3,X}C_{X,5}(i,j,k)\left(1-\frac{C_{X,5}(i,j,k)}{C_{X,max}}\right)) + (C_{X,5}(i-1,j,k) - C_{X,max})k_{bb} + C_{X,5}(i,j,k)$ $k_{1,X} = D_{X,5}\left(1-\frac{C_{X,5}(i,j,k)}{C_{X,max}}\right)$ $k_{2,X} = \frac{D_{X,5}}{r}\left(1-\frac{C_{X,5}(i,j,k)}{C_{X,max}}\right) - \frac{D_{X,5}}{C_{X,max}}\frac{C_{X,5}(i+1,j,k)-C_{X,5}(i,k)}{\Delta r}$ $k_{3,X} = \mu_{max}\frac{C_{S,5}(i,j,k)}{K_S+C_{S,5}(i,j,k)} - k_{dec}$	BC1 $C_{X,5}(i,j,k) = f_{inequality\ distribution} \quad \forall z\ \forall r \in [r_4, r_5]\ , at\ t = t_{crit}$ BC2 $C_{X,5}(i,j,k) = C_{X,5}(i+1,j,k) + \frac{C_{X,5}(i+1,j,k)}{k0_{X,5}} \quad \forall z\ , \forall t \setminus t_{crit}\ at\ r = r_4$
	4	S	$C_{S,4}(i,j,k+1) = \Delta t(k_{1,S}\frac{C_{S,4}(i+1,j,k)-2C_{S,4}(i,j,k)+C_{S,4}(i-1,j,k)}{\Delta r^2} + k_{2,S}\frac{C_{S,4}(i+1,j,k)-C_{S,4}(i,j,k)}{\Delta r} - k_{3,S}\frac{C_{S,4}(i,j,k)}{K_S+C_{S,4}(i,j,k)} - k_{4,S}) + C_{S,4}(i,j,k)$ $k_{1,S} = D_{S,4}\left(1-\frac{C_{X,4}(i,j,k)}{C_{X,max}}\right)$ $k_{2,S} = \frac{D_{S,4}}{r}\left(1-\frac{C_{X,4}(i,j,k)}{C_{X,max}}\right) - \frac{D_{S,4}}{C_{X,max}}\frac{C_{X,4}(i+1,j,k)-C_{X,4}(i,j,k)}{\Delta r}$ $k_{3,S} = \frac{\mu_{max}C_{X,4}(i,j,k)}{Y_{X/S}}$ $k_{4,S} = k_m C_{X,4}(i,j,k)$	BC1 $C_{S,4}(i,j,k) = H_{4,5}C_{S,5}(1,j,k) \quad \forall z\ , \forall t\ at\ r = r_4$ BC2 $C_{S,4}(i,j,k) = C_{S,4}(i+1,j,k) - \frac{C_{S,4}(i+1,j,k)}{k0_{S,4}} \quad \forall z\ \forall r \in [r_3, r_4 - \Delta r]\ at\ t = t_0$ BC3 $C_{S,4}(i,j,k) = C_{S,4}(i+1,j,k) - \frac{C_{S,4}(i+1,j,k)}{k0_{S,4}} \quad \forall z\ , \forall t \setminus t_0\ at\ r = r_3$
		H	$C_{H,4}(i,j,k+1) = \Delta t(k_{1,H}\frac{C_{H,4}(i+1,j,k)-2C_{H,4}(i,j,k)+C_{H,4}(i-1,j,k)}{\Delta r^2} + k_{2,H}\frac{C_{H,4}(i+1,j,k)-C_{H,4}(i,j,k)}{\Delta r} + k_{3,H}\left(1-\frac{C_{H,4}(i,j,k)}{C_{H,sat}}\right)^n\left(\frac{C_{H,crit}}{C_{H,4}+C_{H,crit}}\right)) + C_{H,4}(i,j,k)$ $k_{1,H} = D_{H,4}\left(1-\frac{C_{X,4}(i,j,k)}{C_{X,max}}\right)$ $k_{2,H} = \frac{D_{H,4}}{r}\left(1-\frac{C_{X,4}(i,j,k)}{C_{X,max}}\right) - \frac{D_{H,4}}{C_{X,max}}\frac{C_{X,4}(i+1,j,k)-C_{X,4}(i,j,k)}{\Delta r}$ $k_{3,H} = \frac{\mu_{max}}{Y_{X/H}}\frac{C_{S,4}(i,j,k)C_{X,4}(i,j,k)}{K_S+C_{S,4}(i,j,k)}$	BC1 $C_{H,4}(i,j,k) = H_{4,5}C_{H,5}(1,j,k) \quad \forall z\ , \forall t\ at\ r = r_4$ BC2 $C_{H,4}(i,j,k) = C_{H,4}(i+1,j,k) - \frac{C_{H,4}(i+1,j,k)}{k0_{H,4}} \quad \forall z\ \forall r \in [r_3, r_4 - \Delta r]\ at\ t = t_0$ BC3 $C_{H,4}(i,j,k) = C_{H,4}(i+1,j,k) - \frac{C_{H,4}(i+1,j,k)}{k0_{H,4}} \quad \forall z\ , \forall t \setminus t_0\ at\ r = r_3$
		X	$C_{X,4}(i,j,k+1) = \Delta t(k_{1,X}\frac{C_{S,4}(i+1,j,k)-2C_{S,4}(i,j,k)+C_{S,4}(i-1,j,k)}{\Delta r^2} + k_{2,X}\frac{C_{S,4}(i+1,j,k)-C_{S,4}(i,j,k)}{\Delta r} + k_{3,X}C_{X,4}(i,j,k)\left(1-\frac{C_{X,4}(i,j,k)}{C_{X,max}}\right)) + (C_{X,4}(i-1,j,k) - C_{X,max})k_{bb} + C_{X,4}(i,j,k)$ $k_{1,X} = D_{X,4}\left(1-\frac{C_{X,4}(i,j,k)}{C_{X,max}}\right)$ $k_{2,X} = \frac{D_{X,4}}{r}\left(1-\frac{C_{X,4}(i,j,k)}{C_{X,max}}\right) - \frac{D_{X,4}}{C_{X,max}}\frac{C_{X,4}(i+1,j,k)-C_{X,4}(i,k)}{\Delta r}$ $k_{3,X} = \mu_{max}\frac{C_{S,4}(i,j,k)}{K_S+C_{S,4}(i,j,k)} - k_{dec}$	BC1 $C_{X,4}(i,j,k) = C_{X,0} \quad \forall z\ at\ r = r_4\ , at\ t = t_0$ BC2 $C_{X,4}(i,j,k) = C_{X,4}(i+1,j,k) - \frac{C_{X,4}(i+1,j,k)}{k0_{X,4}} \quad \forall z\ \forall r \in [r_3, r_4 - \Delta r]\ at\ t = t_0$ BC3 $C_{X,4}(i,j,k) = C_{X,4}(i+1,j,k) - \frac{C_{X,4}(i+1,j,k)}{k0_{X,4}} \quad \forall z\ , \forall t \setminus t_0\ at\ r = r_3$

Annex K

Parameters

This chapter presents the procedure to estimate parameters considering different source types and assumptions, and provides a summary of the model's parameters.

Information sources used

The development of the chapter is based on information obtained through different methods, which are presented below:

S1 Bibliographic source.

S2 Common calculation. These are: linear interpolation, weighing, average calculation.

S3 External consultant criteria.

S4 Internal consultant, design, or modeling criteria.

Assumptions

Some assumptions are used to estimate the parameters' values:

A1 The initial bioactive layer is composed of a monolayer of *Clostridium* strains, considering that its width is equal to the cell's average length (1.5 – 20 μm) [239].

A2 Cells only grow within the immobilized cell layer and towards the sealant layer/mixed liquor interface due to substrate availability. N.b. that the cell seed is put in the immobilized layer at t_0.

A3 The effective diffusion coefficient of a species in a bioactive membrane is described as a linear function of the cell concentration and the diffusivity at inert conditions (Eq. (4.1)) [90].

A4 Due to the hydrophobicity of the hollow-fiber support [221], the wastewater does not enter this layer. Thus, no substrate molecule is present in the hollow-fiber layer nor lumen, and the effective diffusion coefficient is estimated to be close to zero in those domains. N.b. a low value, but different to zero, was chosen to avoid indeterminate values during model solving.

A5 Due to Asm. (A2), the effective diffusion coefficient of cells is estimated to be close to zero in the lumen side, hollow-fiber layer, and PDA-support layer. N.b. a low value, but different to zero, was chosen to avoid indeterminate values during model solving.

A6 The effective diffusion coefficient of cells in the wastewater is assumed to be equal to the one in water (3.6e-10 $\frac{m^2}{s}$ [240]).

A7 To describe the absence of a species in certain domains, the respective equilibrium distribution coefficient is assumed to be zero.

A8 For all species, the equilibrium distribution coefficient at interfaces that are within the membrane is assumed to be equal to one as those interfaces are less incidental in terms of material change.

A9 The equilibrium distribution coefficient of substrate between the membrane and mixed liquor is expected to be less than one due to the substrate's affinity to remain in the wastewater. Thus, a value of 0.8 is assumed.

A10 The properties of wastewater are similar to those of pure liquid water.

A11 The H_2 critical inhibitory concentration can be estimated by using Henry's law (with Henry's law constants for H_2 gas in water at 25° C being K_H=$7.8 \cdot 10^{-4}$ $\frac{mol}{atm\,L}$ [241]) and the pressure threshold of 10^{-3} atm [162].

A12 Even though the maximum physically attainable biomass concentration is specific to the membrane composition and bacterial species, the value reference of a study of *Nitrobacter agilis* immobilized in Carrageenan (950 $\frac{kg}{m^3}$) is assumed to apply for the bioactive layers of the CBMem [242]. In general, the maximum attainable cell concentration for domain 4 was initially set to a lower value of 300 $\frac{kg}{m^3}$, with a gradually increasing recalculation according to advances in cell migration until reaching 950 $\frac{kg}{m^3}$.

A13 Some kinetic parameters (such as k_{dec}, k_m, and $Y_{X/H}$) are assumed to be in function of bibliographic values to ensure proportionality during calibration.

A14 The half-saturation constant (K_S), as well as the bibliographic references for some kinetic parameters (such as k_{dec}, k_m, and $Y_{X/S}$) are assumed to be similar to those of mesophilic monosaccharides degraders [37, 96].

A15 Although the degree of H_2 inhibition constant has been reported to be 1.39 in certain experimental trials [243], this study assumes a degree of 1 to avoid indetermination during model solving.

A16 Based on dimensional analysis, the yield coefficient of biomass on hydrogen ($Y_{X/H}$) is defined as $Y_{X/H} = \frac{Y_{X/S}}{Y_{H/S}}$. For this, $Y_{H/S}$ is estimated as the average of the values found in the literature for fermentation processes using wastewater as substrate, resulting in $1.618 \cdot 10^{-2}$ $\frac{g\,H_2}{g\,COD}$ (see Annex B.2.5).

Summary of parameters

Table K.1: Geometrical parameters.

Parameter	Definition	Value	Unit	Ref.
A_f	Cross-sectional area of a fiber	πr_1^2	$[m^2]$	NA[a]
A_M	Total cross-sectional area of CBMem module	$A_f N_f$	$[m^2]$	NA[a]
Δr_3	PDA layer thickness	50e-09	$[m]$	[S1],[63]
Δr_4	Bioactive layer thickness	10.75e-06	$[m]$	[S1,A1],[239]
Δr_5	PVA layer thickness	1e-03	$[m]$	[S1],[63]
L	Fiber length	6e-02	$[m]$	[S1],[63]
N_f	Number of fibers	135	[-]	[S4]
r_0	Fiber center	0	$[m]$	[S4]
r_1	Lumen radius	105e-06	$[m]$	[S1],[221]
r_2	Hollow-fiber outer radius	150e-06	$[m]$	[S1],[221]
r_3	Radius of the interface that separates PDA and bioactive layer	$r_2+\Delta r_3$	$[m]$	NA[a]
r_4	Radius of the interface that separates bioactive and PVA layer	$r_3+\Delta r_4$	$[m]$	NA[a]
r_5	Membrane radius	$r_4+\Delta r_5$	$[m]$	NA[a]
r_{57}	Radius measured at the center between r_5 and r_7	$r_5 + \frac{r_7-r_5}{2}$	$[m]$	NA[a]
r_7	Reactor radius	8.25e-02	$[m]$	[S4]
V_{4,t_0}	Bioactive layer's initial volume	$\frac{\pi \cdot L \cdot \left((2r_3+2\Delta_{r_4})^2-(2r_3)^2\right)}{4}$	$[m^3]$	[S4,A1]
z_0	Height of fiber's inlet	0	$[m]$	[S4]
z_f	Height of fiber's outlet	$L + z_0$	$[m]$	NA[a]

[a]Not applicable.

Table K.2: Operational parameters.

Parameter	Definition	Value	Unit	Ref.
$C_{H,6,z_0}$	Hydrogen concentration on the mixed liquor side at z_0	$C_{H,sat}$	$\left[\frac{kg}{m^3}\right]$	[S4,S1],[63]
$C_{S,6,0}$	Substrate concentration on the mixed liquor side	6.92	$\left[\frac{kg}{m^3}\right]$	[S4]
$C_{X,0}$	Initial cell concentration in the bioactive layer	$\frac{m_{X0}}{V_{4,t_0}}$	$\left[\frac{kg}{m^3}\right]$	[S4,A1]
$C_{X,6,z_0}$	Cell concentration on the mixed liquor side at z_0	0	$\left[\frac{kg}{m^3}\right]$	[S4, A2]
m_{X0}	Initially immobilized cell mass	0.2e-06	$[kg]$	[S4,S1],[63]
P_{1,z_0}	Inlet pressure of sparging gas	34473.8	$\left[\frac{kg}{m\,s^2}\right]$	[S4]
P_{1,z_f}	Outlet pressure of sparging gas	$P_{1,z0} \cdot 0.999$	$\left[\frac{kg}{m\,s^2}\right]$	[S4]
P_{6,z_0}	Inlet wastewater pressure	1343569.5	$\left[\frac{kg}{m\,s^2}\right]$	[S4]
P_{6,z_f}	Outlet wastewater pressure	1074045	$\left[\frac{kg}{m\,s^2}\right]$	[S4]
$Q_{G,i}$	Inlet gas flow	1.667e-07	$\left[\frac{m^3}{s}\right]$	[S4,S1],[63]
$Q_{L,i}$	Inlet wastewater feed flow	4.167e-08	$\left[\frac{m^3}{s}\right]$	[S4,S1],[63]
$v_{z,1,i}$	Axial velocity at the lumen side's inlet	$\frac{Q_{G,i}}{A_M}$	$\left[\frac{m}{s}\right]$	NA[a]

[a]Not applicable.

Table K.3: Physical Parameters.

Parameter	Definition	Value	Unit	Ref.
$C_{H,sat}$	Hydrogen saturation concentration	1.6e-03	$\left[\frac{kg}{m^3}\right]$	[S1],[63]
$D_{eff,H,1}$	Effective diffusion coefficient of H_2 in lumen gas mixture	SC[a]	$\left[\frac{m^2}{s}\right]$	NA[b]
$D_{eff,H,2}$	Effective diffusion coefficient of H_2 in polypropylene	SC[a]	$\left[\frac{m^2}{s}\right]$	NA[b]
$D_{eff,H,3}$	Effective diffusion coefficient of H_2 in poly(dopamine)	SC[a]	$\left[\frac{m^2}{s}\right]$	NA[b]
$D_{eff,H,4}$	Effective diffusion coefficient of substrate in bioactive layer	SC[a]	$\left[\frac{m^2}{s}\right]$	[A3]
$D_{eff,H,5}$	Effective diffusion coefficient of substrate in poly(vinyl alcohol)	SC[a]	$\left[\frac{m^2}{s}\right]$	[A3]

[a]Subject to calibration.

[b]Not applicable.

Table K.3 (cont.): Physical Parameters.

Parameter	Definition	Value	Unit	Ref.
$D_{eff,H,6}$	Effective diffusion coefficient of H_2 in wastewater	SC[a]	$\left[\frac{m^2}{s}\right]$	NA[b]
$D_{eff,S,1}$	Effective diffusion coefficient of substrate in lumen gas mixture	1e-20	$\left[\frac{m^2}{s}\right]$	[S4,A4]
$D_{eff,S,2}$	Effective diffusion coefficient of substrate in polypropylene	1e-20	$\left[\frac{m^2}{s}\right]$	[S4,A4]
$D_{eff,S,3}$	Effective diffusion coefficient of substrate in poly(dopamine)	SC[a]	$\left[\frac{m^2}{s}\right]$	NA[b]
$D_{eff,S,4}$	Effective diffusion coefficient of substrate in bioactive layer	SC[a]	$\left[\frac{m^2}{s}\right]$	[A3]
$D_{eff,S,5}$	Effective diffusion coefficient of substrate in poly(vinyl alcohol)	SC[a]	$\left[\frac{m^2}{s}\right]$	[A3]
$D_{eff,S,6}$	Effective diffusion coefficient of substrate in wastewater	SC[a]	$\left[\frac{m^2}{s}\right]$	NA[b]
$D_{eff,X,1}$	Effective diffusion coefficient of cells in lumen gas mixture	1e-20	$\left[\frac{m^2}{s}\right]$	[S4,A5]
$D_{eff,X,2}$	Effective diffusion coefficient of cells in polypropylene	1e-20	$\left[\frac{m^2}{s}\right]$	[S4,A5]
$D_{eff,X,3}$	Effective diffusion coefficient of cells in poly(dopamine)	1e-20	$\left[\frac{m^2}{s}\right]$	[S4,A5]
$D_{eff,X,4}$	Effective diffusion coefficient of cells in bioactive layer	SC[a]	$\left[\frac{m^2}{s}\right]$	[A3]
$D_{eff,X,5}$	Effective diffusion coefficient of cells in poly(vinyl alcohol)	SC[a]	$\left[\frac{m^2}{s}\right]$	[A3]
$D_{eff,X,6}$	Effective diffusion coefficient of cells in wastewater	$3.6{\cdot}10^{-10}$	$\left[\frac{m^2}{s}\right]$	[S1,A6],[240]
g	Gravitational acceleration (vector)	-9.807	$\left[\frac{m}{s^2}\right]$	[S1],[244]
H_0	Zero equilibrium distribution coefficient	0	[-]	[S4, A7]
$H_{1,2}$	Equilibrium distribution coefficient between domain 1 and 2	SC[c]	[-]	NA[b]

[a]Subject to calibration.

[b]Not applicable.

[c]Subject to calibration; previous to CBMem modeling, its value was considered to be 1.1.

Table K.3 (cont.): Physical Parameters.

Parameter	Definition	Value	Unit	Ref.
$H_{2,3}$	Equilibrium distribution coefficient between domain 2 and 3	1	[-]	[S4, A8]
$H_{3,4}$	Equilibrium distribution coefficient between domain 3 and 4	1	[-]	[S4]
$H_{4,5}$	Equilibrium distribution coefficient between domain 4 and 5	1	[-]	[S4]
$H_{H,5,6}$	Equilibrium distribution coefficient of species H between domain 5 and 6	SC[a]	[-]	NA[b]
$H_{S,5,6}$	Equilibrium distribution coefficient of species S between domain 5 and 6	0.8	[-]	[S4, A9]
μ_g	Dynamic viscosity of gas mixture in lumen side	$1.737{\cdot}10^{-5}$	$\left[\frac{kg}{m\,s}\right]$	[S1,S2],[244]
μ_w	Dynamic viscosity of wastewater	$0.891{\cdot}10^{-3}$	$\left[\frac{kg}{m\,s}\right]$	[S1,A10],[244]
ρ_H	Density of H_2 at 1 atm and 25C	0.08299	$\left[\frac{kg}{m^3}\right]$	[S1,S2],[244]
ρ_w	Density of wastewater	1,000	$\left[\frac{kg}{m^3}\right]$	[S1,A10],[244]

[a]Subject to calibration; previous to CBMem modeling, its value was considered to be 0.8.

[b]Not applicable.

Table K.4: Biological parameters.

Parameter	Definition	Value	Unit	Ref.
$C_{H,max}$	H_2 critical inhibitory concentration	1.560e-06	$\left[\frac{kg}{m^3}\right]$	[S1,A11],[162]
$C_{X,max,4}$	Maximum attainable cell concentration within domain 4	300[a] or 950	$\left[\frac{kg}{m^3}\right]$	[S1,A12],[242]
$C_{X,max,5}$	Maximum attainable cell concentration within domain 5	950	$\left[\frac{kg}{m^3}\right]$	[S1,A12],[242]
k_{dec}	Biomass decay constant	$\frac{k_{dec,bib}}{\mu_{max,bib}}\mu_{max}$	$\left[\frac{1}{s}\right]$	[S4, A13]
$k_{dec,bib}$	Bibliographic biomass decay constant	9.260e-06	$\left[\frac{1}{s}\right]$	[S1, A14],[37, 96]

[a]The value will always tend to increase towards 950 $\left[\frac{kg}{m^3}\right]$; however, a lower value could have been initially defined to stimulate cell migration.

Table K.4 (cont.): Biological parameters.

Parameter	Definition	Value	Unit	Ref.
k_m	Microbial maintenance coefficient	$\frac{k_{m,bib} Y_{X/S,bib}}{\mu_{max,bib}} \frac{\mu_{max}}{Y_{X/S}}$	$\left[\frac{kg_{COD}}{kg_{cells}\, s}\right]$	[S4,A13]
$k_{m,bib}$	Bibliographic microbial maintenance coefficient	3.125e-04	$\left[\frac{kg_{COD}}{kg_{cells}\, s}\right]$	[S1,A14],[37, 96]
K_S	Half-saturation constant	0.05	$\left[\frac{kg_{COD}}{m^3}\right]$	[S1,A14],[37, 96]
μ_{max}	Maximum specific growth rate	SC[a]	$\left[\frac{1}{s}\right]$	NA[b]
$\mu_{max,bib}$	Bibliographic maximum specific growth rate	4.630e-05	$\left[\frac{1}{s}\right]$	[S1,A14],[37]
n	Degree of H_2 inhibition constant	1	$[-]$	[S4,S1,A15],[243]
$Y_{H/S}$	Yield of H_2 on substrate	1.618e-02	$\left[\frac{kg_{H_2}}{kg_{COD}}\right]$	[S1,A13,A16]
$Y_{X/H}$	Yield of biomass on H_2	$\frac{Y_{X/S,bib}}{Y_{H/S}}$	$\left[\frac{kg_{cells}}{kg_{H_2}}\right]$	[S4,A16,A13]
$Y_{X/S}$	Yield of biomass on substrate	SC[c]	$\left[\frac{kg_{cells}}{kg_{COD}}\right]$	NA[a]
$Y_{X/S,bib}$	Bibliographic yield of biomass on substrate	0.15	$\left[\frac{kg_{cells}}{kg_{COD}}\right]$	[S1,A14],[37, 96]

[a]Subject to calibration. For initial modeling exercises, it was estimated at 1.5e-6.

[b]Not applicable.

[c]Subject to calibration. For initial modeling exercises, it was estimated at 0.15e+4

Table K.5: Numerical parameters.

Parameter	Definition	Value	Unit	Ref.
Δr_1	Radial step size for domain 1	$\frac{r_1 - r_0}{r_{pts,1}}$	$[m]$	NA[a]
Δr_2	Radial step size for domain 2	$\frac{r_2 - r_1}{r_{pts,2}}$	$[m]$	NA[a]
Δr_3	Radial step size for domain 3	$\frac{r_3 - r_2}{r_{pts,3}}$	$[m]$	NA[a]
Δr_4	Radial step size for domain 4	2e-06	$[m]$	[S4]
Δr_5	Radial step size for domain 5	2e-06	$[m]$	[S4]
Δr_6	Radial step size for domain 6	$\frac{r_{57} - r_5}{r_{pts,6}}$	$[m]$	NA[a]
Δz	Axial step size	$\frac{z_f - z_0}{z_{pts}}$	$[m]$	NA[a]
λ	Cell redistribution parameter	0.01	[-]	[S4]
$r_{pts,1}$	Number of radial points in domain 1	6	[-]	[S4]
$r_{pts,2}$	Number of radial points in domain 2	10	[-]	[S4]
$r_{pts,3}$	Number of radial points in domain 3	10	[-]	[S4]

[a]Not applicable.

Table K.5 (cont.) Numerical parameters.

Parameter	Definition	Value	Unit	Ref.
$r_{pts,6}$	Number of radial points in domain 6	10	[-]	[S4]
t_0	Initial time	0	$[s]$	[S4]
t_f	Initial time	SM[a]	$[s]$	[S4]
t_{pts}	Number of time points	$\frac{t_f - t_0}{t_{pts}}$	[-]	NA[b]
z_{pts}	Number of axial points	3	[-]	[S4]
Δt	Time step for cell growth	21,600	$[s]$	[S4]

[a]Subject to modeling: t_f=259,200 for each domain calibration; t_f=2,599,200 for CBMem calibration t_f=2,559,600 for CBMem validation; t_f=1.555e+07 for a six-month simulation

[b]Not applicable.

Table K.6: Other modeling parameters

Parameter	Definition	Value	Unit	Ref.
f_0	Zero function for boundary conditions	0	SBC[a]	NA[b]
$k0_{H,1}$	Constant for boundary condition of hydrogen in domain 1	100	[-]	[S4]
$k0_{H,4}$	Constant for boundary condition of hydrogen in domain 4	5	[-]	[S4]
$k0_{S,4}$	Constant for boundary condition of substrate in domain 4	1000	[-]	[S4]
$k0_{X,4}$	Constant for boundary condition of cells in domain 4	1000	[-]	[S4]
$k0_{H,5}$	Constant for boundary condition of hydrogen in domain 5	250	[-]	[S4]
$k0_{S,5}$	Constant for boundary condition of substrate in domain 5	10,000,000	[-]	[S4]
$k0_{X,5}$	Constant for boundary condition of cells in domain 5	100,000	[-]	[S4]
$k1_{P,1}$	Constant of pressure model in domain 1	SC[c]	$[-]$	NA[b]
$k2_{P,1}$	Constant of pressure model in domain 1	SC[c]	$[\frac{kg}{m^3 s}]$	NA[b]
$k1_{P,6}$	Constant of pressure model in domain 6	SC[d]	$[-]$	NA[b]

[a]Unit subject to form of boundary condition.

[b]Not applicable.

[c]Subject to calibration.

[d]Subject to calibration. For initial modeling exercises, it was estimated at 0.002

Tanle K.6 (cont.): Other modeling parameters

Parameter	**Definition**	**Value**	**Unit**	**Ref.**
$k2_{P,6}$	Constant of pressure model in domain 6	SC[a]	$[\frac{kg}{m^3 s}]$	NA[b]
$k0_{H,6}$	Constant for boundary condition of hydrogen in domain 6	800	[-]	[S4]
$k0_{S,6}$	Constant for boundary condition of substrate in domain 6	5000	[-]	[S4]
$k1_{H,6}$	Constant for boundary condition of hydrogen in domain 6	1.00001	[-]	[S4]
$k1_{S,6}$	Constant for boundary condition of substrate in domain 6	0.99999	[-]	[S4]
$k2_{H,6}$	Constant for boundary condition of hydrogen in domain 6	1.03	[-]	[S4]
$k2_{S,6}$	Constant for boundary condition of substrate in domain 6	0.999	[-]	[S4]
$k3_{H,6}$	Constant for boundary condition of hydrogen in domain 6	SC[c]	[-]	NA[b]
$k3_{S,6}$	Constant for boundary condition of substrate in domain 6	-1e-9	[-]	[S4]
$k_{v,1}$	Axial velocity profile constant in domain 1	SC[d]	[-]	NA[b]
$N0$	Zero mass flux	0	[-]	NA[b]

[a]Subject to calibration. For initial modeling exercises, it was estimated at 4.5e-05

[b]Not applicable.

[c]Subject to calibration. For initial modeling exercises, it was estimated at 1e-11.

[d]Subject to calibration.

Annex L

Parameter calibration and CBMem simulations

This chapter presents the results and discussion of the parameter adjustment in detail. The calibrations were conducted for the transport model and individual CBMem domains using verisimilar data. After implementing the Levenberg-Marquardt nonlinear regression in Octave, input and output arguments were obtained for each calibration. In addition, the chapter also includes results of further CBMem simulations.

L.1. Transport parameters

Calibrations for the transport parameters of both domain 1 (lumen side) and 6 (mixed liquor) were conducted, which are detailed below.

First, the parameters ($k_{1,P,1}$ and $k_{2,P,1}$) of the pressure model for domain 1, represented through Eq.(L.1), were adjusted by considering the fit of the pressure and velocity model (Eq. (L.2)) simultaneously.

$$P_1 = P_{1,z_0} + k_{1,P,1}\frac{P_{1,z_f} - P_{1,z_0}}{z_f - z_0}z + k_{2,P,1}z^2 \quad \text{(L.1)} \qquad\qquad v_{z,1} = -\frac{r_1^2}{4\mu_g}\left(1 - \frac{r^2}{r_1^2}\right)\frac{dP_1}{dz} \quad \text{(L.2)}$$

Table L.1 shows the input and output arguments of the transport model calibration for domain 1 before deciding to change its model structure due to the parameters' undefined confidence intervals. It is worth mentioning that the statistical weights matrix differentiates its value according to the data, giving more importance (set to 1) to the velocity and less importance (set to 0.3) to the pressure, as the velocity profile is of more relevance for the subsequent domain modeling. Convergence was achieved after three iterations, while only changing the value of the second parameter from its initial guess.

The covariance matrix for parameters resulted to have missing data (with NA outputs). Therefore, the parameters' p-values nor confidence interval could be determined. Nevertheless, the calibration allowed a graphical output. Fig. L.1 shows the calibration for the normalized pressure profile, while Fig. L.2 shows the calibration for the velocity profile in the gas phase for different axial positions. Visual inspection reveals a good fit for the velocity profile, but not for the pressure profile.

Table L.1: Arguments of the transport model calibration for domain 1 before changing transport model structure.

Input argument	**Value**
$k0_{k_{1,P,1}}$	1.300e+12
$k0_{k_{2,P,1}}$	1.000e-03
tol	1.000e-03
$miter$	10
$dp_{k_{1,P,1}}$	1.000e-03
$dp_{k_{2,P,1}}$	1.000e-02
$options.bounds_{k_{1,P,1}}$	$\begin{bmatrix} 1 & 1.400\text{e+}12 \end{bmatrix}$
$options.bounds_{k_{2,P,1}}$	$\begin{bmatrix} 0 & 1 \end{bmatrix}$
Output argument	**Value**
$kopt_{k_{1,P,1}}$	1.303e+12
$kopt_{k_{2,P,1}}$	1.000e-03
$varp$	$\begin{bmatrix} \text{NA} & \text{NA} \end{bmatrix}$
cvg	1
$iter$	3

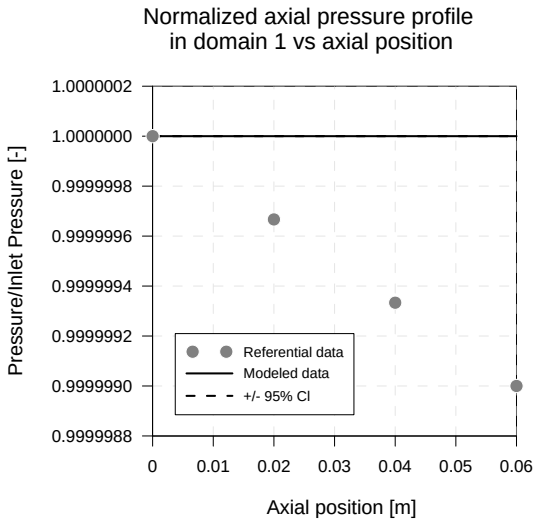

Fig. L.1: First calibration of pressure model of domain 1 using the calibrated parameters of Table L.1.

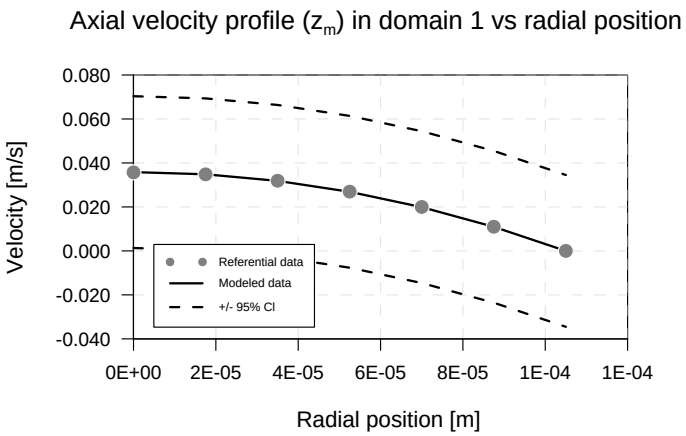

Fig. L.2: First calibration of axial velocity model of domain 1 using the calibrated parameters of Table L.1.

Due to the undefined confidence interval, we decided to separate the velocity equation from the pressure profile by proposing a new velocity equation and conducting for each model the parameter adjustment. First, the parameters ($k_{1,P,1}$ and $k_{2,P,1}$) of the pressure model (Eq.(L.1)) were adjusted. Then, the parameter ($k_{v,1}$) of the axial velocity model (Eq.(L.3)) was calibrated.

$$v_{z,1} = -v_{z,1,z0}\left(1 - \frac{r}{r_1}\right)^{k_{v,1}} \tag{L.3}$$

Table L.2 shows the input and output arguments of the pressure model calibration. Convergence was achieved after three iterations, while the parameters did not moved from its initially guessed values due to the good fit. In this case we noticed that the calibration did not provide the p-value

nor confidence interval for the pressure parameters ($k_{1,P,1}$ and $k_{2,P,1}$) either. This could be due to model structure and parameters, where some of those are dependent of others. Thus, analysis to identify independent parameters are recommended. Also, parameter aggregation can be a useful method.

In turn, Table L.3 shows the input and output arguments of the calibration for the modified velocity model. Convergence was achieved after four iterations, by changing the value of the parameter from its initial guess. By decoupling the velocity model from the pressure model for calibration, the p-value and confidence interval for $k_{v,1}$ could be obtained. As the p-value is less as the desired significance level of 0.05, the parameter is statistically significant. As for the confidence interval, the difference between the limits and the optimized value is of $\pm 10\,\%$, which was considered as acceptable.

Table L.2: Arguments of the pressure model calibration for domain 1.

Input argument	**Value**
$k0_{k_{1,P,1}}$	1
$k0_{k_{2,P,1}}$	0
tol	1.000e-03
$miter$	10
$dp_{k_{1,P,1}}$	1.000e-01
$dp_{k_{2,P,1}}$	1.000e-01
$options.bounds_{k_{1,P,1}}$	$\begin{bmatrix} 0 & 10 \end{bmatrix}$
$options.bounds_{k_{2,P,1}}$	$\begin{bmatrix} 0 & 10 \end{bmatrix}$
Output argument	**Value**
$kopt_{k_{1,P,1}}$	1
$kopt_{k_{2,P,1}}$	0
$varp$	$\begin{bmatrix} \text{NA} & \text{NA} \end{bmatrix}$
cvg	1
$iter$	1

Table L.3: Arguments of the velocity model calibration for domain 1.

Input argument	**Value**
$k0_{k_{v,1}}$	1.000e-02
tol	1.000e-03
$miter$	10
$dp_{k_{v,1}}$	1.000e-01
$options.bounds_{k_{v,1}}$	$\begin{bmatrix} 0 & 10 \end{bmatrix}$
Output argument	**Value**
$kopt_{k_{v,1}}$	5.170e-01
$pval_{k_{v,1}}$	0
$CI_{k_{v,1}}$	$\begin{bmatrix} 4.638\text{e-}01 & 5.694\text{e-}01 \end{bmatrix}$
cvg	1
$iter$	4

According to Fig. L.3 and Fig. L.4, visual inspection shows that both the pressure and velocity model are similar to the proposed referential data, maintaining the latter within the models' confidence region. The calibrated parameters cause a negligible pressure decrease for domain 1 (Fig. L.3), which is expected for the gas phase as there is almost no friction with the membrane walls. Moreover, the modeled velocity profile in domain 1 fulfills the expected tendency, expressing the maximum velocity at the lumen center (at radial position zero of Fig. L.4) and zero velocity at the domain's border (most right position of Fig. L.4).

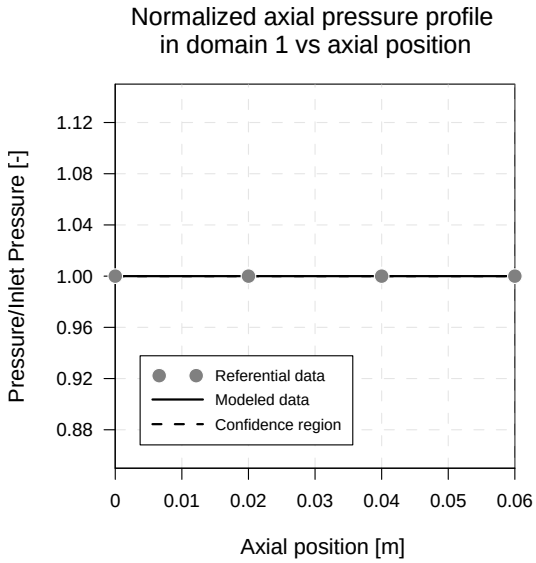

Fig. L.3: Final calibration of pressure model of domain 1 using the calibrated parameters of Table L.2.

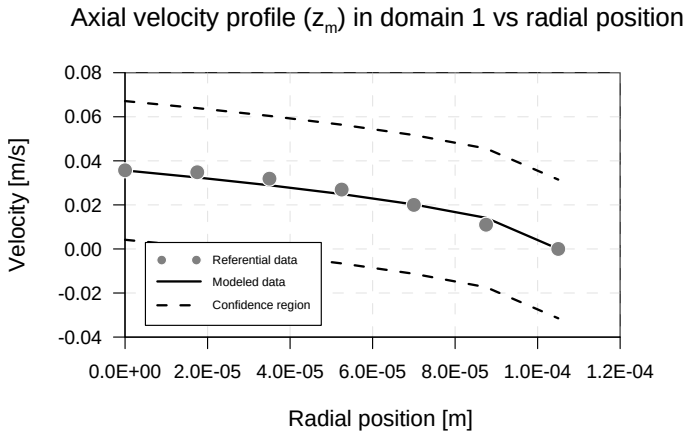

Fig. L.4: Final calibration of axial velocity model of domain 1 using the calibrated parameter of Table L.3.

Unlike domain 1, we maintained the dependency of the axial velocity on the pressure model for domain 6. First, the parameters ($k_{1,P,6}$ and $k_{2,P,6}$) of the pressure model for domain 6, represented through Eq.(L.4), were adjusted by considering the fit of the pressure and velocity model (Eq. (L.5)) simultaneously.

$$P_6 = P_{6,z_0} + k_{1,P,6}\frac{P_{6,z_f} - P_{6,z_0}}{z_f - z_0}z + k_{2,P,6}z^2 \quad \text{(L.4)} \qquad v_{z,6} = \frac{\varepsilon}{4\mu_w}\left(\frac{dP_6}{dz} - \rho g\right) \quad \text{(L.5)}$$

Table L.4 shows the arguments of the transport model calibration for domain 6. It is worth mentioning that the statistical weights matrix differentiates its value according to the data, giving more importance to the velocity (set to 1, if its the entrance velocity, or 0.5 for the remaining data points) and less importance (set to 0.3) to the pressure. Convergence was achieved after one iteration, by changing the values of both parameters from their initial guess. The calibrated parameters concluded the modeled pressure profiles shown in Fig. L.5 and the velocity profiles shown in Fig. L.6.

Both parameters' p-values resulted to be greater than the significance level (0.05), i.e., the parameters are considered to be not significant. This result implies that there is not enough data-based evidence to conclude that the parameter differs from zero. However, it can also mean that the parameter might not be contributing significantly to the model.

When analyzing the parameters' confidence interval, it can be observed that the difference between the limits and the optimized value for $k_{1,P,6}$ is large ($\pm 106\,\%$), suggesting that the margin of error of the parameter estimate is also large. This is because the calibration does not allow a good fit for the pressure profile, where $k_{1,P,6}$ is highly influential. In turn, the difference between the limits and the optimized value of $k_{2,P,6}$ is narrow, around 4e-08.

Table L.4: Arguments of the transport model calibration for domain 6

Input argument	**Value**
$k0_{k_{1,P,6}}$	21,831,781.532e-13
$k0_{k_{2,P,6}}$	1.000e-03
tol	1.000e-03
$miter$	10
$dp_{k_{1,P,6}}$	1.000e-03
$dp_{k_{2,P,6}}$	1.000e-02
$options.bounds_{k_{1,P,6}}$	$\begin{bmatrix} 21{,}831{,}781.525\text{e-}13 & 21{,}831{,}781.535\text{e-}13 \end{bmatrix}$
$options.bounds_{k_{2,P,6}}$	$\begin{bmatrix} 0 & 1 \end{bmatrix}$
Output argument	**Value**
$kopt_{k_{1,P,6}}$	21,831,781.529e-13
$kopt_{k_{2,P,6}}$	0
$pval_{k_{1,P,6}}$	1
$pval_{k_{2,P,6}}$	6.511e-02
$CI_{k_{1,P,6}}$	$\begin{bmatrix} \text{-}1.454\text{e-}04 & 4.512\text{e-}03 \end{bmatrix}$
$CI_{k_{2,P,6}}$	$\begin{bmatrix} \text{-}4.222\text{e-}08 & 4.222\text{e-}08 \end{bmatrix}$
cvg	1
$iter$	1

Visual inspection shows that the modeled data for domain 6 did not fit the expected pressure decrease by 26 [atm] between the initial and final fiber height (Fig. L.5). This result can be explained due to the adjusted parameters while setting a low weight value for the pressure data.

Nevertheless, the velocity model is similar to the proposed referential data, maintaining the latter within the model's confidence region. The modeled profile in domain 6 shows that the maximum velocity is displaced from the center of the domain's width (most right position of Fig. L.6). This is expected due to the influence of the reactor's wall on the fluid flow.

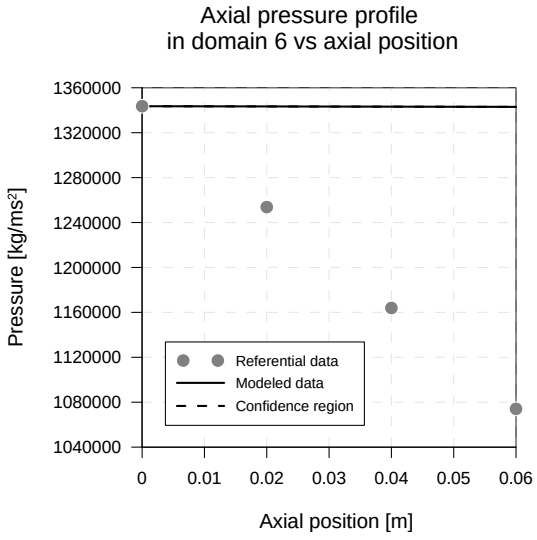

Fig. L.5: Calibration of pressure model of domain 6 using the calibrated parameters of Table L.4.

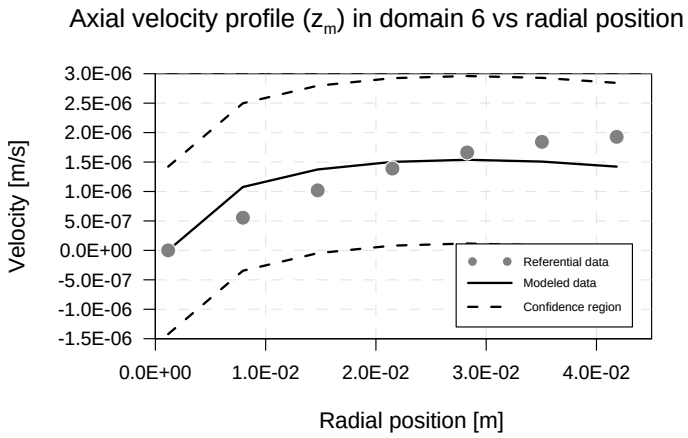

Fig. L.6: Calibration of axial velocity model of domain 6 using the calibrated parameters of Table L.4.

In summary, Table L.5 presents the calibrated values of the transport parameters that were used for subsequent modeling, as well as their confidence interval and p-values.

When considering a velocity profile based on axial pressure difference, we observed that the parameters $k_{1,P,1}$ and $k_{1,P,6}$ are the most influential to simultaneously calibrate the pressure and velocity profile, requiring high values to follow Eq. (4.14) (and Eq. (I.12)), but small values (tending to a magnitude of one) to fit the expected decreasing pressure. The latter is because the slope is already expressed by the term $\frac{P_{d,z_f} - P_{d,z_0}}{z_f - z_0}$ of Eq. (4.17).

Contrarily, the calibrated values of $k_{2,P,1}$ and $k_{2,P,6}$ tended to zero, showing that the term z^2 of Eq. (4.17) is negligible. This result will not affect the proposed model; however, if it is of interest to express the fluids' radial velocity, then these parameters must be different to zero (see Eqs. (I.17) and (I.29)).

In conclusion, the CBMem's velocity model does not synchronize well with the proposed pressure equation and a negligible change of the velocity was observed in the axial direction. For the scope of this research, the results do not undermine representativeness because of the small reactor scale. Thus, model improvements could neglect the axial pressure difference model if the radial velocity profile through the membrane is not an operational variable of interest.

Table L.5: Transport parameters calibrated to referential data.

Parameter	**Calibrated value**	**95 % CI**	**P-value (significance)**
$k_{1,P,1}$, Pressure parameter for domain 1 that describes the variation of the axial position, [−]	1	NA[a]	NA[a]
$k_{2,P,1}$, Pressure parameter for domain 1 that describes the squared variation of the axial position, $[\frac{kg}{m^3 s}]$	0	NA[a]	NA[a]
$k_{1,P,6}$, Pressure parameter for domain 6 that describes the variation of the axial position, [−]	2.183e-03	[-1.454e-04 4.512e-03]	1 (not significant)
$k_{2,P,6}$, Pressure parameter for domain 6 that describes the squared variation of the axial position, $[\frac{kg}{m^3 s}]$	0	[-4.222e-08 4.222e-08]	6.511e-02 (not significant)
$k_{v,1}$, Axial velocity profile parameter in domain 1 that describes the power law index position, [−]	5.166e-01	[4.638e-01 5.694e-01]	0 (very significant)

[a]NA = Not available.

L.2. Mass balance parameters

L.2.1. Parameters for domain 6

The parameters ($D_{eff,S,6}$ and $D_{eff,H,6}$) of the mass balance model for domain 6, represented through the discretization of Eqs.(L.6) and (L.7), were adjusted by considering the fit of the substrate and H_2 concentration profiles to verisimilar data simultaneously.

$$v_{z,6}\frac{\partial C_{S,6}}{\partial z} = D_{eff,S,6}\left(\frac{1}{r}\frac{\partial C_{S,6}}{\partial r} + \frac{\partial^2 C_{S,6}}{\partial r^2}\right) \quad \text{(L.6)} \quad v_{z,6}\frac{\partial C_{H,6}}{\partial z} = D_{eff,H,6}\left(\frac{1}{r}\frac{\partial C_{H,6}}{\partial r} + \frac{\partial^2 C_{H,6}}{\partial r^2}\right) \quad \text{(L.7)}$$

Table L.6 shows the input and output arguments of the mass balance model calibration for domain 6. Convergence was achieved after 5 iterations, changing the value of both parameters

from their initial guess, which were benchmarks derived from the bibliography. The calibrated parameters concluded the modeled concentration profiles shown in Fig. L.7 for domain 6.

Table L.6: Arguments of the mass balance model calibration for domain 6

Input argument	**Value**
$k0_{D_{eff,S,6}}$	1.201e-09 [a]
$k0_{D_{eff,H,6}}$	5.110e-09 [b]
tol	1.000e-03
$miter$	20
wts	$[ones(size(C_{SH,6,ref})]$
$dp_{D_{eff,S,6}}$	1.000e-06
$dp_{D_{eff,H,6}}$	1.000e-03
$options.bounds_{D_{eff,S,6}}$	$\begin{bmatrix}1.000\text{e-}10 & 1.300\text{e-}09\end{bmatrix}$
$options.bounds_{D_{eff,H,6}}$	$\begin{bmatrix}1.000\text{e-}09 & 6.000\text{e-}09\end{bmatrix}$
Output argument	**Value**
$kopt_{D_{eff,S,6}}$	3.925e-10
$kopt_{D_{eff,H,6}}$	2.498e-09
$pval_{D_{eff,S,6}}$	3.460e-04
$pval_{D_{eff,H,6}}$	5.220e-01
$CI_{D_{eff,S,6}}$	$\begin{bmatrix}1.782\text{e-}10 & 6.068\text{e-}10\end{bmatrix}$
$CI_{D_{eff,H,6}}$	$\begin{bmatrix}\text{-}5.158\text{e-}09 & 1.015\text{e-}08\end{bmatrix}$
cvg	1
$iter$	5

[a]Value derived from [245] ; [b]Value derived from [246, 247].

Table L.7 summarizes the most relevant comparisons to be discussed. On the one hand, $D_{S,6}$ resulted to be 33 % its bibliographic value. On the other hand, $D_{H,6}$ was 49 % its bibliographic value. As for the first parameter, its p-value demonstrated a very strong evidence against null hypothesis, concluding a parameter of high significance. The difference from the parameter's optimized value with respect to its limits is of ±55 %, which we considered as acceptable. However, the second parameter resulted to be non-significant, with a large difference from the optimized value with respect to its limits (±306 %), suggesting that the margin of error of the parameter estimate is large and, thus, is uncertain. Nevertheless, considering the nature of the referential data (verosimilar tendency, but not necessarily real) and that the substrate and H_2 concentration profiles achieved a good fit, we concluded the calibration to be acceptable.

Table L.7: Transport parameters calibrated to referential data.

Parameter	**Calibrated value**	**95 % CI**	**P-value (significance)**	**Bibliographic value**
$D_{S,6}$, Effective diffusion coefficient of substrate in domain 6 $[\frac{m^2}{s}]$	3.925e-10	$\begin{bmatrix}1.782\text{e-}10 & 6.068\text{e-}10\end{bmatrix}$	3.460e-04 (very significant)	1.201e-09 [245]
$D_{H,6}$, Effective diffusion coefficient of H_2 in domain 6 $[\frac{m^2}{s}]$	2.498e-09	$\begin{bmatrix}\text{-}5.158\text{e-}09 & 1.015\text{e-}08\end{bmatrix}$	5.220e-01 (not significant)	5.110e-09 [246, 247]

Visual inspection shows that the concentration profiles for both substrate and H_2 are similar to the proposed referential data. Only one referential data point of the H_2 profile is placed at the border of the confidence region. This outlier is due to the defined model parameters to describe the concentration slope near the interface. One boundary condition parameter of this domain was adjusted in a subsequent calibration for the whole CBMem module.

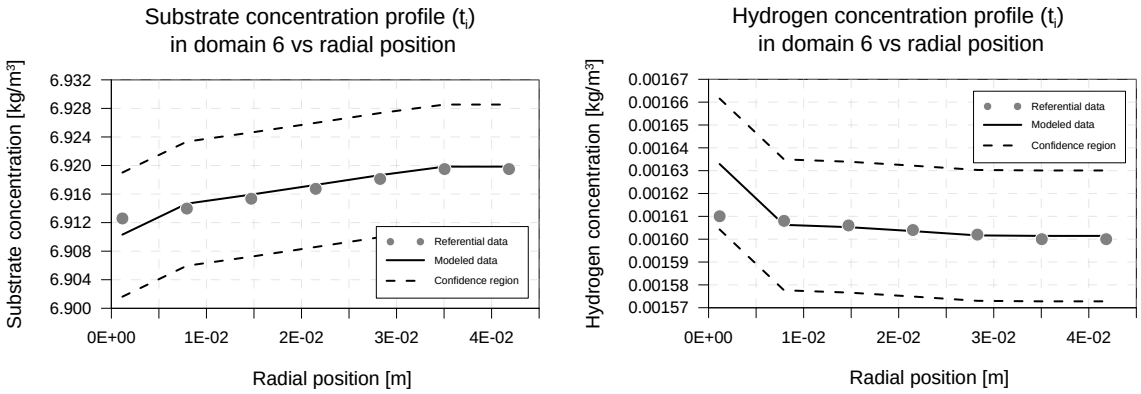

Fig. L.7: Calibration of the mass balance model of domain 6 using the calibrated parameters of Table L.6.

L.2.2. Parameters for domain 4 and 5

Calibration of domains 4 and 5 (at both its inactive and bioactive state) were conducted to estimate the parameters' values. Only the results of the numeric calibration (using *leasqr*) of domain 5 in its inactive state was employed for future modeling. As for the bioactive domains, after some trials we decided to conclude with a manual calibration due to the several unknown parameters and the model's sensitivity to parameter values, which can cause numeric instability.

The parameters ($D_{eff,S,5}$ and $D_{eff,H,5}$) of the mass balance model for domain 5 at its inactive state, represented through the discretization of Eqs.(L.8) and (L.9), were adjusted by considering the fit of the substrate and H_2 concentration profiles to verisimilar data simultaneously.

$$\frac{D_{eff,S,5}}{r}\frac{\partial}{\partial r}\left(r\frac{\partial C_{S,5}}{\partial r}\right)=0 \qquad \text{(L.8)} \qquad\qquad \frac{D_{eff,H,5}}{r}\frac{\partial}{\partial r}\left(r\frac{\partial C_{H,5}}{\partial r}\right)=0 \qquad \text{(L.9)}$$

Table L.8 shows the input and output arguments of the mass balance model calibration for domain 5. Convergence was achieved after one iteration, changing the value of both parameters from their initial guess. The calibrated parameters concluded the modeled concentration profiles shown in Fig. L.8 for domain 5.

Table L.9 summarizes the most relevant comparisons to be discussed. On the one hand, $D_{S,5}$ resulted to be 12 times (1215 %) its bibliographic value. On the other hand, $D_{H,5}$ was 3 times (318 %) its bibliographic value. This difference is due to the numeric steps that we decided to use for the modeling of the CBMem. These steps force the diffusive parameters to remain in a certain range to avoid model instability. In addition, the calibrated parameters can be compared to their confidence interval and their p-values analyzed. On the one hand, the difference from the optimized value of $D_{S,5}$ with respect to its limits is of ± 0.06 %, indicating a high confidence on the estimated parameter. On the other hand, the difference for $D_{H,5}$ is of ± 15 %, which can be considered as acceptable. Both the parameters' p-value are zero compared to the 0.05 significance level, indicating that they probably have a meaningful impact on the model's outcome. It is worth mentioning that these results are subject to the verisimilar data that were used and are, thus, only indicative.

Table L.8: Arguments of the mass balance model calibration for domain 5

Input argument	**Value**
$k0_{D_{eff,S,5}}$	9.600e-10
$k0_{D_{eff,H,5}}$	4.088e-09
tol	1.000e-01
$miter$	20
wts	$[ones(size(C_{SH,5,ref})]$
$dp_{D_{eff,S,6}}$	1.000e-02
$dp_{D_{eff,H,6}}$	1.000e-02
$options.bounds_{D_{eff,S,6}}$	$\begin{bmatrix} 1.000\text{e-}10 & 9.900\text{e-}10 \end{bmatrix}$
$options.bounds_{D_{eff,H,6}}$	$\begin{bmatrix} 1.000\text{e-}09 & 4.500\text{e-}09 \end{bmatrix}$
Output argument	**Value**
$kopt_{D_{eff,S,5}}$	9.329e-10
$kopt_{D_{eff,H,5}}$	3.969e-09
$pval_{D_{eff,S,5}}$	0
$pval_{D_{eff,H,5}}$	0
$CI_{D_{eff,S,5}}$	$\begin{bmatrix} 9.324\text{e-}10 & 9.335\text{e-}10 \end{bmatrix}$
$CI_{D_{eff,H,5}}$	$\begin{bmatrix} 3.358\text{e-}09 & 4.582\text{e-}09 \end{bmatrix}$
cvg	1
$iter$	1

Table L.9: Transport parameters calibrated to referential data.

Parameter	**Calibrated value**	**95 % CI**	**P-value (significance)**	**Bibliographic value**
$D_{S,5}$, Effective diffusion coefficient of substrate in domain 5 $[\frac{m^2}{s}]$	9.329e-10	$\begin{bmatrix} 9.324\text{e-}10 & 9.335\text{e-}10 \end{bmatrix}$	0 (very significant)	7.680e-11 [248]
$D_{H,5}$, Effective diffusion coefficient of H_2 in domain 5 $[\frac{m^2}{s}]$	3.969e-09	$\begin{bmatrix} 3.358\text{e-}09 & 4.582\text{e-}09 \end{bmatrix}$	0 (very significant)	1.250e-09 [249]

Visual inspection shows that the concentration profiles for both substrate and H_2 are similar to the proposed referential data. These remain within the modeled concentrations' confidence region, indicating a good fit.

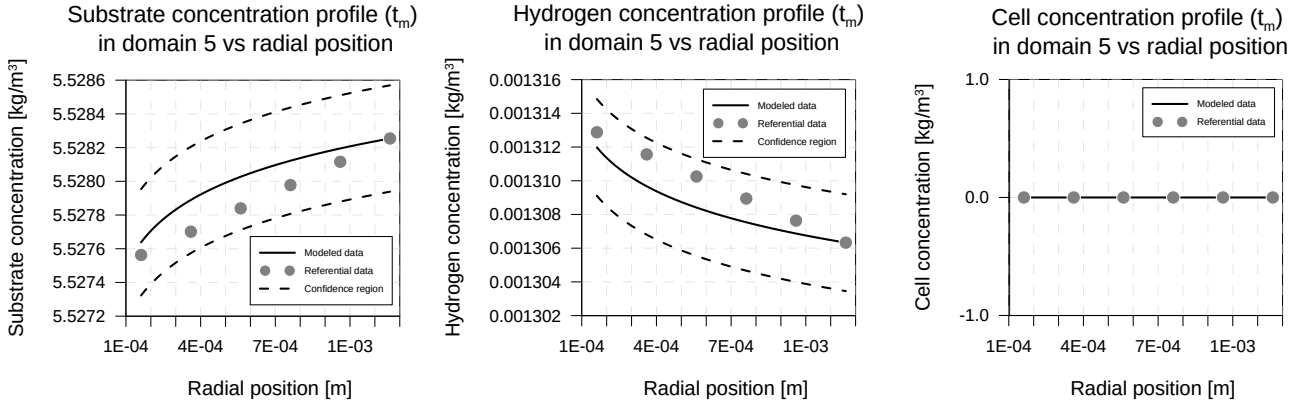

Fig. L.8: Calibration of the mass balance model of domain 5 at its inactive state using the calibrated parameters of Table L.8.

The use of the calibrated parameters of domain 5 in its inactive state and the considered parameters for domain 4 concluded the concentration profiles for the bioactive layer shown in Fig. L.9. The H_2 concentration profile indicate a high dependence of the boundary conditions.

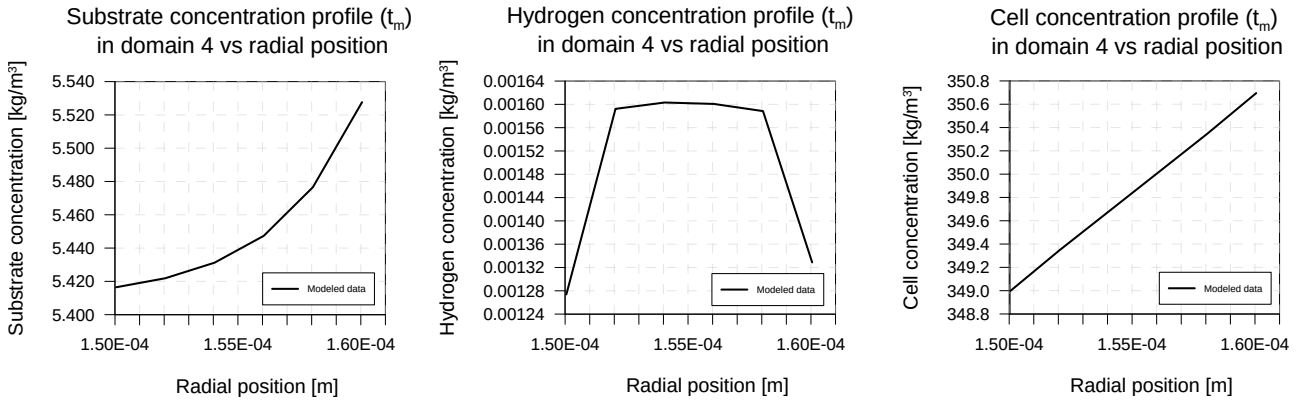

Fig. L.9: Concentration profiles of the mass balance model of domain 4, adjacent to domain 5 in its inactive state, using the calibrated parameters of Table L.8.

The previous results are useful, if domain 5 remains inactive. However, we decided to induce its bioactive state from the start to observe the behavior of cell population and their influence on the substrate and H_2 concentrations. Thus, the parameters for domain 4 and 5, both active, were manually calibrated by considering the concentration profiles of the substrate, H_2, and cells. For this, we tested the influence of changing transport and biological parameters of the mass balance model of domain 5 and 4, represented through the discretization of Eqs. (L.10)-(L.15). Note that the effective diffusion coefficients is defined by Eq. (4.1) and calibration was conducted for the diffusion coefficients in the membrane matrix at inert conditions ($D_{eff,S,5,M}$, $D_{eff,H,5,M}$, $D_{eff,X,5,M}$, $D_{eff,S,4,M}$, $D_{eff,H,4,M}$, $D_{eff,X,4,M}$,).

$$\frac{\partial C_{S,5}}{\partial t} - \frac{1}{r}\frac{\partial}{\partial r}\left(D_{eff,S,5} r \frac{\partial C_{S,5}}{\partial r}\right) = \hat{r}_{S,5} \quad \text{(L.10)}$$

$$\frac{\partial C_{H,5}}{\partial t} - \frac{1}{r}\frac{\partial}{\partial r}\left(D_{eff,H,5} r \frac{\partial C_{H,5}}{\partial r}\right) = \hat{r}_{H,5} \quad \text{(L.11)}$$

$$\frac{\partial C_{X,5}}{\partial t} - \frac{1}{r}\frac{\partial}{\partial r}\left(D_{eff,X,5} r \frac{\partial C_{S,5}}{\partial r}\right) = \hat{r}_{X,5} \quad \text{(L.12)}$$

$$\frac{\partial C_{S,4}}{\partial t} - \frac{1}{r}\frac{\partial}{\partial r}\left(D_{eff,S,4} r \frac{\partial C_{S,4}}{\partial r}\right) = \hat{r}_{S,4} \quad \text{(L.13)}$$

$$\frac{\partial C_{H,4}}{\partial t} - \frac{1}{r}\frac{\partial}{\partial r}\left(D_{eff,H,4} r \frac{\partial C_{H,4}}{\partial r}\right) = \hat{r}_{H,4} \quad \text{(L.14)}$$

$$\frac{\partial C_{X,4}}{\partial t} - \frac{1}{r}\frac{\partial}{\partial r}\left(D_{eff,X,4} r \frac{\partial C_{S,4}}{\partial r}\right) = \hat{r}_{X,4} \quad \text{(L.15)}$$

Table L.10 summarizes the manually calibrated parameters and their comparison with bibliographic values, which will be discussed below. The concluded parameters obtained the modeled concentration profiles shown in Fig. L.10 and L.11, for domain 5 and 4, respectively.

The manual calibration resulted in a significant change of almost all parameters, compared to their bibliographic value. As observed for other domains, this difference is due to the numeric steps that we decided to use for the modeling of the CBMem.

Moreover, we observed that model stability was highly dependent on the substrate concentration behavior due to the species' coupled mass balances. For example, the modeled concentration profiles for all species were stable when assuming a low maximum specific growth constant (μ_{max}) while maintaining the bibliographic reference for the yield of biomass on substrate ($Y_{X/S}$) value. This is because μ_{max} influences directly on the substrate consumption rate. However, this also

means a slow growth of cell population. In turn, it was expected to observe cell growth, especially after simulating for timespans that cover weeks to months. This could be achieved with μ_{max} values close to the bibliographic values. By using referential values for μ_{max} and $Y_{X/S}$, rapid consumption of substrate concentration was observed, reaching its depletion and, consequently, producing model instability.

To ensure model analysis, we concluded the model calibration with a μ_{max} that is 3 % its bibliographic value to achieve enough observable cell growth. Hence, $Y_{X/S}$ considerably needed to be changed: the calibrated yield was 10,000 times its bibliographic value to ensure sufficient substrate concentration within the bioactive domains.

Furthermore, as the biomass decay constant (k_{dec}) operates in the same mathematical term as μ_{max}, we chose consistency over the change of magnitudes, i.e., k_{dec} is proportional to the calibrated μ_{max} parameter and their bibliographic values according to Eq. (L.16). Analogously, this was decided for the microbial maintenance coefficient, as shown in Eq. (L.17).

$$k_{dec} = \frac{k_{dec,bib}}{\mu_{max,bib}} \mu_{max} \qquad \text{(L.16)} \qquad\qquad k_m = \frac{k_{m,bib} Y_{X/S,bib}}{\mu_{max,bib}} \frac{\mu_{max}}{Y_{X/S}} \qquad \text{(L.17)}$$

It should be mentioned that other biological parameters, such as the half-saturation constant, the yield of H_2 on substrate, and the yield of biomass on H_2, did not changed with respect to their bibliographical value.

Table L.10: Transport and biological parameters after manual calibration considering the species' concentration profiles in bioactive domains.

Parameter	**Calibrated value**	**Bibliographic value**
$D_{eff,S,5,M}$, Effective diffusion coefficient of substrate in domain 5 (at inert conditions) $[\frac{m^2}{s}]$	1.000e-17	9.600e-10[a] [247, 250]
$D_{eff,H,5,M}$, Effective diffusion coefficient of H_2 in domain 5 (at inert conditions) $[\frac{m^2}{s}]$	1.000e-17	4.088e-09[a] [247, 250]
$D_{eff,X,5,M}$, Effective diffusion coefficient of cells in domain 5 (at inert conditions) $[\frac{m^2}{s}]$	-1.000e-25	5.000e-11 [251]
$D_{eff,S,4,M}$, Effective diffusion coefficient of substrate in domain 4 (at inert conditions) $[\frac{m^2}{s}]$	1.300e-16	9.600e-10[a] [247, 250]
$D_{eff,H,4,M}$, Effective diffusion coefficient of H_2 in domain 4 (at inert conditions) $[\frac{m^2}{s}]$	1.000e-17	4.088e-09[a] [247, 250]
$D_{eff,X,4,M}$, Effective diffusion coefficient of cells in domain 4 (at inert conditions) $[\frac{m^2}{s}]$	-1.000e-18	5.000e-11 [251]
k_{dec}, Biomass decay constant $\left[\frac{1}{s}\right]$	3.000e-07	9.259e-06 [37, 96]
k_m, Microbial maintenance coefficient $\left[\frac{kg_{COD}}{kg_{cells}\, s}\right]$	1.013e-09	3.125e-04 [37, 96]
μ_{max}, Maximum specific growth rate $\left[\frac{1}{s}\right]$	1.500e-06	4.630e-05 [37]
$Y_{X/S}$, Yield of biomass on substrate $\left[\frac{kg_{cells}}{kg_{COD}}\right]$	15.000e+02	15.000e-02 [37, 96]

[a] Value derived from using $D_{a,d} = f_D \cdot D_{a,6}$, with f_D=0.8 [247, 250].

As shown in Fig. L.10, the concentration profiles for all species in domain 5 fulfill the expected tendency. The substrate concentration presents high values at the most right border, which separates the membrane with the mixed liquor. As the substrate penetrates the domain, it is

consumed, thus decreasing its concentration. The rate of this consumption is higher in the most left border, where cells are present in higher concentrations. However, when considering the axis-values, small change in the substrate concentration is observed. This is due to the small timespan and the calibrated biological parameters. Lastly, for temporal points that are different to the initial time, a peak can be observed at the most right border, which is produced due to the imposed border condition, but also due to the model sensitivity to concentration differences described in its mass balance.

The H_2 concentration in Fig. L.10 is analogous to the substrate concentration. H_2 concentration that is already within the wastewater enters the membrane and diffuses. The concentration profile is influenced by the cylindrical shape of the CBMem. Moreover, for more advanced time points, a small increase of the H_2 concentration can be observed at the most left positions. This tendency is due to the biological H_2 production, which is a consequence of the cell population.

Finally, the cell concentration shows peaks at the most left border, and decreases towards the right border. Moreover, we can clearly observe an increase of cell concentration over time. This trend is consistent with the expected cell migration and growth behavior for a small timespan.

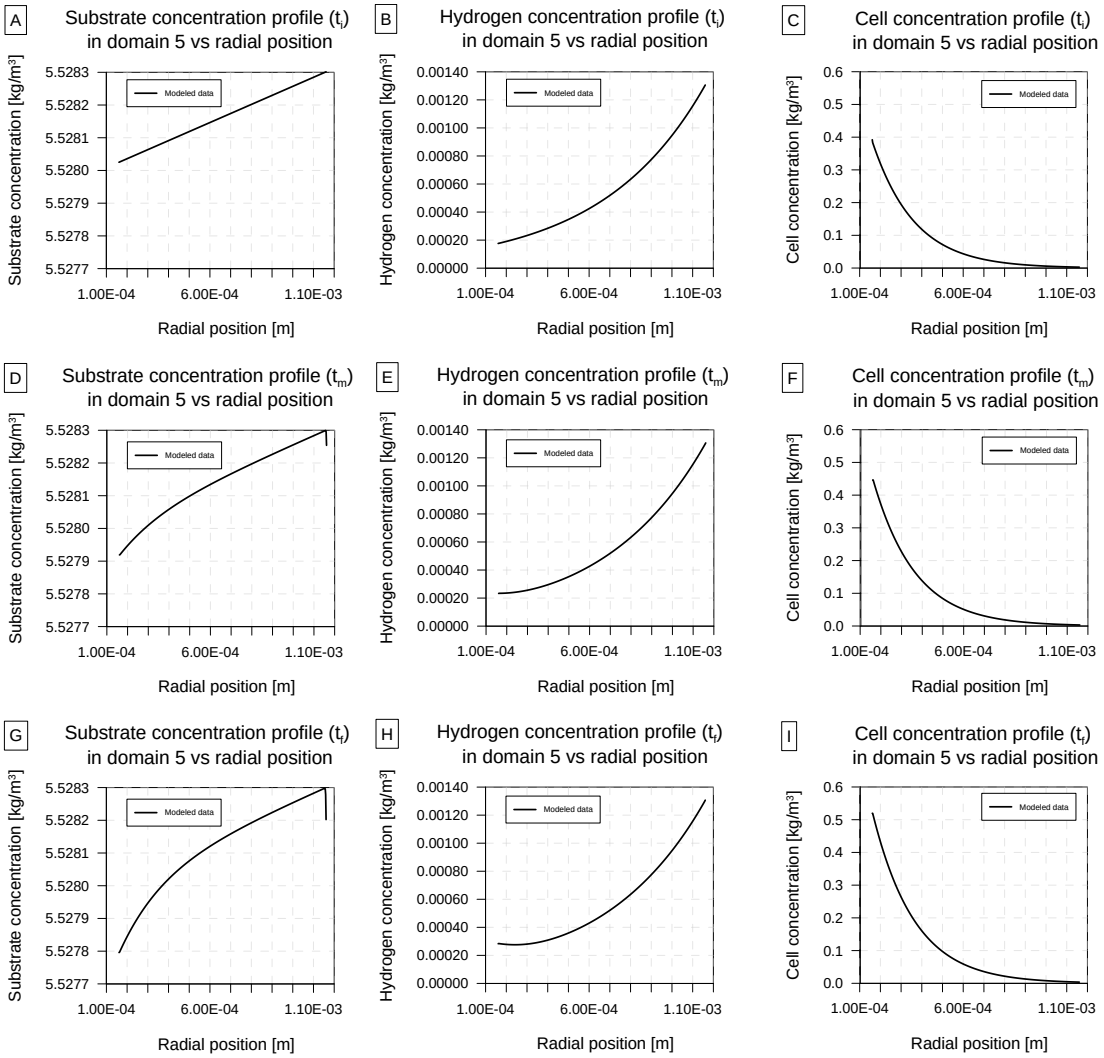

Fig. L.10: Manual calibration of the mass balance of domain 5 at its bioactive state using the parameter values of Table L.10.

Moreover, from Fig. L.11 it can be concluded that the substrate and cell concentration profiles are aligned with the expected tendencies in domain 4, while the H_2 concentration profile is a rather interesting outcome. The substrate concentration presents high values at the most right border, which is closer to the mixed liquor. As the substrate penetrates the domain, it is consumed, thus decreasing its concentration. Due to the high presence of cells within this domain, the consumption rate allows to observe a notorious decrease of substrate in both space and time. This rate is higher in the most right border, where cells are present in higher concentrations.

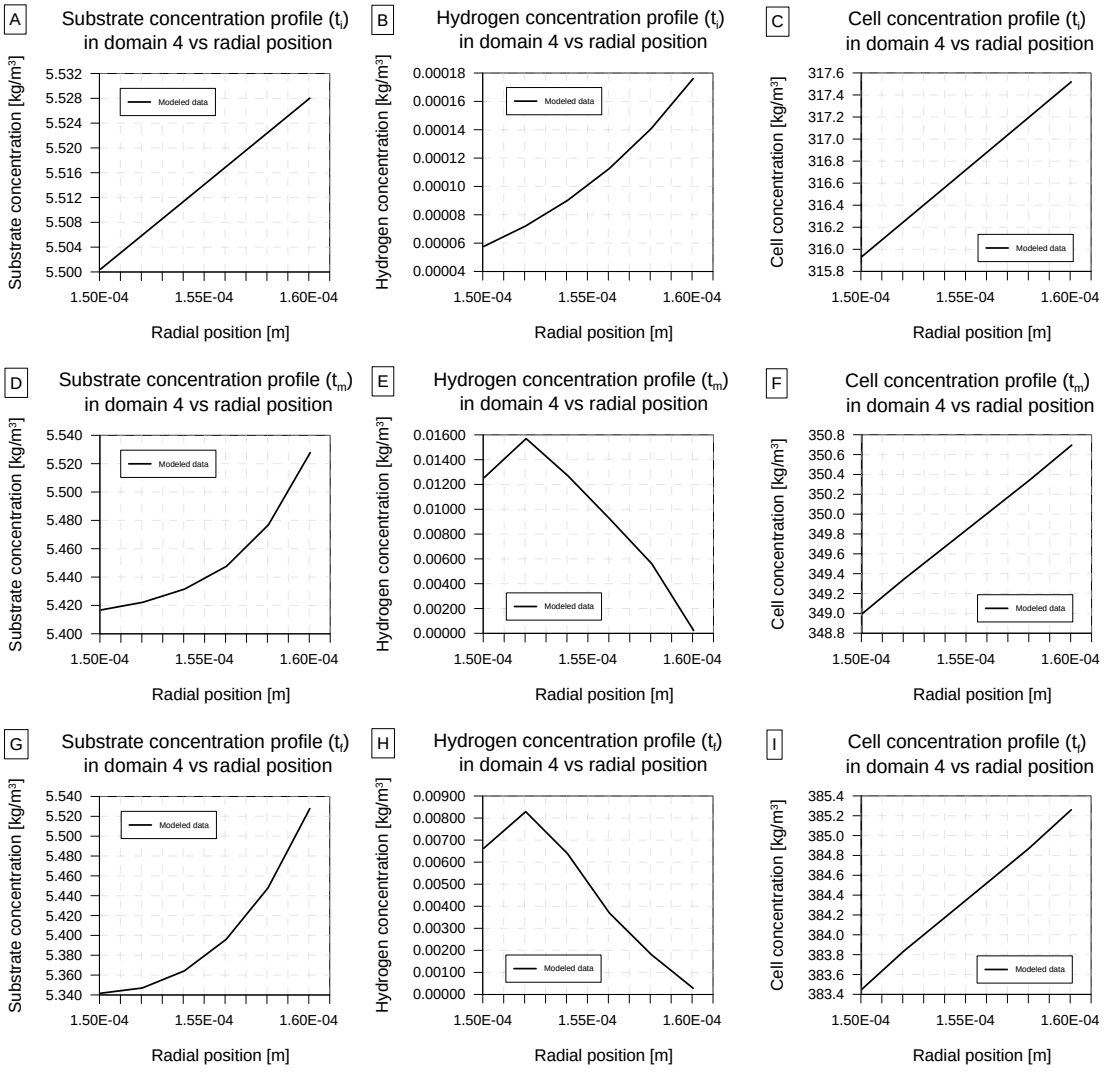

Fig. L.11: Manual calibration of the mass balance of domain 4 using the parameter values of Table L.10

The H_2 concentration in Fig. L.11B shows the expected tendency for the initial moment; higher concentrations are correlated to the most right position, being close to the mixed liquor and higher cell concentrations. However, this tendency changes, developing a concentration peak towards a radial position that is closer to the left border. The observed peak could be attributed to the imposed boundary conditions at both borders. In addition, as shown in Fig L.11E, the H_2 concentration profile increases significantly its value compared to the initial condition. However, when comparing it with Fig L.11H, the concentration values decreases, diminishing the peak. A possible explanation for this might be the model sensitivity towards concentration differences at adjacent positions. We also conclude that, due to the small domain width, this would not affect

the overall biological phenomena analysis.

Finally, the cell concentrations maintain the tendency as the initial condition, showing higher values at the most right border and lower values towards the left border. Moreover, the cell concentrations increase over time, which is attributed to the cell growth.

In conclusion, calibration of bioactive domains is difficult to conduct, especially if not sufficient and reliable data is available. The considered values, shown in Table L.10, should not be interpreted as the physical meaning of biological and transport parameters. For example, these values induce concentration profiles based on the assumption of sufficient substrate concentration for biological phenomena. However, according to the observed modeling results, the substrate concentration in the wastewater feed stream ($6.92\frac{g}{L}$) of the experimental set-up (Table G.1) is not sufficient for wastewater-to-H_2 operations. Therefore, the results by using the calibrated parameters do not represent accurately the case study. Nevertheless, the calibrated values allowed to observe and analyse the model's capacity to simulate biological behavior coherently.

We also observed that the selection of the numerical steps is incidental on the parameter's value to ensure model stability. Stability analysis is highly recommended to obtain stability conditions for each mass balance and avoid time-consuming simulation trials. This condition would provide a relationship between diffusion coefficients and the modeling steps for both space and time. By imposing the modeling steps, it is straightforward to conclude the parameter's value than otherwise. However, as this produce deviation from the parameter's expected values, future research can explore the search for appropriate combinations of modeling steps from a stability analysis based on more realistic parameter values.

L.2.3. Parameters for domain 3

The parameters ($D_{eff,S,3}$ and $D_{eff,H,3}$) of the mass balance model for domain 3, represented through Eqs.(L.18) and (L.19), were adjusted by considering the fit of the substrate and H_2 concentration profiles to verisimilar data simultaneously.

$$\frac{D_{eff,S,3}}{r}\frac{\partial}{\partial r}\left(r\frac{\partial C_{S,3}}{\partial r}\right)=0 \qquad \text{(L.18)} \qquad\qquad \frac{D_{eff,H,3}}{r}\frac{\partial}{\partial r}\left(r\frac{\partial C_{H,3}}{\partial r}\right)=0 \qquad \text{(L.19)}$$

Table L.11 shows the input and output arguments of the mass balance model calibration for domain 3. Convergence was achieved after 4 iteration, changing the value of both parameters from their initial guess. The calibrated parameters concluded the modeled concentration profiles shown in Fig. L.12 for domain 3.

Table L.12 summarizes the most relevant comparisons to be discussed. On the one hand, $D_{S,3}$ resulted to be 0.005 % its bibliographic value. On the other hand, $D_{H,3}$ was 2 % its bibliographic value. This difference is due to the numeric steps that we decided to use for the modeling of the CBMem. In addition, the calibrated parameters can be compared to their confidence interval. As for the first parameter, the p-value showed that it is not significant; the second parameter is not so. Moreover, the difference from the first parameter's optimized value with respect to its limits is of ±2230 % indicating a low confidence on the estimated parameter. In turn, the difference for the second parameter is ±0.005 %, which can be considered as acceptable. It is worth mentioning that these results are subject to the verisimilar data that were used and are, thus, only indicative.

Visual inspection shows that the concentration profiles for substrate and H_2 are similar to the proposed referential data. These remain within the confidence region, indicating a good fit.

Table L.11: Arguments of the mass balance model calibration for domain 3

Input argument	**Value**
$k0_{D_{eff,S,3}}$	1.000e-15
$k0_{D_{eff,H,3}}$	2.000e-10
tol	1.000e-03
$miter$	10
wts	$[ones(size(C_{SH,3,ref})]$
$dp_{D_{eff,S,3}}$	1.000e-03
$dp_{D_{eff,H,3}}$	1.000e-01
$options.bounds_{D_{eff,S,3}}$	[1.000e-16 9.000e-13]
$options.bounds_{D_{eff,H,3}}$	[5.000e-12 9.000e-10]
Output argument	**Value**
$kopt_{D_{eff,S,3}}$	5.497e-16
$kopt_{D_{eff,H,3}}$	5.000e-12
$pval_{D_{eff,S,3}}$	9.299e-01
$pval_{D_{eff,H,3}}$	0
$CI_{D_{eff,S,3}}$	[-1.171e-14 1.281e-14]
$CI_{D_{eff,H,3}}$	[4.999e-12 5.000e-12]
cvg	1
$iter$	4

Table L.12: Transport parameters calibrated to referential data.

Parameter	**Calibrated value**	**95 % CI**	**P-value (significance)**	**Bibliographic value**
$D_{S,3}$, Effective diffusion coefficient of substrate in domain 3 $[\frac{m^2}{s}]$	5.497e-16	[-1.171e-14 1.281e-14]	9.299e-01 (not significant)	1.160e-11 [248]
$D_{H,3}$, Effective diffusion coefficient of H_2 in domain 3 $[\frac{m^2}{s}]$	5.000e-12	[4.999e-12 5.000e-12]	0 (very significant)	2.100e-10 [252]

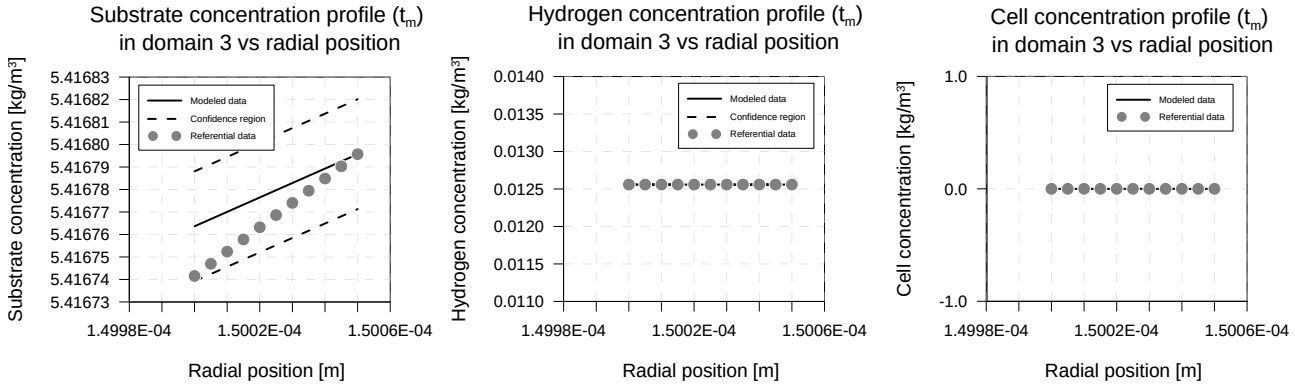

Fig. L.12: Calibration of the mass balance of domain 3 using the calibrated parameters of Table L.11.

L.2.4. Parameters for domain 2

The parameter ($D_{eff,H,2}$) of the mass balance model for domain 2, represented through Eq. (L.20), was adjusted by considering the fit of the H_2 concentration profile to verisimilar data.

$$\frac{D_{eff,H,2}}{r}\frac{\partial}{\partial r}\left(r\frac{\partial C_{H,2}}{\partial r}\right) = 0 \tag{L.20}$$

Table L.13 shows the input and output arguments of the mass balance calibration for domain 2. Convergence was achieved after two iterations, changing the parameter's value from its initial guess. The calibrated parameter concluded the concentration profile shown in Fig. L.13.

Table L.13: Arguments of the mass balance model calibration for domain 2

Input argument	**Value**
$k0_{D_{eff,H,2}}$	2.100e-10
tol	1.000e-01
$miter$	10
wts	$[ones(size(C_{S,2,ref})]$
$dp_{D_{eff,H,2}}$	1.000e-01
$options.bounds_{D_{eff,H,2}}$	$\begin{bmatrix}1.000\text{e-}10 & 3.000\text{e-}10\end{bmatrix}$
Output argument	**Value**
$kopt_{D_{eff,H,2}}$	1.000e-10
$pval_{D_{eff,H,2}}$	0
$CI_{D_{eff,H,2}}$	$\begin{bmatrix}9.999\text{e-}11 & 1.000\text{e-}10\end{bmatrix}$
cvg	1
$iter$	2

Table L.14 summarizes the most relevant comparisons to be discussed. $D_{H,2}$ resulted to be 48 % its bibliographic value. This difference is due to the numeric steps that we decided to use for the modeling of the CBMem. In addition, the difference from the optimized value of $D_{H,2}$ with respect to its limits is of ±3.586e-06 %, indicating a high confidence on the estimated parameter. It is worth mentioning that this result is subject to the verisimilar data that were used and is, thus, only indicative.

Table L.14: Transport parameters calibrated to referential data.

Parameter	**Calibrated value**	**95 % CI**	**P-value (significance)**	**Bibliographic value**
$D_{H,2}$, Effective diffusion coefficient of H_2 in domain 2 $[\frac{m^2}{s}]$	1.000e-10	$\begin{bmatrix}9.999\text{e-}11 & 1.000\text{e-}10\end{bmatrix}$	0 (very significant)	2.100e-10 [252]

Visual inspection shows that the H_2 concentration profile is similar to the proposed referential data. These remain within the modeled concentrations' confidence region, indicating a good fit.

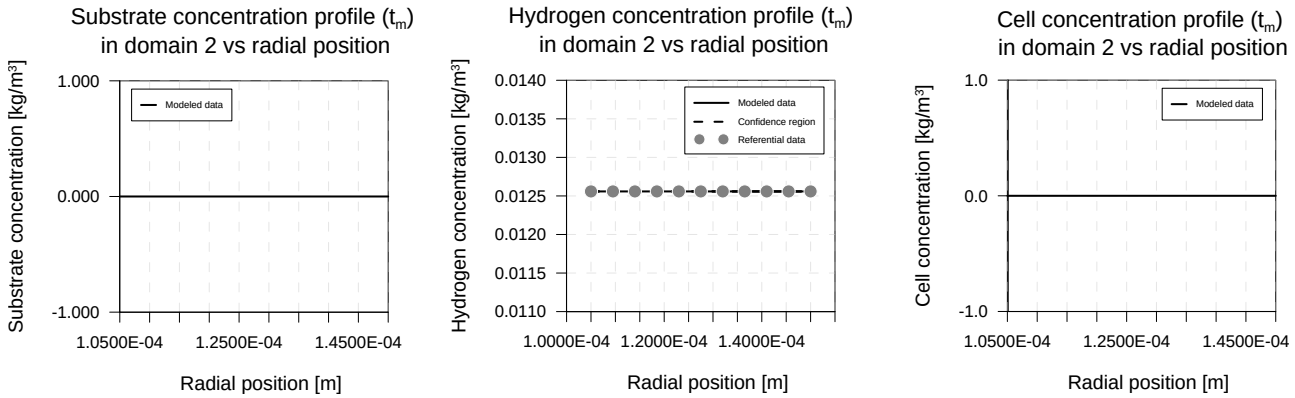

Fig. L.13: Calibration of the mass balance model of domain 2 using the calibrated parameter of Table L.13.

L.2.5. Parameters for domain 1

The parameter ($D_{H,1}$) of the mass balance model for domain 1, represented through Eq. (L.21), was adjusted by considering the fit of the H−2 concentration profile to verisimilar data.

$$v_{z,1}\frac{\partial C_{H,1}}{\partial z} = D_{eff,H,1}\left(\frac{1}{r}\frac{\partial C_{H,1}}{\partial r} + \frac{\partial^2 C_{H,1}}{\partial r^2}\right) \tag{L.21}$$

Table L.15 shows the input and output arguments of the mass balance model calibration for domain 1. Convergence was achieved after one iteration, changing the parameter's value from its initial guess. The calibrated parameter concluded the modeled concentration profiles shown in Fig. L.14 for domain 1.

Table L.15: Arguments of the mass balance model calibration for domain 1

Input argument	**Value**
$k0_{D_{H,1}}$	2.000e-10
tol	1.000e-01
$miter$	10
wts	$[ones(size(C_{H,1,ref})]$
$dp_{D_{H,1}}$	1.000e-01
$options.bounds_{D_{H,1}}$	$\begin{bmatrix}1.000\text{e-}10 & 5.000\text{e-}10\end{bmatrix}$
Output argument	**Value**
$kopt_{D_{H,1}}$	1.930e-10
$pval_{D_{H,1}}$	0
$CI_{D_{H,1}}$	$\begin{bmatrix}1.662\text{e-}10 & 2.198\text{e-}10\end{bmatrix}$
cvg	1
$iter$	1

Table L.16 summarizes the most relevant comparisons to be discussed. $D_{H,1}$ resulted to be 2.000e-04 % its bibliographic value. In addition, the difference from the optimized value of $D_{H,1}$ with respect to its limits is of ±14 %, indicating an acceptable confidence on the estimated parameter. It is worth mentioning that this result is subject to the verisimilar data that were used and is, thus, only indicative.

Table L.16: Transport parameters calibrated to referential data.

Parameter	**Calibrated value**	**95 % CI**	**P-value (significance)**	**Bibliographic value**
$D_{H,1}$, Effective diffusion coefficient of H_2 in domain 1 $[\frac{m^2}{s}]$	1.930e-10	[1.662e-10 2.198e-10]	0 (very significant)	7.960e-5 [247]

Visual inspection showed that the H_2 concentration profile is not similar to the proposed referential data as these do not remain within the modeled concentrations' confidence region, indicating a poor fit. This is due to the considered boundary condition based on Henry-like equilibrium and the calibrated diffusive parameter that influences the sharp decrease near the border. Furthermore, the referential data are not necessarily representing real tendency. Thus, we decided to continue with the calibrated parameter.

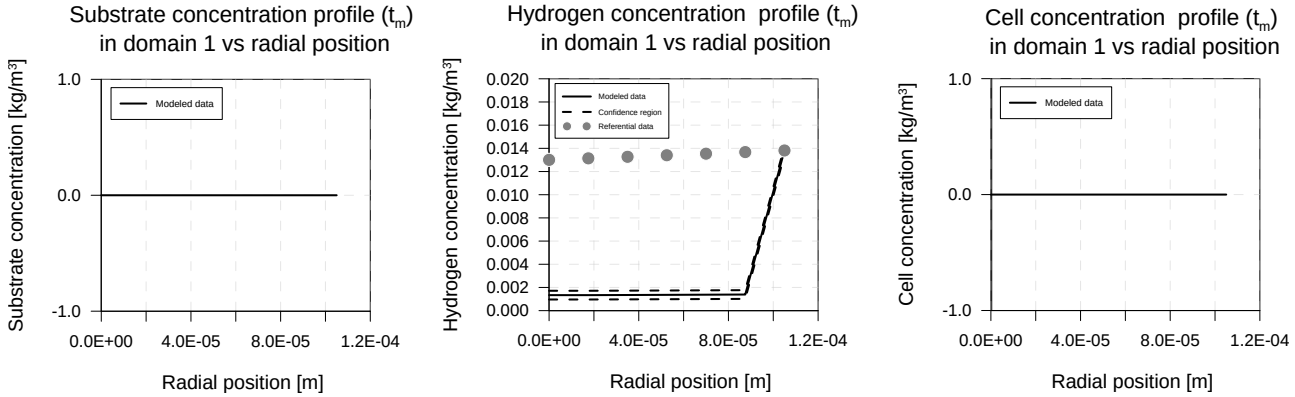

Fig. L.14: Calibration of the mass balance model of domain 1 using the calibrated parameter of Table L.15.

L.3. CBMem parameters

As explained in Section 6.1.3, three consecutive calibrations were conducted over the complete CBMem modeling, considering the model fitting with experimental data. Tables L.17-L.19 show the input and output arguments of the parameter calibrations.

Table L.17: Arguments of the first CBMem model calibration.

Input argument	**Value**
$k0_{H_{H,5,6}}$	8.000e-01
$k0_{H_{H,1,2}}$	11.000e-01
tol	1.000e-03
$miter$	20
wts	$[ones(size(F_{H-G,out,ref})]$
$dp_{H_{H,5,6}}$	1.000e-01
$dp_{H_{H,1,2}}$	1.000e-01
$options.bounds_{H_{H,5,6}}$	$\begin{bmatrix}7.500\text{e-}01 & 9.999\text{e-}01\end{bmatrix}$
$options.bounds_{H_{H,1,2}}$	$\begin{bmatrix}11.000\text{e-}01 & 20.000\text{e-}01\end{bmatrix}$
Output argument	**Value**
$kopt_{H_{H,5,6}}$	9.999e-01
$kopt_{H_{H,1,2}}$	10.574e-01
$pval_{H_{H,5,6}}$	0
$pval_{H_{H,1,2}}$	8.582e-03
$CI_{H_{H,5,6}}$	$\begin{bmatrix}9.512\text{e-}01 & 10.488\text{e-}01\end{bmatrix}$
$CI_{H_{H,1,2}}$	$\begin{bmatrix}2.989\text{e-}01 & 18.158\text{e-}01\end{bmatrix}$
cvg	1
$iter$	1

Table L.18: Arguments of the second CBMem model calibration.

Input argument	**Value**
$k0_{k_{3,H,6}}$	9.999e-12
tol	1.000e-01
$miter$	20
wts	$[ones(size(F_{H-G,out,ref})]$
$dp_{k_{3,H,6}}$	1.000e-01
$options.bounds_{k_{3,H,6}}$	$\begin{bmatrix}7.000\text{e-}12 & 9.999\text{e-}12\end{bmatrix}$
Output argument	**Value**
$kopt_{k_{3,H,6}}$	9.999e-12
$pval_{k_{3,H,6}}$	0
$CI_{k_{3,H,6}}$	$\begin{bmatrix}9.4294\text{e-}12 & 1.057\text{e-}11\end{bmatrix}$
cvg	1
$iter$	1

Table L.19: Arguments of the third CBMem model calibration.

Input argument	**Value**
$k0_{\mu_{max}}$	1.500e-06
tol	1.000e-03
$miter$	20
wts	$[ones(size(F_{H-G,out,ref})]$
$dp_{\mu_{max}}$	1.000e-01
$options.bounds_{\mu_{max}}$	$\begin{bmatrix}1.480\text{e-}06 & 1.500\text{e-}06\end{bmatrix}$
Output argument	**Value**
$kopt_{\mu_{max}}$	1.480e-06
$pval_{\mu_{max}}$	0
$CI_{\mu_{max}}$	$\begin{bmatrix}1.476\text{e-}06 & 1.484\text{e-}06\end{bmatrix}$
cvg	1
$iter$	1

L.4. CBMem simulation for six months

As explained in Section 7, process simulation was conducted by considering the calibrated model for a six month operation. Fig. L.15A-C shows the species concentration profiles in domain 5 in its bioactive state in detail through nine different times. Similarly, Fig. L.15D-F represent domain 4.

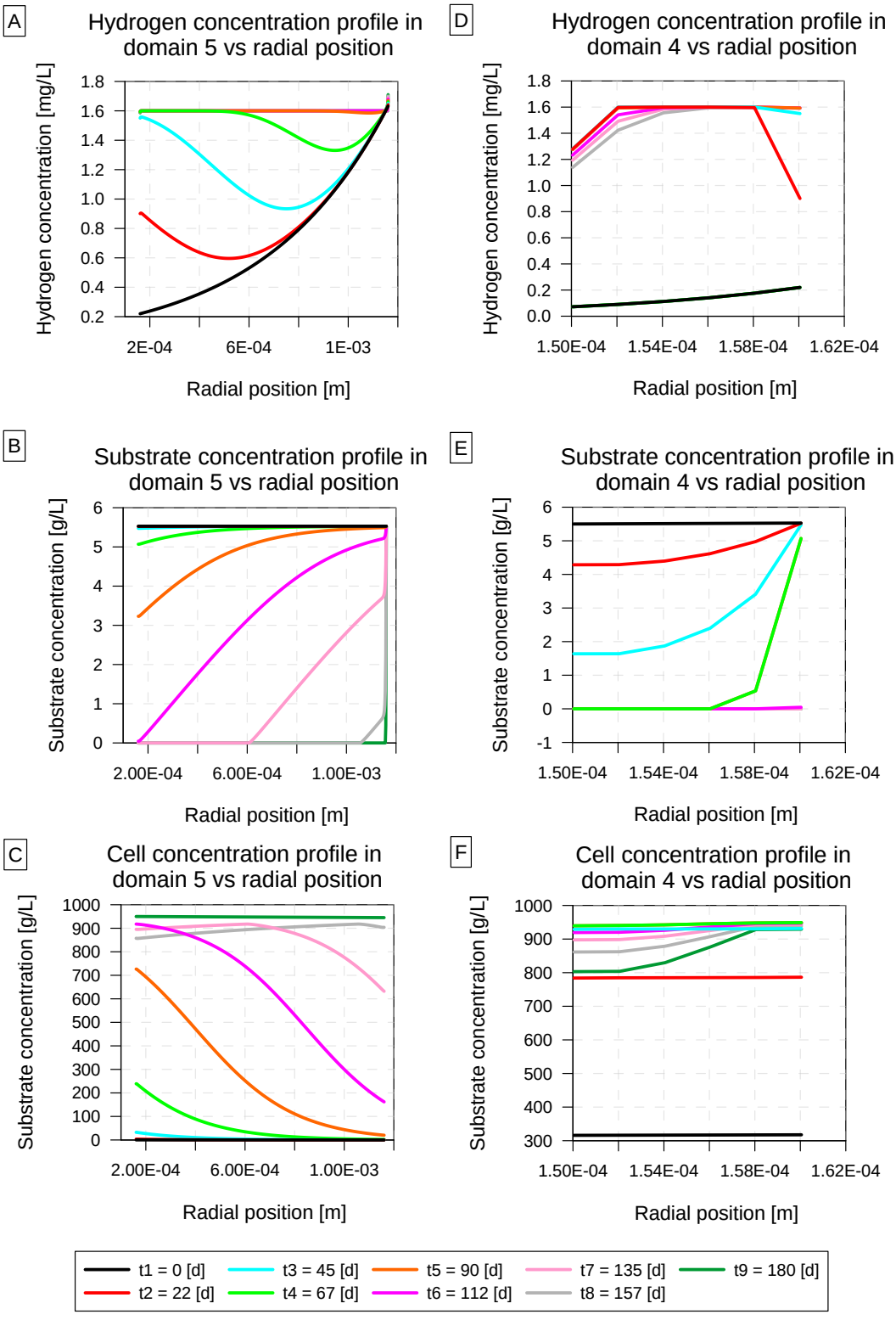

Fig. L.15: Substrate concentration profiles in domain 5 (sealant layer) during a six months operation.

L.5. Sensitivity analysis on initial immobilized cell layer width

The last sensitivity analysis was conducted on the change of initial immobilized cell layer width (Δr_4), comparing three cases: 10.75 μm, 16.13 μm, and 21.50 μm. Fig. L.16 and L.17 present the sensitivity analysis of the H_2 yield and capture efficiency on Δr_4. It is apparent from these figures that the tendencies are similar as those presented in the previous section when studying the effect of initial cell mass and the most likely cause of increase of these performance indicators is product formation associated with cell growth.

What is interesting about the data in Fig. L.16 is that the chosen cases of layer width improve H_2 compared to the cases of initial cell mass. For example, the yield of 4.8 $\frac{ml\,H_2}{g\,COD}$ grew to 6.6 $\frac{ml\,H_2}{g\,COD}$ when increasing Δr_4) from 10.75 μm to 16.13 μm. The increase to 21.50 μm produced a yield of 7.9 $\frac{ml\,H_2}{g\,COD}$, i.e., an increase in 65 % compared to the base case yield.

As for the capture efficiency, Fig. L.17 also shows a a clear trend of increasing its values for greater widths. The most favorable condition was observed when using the highest width (21.50 μm), resulting in an efficiency of 70.9 %, i.e., an increase in 23 % compared to the base case.

Table L.20 summarizes the lifespan results based on the proposed definitions and sensitivity analysis. The CBMem lifespan can be predicted for all analysis. What stands out in this table is the undefined lifespan when considering the H_2 capture efficiency criteria with a threshold of 30 %, which equals the result of the before-mentioned sensitivity analysis

The results can be analyzed according to the worst scenarios: (1) the base case (Δr_4=10.75 μm) had a membrane life of 112.5 days (3.75 months), (2) the life a CBMem with an initial Δr_4 of 16.13 μm would end at day 102.3 (3.4 months), and (3) the CBMem would be replaced after 102.8 days (3.4 months) when starting operation from 21.50 μm. Overall, the membrane's lifespan could be reduced by 10 days, while the effect of increasing in 50 % and 100 % the layer's width would not be of a significant difference.

Although the worst scenario for the base case is a result of considering the H_2 capture efficiency, this criteria shows an increase of the membrane's life for greater widths, even to such an extend that the case of a Δr_4 of 21.50 μm would not risk its lifespan. However, worst scenario for the sensibility cases were concluded according to the cell concentration in bioactive domains criteria. This is coherent with the provided explanation for the gradual increase in the average H_2 yield and efficiency.

When considering cell concentration criteria, the CBMem lifespan was modeled between 144 - 159 days (for 10.75 μm), 102.3 - 141 days (for 16.13 μm), and 102.8 - 141.8 days (for 21.50 μm). Hence, both analyzed variations in the layer's width showed earlier membrane deterioration. The possible reason why the CBMem life has declined is that cells would have more space to grow. However, Contrary to this explanation, the sensibility analysis did not find a significant difference between the width's increase in 50 % and 100 %. Thus, an alternative explanation for this result is that the overall cell growth rates were similar in time and the cell concentration tended to reach the maximum cell capacity. It is also likely to be related to the low mass trans-

fer of the calibrated model; thus, domain widths would no induce a pronounced effect on this result.

Finally, lifespan reduction was observed for higher width according to the substrate depletion criteria. Analogous to the other conducted sensibility analysis, this may demonstrates the causal role of cell concentration in the substrate concentration.

This analysis has identified that initial immobilized cell layer width impacts positively on the H_2 yield and H_2 efficiency, because of enhanced cell growth due to space availability. Thus, H_2 formation is stimulated. Despite this encouraging result, a trade-off relation between cell growth-associated H_2 yield and efficiency and biological-based membrane deterioration was concluded.

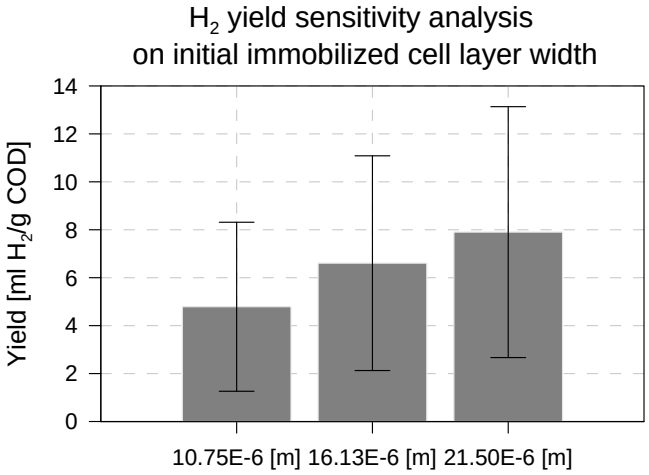

Fig. L.16: Sensitivity analysis of H_2 yield on immobilized cell layer width.

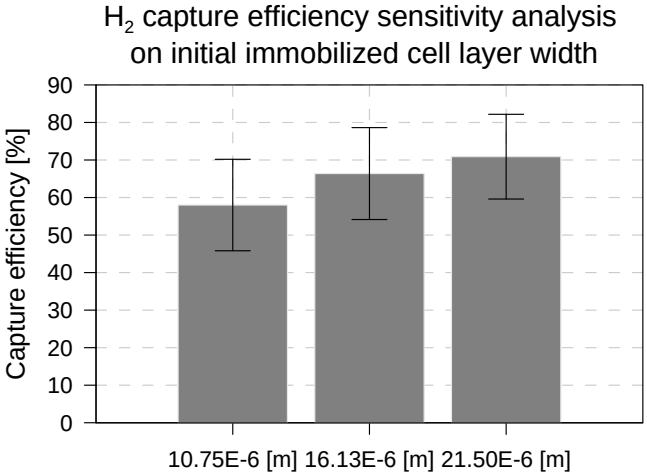

Fig. L.17: Sensitivity analysis of H_2 capture efficiency immobilized cell layer width.

Table L.20: CBMem lifespan analysis according to different criteria.

Criteria	**Threshold**	**Life [days] when Δr_4=10.75 [μm]**	**Life [days] when Δr_4=16.13 [μm]**	**Life [days] when Δr_4=21.50 [μm]**
H_2 capture	$\leq 50\,\%$	112.5	173.3	NA[a]
efficiency	$\leq 30\,\%$	NA[a]	NA[a]	NA[a]
Cell concentration in	$\geq 30\,\%\ C_{X,max}$ [b]	144	102.3	102.8
bioactive domains	$\geq 50\,\%\ C_{X,max}$ [b]	148	123.8	124.3
	$\geq 70\,\%\ C_{X,max}$ [b]	159	141	141.8
Substrate concentration	$\leq 50\,\% C_{S,6,z_0}$ [c]	127.5	104.8	105.5
in bioactive domains	$\leq 30\,\% C_{S,6,z_0}$ [c]	148.5	118.8	119.8

[a] NA = Not available; [b] $C_{X,max} = 950\ \frac{kg}{m^3}$; [c] $C_{S,6,z_0} = 6.92\ \frac{kg}{m^3}$